

**DEVELOPMENT AND APPLICATION OF NEW CONSTITUTIVE MODELS TO
SIMULATE THE HYDRAULIC-MECHANICAL BEHAVIOUR OF
UNSATURATED SWELLING CLAY**

by

DENI GUNAWAN PRIYANTO PUTRO

A Thesis
Submitted to the Faculty of Graduate Studies
In Partial Fulfillment of the Requirements for the Degree of

DOCTOR OF PHILOSOPHY

Department of Civil Engineering
University of Manitoba
Winnipeg, Manitoba, Canada

© August 2007

ABSTRACT

Unsaturated swelling clays are used in engineered barriers for waste disposal facilities due to their self-sealing ability and low hydraulic conductivity. The characterization of unsaturated clay behaviour is required for design of these barriers. In recent years, several small-scale laboratory and full-scale field tests have been conducted to characterize the mechanical and hydraulic behaviour of the unsaturated swelling clay.

This focus of the present study is towards the development of constitutive models to simulate hydraulic and mechanical behaviour of precompacted unsaturated swelling clay, called the bentonite-sand buffer (BSB) material. Development, calibration, implementation, and application of the proposed constitutive models form the scope of the study.

The results of laboratory triaxial tests with controlled suction and suction measurements are used to calibrate the constitutive models presented. An algorithm, called the PEM (Parameter Evaluation Method), which is useful to estimate constitutive model parameters and evaluate the performance of constitutive models is proposed. This algorithm has been used to estimate the parameters of two elasto-plastic constitutive models (i.e., the BBM (Alonso et al. 1990) and the BGM (Blatz and Graham 2003)) based on the laboratory tests results on the BSB material.

New 3-dimensional porosity-dependent permeability model (kwn) and water retention surface (WRS) are developed in this study. The mathematical formulations of these models using parameters calibrated with laboratory tests conducted on the BSB material are provided. Implementation algorithms of the BBM, the BGM, the kwn, and the WRS in 2-phase flow hydraulic-mechanical (H-M) analysis using a 2D-finite difference method are also provided .

Three combinations of hydraulic and mechanical constitutive models (linear elastic model, BGM, vanGenuchten (1980) and kwn models) are used to simulate small-scale infiltration processes in the BSB material. Two types of tests, constant volume (CV) and constant mean stress (CMS) tests are simulated using 2D-finite difference H-M analysis.

The full-scale isothermal test (ITT) of AECL is modelled using 3 combinations of H-M constitutive models. The ITT experiment comprises of buffer, rock, and concrete materials. The selected combinations of H-M constitutive models are used in three types of analyses: buffer-only (BO); buffer-rock with 20x30m domain (BR); and time-dependent boundary conditions (BCt).

The results of the study show that the applications of the elasto-plastic mechanical constitutive models and porosity-dependent permeability (kwn) model are improvements over existing constitutive models to model this class of problem. The rock properties and applied boundary conditions are significant in modelling the ITT experiment. The application of the time-dependent boundary condition can reduce the uncertainty of the rock properties and boundary conditions within the rock, so that it improves the model ability to simulate the hydraulic-mechanical behaviour of unsaturated swelling clay.

dedicated to:

HIM

*"Dia
turut bekerja dalam segala sesuatu untuk mendatangkan
kebaikan bagi mereka yang mengasihi
Dia"*

(17.8.2007)

ACKNOWLEDGEMENTS

I wish to give sincerest thanks to my advisor, Dr. James Blatz, for his patience, guidance, friendship, support, and encouragement throughout this study. The opportunity that he provided to start this study has been a life changing experience for me. I am looking forward to working together with him in the future.

Thanks also to Dr. Greg Siemens for his friendships, discussions, and encouragements throughout the program. I would like to sincerely thank Dr. Neil Chandler, Dr. Brian Stimpson, Dr. Sai Vanapalli, and Dr. Jonathan Bartley that have taken incredible amount of time to review this thesis and given constructive suggestions. Thanks to Dr. Marolo Alfaro, Dr. Jim Graham, Dr. Bruce Kjartanson, Dr. Jamie VanGulck, and Dr. Gary Wang that have provided valuable discussions during this study. Special thanks to Dr. David Dixon, Dr. Alex Man, Dr. Ruiping Guo, Mr. Peter Baumgartner, Mr. Paul Thompson, Mr. Jason Martino, and Dr. Peter Sargent of Atomic Energy of Canada Limited (AECL) for their support, and encouragement throughout the completion of this program. The author would like to acknowledge the financial support provided by Atomic Energy of Canada Limited (AECL), Natural Sciences and Engineering Research Council of Canada, the friends and colleagues of Neil Burgess, and Ontario Power Generation. Thanks to all University of Manitoba geotechnical engineering graduate students for their friendships and encouragement. Valuable discussions with Yadav Pathak, Chang-Seok Kim, and Mike VanHelden are acknowledged.

I would like to sincerely thanks my new friends in Winnipeg that have been very helpful, especially Mark and Liz Stone, Mr. Richard and Mrs. Esther Quiring, and Budi Trisno. I would like to show my sincerest gratitude to Mr. Raymond and Mrs. Betty McCready for their neverending help, care, and encouragement since the beginning of my 'journey' in Canada. Special thanks to family that has always been very supportive: 'Papi' Yapi and 'Mami' Pujiastuti Priyanto, 'Cik' Imelda, 'Koh' Octavianus, 'Koh' Hengki, Yongki, 'Emak' Siong. Finally the most special thanks to my beautiful-but-smart fiancée, Amina Radyastuti, who has been very supportive, loving, and caring, since the beginning of this 'journey' in Niagara Falls.

TABLE OF CONTENTS

ABSTRACT	i
ACKNOWLEDGEMENTS	iv
TABLE OF CONTENTS	v
LIST OF TABLES	ix
LIST OF FIGURES.....	x
LIST OF SYMBOLS AND ABBREVIATIONS.....	xvi
CHAPTER 1 INTRODUCTION	1
1.1 General Overview.....	1
1.2 Background	5
1.2.1 General	5
1.2.2 Development of New Hydraulic-Mechanical Constitutive Models.....	6
1.3 Scope	10
1.4 Definitions.....	10
1.5 Objectives.....	11
1.6 Organization of Thesis.....	12
CHAPTER 2 LITERATURE REVIEW	19
2.1 Introduction.....	19
2.2 Mechanical Constitutive Models	19
2.2.1 Stress-state Variables.....	19
2.2.2 Mechanical Constitutive Models for Unsaturated Soils	21
2.2.2.1 Linear Elastic Model	21
2.2.2.2 Mohr-Coulomb Model.....	22
2.2.2.3 Critical State Model	22
2.3 Hydraulic Constitutive Models	28
2.3.1 Water Retention Curve (WRC) Equations	29
2.3.2 Generic Form of Water Retention Curve	30
2.3.3 Hysteresis of Water Retention Curve.....	32
2.3.4 Permeability Functions.....	33
2.3.5 Mathematical Equations, Implementation, and Measurements	36
2.4 Implementation Formulations of Fluid-Mechanical Constitutive Models for Unsaturated Soil	37
2.5 Justification of Research	39
CHAPTER 3 IMPLEMENTATION OF MECHANICAL CONSTITUTIVE MODELS	51
3.1 Summary	51
3.2 The BBM (Alonso et al. 1990) and the BGM (Blatz and Graham 2003).....	51

3.3 Mathematical Formulation	53
3.3.1 Implementation Method	53
3.3.2 Constant Suction.....	53
3.3.2.1 Incremental Elastic Law	54
3.3.2.2 Yield and Potential Function.....	57
3.3.2.3 Plastic Correction	59
3.3.2.4 Hardening Law	63
3.3.3 Suction Changes.....	65
3.3.3.1 Methodology.....	65
3.3.3.2 Updating Suction	66
3.3.3.3 Coefficients of Compressibility	67
3.3.3.4 Yield Surface on p-s Space.....	69
3.3.3.5 Critical State Slope (M)	69
3.4 Verification.....	70
3.5 Concluding Remarks	71
CHAPTER 4 NEW 3-D PERMEABILITY MODEL AND WATER RETENTION SURFACE	86
4.1 Introduction.....	86
4.2 Theoretical Background.....	86
4.2.1 Conceptual Models to Illustrate the Mechanisms of the Constitutive Models	86
4.2.2 Permeability Surface.....	88
4.2.3 Experimental Evidence and Calibration	89
4.2.4 Boundary Conditions Effects.....	90
4.2.5 Three-dimensional Water Retention Surface.....	92
4.3 Permeability Surface	94
4.3.1 Mathematical Formulation.....	94
4.3.2 Calibration of Parameters	96
4.3.3 Implementation Algorithm	97
4.4 Water Retention Surface (WRS)	97
4.4.1 Mathematical Formulation of the Surface and the Parameters.....	97
4.4.2 Calibration.....	98
4.4.3 Limitation of the Volume-Mass Relationship for Unsaturated Swelling Clay	99
4.5 Concluding Remarks	101
CHAPTER 5 IMPLEMENTATION OF NEW 3D WATER RETENTION SURFACE	121
5.1 Introduction.....	121
5.2 Water Retention Surface	121
5.3 Mathematical Formulation	123
5.3.1 Governing Equations	124
5.3.1.1 Transport Laws.....	124
5.3.1.2 Permeability Laws	125
5.3.1.3 Capillary Pressure Laws.....	127
5.3.1.4 Saturation	127
5.3.1.5 Fluid Balance Laws	127
5.3.1.6 Fluid Constitutive Laws	128
5.3.1.7 Balance of Momentum	129
5.3.1.8 Mechanical Constitutive Laws	130
5.3.1.9 Compatibility Equation.....	131
5.3.2 Boundary and Initial Conditions	131
5.4 Numerical Formulation	131

5.4.1 Derivation of Element “Stiffness Matrix”	132
5.4.2 Nodal Formulation of the Fluid Balance Laws	136
5.4.3 Derivative of Water Retention Surface (WRS).....	139
5.4.4 Nodal Flow Rate	140
5.4.5 Time Step.....	141
5.4.6 Mechanical Coupling.....	142
5.5 Concluding Remarks	142
CHAPTER 6 PARAMETER EVALUATION METHOD (PEM)	147
6.1 Introduction.....	147
6.2 Background	148
6.3 Parameter Evaluation Method (PEM).....	149
6.3.1 General Overview	149
6.3.2 Process	150
6.4 Stress Paths	154
6.5 Discussion	156
6.5.1 Specimens JB104 and JB105 (After Priyanto et al. 2005).....	156
6.5.1.1 Laboratory Results versus Simulation Response (Criteria 1).....	156
6.5.1.2 Parameters Variation (Criteria 2).....	157
6.5.1.3 Yield Line (Criteria 3).....	158
6.5.1.4 Modifications and Limitations of Constitutive Models	159
6.5.2 Simulation of the Specimen GS041 (After Priyanto et al. 2006).....	160
6.5.2.1 Stress-Volume (s-v) Analysis	161
6.5.2.2 Volume-Stress (v-s) Analysis	162
6.5.2.3 Modifications of Constitutive Models	162
6.5.2.4 Modelling Specimen GS041 using FLAC2D	163
6.6 Concluding Remarks	165
6.7 Justification of Mechanical Constitutive Model and Its Parameters	166
6.8 Suggestions of Future Research	167
CHAPTER 7 MODELLING INFILTRATION TEST IN TRIAXIAL CELL	180
7.1 Introduction.....	180
7.2 General Overview of Laboratory Tests	181
7.2.1 Bentonite-Sand Buffer Material.....	181
7.2.2 Triaxial Apparatus with Controlled Suction and Suction Measurement	182
7.2.3 Definition of the Stages and Conditions.....	182
7.3 Hydro-Mechanical Analysis using FLAC	184
7.3.1 Boundary Conditions.....	184
7.3.2 Mechanical Constitutive Models	184
7.3.3 Hydraulic Constitutive Models.....	185
7.3.4 Summary.....	185
7.4 Comparison of the Numerical Model Results with Laboratory Measurements....	185
7.5 Discussion	186
7.5.1 Constant Volume (CV) test	186
7.5.2 Constant Mean Stress (CMS) test.	187
7.5.3 Volume-Mass Relationship at the End of the Test.....	188
7.5.4 Model Limitations	190
7.6 Concluding Remarks and Future Research	191
CHAPTER 8 MODELLING FULL-SCALE ISOTHERMAL TEST (ITT).....	213
8.1 Introduction.....	213

8.2 General Overview of Large Scale Isothermal Test (ITT)	215
8.3 Material Properties	216
8.3.1 Fluid Properties.....	217
8.3.2 Buffer Properties	217
8.3.2.1 Mechanical Parameters.....	217
8.3.2.2 Hydraulic Parameters.....	218
8.3.2.3 Rock	219
8.3.2.4 Concrete.....	220
8.4 Numerical Modelling	221
8.4.1 Fast Lagrangian Analysis of Continua (FLAC).....	221
8.4.2 Boundary Conditions.....	221
8.5 Comparison of the Numerical Models and Field Measurements	222
8.5.1 Stage 1: Seepage into an Empty Borehole.....	223
8.5.2 Stage 2: Seepage from the Rock to the Buffer Material	223
8.5.3 End-of-Test Measurement	228
8.6 Concluding Remarks	232
8.7 Future Research.....	233
CHAPTER 9 TIME-DEPENDENT BOUNDARY CONDITIONS TO SIMULATE LARGE- SCALE ISOTHERMAL TEST (ITT)	267
9.1 Background	267
9.2 Time-Dependent Boundary Conditions	268
9.3 Constitutive Models	269
9.4 Comparison of the Model and Field Measurements	269
9.4.1 Seepage into an Empty Borehole	269
9.4.2 Pore water Pressure at the Buffer-Rock Interface	269
9.4.3 Gravimetric Water Content (w) and Dry Density (ρ_{dry}) in the Buffer	270
9.5 Concluding Remarks	271
9.6 Suggestion for Future Research.....	272
CHAPTER 10 SUMMARY, CONCLUSIONS, CONTRIBUTIONS AND SUGGESTIONS FOR FUTURE RESEARCH	285
10.1 Summary and Conclusions.....	285
10.2 Objectives versus Findings.....	290
10.3 Contributions	292
10.4 Suggestions for Future Research.....	294
REFERENCES.....	297
APPENDICES.....	293
Appendix 1. Verification of the BBM Implementation in FLAC for Constant Suction ..	307
Appendix 2. Verification of the Implementation of the BBM and the BGM in FLAC for H-M Analysis (Suction Changes)	310
Appendix 3. Algorithm to Calculate Volume-Mass Relationships in FLAC	316
Appendix 4. Input Data Files for Modelling Small-Scale Infiltration Test.....	319
Appendix 5. Input Data Files for Modelling Large Scale Isothermal Test	320

LIST OF TABLES

Table 3.1. Yield surface due to the BBM and the BGM	72
Table 3.2. Equivalent coefficients of compressibility of the BBM and the BGM for FLAC formulation	73
Table 4.1 Proposed equations of WRC for BSB materials from various tests	102
Table 4.2. Summary of material properties of WRC measurements.....	103
Table 4.3 vanGenuchten parameters used to generate curve in Figure 4.15.....	104
Table 6.1 Parameters used in the numerical simulation stress paths #1 (after Priyanto et al. 2005).....	170
Table 6.2 Parameters used in the numerical simulation stress paths #2 (after Priyanto et al. 2006).....	170
Table 7.1 As-compacted, Pre-infiltration, and End-of-test Conditions of Constant Volume (CV) Test with 500 kPa Confining Pressure	193
Table 7.2 As-compacted, Pre-infiltration, and End-of-test Conditions of Constant Mean Stress (CMS) Test with 500 kPa Confining Pressure	194
Table 7.3.Linear Elastic (LE) Model Parameters	195
Table 7.4. Blatz and Graham (2003) model (BGM) Parameters.....	195
Table 7.5.Hydraulic constitutive model equations and parameters for van Genuchten models (1980) for Bentonite Sand Buffer (BSB) material.	196
Table 7.6.Hydraulic constitutive model equations for porosity-dependent model (kwn) for Bentonite Sand Buffer (BSB) material.	197
Table 7.7.Hydraulic constitutive model parameters for porosity-dependent model (kwn) for Bentonite Sand Buffer (BSB) material.	198
Table 7.8. Combinations of boundary condition, mechanical constitutive models, and hydraulic constitutive models used in the analyses	198
Table 8.1. Hydraulic constitutive model equations and parameters for van Genuchten (1980) model for Bentonite Sand Buffer (BSB) material.....	235
Table 8.2. Hydraulic constitutive model parameters for porosity-dependent model (kw-n) for Bentonite Sand Buffer (BSB) material.	235
Table 8.3. Hydraulic constitutive model equations and parameters for van Genuchten models for the rock (1980).....	236
Table 8.4. Water uptake calculations of the numerical models.....	236
Table 9.1 Constitutive models used in the time-dependent boundary condition (BCt) models	274

LIST OF FIGURES

Figure 1.1 The characteristics of unsaturated clay and its applications	15
Figure 1.2 Characterization of unsaturated clay	15
Figure 1.3 Application of the constitutive models.....	16
Figure 1.4 Constitutive models for unsaturated swelling clay	16
Figure 1.5 AECL's isothermal test configuration (Dixon et al. 2002).....	17
Figure 1.6 Hydraulic conductivity curves for the buffer	17
Figure 1.7 Hypothetical hydraulic conductivity surface	18
Figure 2.1. Classification of the mechanical constitutive models for clay	41
Figure 2.2. Mohr-Coulomb criteria for saturated soil (after Terzaghi 1936)	41
Figure 2.3. Mohr-Coulomb criteria for unsaturated soil (after Fredlund et al. 1978)	42
Figure 2.4. Modified Cam-clay model (after Roscoe and Burland 1968).	42
Figure 2.5 The Basic Barcelona Model (BBM): (a) p-q space; (b) p-s space; (c) v-lnp; (d) v-lns (after Alonso et al. 1990).	43
Figure 2.6 The Basic Barcelona Model (BBM) yield surface (after Alonso et al. 1990) .	44
Figure 2.7 Form of normal compression lines due to the: (a) BBM (Alonso et al. 1990); (b) Wheeler and Sivakumar (1995). (after Wheeler and Karube 1996)	44
Figure 2.8 Yield surface for BExM (after Alonso et al. 1999).....	45
Figure 2.9 Coupling yield surfaces in p-s space (after Tang and Graham 2002, Delage and Graham 1996, Alonso et al. 1990).....	45
Figure 2.10 Yield surfaces on p-s space due to the BBM and the BGM.....	46
Figure 2.11 Planar critical state surface (after Wiebe et al. 1998, Blatz and Graham 2003).....	46
Figure 2.12 Critical state slope as a function of suction in BGM (after Blatz and Graham 2003).....	47
Figure 2.13 Comparison of the yield surface on p-q space of the: (a) BBM; and (b) BGM	47
Figure 2.14 Yield surface and critical state surface for the BGM (after Blatz and Graham 2003).....	48
Figure 2.15 Definitions of terms of typical water retention curve (after Fredlund and Xing 1994).....	48
Figure 2.16 Water retention curves for sandy soil, silty soil, and clayey soil (after Fredlund and Xing 1994)	49
Figure 2.17 Conceptual illustration of hysteresis in water retention curve.	49
Figure 2.18 Water relative permeability curve in: (a) linear scale; and (b) log scale.....	50

Figure 3.1 Yield loci and critical state lines at constant suction in p-q space due to: (a) the BBM and (b) the BGM.....	74
Figure 3.2 Yield loci in p-s space in isotropic conditions (q=0) due to: (a) the BBM; and (b) the BGM	74
Figure 3.3 Stress-volume relationship (lnp-v) due to: (a) the BBM; and (b) the BGM....	75
Figure 3.4 Stress-volume relationship (lns-v) due to: (a) the BBM; and (b) the BGM....	75
Figure 3.5 Yield surfaces in p-q and p-s spaces for the BBM (after Alonso et al. 1990)	76
Figure 3.6 Hardening laws algorithm plotted in 3D p-s-v space.....	76
Figure 3.7 Hardening laws algorithm plotted in ln p-v space	77
Figure 3.8 Hardening laws algorithm plotted in ln s-v space.....	78
Figure 3.9 Hardening laws algorithm plotted in p-s space	78
Figure 3.10 Algorithm to implement elasto-plastic model with suction changes in FLAC79	
Figure 3.11 Algorithm to use FISH function for the BBM and the BGM	79
Figure 3.12 Grid variables and zone variables.....	80
Figure 3.13 Equivalent coefficients of compressibility.....	80
Figure 3.14 Equivalent coefficients of compressibility for the BBM.....	81
Figure 3.15 Equivalent yield lines (T-line and LY-line) on p-s space	81
Figure 3.16 Equivalent slope of the critical state surface.....	82
Figure 3.17 The FLAC simulation results using the BBM compared with the results from Alonso et al. (1990) in: (a) p-s space; and (b) p-v space	83
Figure 3.18 Mean stress, p vs deviatoric stress, q and the yield loci for Lightly Over Consolidated clay (LOC).....	84
Figure 3.19 Mean stress, p vs specific volume, v for Lightly Over Consolidated (LOC) clay.....	84
Figure 3.20 Mean stress, p vs deviatoric stress, q and the yield loci for Highly Over Consolidated (HOC) clay	85
Figure 3.21 Mean stress, p vs specific volume, v for Highly Over Consolidated (HOC) clay.....	85
Figure 4.1 (a) Permeability Function, (b) Water retention Curve, (c) Conceptual distributions of pore water and pore air in a cross-sectional area of rigid soil matrix (constant porosity)	105
Figure 4.2 (a) Water permeability versus total porosity; (b) Suction versus total porosity;	106
Figure 4.3 (a) Suction versus water permeability for constant total specific volume; (b) Corresponding MIP test results; (c) Corresponding cross-sectional area; (d) Corresponding capillary rise	107
Figure 4.4 Hydraulic conductivity curves for the BSB (bentonite sand buffer) (after Thomas et al. 2003).....	108
Figure 4.5 Hypothetical hydraulic conductivity surface	108
Figure 4.6 a. Water permeability vs effective porosity (data after Dixon et al. 2002)..	109
Figure 4.7 Results of infiltration test on compacted Bentonite-Sand-Buffer (BSB) on p-w-v space (Siemens 2006)	111
Figure 4.8 Typical results of infiltration test using triaxial cell with controlled suction and suction measurements (after Siemens 2006).....	112
Figure 4.9 End-of test gravimetric water content (w) and degree of saturation (S _w) as a function of specific volume v (data after Siemens 2006)	113
Figure 4.10 Conceptual model illustrated end-of test degree of saturation measurements	114
Figure 4.11 Relationship of flow porosity and : (a) dry density; (b) specific volume	115
Figure 4.12 Three-dimensional water retention curve – specific volume versus suction versus gravimetric water content (Siemens 2006).....	116

Figure 4.13 Water retention surface.....	117
Figure 4.14 Hysteresis of water retention curve (WRC) located on the water retention surface	118
Figure 4.15 Laboratory measurements of WRC of BSB material (w vs suction) (without data from Siemens 2006).....	119
Figure 4.16 Laboratory measurements of WRC of BSB material (S_w vs suction).....	120
Figure 5.1 The water retention surface	144
Figure 5.2 End-of test gravimetric water content (w) and degree of saturation (S_w) as a function of specific volume v (data after Siemens 2006)	145
Figure 5.3 The relationship between the relative permeabilities (κ_r^w, κ_r^a) and the effective degree of saturation (S_e).....	145
Figure 5.4 The permeability surface.....	146
Figure 5.5 (a) Overlaid quadrilateral elements used in FLAC; (b) Typical triangular element with velocity vectors; (c) Nodal flow vector	146
Figure 6.1 Parameter Evaluation Method (PEM)	171
Figure 6.2 Iteration Process for a Single Stress Path	172
Figure 6.3 The Calculation of Total Absolute Difference (TAD) (after Priyanto et al. 2004)	172
Figure 6.4 Stress paths in p'-s stress space (after Blatz 2000).....	173
Figure 6.5 Experimental results and simulation responses using the two models in $V-\ln(p')$ space (after Priyanto et al. 2005).....	173
Figure 6.6 Experimental stress paths and LC-curve of the BBM and the BGM (after Priyanto et al. 2005).....	174
Figure 6.7 Experimental yield point and LC-curve calculated with PEM parameters for the BBM and the BGM for suction of 0 to 12MPa (after Priyanto et al. 2005)	174
Figure 6.8 Experimental yield point and LC curve calculated with PEM parameters for the BBM and the BGM for suction of 0 to 120MPa (after Priyanto et al. 2005)	175
Figure 6.9 Possible modification of LC-line for the BGM (after Priyanto et al. 2005)...	175
Figure 6.10 (a) Laboratory stress paths of specimens JB104 and GS041 plotted in p-s space with the initial yield lines; (b). Results of s-v analysis for specimen GS041 plotted in v-p space with the laboratory test results (after Priyanto et al. 2006)	176
Figure 6.11 Stress paths calculated from the v-s analysis and stress path generated from FLAC (after Priyanto et al. 2006).....	176
Figure 6.12 (a) Mechanical and hydraulic initial and boundary conditions; (b) Total suction; (c) Water added to the specimen; and (d) Total mean stress vs. time (after Priyanto et al. 2006).....	177
Figure 6.13 'Parameter generator concept' to determine mechanical and hydraulic constitutive models of unsaturated clay	179
Figure 7.1 Hydraulic and mechanical boundary conditions used in numerical modelling of the constant volume (CV) and constant mean stress (CMS) tests	199
Figure 7.2 Stages and conditions in the infiltration test.....	200
Figure 7.3 Volume of water added to the specimen versus time for constant volume (CV) test.....	201
Figure 7.4 Volume strain versus time for constant volume (CV) test	201
Figure 7.5 Radial strain versus time for constant volume (CV) test	202
Figure 7.6 Axial strain versus time for constant volume (CV) test	202
Figure 7.7 Total suction versus time for constant volume (CV) test (a) average; (b) at the center; (c) at perimeter.....	203
Figure 7.8 Total mean stress versus time for constant volume (CV) test (a) average; (b) at the center; (c) at perimeter.....	204

Figure 7.9 Volume of water added to the specimen versus time for constant mean stress (CMS) test.....	205
Figure 7.10 Volume strain versus time for constant mean stress (CMS) test.....	205
Figure 7.11 Radial strain versus time for constant mean stress (CMS) test.....	206
Figure 7.12 Axial strain versus time for constant mean stress (CMS) test.....	206
Figure 7.13 Total suction versus time for constant mean stress (CMS) test (a) average; (b) at the center; (c) at perimeter	207
Figure 7.14 Total mean stress versus time for constant mean stress (CMS) test (a) average; (b) at the center; (c) at perimeter	208
Figure 7.15 Degree of saturation versus radial distance at the post-test for: (a) constant volume (CV) test; (b) constant mean stress (CMS) test	209
Figure 7.16 Dry density versus radial distance at the post-test for: (a) constant volume (CV) test; (b) constant mean stress (CMS) test.....	210
Figure 7.17 Gravimetric water content versus radial distance at the post-test for: (a) constant volume (CV) test; (b) constant mean stress (CMS) test.....	211
Figure 7.18 Bulk density versus radial distance at the post-test for: (a) constant volume (CV) test; (b) constant mean stress (CMS) test.....	212
Figure 8.1 Two types of permeability function to model large scale Isothermal Test (after Thomas et al. 2003).....	237
Figure 8.2 Permeability surface in S_w - n - k_w space	237
Figure 8.3 General layout of the AECL's Underground Research Laboratory (URL) at Lac du Bonnet, Manitoba, Canada (Dixon et al. 2002).....	238
Figure 8.4 Configuration of the isothermal test (Dixon et al. 2002).....	238
Figure 8.5 Configuration of the Isothermal Test Seepage Collection System (Dixon et al. 2001).....	239
Figure 8.6 Groundwater pressures (kPa) at the 240 level of the URL (Dixon et al. 2001)	240
Figure 8.7 Water retention curve used to in the model compared with the laboratory measurements of the BSB material	241
Figure 8.8 Water and air relative permeability as a function of degree of water saturation	242
Figure 8.9 Hydraulic conductivity as a function of the effective flow porosity (data points after Dixon et al. 1999).....	242
Figure 8.10 Water retention curve for the rock.....	243
Figure 8.11 Two types of boundary conditions used in the numerical models.....	244
Figure 8.12 Finite difference grids used to model stage 1 of the isothermal test (ITT) .	245
Figure 8.13 Pore pressure versus radial distance from center of borehole in the empty borehole at $t = 1$ month, 1 year, 2 years, and 3 years at $y = 4$ m (middle of the buffer).....	245
Figure 8.14 Pore pressure versus radial distance from center of borehole in the empty borehole at various depths at the initial conditions of isothermal test ($t = 3$ years)	246
Figure 8.15 Pore pressure contours at the start of isothermal test	247
Figure 8.16 Pore water pressure measurements compared with buffer-only analysis using linear elastic model (BO-LE) at locations IBP01 and IBP02.....	248
Figure 8.17 Pore water pressure measurements compared with buffer-rock analysis using linear elastic model (BR-LE) at locations IBP01 and IBP02.....	248
Figure 8.18 Pore water pressure measurements compared with buffer-rock analysis using BGM and porosity-dependent models (BR-BGMkwn) at locations IBP01 and IBP02	249
Figure 8.19 De-saturation mechanism in the buffer-rock interface (BR-BGMkwn analysis).....	249

Figure 8.20 Total pressure measurements compared with buffer-only analysis using linear elastic model (BO-LE) at locations IBG1, IBG2, and IBG3	250
Figure 8.21 Total pressure measurements compared with buffer-rock analysis using linear elastic model (BR-LE) at locations IBG1, IBG2, and IBG3	250
Figure 8.22 Total pressure measurements compared with buffer-rock analysis using BGM and kwn model (BR-BGMkwn) at locations IBG1, IBG2, and IBG3.....	251
Figure 8.23 Total pressure measurements compared with buffer-only analysis using linear elastic model (BO-LE) at locations IBR1, IBR2, and IBR3	251
Figure 8.24 Total pressure measurements compared with buffer-rock analysis using linear elastic model (BR-LE) at locations IBR1, IBR2, and IBR3	252
Figure 8.25 Total pressure measurements compared with buffer-rock analysis using BGM and kwn model (BR-BGM kwn) at locations IBR1, IBR2, and IBR3	252
Figure 8.26 Total pressure measurements compared with buffer-only analysis using linear elastic model (BO-LE) at locations IBK1, IBK2, IBK3 and IBK4.....	253
Figure 8.27 Total pressure measurements compared with buffer-rock analysis using linear elastic model (BR-LE) at locations IBK1, IBK2, IBK3 and IBK4	253
Figure 8.28 Total pressure measurements compared with buffer-rock analysis using BGM and kwn model (BR-BGM kwn) at locations IBK1, IBK2, IBK3 and IBK4	254
Figure 8.29 Psychrometer locations at the large-scale isothermal test (IBX1-24) (after Dixon et al. 2001).....	255
Figure 8.30 Evolution of water content of buffer-only analysis using linear elastic model (BO-LE) at psychrometer locations.....	256
Figure 8.31 Evolution of water content of buffer-rock analysis using linear elastic model (BR-LE) at psychrometer locations	256
Figure 8.32 Evolution of water content of buffer-rock analysis using BGM and kwn model (BR-BGM kwn) at psychrometer locations.....	257
Figure 8.33 Evolution of gravimetric water content measurements compared with the three FLAC model results at location IBX18	257
Figure 8.34 Water uptake measurements compared with buffer-rock analysis using linear elastic model (BR-LE) (Total water uptake = 108.91 litres).....	258
Figure 8.35 Water uptake measurements compared with buffer-rock analysis using linear elastic model (BR-LE) (Total water uptake = 58.14 litres).....	258
Figure 8.36 Water uptake measurements compared with buffer-rock analysis using BGM and kwn model (BR-BGM kwn) (Total water uptake = 47.76 litres).....	259
Figure 8.37 End of test gravimetric water content measurements compared with the three FLAC models	259
Figure 8.38 End of test dry density measurements compared with the three FLAC models	260
Figure 8.39 Gravimetric water content versus dry density at the end of test measurements compared with the three FLAC models.....	260
Figure 8.40 Gravimetric water content contours at the end of test from: (a) field measurements; (b) BR-LE analysis; and (c) BR-BGM kwn analysis	261
Figure 8.41 Dry density contours at the end of test from: (a) field measurements; (b) BR-LE analysis; and (c) BR-BGM kwn analysis	262
Figure 8.42 Degree of saturation versus radial distance of two FLAC models at initial and final conditions	263
Figure 8.43 Degree of water saturation versus depth for various radial distance of two different FLAC models	264
Figure 8.44 Pore water pressure versus depth for various radial distance of two different FLAC models	265

Figure 8.45 Comparison between FLAC models and field measurements of the pore water pressure versus radial distance from borehole center at initial and final conditions.....	266
Figure 9.1 Location of pore water pressure measurements at rock.....	275
Figure 9.2 Boundary conditions as a function of time	276
Figure 9.3 Seepage into an empty borehole: (a) time dependent boundary condition (BCt) model; (b) buffer-rock (BR) model.....	277
Figure 9.4 Locations of IBP1 and IBP2.....	278
Figure 9.5 Pore water pressure measurements at locations IBP1 and 2 for BCt-LE model	278
Figure 9.6 Pore water pressure measurements at locations IBP1 and 2 for BCt-BGM model.....	279
Figure 9.7 Pore water pressure measurements at locations IBP1 and 2 for BCt-BGM-kwn model.....	279
Figure 9.8 End of test gravimetric water content (w) measurements compared with the all FLAC models.....	280
Figure 9.9 Gravimetric water content (w) evolution of BCt-BGM-kwn model at location IBX9 compared with the field measurements (calculated gravimetric water content after Dixon et al. 2000) (<i>see Figure 8.28 for location</i>).....	280
Figure 9.10 Gravimetric water content (w) evolution of BCt-BGM-kwn model at location IBX11 compared with the field measurements (calculated gravimetric water content after Dixon et al. 2000) (<i>see Figure 8.28 for location</i>).....	281
Figure 9.11 Gravimetric water content (w) evolution of BCt-BGM-kwn model at location IBX1-24 (<i>see Figure 8.28 for locations</i>)	281
Figure 9.12 Dry density at the end of the test	282
Figure 9.13 End of test gravimetric water content (w) measurements compared with the all FLAC models.....	283
Figure 9.14 Back-analysis to define properties of the rock	284

LIST OF SYMBOLS AND ABBREVIATIONS

A	parameter defining the relationship of S_{max} and v (kwn model)
AECL	Atomic Energy of Canada Limited
a	vanGenuchten (1980) parameter
B	parameter defining the relationship of S_{max} and v (kwn model)
BBM	Basic Barcelona Model (Alonso et al. 1990)
BC/E	Buffer Container Experiment
BCt	Time-dependent Boundary Condition model
BExM	Barcelona Expansive Model (Alonso et al. 1999)
BGM	Blatz and Graham Model (Blatz and Graham 2003)
BO	Buffer Only model/ analysis
BR	Buffer-Rock model/ analysis
BSB	Bentonite Sand Buffer
b	vanGenuchten (1980) parameter
CMS	constant mean stress
CV	constant volume
c	cohesion
c	vanGenuchten (1980) parameter
c'	cohesion (correspond to the σ_n)
E	Young's modulus of elasticity
EBS	Engineered Barrier System
ECDD	Effective Clay Dry Density
EDZ	Excavation Damage Zone
EMDD	Effective Montmorillonite Dry Density
e	void ratio
FE	Finite Element
FEM	Finite Element Method
FD	Finite Difference

FLAC	Fast Lagrangian Analysis of Continua (Itasca 2000)
FV	Finite Volume
f	yield function
G	shear modulus
G_s	specific gravity/ relative density of soil solids.
g	potential function
H-M	Hydro-Mechanical
HOC	highly overconsolidated clay
ITT	Isothermal Test
K	bulk modulus
K_a	air bulk modulus
K_w	water bulk modulus
k	slope of k-line (BBM)
k_a	air permeability coefficient
k_a^{sat}	air permeability at air saturated conditions
k_{max}	maximum water permeability correlated with the maximum porosity n_{max}
k_{sat}	saturated water permeability
k_w	water permeability coefficient
k_w^{sat}	water permeability at air saturated conditions
k-line	cohesion line (BBM)
kwn	porosity dependent permeability model
LC-curve	loading collapse curve (BBM)
LOC	lightly overconsolidated clay
LY-line	load yield line (BGM)
M	slope of the critical state line that is constant (BBM)
M^p	slope of p-q on critical state surface (BGM)
M^{ps}	equivalent critical state slope (BGM) [$M^{ps} = f(M^p, M^s)$]
M^s	slope of p-s on critical state surface (BGM)
MCC	Modified Cam-Clay
N	slope of critical state line [$N = N(s)$] (BGM)
NL	Normal-line (BExM)
OCR	over consolidation ratio
PEM	Parameter Estimation Method
n	porosity

n_e	effective porosity
n_F	flow porosity
n_{max}	maximum porosity
n_{min}	minimum porosity
n_{NF}	non-flow porosity
na	parameter defining the relationship of permeability and porosity (kwn model)
P_0	threshold pressure (vanGenuchten 1980)
p	mean net stress
p_1	reference mean stress (BBM)
p_o	mean stress at corresponding suction s located on LC-line (BBM) or LY-line (BGM)
p_o^*	mean stress at zero suction located on LC-line (BBM) or LY-line (BGM)
p_s	mean stress at corresponding suction s located on k-line (BBM) or T-line (BGM)
q	deviator stress
q_{cs}	deviatoric stress at the critical state surface (BGM)
r	BBM parameter for LC-curve
S_a	degree of air saturation
S_e	effective degree of saturation (water)
S_{max}	maximum degree of saturation
S_r	residual degree of saturation
S_w	degree of (water) saturation
SD	Suction Decrease (BExM)
SI	Suction Increase (BExM)
SI-line	suction increase line (BBM)
SWCC	Soil Water Characteristic Curve
SWCS	Soil Water Characteristic Surface
s	total suction
s_o	suction limit defining SI-line (BBM)
TAD	Total Absolute Difference (Chapter 6)
T-H-M	Thermo-Hydro-Mechanical
T-line	tension line (BGM)
URL	Underground Research Laboratory

USC	Unsaturated Swelling Clay
u_a	pore air pressure
u_w	pore water pressure
VF	Vertical Flow
VGM	van Genuchten (1980) Model
v	specific volume
WRC	Water Retention Curve
WRS	Water Retention Surface
WSM	Wheeler and Sivakumar (1995) Model
w	gravimetric water content
w_{max}	maximum gravimetric water content
V	volume of reference soil
V_s	volume of solid particles
v_0	initial specific volume
β	BBM parameter for LC-curve
χ	Bishop's effective stress parameter
Δv	specific volume increment
$\Delta \varepsilon_i$	principal strain increment (i= 1,2,3)
$\Delta \varepsilon_i^e$	elastic principal strain increment (i= 1,2,3)
$\Delta \varepsilon_i^p$	plastic principal strain increment (i= 1,2,3)
$\Delta \varepsilon_q$	distortional strain increment
$\Delta \varepsilon_{vp}$	volumetric strain increment
ε	volumetric strain
ϕ'	friction angle
ϕ_b	parameter describes the increase of shear strength with increase of suction (Fredlund and Rahardjo 1993)
κ	slope of $\ln p$ versus v within elastic range
κ^r	relative permeability
κ_a^r	air relative permeability
κ_w^r	water relative permeability
κ_r^{sat}	relative permeability at water saturated condition
κ_s	slope of $\ln s$ versus v within elastic range
λ	slope of $\ln p$ versus v when plastic strain occurs

λ_s	slope of $\ln s$ versus v when plastic strain occurs
λ_{bc}	“pore size distribution index” for Brooks and Corey (1964) WRC
μ_{rat}	viscosity ratio
μ_w	viscosity of water
μ_a	viscosity of air
ν	poisson’s ratio
π	osmotic suction
Θ	normalized volumetric water content
θ	volumetric water content
θ_a	residual volumetric air content
θ_r	residual volumetric water content
θ_s	saturated volumetric water content
θ_w	volumetric water content
ρ	bulk density
ρ_{dry}	dry density
ρ_w	water density
σ	total stress
σ'	effective stress
σ_i	principal stresses ($i= 1,2,3$)
σ_n	net effective normal stress
τ	shear stress
Ψ	total suction
Ψ_b	air entry or bubbling pressure

PART 1:
INTRODUCTION

CHAPTER 1

INTRODUCTION

1.1 General Overview

Fine-grained soils with a plasticity index greater than 35 are characterized as high plastic clays (Holtz and Kovacs 1981). Volume change of high plastic clays is sensitive to the changes in water content. High plastic clays swell as a result of increase in the gravimetric water content and shrink as a result of decrease in the gravimetric water content. Consequently, the term 'swelling clay' is often used to describe high plastic clay.

The characteristics of unsaturated swelling clay and its applications are schematically illustrated in Figure 1.1. Due to its swelling and shrinking behaviour, unsaturated swelling clay has been shown to cause considerable damage to physical infrastructures (Jones and Holtz 1973). Unlike natural clays with low plasticity, the swelling and shrinking behaviours have to be considered in the design of engineered structures involving unsaturated swelling clay, such as shallow foundations, pavements, embankments, and dams.

Despite of its disadvantages, the high sensitivity of swelling clay to gravimetric water content changes provides a self-sealing ability (through swelling) and a low hydraulic conductivity that is beneficial for applications as engineered sealing materials (Figure 1.1). The application of swelling clay as liners is not limited to landfill applications (e.g., to produce geosynthetic clay liners) (Koerner 1998), but swelling clay is also proposed as a buffer material to seal nuclear fuel waste containers in the deep geological repository (DGR) concept (AECL 1994, Graham et al. 1997). The DGR concept in Canada involves surrounding nuclear fuel waste containers with clay-based sealing material within stable granitic deposits (AECL 1994, Russell and Simmons 2003, Maak and Simmons 2005).

Characterization of the unsaturated swelling clay (USC) behaviour is a study of considerable importance. The characterization of USC behaviour can be classified into physical models and numerical models (Figure 1.2). The physical models include *in-situ* measurements (e.g. Agus et al. 2005) or laboratory tests (Figure 1.2). The laboratory tests can be small-scale, large-scale, or centrifuge tests. The small-scale tests include oedometer tests (e.g. Alonso et al. 1990, Wheeler and Sivakumar 1995, Dueck 2004) or triaxial tests (e.g. Tang 1999, Blatz 2000, Anderson 2003, Siemens 2006) for unsaturated clay. Examples of large-scale tests include full-scale isothermal test (ITT) and buffer/container experiment (BCE) by Atomic Energy of Canada Limited (AECL) (Dixon et al. 2002).

The characterization of USC using numerical models includes the developments of conceptual models (e.g. Siemens 2006) and constitutive models (e.g. Alonso et al. 1990, Wheeler and Sivakumar 1995, Tang and Graham 2002, Blatz and Graham 2003).

Conceptual models are defined as models that are used to understand the process occurring as opposed to providing a rigorous mathematical formulation (e.g. capillary tube model (Siemens 2006)). Although, the capillary tube model (Siemens 2006) increases understanding of the process occurring in the USC, its application is for a limited number of cases. Limited studies in the conceptual model application are currently undertaken in this area and the conceptual model is only applicable for small-scale laboratory test.

The application of a conceptual model to simulate 'real-life' engineered system will require implementation of a conceptual model into numerical analysis methods (e.g., finite element (FE) or finite difference (FD) methods). The formulations and parameters of a conceptual model are generally different from those of currently used in a constitutive model of USC. Additional laboratory tests to define these parameters are still required in the application of a conceptual model. A method to determine the parameters of a constitutive model from a conceptual model or vice versa is required in the application of the conceptual model.

On the other hand, the application of constitutive models has been used to simulate 'real-life' engineered systems. The application process of constitutive models is illustrated in Figure 1.3. The constitutive models can be combined with the laws of physics (e.g. equation of equilibrium, conservation of mass and energy) to generate a set of partial differential equations. This set of partial differential equations can be implemented using numerical analysis methods, such as the finite element (FE) or finite difference (FD) methods. Application of the realistic boundary conditions in this method can then be used to solve a boundary value problem to simulate a 'real-life' engineered system (Figure 1.3).

Numerical models cannot be separated from laboratory or *in-situ* testing in terms of their importance in the engineering design process (Figure 1.3). The results of laboratory tests are used to calibrate the constitutive model parameters, while the results of the numerical modelling are used to verify the laboratory or *in-situ* measurements (Figure 1.3). The focus of this thesis is towards the application of constitutive models proposed for hydraulic-mechanical (H-M) analysis of the USC using 2-D finite difference (FD) method.

The infiltration process in the USC includes mechanical (M), hydraulic (H), and thermal (T) processes as illustrated in Figure 1.4. The mechanical constitutive model is required to describe the mechanical behaviour of the unsaturated swelling clay. The mechanical constitutive model comprises the stress-strain relationship and plasticity models. The hydraulic constitutive model includes the water retention curve (WRC) and permeability function. The term water retention curve (WRC) describes the relationship of suction (ψ) as a function of degree of water saturation (S_w), volumetric (θ) or gravimetric water content (w). The WRC is also called soil water characteristic curve (SWCC). The term water retention curve (WRC) will be used in this thesis. The permeability function describes the relationship of the water permeability (k_w) and air permeability (k_a) of the USC as a function of the degree of water saturation (S_w).

Thermal constitutive model for the USC relates thermal conductivity as a function of degree of water saturation (S_w). Only isothermal condition is included in this research, so that only hydraulic (H) and mechanical (M) constitutive models are discussed in this thesis.

1.2 Background

1.2.1 General

A dilemma exists in the application of a constitutive model for engineering application. The more complex constitutive model can represent more features of material behaviour and may increase the reliability of the numerical modelling results. However, it is more difficult to calibrate the parameters of this constitutive model and to implement this constitutive model in a numerical framework.

In comparison with other engineering materials, unsaturated soil is notably difficult to characterize (Lade 2005). Due to the complex mechanical behaviour of USC, conventional constitutive models, such as the traditional linear elasticity and linear elastic-perfectly plastic models that use the Mohr-Coulomb failure criteria (Terzaghi 1936) may not be sufficient to describe the general behaviour of USC in some applications. Consequently, more comprehensive models, such as that of the critical state soil mechanics for saturated soil (e.g., Roscoe et al. 1958, Schofield and Wroth 1968, Roscoe and Burland 1968) are required.

Application of continuum mechanics requires a constitutive model that can describe the general behaviour of the material. The proposed use of USC as a buffer in nuclear fuel waste disposal barrier systems demands reliable numerical modelling, since it is related to societal and environmental safety. This research attempts to address the difficulties related to calibration, implementation, and application of the rigorous constitutive models that may better represent USC H-M behaviour.

The significance of the effect of the boundary conditions on the behaviour of USC was examined using triaxial experiments with controlled suction and suction measurements (Blatz 2000, Anderson 2003, Siemens 2006). This research will incorporate the effects of the boundary conditions within the constitutive models and numerically model the system incorporating USC behaviour.

1.2.2 Development of New Hydraulic-Mechanical Constitutive Models

Effect of Boundary Conditions

The application of unsaturated swelling clay as a buffer material to seal nuclear fuel waste in the deep geological repository (DGR) concept requires the prediction of a long-term response of the USC due to the lifetime of the radioactive waste. The current numerical modelling in geotechnical engineering is limited to back-analysis to understand the process occurring in the engineered system (Barbour and Krahn 2004, Potts 2003). Prediction of the long-term behaviour of the USC will require greater accuracy in the overall numerical modelling process. Existing constitutive models have not allowed the long-term prediction of hydraulic (H) and mechanical (M) behaviours of the USC. Improvement of the existing constitutive models for the USC is still required to simulate the DGR.

When the general behaviour of a material can be demonstrated using constitutive models, the constitutive models can be implemented in continuum mechanics to simulate the engineered system. This research attempts to develop new constitutive models that can improve the performance of numerical modelling of barrier materials under stress and environmental conditions consistent with the underground conditions by including the effect of boundary condition within the constitutive models. This improvement may be able to extend the limit of numerical modelling of the engineered

system from understanding the process through the back-analysis to the long-term prediction of the engineered system.

Three-Dimensional Hydraulic Conductivity Surface

A number of full-scale experiments were conducted at Atomic Energy of Canada Limited's (AECL) underground research laboratory (URL) to provide data for calibration and validation of numerical models that were developed to predict the behaviour of the DGR. One of the experiments was the isothermal test (ITT) that monitored behaviour during flow of groundwater into a borehole filled with buffer (i.e. swelling clay-sand mixture) (Dixon et al. 2002). A schematic of the test configuration is shown in Figure 1.5. Results observed swelling occurring at the rock-buffer interface combined with an increase in density of the buffer at the center of the borehole.

Numerical model using a conventional hydraulic conductivity model of Brook and Corey (1964) (e.g., 'original curve' in Figure 1.6) to simulate transient water uptake and final distribution of phase properties in the ITT were unsuccessful (Thomas et al. 2003). This 'original curve' shows an increase in hydraulic conductivity with increasing degree of saturation (Figure 1.6).

An 'exponential relationship' (Figure 1.6) assuming the decrease of hydraulic conductivity with increasing degree of water saturation (S_w) for $S_w > 90\%$ was introduced to be able to calibrate the behaviour of the model to the field observation (Thomas et al. 2003). This 'exponential relationship' was opposite the existing permeability models (e.g. Brook and Corey 1964, van Genuchten 1980, Fredlund and Xing 1994). Although the application of this 'exponential relationship' provided results that were comparable to the laboratory test (Thomas et al. 2003), this 'exponential relationship' are limited to this

particular condition and this particular range of time and may not be appropriate for other cases. Consequently, long-term prediction of the system cannot be made using this 'exponential relationship'.

The 'exponential relationship' (Thomas et al. 2003) indicates that the traditional hydraulic conductivity curve may not be sufficient to describe the behaviour of the USC. A new constitutive model is required to fully describe the behaviour of USC, so that the processes occurring in the system are fully understood and the prediction of long-term response of the system can be made.

Traditionally, the hydraulic conductivity relationship ('original' curve in Figure 1.7) uses the assumption that the hydraulic conductivity is independent of the porosity (n) and stress-state along the curve defining the relationship of hydraulic conductivity (k_w) as a function of degree of water saturation (S_w). In the case of USC, which is sensitive to volume change due to the change of water content; this assumption is not sufficient. Thus, this 2-D hydraulic conductivity curve (i.e. k_w versus S_w) is in fact a 3-D hydraulic conductivity surface with either a porosity (n) or a mean stress (p) as the third axis. The key was that the curve presented by Thomas et al. (2003) was in fact not at a constant porosity during the operation of the experiment. A possible surface was presented in Figure 1.7. Using this hypothetical surface, the 'exponential relationship' in Figure 1.6 (Thomas et al. 2003) could be drawn as part of this surface as it was illustrated in Figure 1.6.

Three-Dimensional Water Retention Surface

Siemens (2006) presented three-dimensional water retention curves from the results of infiltration test on unsaturated swelling clay. A small scale of the ITT was examined

using triaxial tests with controlled suction and suction measurement (Blatz and Graham 2000, Siemens 2006) to obtain a better understanding of infiltration process to the unsaturated swelling clay. The data from the ITT (Dixon et al. 2002) and triaxial test (Siemens 2006) were used to calibrate the numerical modelling presented in this research. This research uses the results of laboratory tests from (e.g., Blatz 2000, Siemens 2006) to calibrate the new constitutive models. The mathematical formulations of the water retention curve (S_w-v-s) and permeability surfaces (S_w-v-k_w) will be presented in this research.

Buffer and Rock Interaction

Guo and Dixon (2005) presented numerical modelling of the large-scale isothermal test ITT (Dixon et al. 2002) using CODE_BRIGHT (Olivella et al. 1996). A reasonable match of the measured data and the numerical model result was obtained by greatly decreasing the permeability of the excavation damage zone (EDZ) in the rock close to the borehole (Guo and Dixon 2005). This excavation damage zone (EDZ) is beyond the scope of this thesis that focuses on the behaviour of unsaturated swelling clay and will not be applied in the ITT modelling.

The results of infiltration tests using triaxial tests with controlled suction and suction measurement on sand-bentonite clay shows that the degree of water saturation (S_w) at the end of the test does not reach 100% saturation (Siemens 2006). This indicates that the termination of liquid flow at the end of the test is not only due to the boundary conditions (buffer-rock interaction), but also internal swelling condition. This research will consider both effects in the development to the constitutive models.

1.3 Scope

This thesis focuses on the development of both mechanical (M) and hydraulic (H) constitutive models for the unsaturated swelling clay (USC). The challenges associated with existing numerical models for unsaturated swelling clays (Priyanto et al. 2004, 2005, 2006) include:

- 1) '*Calibration*' of constitutive model parameters;
- 2) '*Selection*' and '*development*' of constitutive models;
- 3) '*Implementation*' of constitutive models; and
- 4) '*Application*' of the constitutive models to model engineered systems.

All of these aspects are related to each other and equally important. These four challenges are the scope of this research.

1.4 Definitions

The terms '*calibration*', '*selection*', '*development*', '*implementation*', and '*application*' used in this thesis are defined as follows.

- '*Calibration*' process is the determination of the constitutive model parameters from the results of laboratory tests.
- '*Selection*' includes the process of selecting existing constitutive models.
- '*Development*' of constitutive models includes the modification of the existing constitutive models and the generation of mathematical formulation of the constitutive models.

- *'Implementation'* of constitutive models includes the following processes:
 - development of mathematical formulation combining the laws of physics and constitutive models formulation, usually it results in a set of partial differential equations;
 - generating numerical formulation from the set of partial differential equations using available numerical methods (i.e., finite element (FE) or finite difference (FD) methods), in this thesis finite difference (FD) method is used; and
 - writing a computer code to solve the numerical formulation.
- *'Application'* of constitutive models is defined as the application of computer code from implementation process to simulate an engineered system.

1.5 Objectives

The overall objective of this research program is to develop and apply constitutive models that can improve the performance of numerical modelling of hydraulic (H) and mechanical (M) behaviour of unsaturated swelling clay over existing constitutive models.

Steps taken to achieve this overall objective include:

- Providing an algorithm to implement a coupled critical state based mechanical constitutive model and hydraulic constitutive model.
- Developing a parameter estimation algorithm for the constitutive model parameters that make use of limited results from laboratory tests.
- Application of the constitutive models to simulate selected engineering systems that consist of infiltration processes into unsaturated high plastic clay material.

- Improvement of mechanical and hydraulic constitutive models by incorporating the effects of boundary conditions within the constitutive models.
- Implementation of the new constitutive models in a numerical framework to directly compare their performance against existing models.

Two specific questions will be addressed at the end of the thesis.

Question 1:

'Is the application of a coupled critical state based mechanical constitutive model and hydraulic permeability model that include the effect of boundary conditions within the constitutive models can improve the performance of the numerical modelling of the infiltration process in unsaturated swelling clay over existing numerical models?'

Question 2:

'Can the estimation of parameter selection for rigorous constitutive models be automated using numerical search algorithm to identify parameters within user specified physical limits?'

1.6 Organization of Thesis

The thesis is organized into 6 parts: 1) Introduction; 2) literature review; 3) development and implementation; 4) calibration; 5) applications; and 6) summary, conclusions, and suggestions for future works.

Part 1: Introduction is discussed in this chapter.

Part 2: Literature Review is provided in Chapter 2. The literature review is to provide a fundamental basis for the concepts and work presented in the thesis. It reviews existing works related to this research and is concluded by outlining the uniqueness of this research to justify the significance of this research.

Part 3: Development and Implementation is provided in Chapters 3, 4, and 5. Implementation of the mechanical constitutive models in two-dimensional finite difference analysis is discussed in detail in Chapter 3. Chapter 4 presents the new hydraulic constitutive models (e.g. porosity dependent permeability (kwn) model and water retention surface (WRS)). Chapter 5 provides the mathematical formulations and algorithms to implement the constitutive models numerically.

Part 4: Proposed Calibration Method is provided in Chapter 6. This chapter proposes a parameter evaluation method (PEM) that can be used to evaluate of two existing constitutive models (the BBM and the BGM) using limited results of physical testing and evaluate the existing constitutive models. This method provides a calibration method for rigorous constitutive models.

Part 5: Application of the hydraulic and mechanical constitutive models are presented in Chapters 7, 8, and 9. Chapter 7 discusses the application of the constitutive models to simulate small-scale infiltration tests using a triaxial cell with controlled suction and suction measurements. Modelling of the full-scale isothermal test (ITT) using various constitutive models and boundary conditions are discussed in Chapters 8. Chapter 9 provides a discussion on the application of time-dependent boundary conditions to model the ITT test (Dixon et al. 2002).

Part 6: Summary, Conclusions, Contributions, and Suggestions for Future Works are presented in Chapter 10. This chapter summarizes the concluding remarks from the previous chapters and examines the objectives and questions presented in this chapter. The unique contributions provided by this thesis are summarized in this chapter. Future works presented in this chapter summarizes several specific ideas that can improve the

numerical modelling of unsaturated swelling clay, but have not been completed in this thesis.

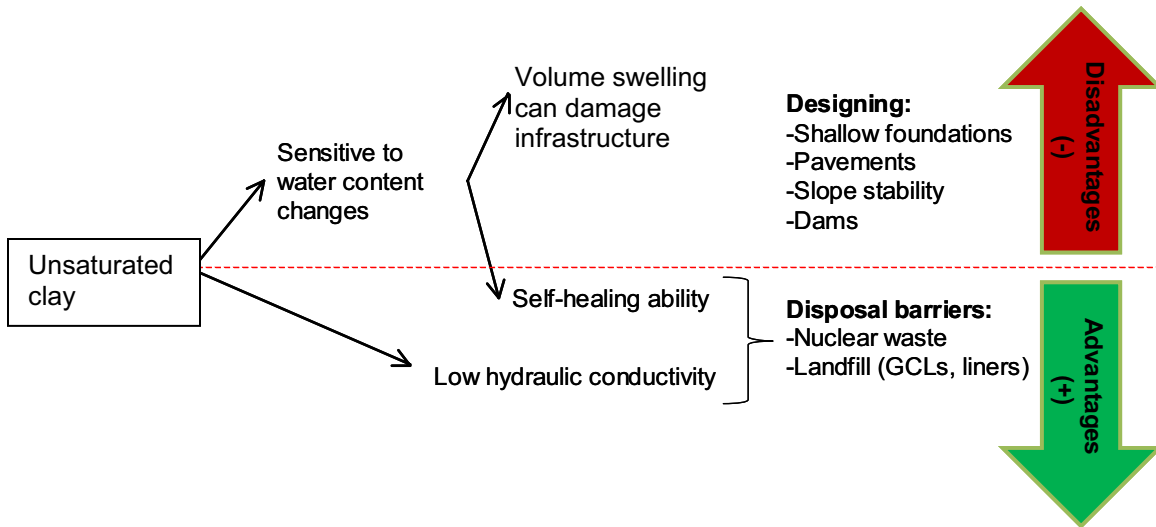


Figure 1.1 The characteristics of unsaturated clay and its applications

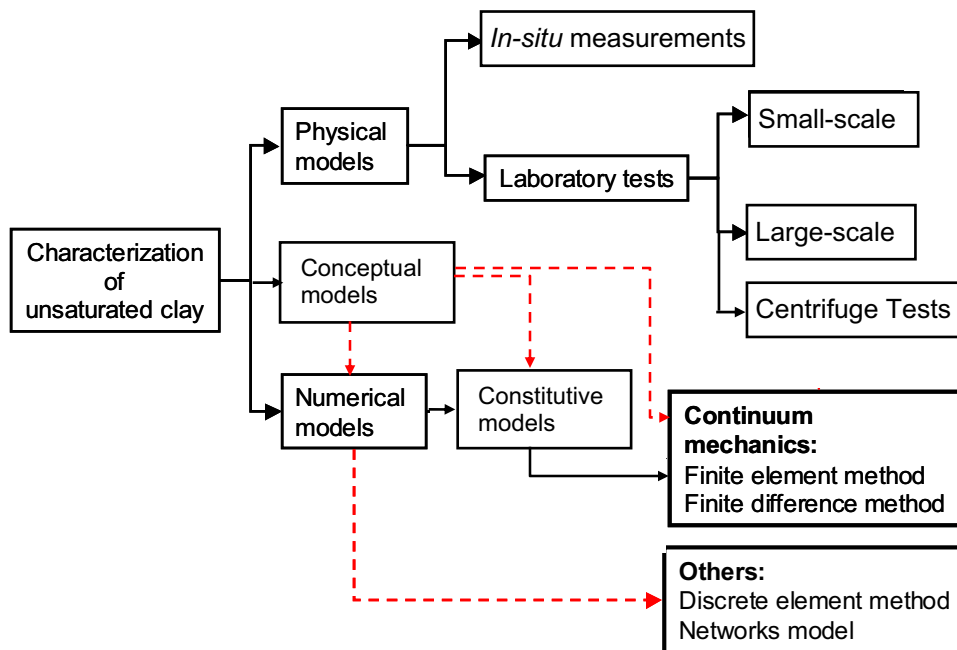
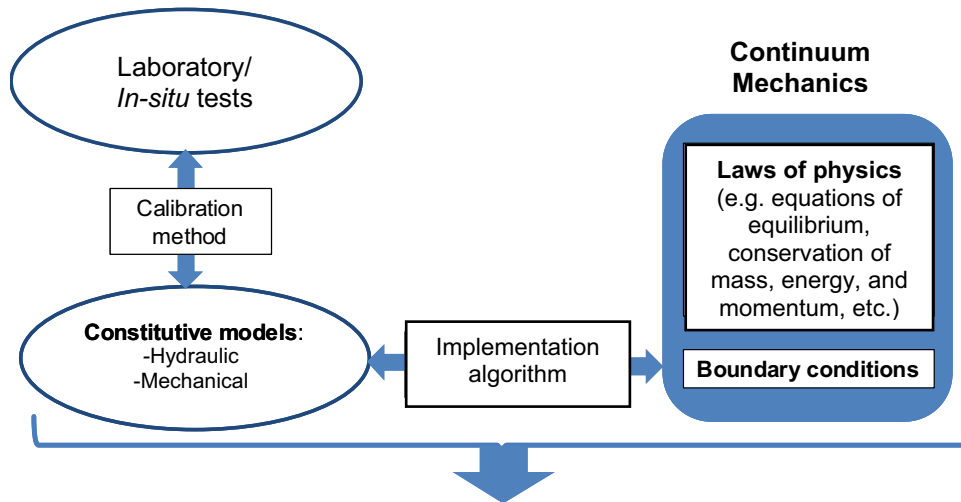


Figure 1.2 Characterization of unsaturated clay



Modelling a “real-life” engineered system
 Figure 1.3 Application of the constitutive models

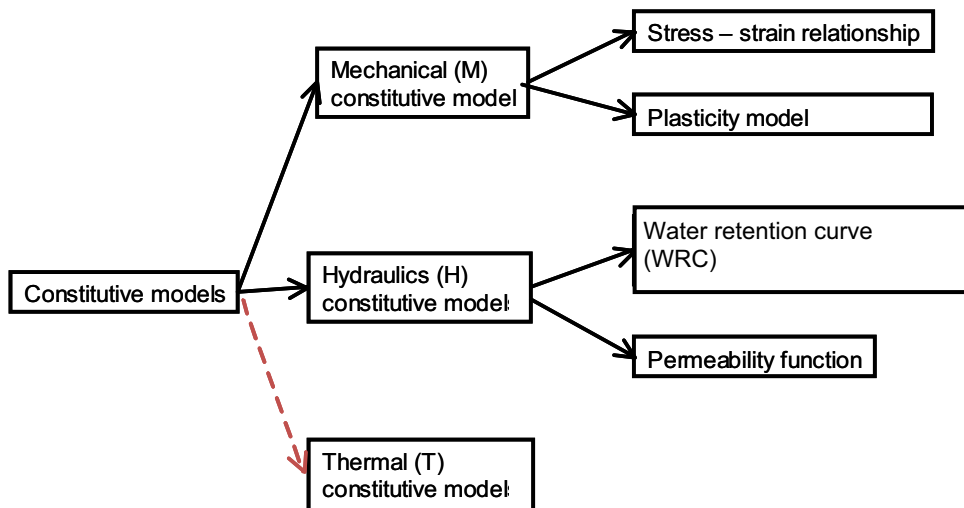


Figure 1.4 Constitutive models for unsaturated swelling clay

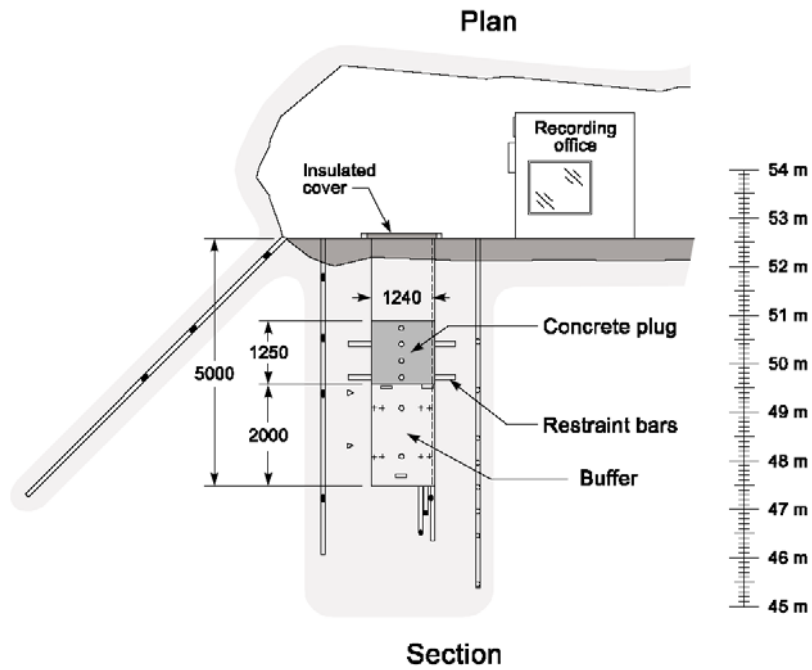


Figure 1.5 AECL's isothermal test configuration (Dixon et al. 2002). Used with permission by Dixon, July 23, 2007.

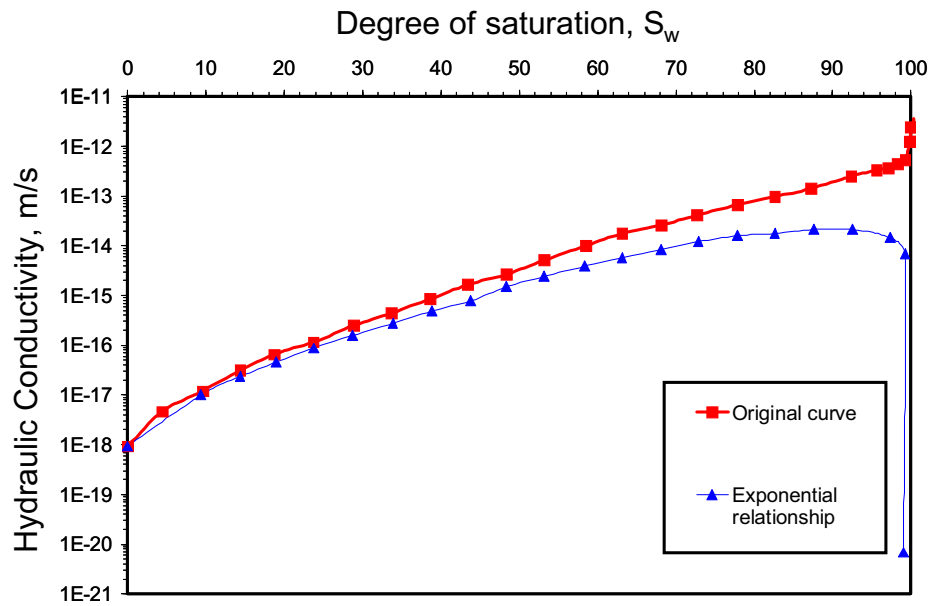


Figure 1.6 Hydraulic conductivity curves for the buffer (after Thomas et al. 2003)

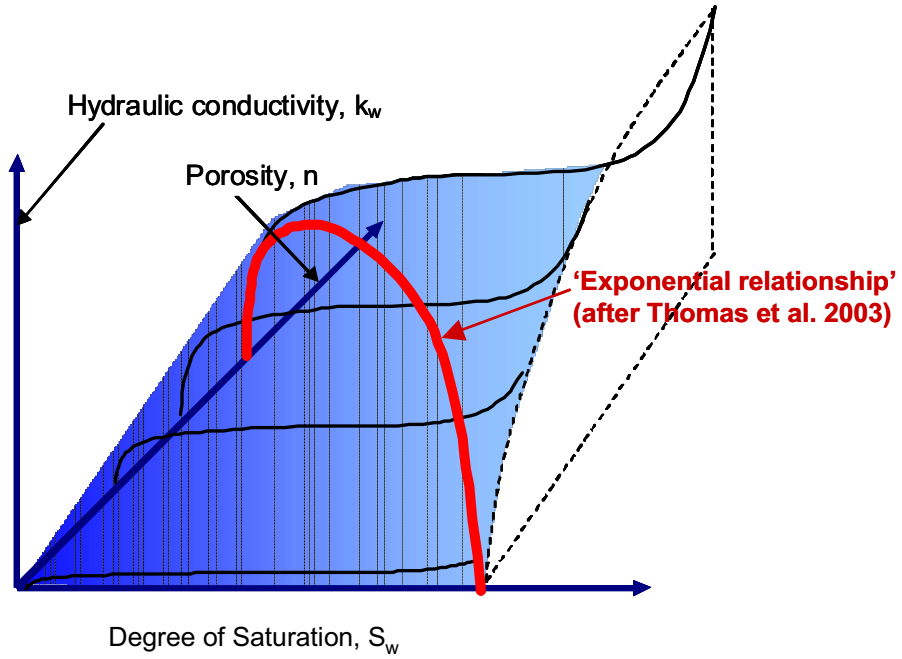


Figure 1.7 Hypothetical hydraulic conductivity surface

PART 2:
LITERATURE REVIEW

CHAPTER 2

LITERATURE REVIEW

2.1 Introduction

Modelling infiltration processes in unsaturated swelling clay requires both mechanical and hydraulic constitutive models. This chapter provides a review of literature of a number of the existing mechanical and hydraulic constitutive models. The uniqueness of this research is discussed as a justification for the research.

2.2 Mechanical Constitutive Models

Mechanical constitutive models describe the relationship between change in stress-state variables and the resulting strains. The stress-state variables and the existing mechanical constitutive models are discussed in this section.

2.2.1 Stress-state Variables

The engineering behaviour of saturated soils can be described using Terzaghi's effective stress equation (Terzaghi 1936). In the case of unsaturated soils, two approaches are generally used to describe the engineering behaviour of unsaturated soils.

The first approach is to use the modified effective stress. Bishop (1959) proposed this equation to interpret originally the shear strength behaviour of unsaturated soils.

$$\sigma' = (\sigma - u_a) + \chi(u_a - u_w) \quad [2.1]$$

where σ' is the effective stress; and χ is the effective stress parameter, which has a value of unity for saturated soils and a value of zero for dry soils.

In this approach, the shear strength is determined on the basis of the effective strength parameters (c' and ϕ') and a single stress variable (σ') defined as:

$$\tau = c' + \phi'(\sigma') \quad [2.2]$$

There has been growing interest in extending Bishop's effective stress approach for the prediction of the shear strength of unsaturated soils (e.g. Khalili and Khabbaz 1998, Fleureau et al. 1995, Oberg and Salfors 1995, Bolzon et al. 1996, Khalili et al. 2000). Although Jennings and Burland (1962) argued the limitations of the effective stress equation to describe the behaviour of unsaturated soil due to the incorporation of a parameter that is a function of material properties. However, this approach is considered advantageous as it facilitates proposing constitutive models using just one stress state variable. The implementation algorithm of this approach is simpler than the second approach as follows.

The second approach is to use an independent stress-state variable approach. Fredlund and Morgenstern (1977) proposed using any two of the stress-state variables $(\sigma-u_a)$, $(\sigma-u_w)$ and (u_a-u_w) to describe the stress-state of an unsaturated soil, where u_w is the pore water pressure and u_a is the pore air pressure. This approach can improve simulation response, but more rigorous algorithms are required to implement such constitutive models. This thesis is based on the philosophy of using two independent stress-state variables for developing constitutive models.

2.2.2 Mechanical Constitutive Models for Unsaturated Soils

The types of constitutive models used to describe the mechanical behaviour can be categorized into broad categories: linear elastic model, Mohr-Coulomb and critical state soil mechanics as illustrated in Figure 2.1.

2.2.2.1 Linear Elastic Model

Although soil is not purely linear elastic, a linear elastic model can be used to model soil behaviour in some cases in geotechnical engineering (Davis and Selvadurai 1995). The linear elastic model follows Hooke's law and requires at least two (2) parameters (i.e., Young's modulus E or bulk modulus K ; Poisson's ratio ν or shear modulus G). A linear elastic model is the simplest of the models and is useful for approximate checks of more rigorous models. Most of the algorithms used to implement more rigorous constitutive models (Mohr-Coulomb or critical state soil mechanics) include a linear-elastic component. The linear elastic model can be extended for both saturated and unsaturated soils (Figure 2.1).

2.2.2.2 Mohr-Coulomb Model

The Mohr-Coulomb criterion (Terzaghi 1936) for saturated soil is usually illustrated as the net effective normal stress (σ_n') versus shear stress (τ). This yield criterion can be developed using two (2) parameters: cohesion (c'), and friction angle (ϕ') (Figure 2.2).

Fredlund et al. (1978) proposed the Mohr-Coulomb model for unsaturated soils in Figure 2.3. The suction (s) is added as the third orthogonal axis to describe the failure criterion for unsaturated soil. The parameter (ϕ_b) that describes the contribution of shear strength with respect of suction is introduced. The linear shear strength envelope for saturated soil conditions becomes a planar surface to describe the shear strength behaviour of unsaturated soil (Figure 2.3). The soil behaves elastically when the stress-state is located under the surface, while plastic strain occurs when the stress-state reaches the criterion (Figure 2.3). This Mohr-Coulomb model produces linear-perfectly plastic response that is linear response within both elastic and plastic stages but having different slopes in both stages.

2.2.2.3 Critical State Model

The critical state model was first identified with the original Cam-Clay formulation (Roscoe et al. 1958, Schofield and Wroth 1968). Roscoe and Burland (1968) presented the Modified Cam-Clay model that incorporated an elliptical yield locus as illustrated in Figure 2.4a. The yield criterion is described in p - q space (Figure 2.4a). Inside the ellipse (Figure 2.4a), the soil behaves as a non-linear elastic material that follows the slope κ on natural logarithmic scale (Figure 2.4(b)). When the mean stress reaches the ellipse, plastic strain occurs and it follows a constant slope λ on natural logarithmic scale

(Figure 2.4b), at the same time the preconsolidation pressure increases and the ellipse grows in size. This feature is known as strain-hardening (Figure 2.4a).

Alonso et al. (1987) presented a conceptual model that was for interpreting the mechanical behaviour of unsaturated clay. Alonso et al. (1990) proposed the mathematical formulation of this model named the Basic Barcelona Model (BBM). This formulation was an extension of the modified cam-clay model (MCC) (Roscoe and Burland 1968). This model utilized three stress-state variables: mean stress (p), deviatoric stress (q), and suction (s) (Alonso et al. 1990). The BBM (Alonso et al. 1990) includes features such as: yield surface, critical state surface, and stress-volume relationships (Figure 2.5). Figure 2.5b shows the yield surface in p - s space that is limited by three lines: LC-curve (loading collapse), k -line (tension) and SI-line (suction increase). The SI-line and k -line can be generated using two parameters (k and s_0), while the LC-curve is dependent on six parameters ($\lambda(0)$, κ , r , β , p_0^* , and p_1). Parameter k is the slope of k -line and s_0 is the suction limit defining SI-line in the BBM. Parameters κ and $\lambda(0)$ are the coefficient of soil compressibility corresponding with the changes in mean stress (p). Parameter κ is the slope of $\ln(p)$ versus v within elastic range. Parameter $\lambda(0)$ is the slope of $\ln(p)$ versus v when plastic strain occurs at saturated conditions. Parameters p_0^* is the mean stress at zero suction located on LC-line. This parameter is the same as the preconsolidation pressure in the Modified Cam-Clay model for saturated clay (Roscoe and Burland 1968). The parameter p_1 is the reference mean stress that defines the LC-curve. The parameters r and β are the other fitting parameters that define the LC-curve.

In p-q space, an ellipse, such as that of the modified cam-clay model shapes the yield surface (Roscoe and Burland 1968). This ellipse increases its area with an increase in suction, as a result of increasing shear strength of clay material when drying occurs. The critical state slope M to build this ellipse is independent of the suction for the BBM. When saturated ($s=0$), the ellipse recovers the modified cam-clay ellipse for saturated soil (Roscoe and Burland 1968).

At stress-state levels located inside the yield surface, the material behaves elastically. When stress-states reach the yield surface, non-recoverable hardening occurs and the yield surface grows in size as a result of permanent deformations experienced by the soil (densification). During yielding, the strain increment consists of elastic and plastic strain components. If the stress path decreases, the size of the yield surface remains at the position corresponding to the maximum stress-state achieved along the stress path. The yield surface and critical state surface in p-q-s space due the BBM are illustrated in Figure 2.6.

Deformation due to a change in suction is controlled by the coefficient of compressibility parameters κ_s and λ_s as illustrated in Figure 2.5(d). The parameters κ_s and λ_s is the slopes of $\ln(s)$ versus specific volume (v) within elastic range and plastic range correspondingly. These parameters κ_s and λ_s are independent of suction changes. Deformations due to changes in mean stress (p) are controlled by the parameters κ and $\lambda(s)$ as illustrated in Figure 2.5(c). In the BBM, the parameter $\lambda(s)$ is a function of suction. This function is developed from coupling of the LC-curve with the stress-volume relationship. The parameter κ in the BBM is independent of suction. However, some of

the laboratory test results show that the parameter κ decreases with increasing suction (s) (e.g., Vicol 1990, Al-Mukhtar et al. 1993, Priyanto et al. 2004, 2005).

Wheeler and Sivakumar (1995) proposed a constitutive model calibrated using the results of triaxial tests on samples of compacted speswhite kaolin. In this discussion it will be called the Wheeler and Sivakumar (1995) Model (WSM). The WSM is slightly different from the BBM. Unlike the BBM, the critical state slope M is dependent on the suction level. Wheeler and Karube (1996) compares the normal compression lines due to the BBM and the WSM as shown in Figure 2.7. The different type of sample materials and laboratory tests used to calibrate and develop constitutive model can affect the features of constitutive model. The BBM and the WSM model were developed based on results of laboratory tests on low to moderate plasticity clay.

Gens and Alonso (1992) proposed a conceptual model for unsaturated swelling clay or expansive clay. The complete mathematical formulation is presented in Alonso et al. (1999). This model, called the Barcelona Expansive Model (BExM) (Alonso et al. 1999), introduced two levels of structures, the macrostructural and microstructural levels. The macrostructural level is mainly saturated and the effective stress concept holds, while the microstructural behaviour is elastic and volumetric. The BExM (Alonso et al. 1999) proposed three (3) additional yield loci: Normal-line (NL), Suction Increase (SI), and Suction Decrease (SD) as illustrated in Figure 2.8. The BExM (Alonso et al. 1999) is calibrated using the results of oedometer controlled suction tests on compacted pellets of Boom clay (Alonso et al. 1995).

The Bentonite-Sand Buffer (BSB) material had been tested at the University of Manitoba using triaxial tests with controlled suction and suction measurements (Blatz and Graham

2000, Siemens and Blatz 2006). The BSB is a 50:50 mixture (by dry mass) of sodium bentonite and silica sand. The sand is well-graded silica sand. The clay is sodium rich bentonite with a liquid limit (w_L) of 585-607% and plastic limit (w_P) of 40-48% (Anderson 2003), which indicates that it is a highly expansive material (Siemens 2006). Extensive series of laboratory tests of the unsaturated BSB at the University of Manitoba (Tang 1999, Blatz 2000, Anderson 2003, and Siemens 2006) has resulted in at least two critical state based constitutive models by: Tang and Graham (2002); and Blatz and Graham (2003).

Delage and Graham (1996) argued that in plastic clays, the LC-curve and SI-line of the BBM are generated by inherently similar mechanisms of plastic hardening in the soil microstructure. Due to this reason the two lines should perhaps be coupled, it resulting in a continuous yield envelope is shown in Figure 2.9. Tang and Graham (2002) combined all three yield lines (e.g., LC, SI, and k-line) of the BBM resulting in a continuous yield locus in Figure 2.9.

The application of the more rigorous model is useful to describe the behaviour of unsaturated swelling clay. The rigorous model usually requires many parameters and the calibration of these parameters is usually challenging in both the laboratory testing and numerical modelling. A constitutive model becomes more useful when it is implemented within a numerical modelling tool such as finite element (FE) or finite difference (FD) analysis software, because it can be applied to model an engineering system. The more rigorous model also requires more complicated formulation. The algorithm used in the numerical implementation within computer software of more rigorous constitutive model is also more complicated and required an excessive time to solve the problem. In some cases the solving time of the numerical modelling can be

longer than the real time of the process. However, development of more rigorous constitutive model is useful to expand the application of numerical modelling from back-analysis to long-term prediction. Although solving the more rigorous constitutive model still requires excessive time at present time, but the development of the faster computer speed in the future can solve this problem. The same finite element analysis problem that was required a day to solve ten years ago can be solved within less than an hour at present time.

Considering only the computer technology at the present time, the simplification of constitutive model is preferred to solve the analysis within reasonable time. Blatz and Graham (2003) simplified the LC-curve of the BBM to a linear relationship called the LY-line in Figure 2.10. This model will be called the BGM (Blatz and Graham 2003) in this thesis. The yield due to suction increase for this material had never been investigated, even for very high suction values (Blatz and Graham 2000, Blatz and Graham 2003, Blatz 2000, Anderson 2003, Siemens 2006). Consequently, the SI-line is not considered significant for this material over the suction range examined. A planar critical state surface in Figure 2.11 is used based on the laboratory measurement of the BSB material (Wiebe et al. 1998). This planar critical state surface (Figure 2.11) and yield loci in p - s space (Figure 2.10) are used to calculate the slope of the critical state line N . Figure 2.12 illustrates nonlinear relationship of parameter N as a function of total suction s . The comparison of p - q yield loci for the BBM and the BGM is illustrated in Figure 2.13. The critical state slope (M) of the BBM is constant (independent of suction s) (Figure 2.13a), while the critical state slope (N) of the BGM is a function of the total suction (s) (Figure 2.13b). Finally, the yield surface and the critical state surface of the BGM in p - q - s space are illustrated in Figure 2.14.

The BBM and the BGM are discussed in detail in this thesis due to the following reasons. The BBM is the first constitutive model based on the critical state soil mechanics, while the BGM is one of the models calibrated using laboratory test results for the compacted BSB material. Other constitutive models calibrated using laboratory results of the BSB (e.g., Delage and Graham 1996 or Tang and Graham 1999) are beyond the scope of this thesis and can be considered as a suggestion for future research.

Some constitutive models suggest incorporating the degree of saturation (S_w) to define stress-state variables (Toll 1990, Toll and Ong 2003, Gallipoli et al. 2003, Tamagnini 2005, Kato et al. 1995, Karube et al. 1995). This approach is beneficial in the implementation algorithm and is applied in the implementation of the mechanical constitutive models in Chapter 3. Consideration of the degree of saturation (S_w) within the constitutive models is one of the methods to couple the mechanical (M) and hydraulic (H) constitutive models. This approach can reduce the complexity of the implementation of the constitutive models. Other constitutive models, such as viscoplastic models incorporating stress-dependent velocity (e.g. Yin 1990, Yin and Graham 1999) are beyond the scope of this thesis.

2.3 Hydraulic Constitutive Models

The hydraulic constitutive models consist of the water retention curve (WRC) and the permeability functions.

2.3.1 Water Retention Curve (WRC) Equations

The water retention curve (WRC) for an unsaturated soil is defined as the relationship between gravimetric water content (w) as a function of total suction (ψ) for a given soil (Williams 1982). The total suction (ψ) corresponds to the free energy of the soil water, which consists of matric and osmotic suction components written as follows (Fredlund and Rahardjo 1993):

$$\psi = (u_a - u_w) + \pi \quad [2.2]$$

where:

- ψ = total suction
- u_a = pore air pressure
- u_w = pore water pressure
- π = osmotic suction

In most geotechnical engineering applications the osmotic suction (π) is much smaller than the matric suction ($u_a - u_w$), such that the total suction (ψ) is the same as the matric suction ($u_a - u_w$) (Fredlund and Rahardjo 1993).

Considering the matric suction ($u_a - u_w$) is equal to the total suction (ψ), the symbol (ψ) can be used to describe the matric suction. A typical water retention curve (WRC) plotted in log matric suction (ψ) versus volumetric water content (θ) is illustrated in Figure 2.15 (after Fredlund and Xing 1994). A few parameters can be defined from this water retention curve (WRC): the saturated volumetric water content (θ_s), the residual

volumetric water content (θ_r), the air-entry value or bubbling pressure (ψ_r), and the residual air content (θ_a). The WRC can also be described by plot of degree of water saturation (S_w) versus matric suction (ψ) or plot of gravimetric or volumetric water content (w or θ) versus matric suction (ψ).

The WRC is dependent on the type of soil. Typical WRCs of three types of soil (e.g., sandy soil, silty soil, and clayey soil) are illustrated in Figure 2.16 (Fredlund and Xing 1994). Clayey soil produces greater suction than sandy soil and silty soil (Figure 2.16) for the same volumetric water content (θ).

Mathematical equation describing the WRC is required in numerical analysis methods (finite element (FE) or finite difference (SD) analyses). Lu and Likos (2004) reviewed several mathematical equations for WRC. The most commonly used in geotechnical engineering applications are those of Brooks and Corey (1964), van Genuchten (1980), and Fredlund and Xing (1994). Other WRCs are also presented such as those of Gardner (1958), Farrel and Larson (1972), Williams et al. (1983), McKee and Bumb (1984, 1987). Most of these equations are developed using an empirical approach based on curve fitting of laboratory test results.

2.3.2 Generic Form of Water Retention Curve

Leong and Rahardjo (1997a) suggested that most WRC can be derived from the following generic form:

$$a_1\theta^{b_1} + a_2 \exp(a_3\theta^{b_1}) = a_4\psi^{b_2} + a_5 \exp(a_6\psi^{b_2}) + a_7 \quad [2.3]$$

where $a_1, a_2, a_3, a_4, a_5, a_6, a_7, b_1,$ and b_2 are constants, ψ is suction pressure; and Θ is normalized volumetric water content, which is defined as:

$$\Theta = \frac{\theta_w - \theta_r}{\theta_s - \theta_r} \quad [2.4]$$

where

θ_w = volumetric water content;

θ_s = the saturated volumetric water content; and

θ_r = the residual volumetric water content.

Substitution of the parameters a_i and b_i in Equation 2.3 with constants presented by Leong and Rahardjo (1997a) results in the WRC of Brooks and Corey (1964), van Genuchten (1980), and Fredlund and Xing (1994). The equations of the three WRC equations are presented as follows.

1. *Brooks and Corey (1964):*

$$\theta_w = \begin{cases} \theta_s & \psi < \psi_b \\ \theta_r + (\theta_s - \theta_r) \left(\frac{\psi_b}{\psi} \right)^{\lambda_{bc}} & \psi \geq \psi_b \end{cases} \quad [2.5]$$

where ψ_b is the air entry pressure

λ_{bc} is “pore size distribution index”

2. *Van Genuchten (1980):*

$$\theta_w = \theta_r + \frac{(\theta_s - \theta_r)}{(1 + a\psi^n)^m} \quad [2.6]$$

where a, m, and n are fitting parameters

3. Fredlund and Xing (1994):

$$\theta_w = C(\psi)\theta_s \left[\frac{1}{\ln(e + (\psi/a)^n)} \right]^m \quad [2.7.a]$$

$$C(\psi) = \left[1 - \frac{\ln(1 + \psi/\psi_r)}{\ln(1 + 10^6/\psi_r)} \right] \quad [2.7.b]$$

where a, m, and n are fitting parameters; e is the natural logarithmic constant; C(ψ) is a correction factor that forces the model through a prescribed suction value of 10^6 kPa at zero water content; and ψ_r is the suction (kPa) estimated at the residual condition.

2.3.3 Hysteresis of Water Retention Curve

The water retention curve (WRC) hysteretic behaviour is with respect to drying and wetting cycles. Such a behaviour has been explained from both experimental and theoretical viewpoints by several researchers (e.g. Haines 1930, Mualem 1984, Israelchvili 1992, Nimmo 1992, Iwata et al. 1995, Dueck 1996). The hysteresis in the WRC is illustrated in Figure 2.17. Hysteretic behaviour has been attributed to several mechanisms that act on both a relatively microscopic (particle) scale and a relatively

macroscopic scale (Lu and Likos 2004). This hysteretic behaviour is also one of the challenges in the development and implementation of hydraulic constitutive models.

2.3.4 Permeability Functions

The permeability function defines the relationship of the hydraulic conductivity (k_w) as a function of the degree of water saturation (S_w) or matric suction (ψ). Leong and Rahardjo (1997b) classified permeability functions for unsaturated soils as: empirical equations, macroscopic models, and statistical models.

Empirical equations describe the dependence of water permeability (k_w) with matric suction (ψ) or volumetric water content (θ_w). The constants in the empirical equations are best determined from a curve fit of the test data (Leong and Rahardjo 1997b). Macroscopic models assume similarity between laminar fluid flow on a microscopic level and macroscopic fluid flow through the soil (e.g., Mualem 1978, Mualem 1986, Lu and Likos 2004, Leong and Rahardjo 1997b).

Leong and Rahardjo (1997b) and Lu and Likos (2004) summarized the empirical and macroscopic equations for modelling unsaturated hydraulic conductivity functions. Several examples of the empirical and macroscopic equations are those of Richards (1931), Averjanov (1950), Wind (1955), Gardner (1958), Brooks and Corey (1964), Davidson et al. (1969), and Campbell (1973). Statistical hydraulic conductivity models may be used to indirectly predict the hydraulic conductivity function from measurements or models of the WRC (Leong and Rahardjo 1997b, Lu and Likos 2004).

This research utilizes FLAC (Itasca 2000a, 2000b, 2001) to implement the hydraulic constitutive models. The empirical model of van Genuchten (1980) is used to describe the permeability function. The permeability function described in term of relative permeability (κ^r) is the ratio of the permeability at arbitrary degree of saturation (k) to the permeability in saturated condition (k^{sat}).

$$\kappa^r = k / k^{\text{sat}} \quad [2.8]$$

Both water and air permeability functions are required in 2-phase flow formulation (Peaceman 1977, Itasca 2001). The permeability of air is estimated from:

$$k_a^{\text{sat}} = (k_w^{\text{sat}}) \times (\mu_{\text{rat}}) \quad [2.9]$$

where:

k_a^{sat} is the air permeability at air saturated conditions;

k_w^{sat} is the water permeability at water saturated conditions;

μ_{rat} is the viscosity ratio, the ratio of viscosity of water (μ_w) to the viscosity of air (μ_a),

which is defined as :

$$\mu_{\text{rat}} = \mu_w / \mu_a \quad [2.10]$$

The dependence of the water (κ_w^r) and air relative permeability (κ_a^r) on the degree of water saturation (S_w) is given by the equation below (Itasca 2001, van Genuchten 1980) is given by:

$$\kappa_w^r = S_e^b [1 - (1 - S_e^{1/a})^2] \quad [2.11]$$

$$\kappa_a^r = (1 - S_e)^c [1 - S_e^{1/a}]^{2a} \quad [2.12]$$

and

$$S_e = \frac{S_w - S_r}{1 - S_r} \quad [2.13]$$

where

S_e = effective degree of water saturation

S_w = degree of water saturation

S_r = residual degree of water saturation

The plots the water relative permeability in linear and log scale are illustrated in Figure 2.18. There is a similarity in shape between the permeability function and water retention curve (WRC), since the water only flows through the water phase in the soil (Leong and Rahardjo 1997b). Thus, theoretically the hysteretic behaviour in the water retention curve (WRC) will also be observed in the permeability function. Generally, the parameters of the water retention curve (WRC) and permeability function are estimated using a curve-fitting method of the laboratory measurements.

2.3.5 Mathematical Equations, Implementation, and Measurements

Generally the mathematical equations of a WRC (Brooks and Corey 1964, van Genuchten 1980, and Fredlund and Xing 1994) relate the soil suction (ψ) to the volumetric water content (θ_w). Most computer software (e.g., FLAC (Itasca 2000b), CODE_BRIGHT (Olivella et al. 1996)) implements the WRC as a relationship between the water degree of saturation (S_w) and suction (s). Consequently, Equation 2.4 is modified as Equation 2.13 in the implementation of WRC.

Most laboratory measurements observe the relationship of total suction (s) as a function of the gravimetric water content (w) (e.g. Wan 1996, Blatz 2000). The conversion from gravimetric water content (w) to degree of water saturation (S_w) is required to calibrate constitutive models. The degree of water saturation (S_w) can be obtained from gravimetric water content (w) using:

$$S_w = w \cdot G_s / e \quad [2.15]$$

where G_s is the specific gravity or relative density that is the ratio of the density of soil solids to the density of water, and e is the void ratio. In many cases, the volume change of the specimen was not directly measured. Consequently, an assumption of constant specific gravity (G_s) and void ratio (e) should be made to calculate the degree of water saturation (S_w) from gravimetric water content (w) using Equation 2.15. In some cases, these assumptions resulted in a degree of water saturation (S_w) that is greater than 100%. This also poses a challenge in the calibration of the WRC.

Villar (2002) proposed that the density of water (ρ_w) could change during testing causing the degree of water saturation (S_w) greater than 100%. Various authors suggested that in the vicinity of clay laminae, the structure of water molecules is disturbed, their properties differing from those of free water (Sposito and Prost 1982). This modification of the properties of the adsorbed water becomes more noteworthy with low contents of water such as within the unsaturated swelling clay with high dry density in this thesis. Martin (1962) showed the variation of the water density adsorbed in montmorillonite as a function of clay water content obtained by means of pycnometers and X-ray diffraction. He also presented the water density calculated to maintain the degree of saturation of the clay at 100 % for different types of test. Push et al. (1990) found that the density of water in sodium montmorillonite depend on the degree of ordering and the presence of molecules of interstitial water. Consideration of clay and pore fluid chemistry and mineralogy to describe the behaviour of unsaturated swelling clay may be required.

Villar (2002) also suggested that the error in determining final water content and inaccuracy in the sample measurement could also cause this anomaly. Further direct measurements of the changes of water density are still required to support this argument. However, this subject is beyond the scope of this thesis and can be considered as a suggestion for future research.

2.4 Implementation Formulations of Fluid-Mechanical Constitutive Models for Unsaturated Soil

Several constitutive models have been suggested to interpret the H-M behaviour of unsaturated soils. These formulations are based on the extending consolidation theory (e.g., Terzaghi 1936, Biot 1941, Biot 1955) or based on multiphase flow formulations (Peaceman 1977). The latter is used in the two-phase flow hydro-mechanical analysis in FLAC (Itasca 2001).

Implementation of the constitutive models for H-M analysis can be made using the finite element (FE), finite volume (FV) or finite difference (FD) method. Other numerical methods, such as a discrete element method (Anandarajah 1994) and pore-network model (Simms and Yanful 2005), have also been proposed to model the soil behaviour. The last two models have not yet been extended or used, but can be alternatives as a suggestion for future research. The discussion of this thesis focuses on a finite difference (FD) method.

This thesis uses 2-phase flow formulation to implement the H-M constitutive models using FLAC (Itasca 2001). The FLAC version 5.0 (Fast Lagrangian Analysis of Continua) (Itasca 2000b) uses the finite difference method to solve a set of partial differential equations. The ability to implement the user-defined constitutive models in FLAC by creating a function within the software (Itasca 2000a) is particularly beneficial in this research, because the focus of this thesis is toward the development of new constitutive models, not the development of the finite element (FE) or finite difference (FD) computer code. Currently, the two-phase flow formulation in FLAC (Itasca 2001) is limited to isothermal conditions, which is adequate for the scope of this thesis.

Mechanical constitutive models based on critical state soil mechanics; especially the BBM and the BGM are implemented in the FLAC formulations. The hydraulic

constitutive model of van Genuchten (1980) is utilized in FLAC (Itasca 2001) formulations. New proposed constitutive models are also presented and implemented in FLAC formulation in this research. The various combinations of the existing and proposed H-M constitutive models are applied to simulate the H-M behaviour of the BSB in the small scale infiltration tests (Siemens 2006) and AECL's large scale isothermal test (ITT) (Dixon et al. 2002).

2.5 Justification of Research

The aspects associated with existing numerical models for unsaturated swelling clays include: '*calibration*' of constitutive model parameters; '*selection*' and '*development*' of constitutive models; '*implementation*' of constitutive models; and '*application*' of the constitutive models to model engineered systems (Priyanto et al. 2004, 2005, 2006). All of these aspects are related to each other and equally important.

Many researches only consider some of these aspects independently, so that the difficulty to connect the physical testings and numerical modelling has not been solved. A three-fold assessment of this research is performed including: calibration to laboratory tests; simulation of laboratory tests with controlled stress paths and boundary conditions, and simulation of a large scale field test conducted by other researchers using a similar swelling clay material. This research considers all the aspects in numerical modelling of unsaturated swelling clay to improve understanding in both numerical models and physical models.

This research proposes new constitutive models for the unsaturated swelling clay (USC); a new calibration approach; new implementation algorithm of constitutive models for the USC; and their applications. These unique contributions are summarized in Chapter 10.

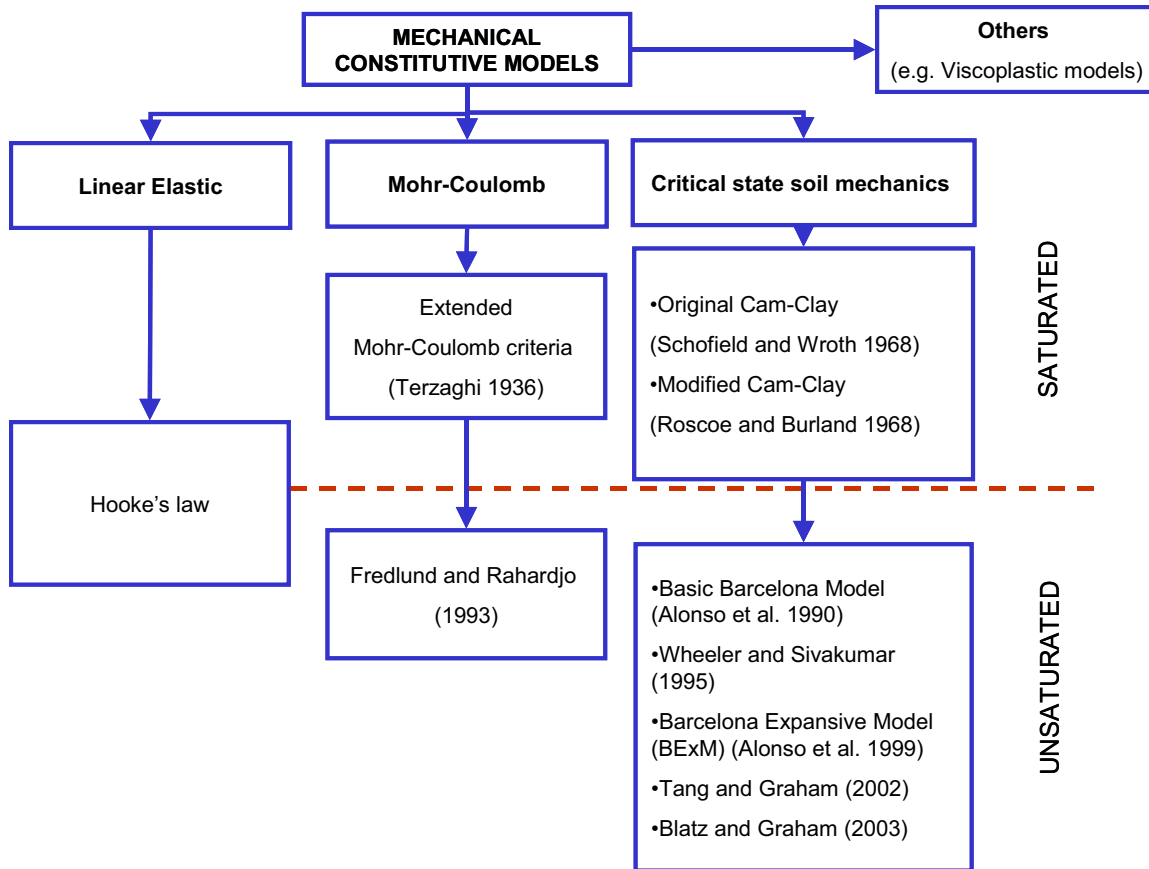


Figure 2.1. Classification of the mechanical constitutive models for clay

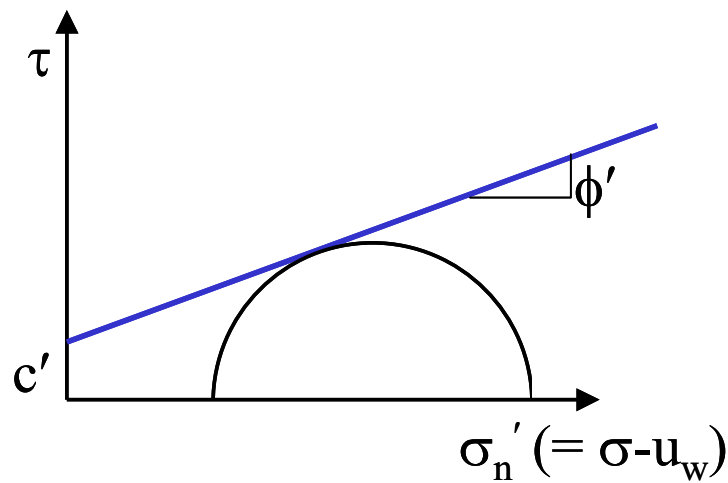


Figure 2.2. Mohr-Coulomb criteria for saturated soil (after Terzaghi 1936)

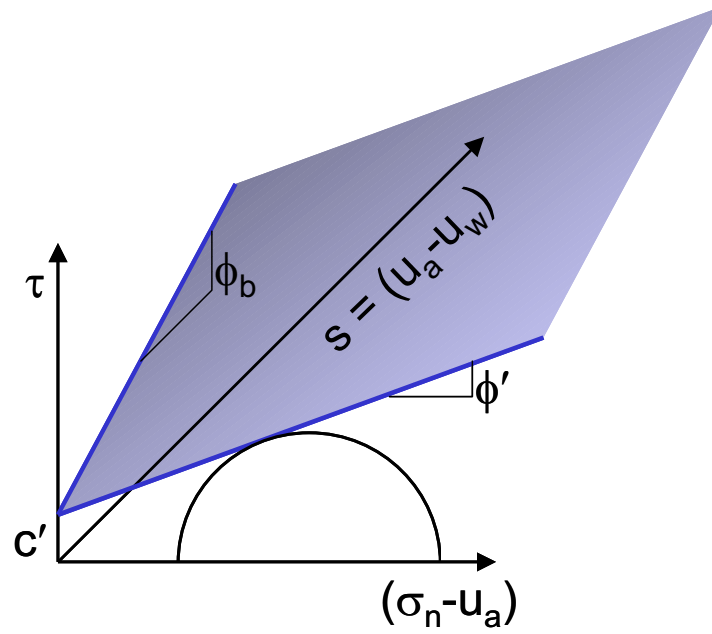


Figure 2.3. Mohr-Coulomb criteria for unsaturated soil (after Fredlund et al. 1978)

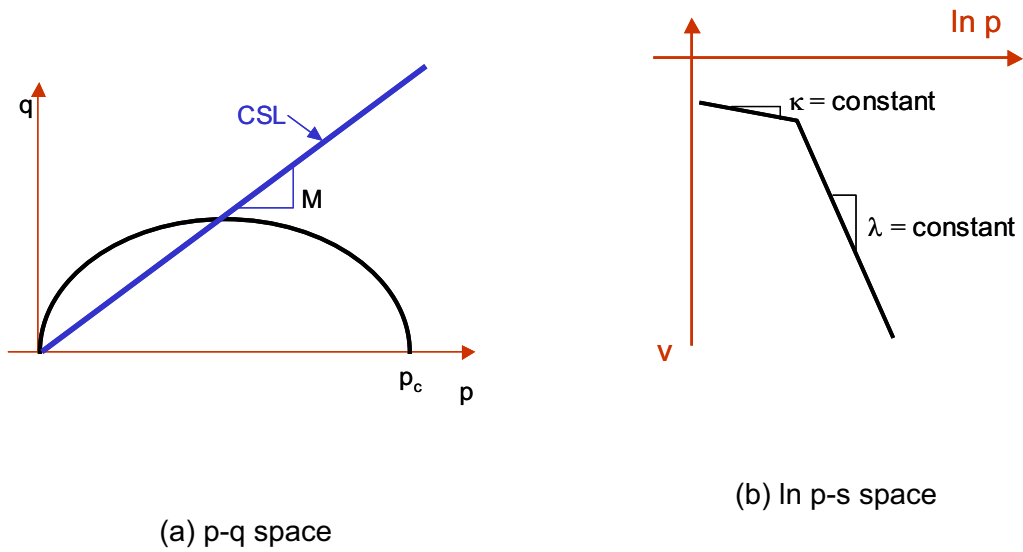


Figure 2.4. Modified Cam-clay model (after Roscoe and Burland 1968).

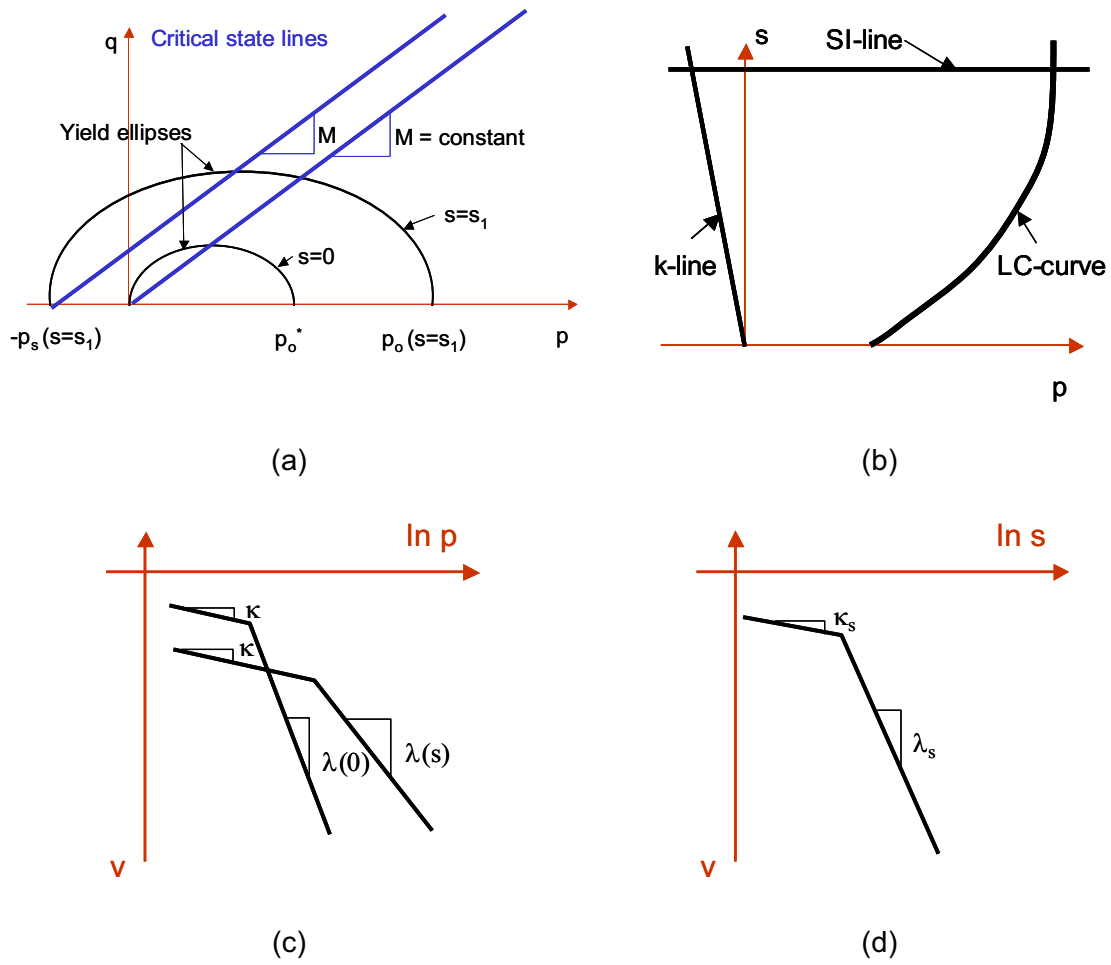


Figure 2.5 The Basic Barcelona Model (BBM): (a) p-q space; (b) p-s space; (c) v-lnp; (d) v-lns (after Alonso et al. 1990).

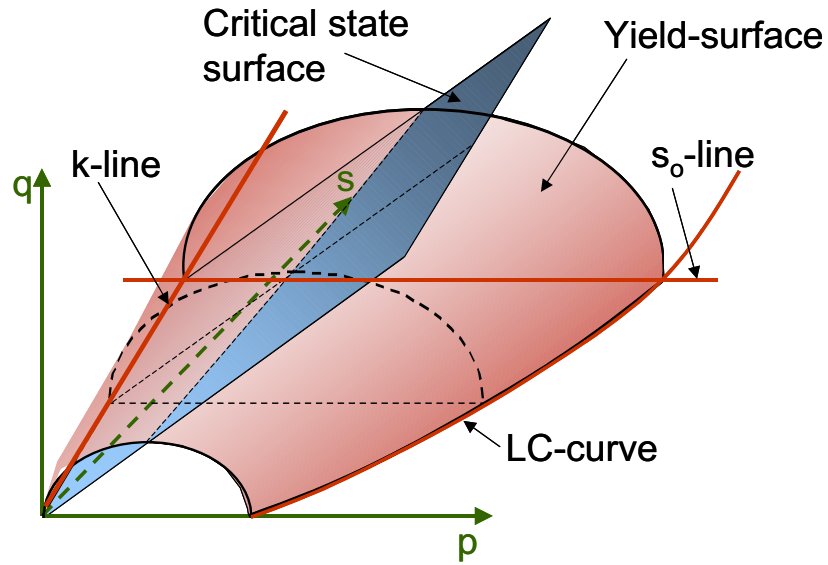


Figure 2.6 The Basic Barcelona Model (BBM) yield surface (after Alonso et al. 1990)

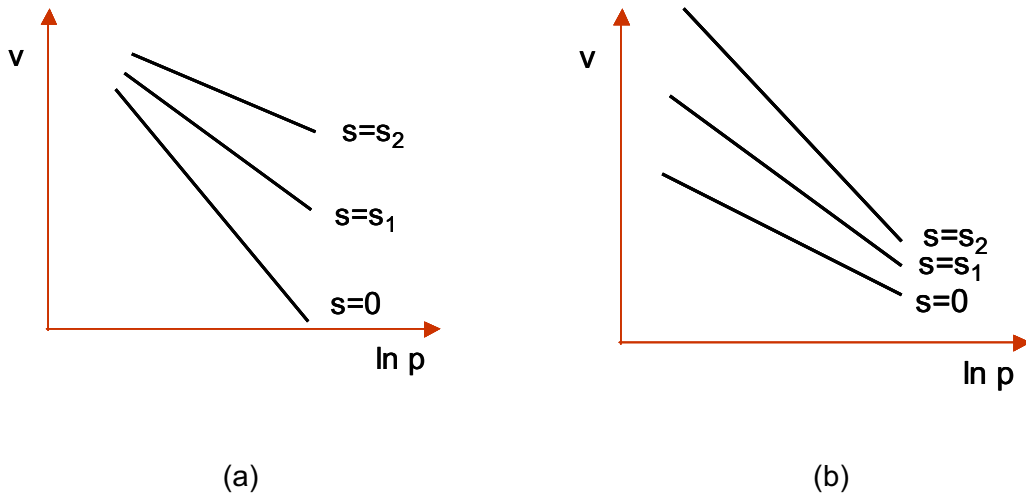


Figure 2.7 Form of normal compression lines due to the: (a) BBM (Alonso et al. 1990); (b) Wheeler and Sivakumar (1995). (after Wheeler and Karube 1996)

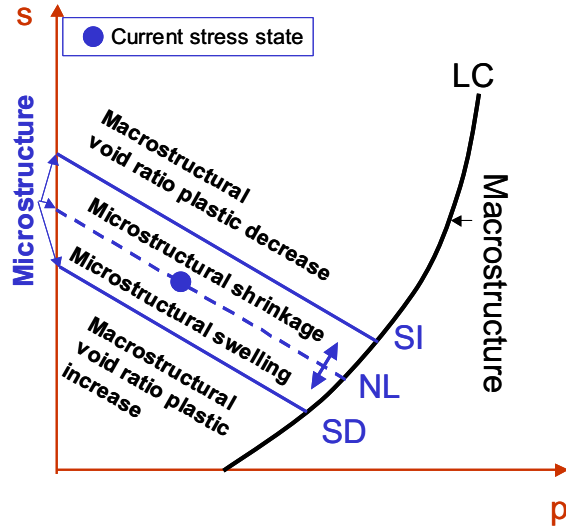


Figure 2.8 Yield surface for BExM (after Alonso et al. 1999)

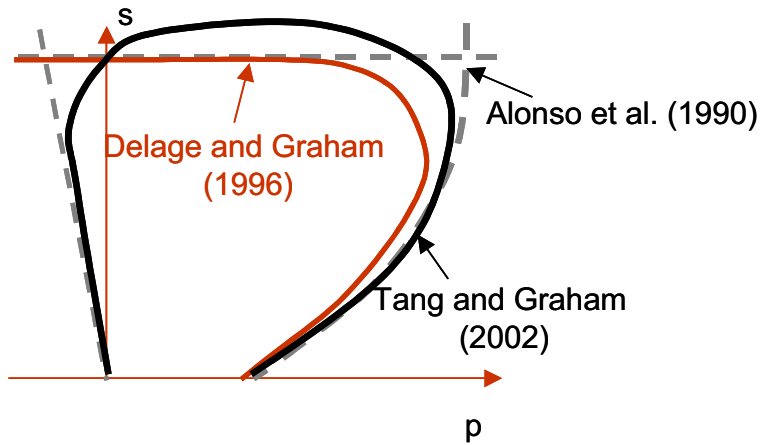


Figure 2.9 Coupling yield surfaces in p-s space (after Tang and Graham 2002, Delage and Graham 1996, Alonso et al. 1990)

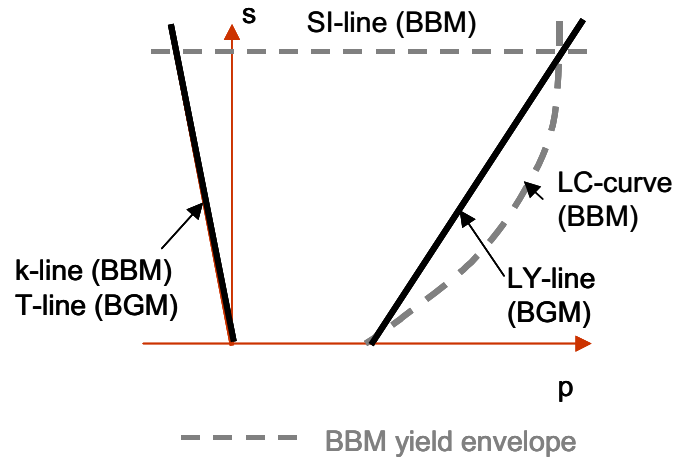


Figure 2.10 Yield surfaces on p-s space due to the BBM and the BGM

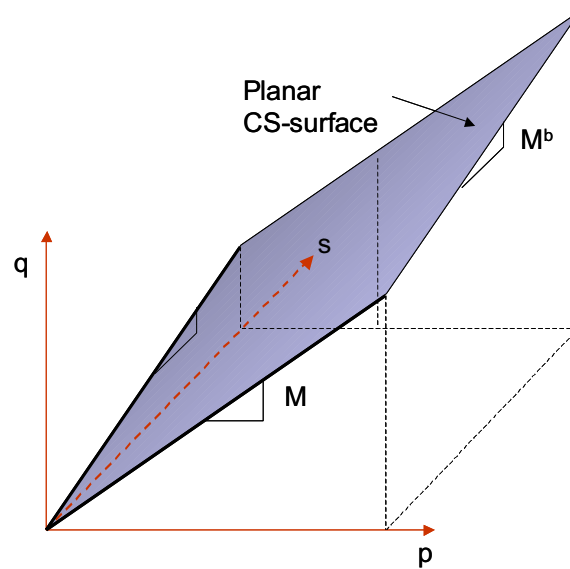


Figure 2.11 Planar critical state surface (after Wiebe et al. 1998, Blatz and Graham 2003)

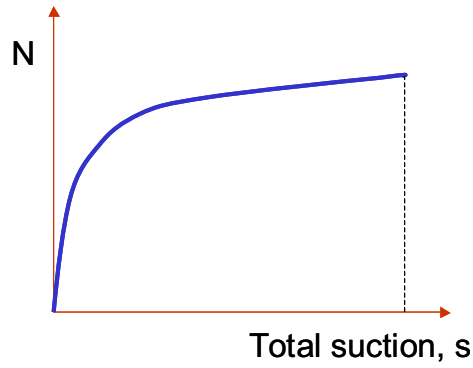


Figure 2.12 Critical state slope as a function of suction in BGM (after Blatz and Graham 2003)

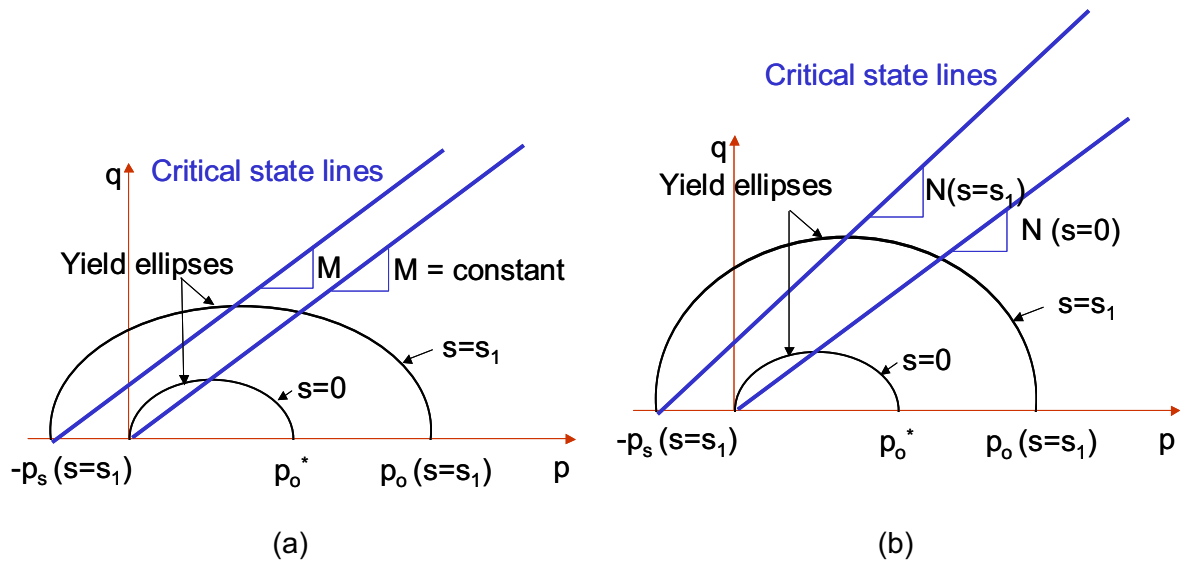


Figure 2.13 Comparison of the yield surface on p-q space of the: (a) BBM; and (b) BGM

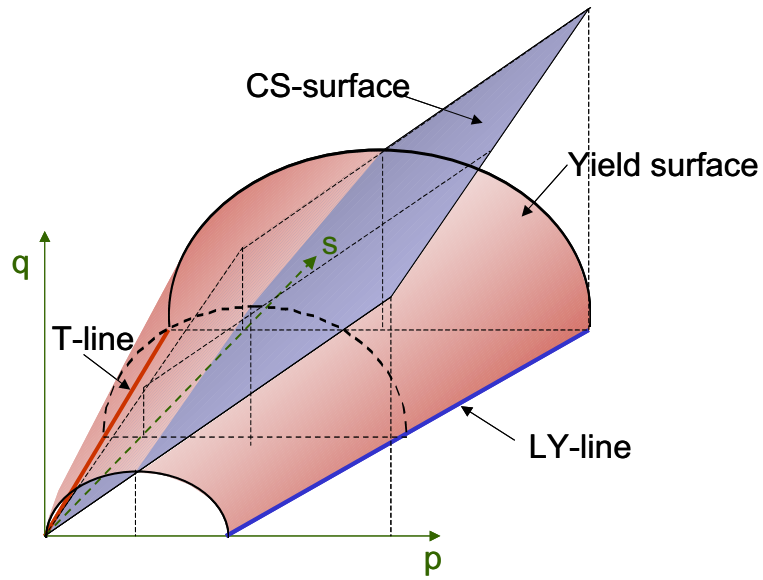


Figure 2.14 Yield surface and critical state surface for the BGM (after Blatz and Graham 2003)

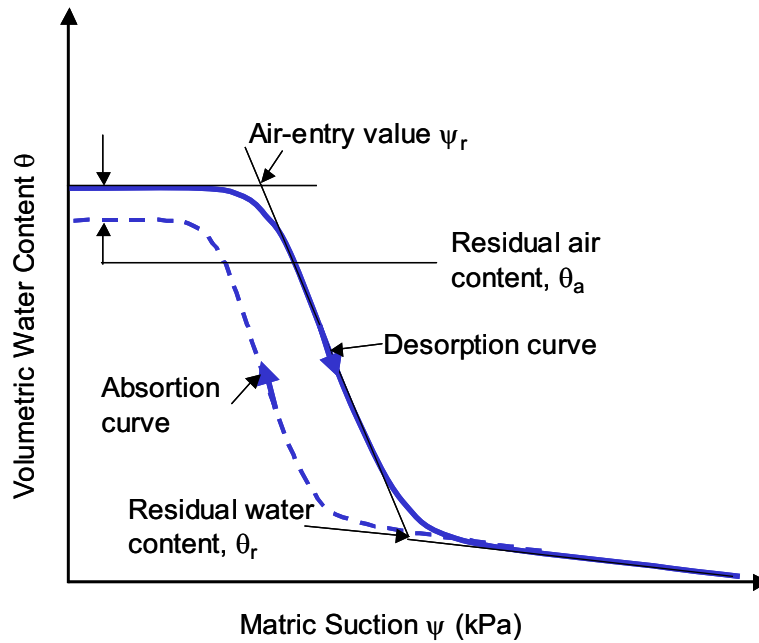


Figure 2.15 Definitions of terms of typical water retention curve (after Fredlund and Xing 1994)

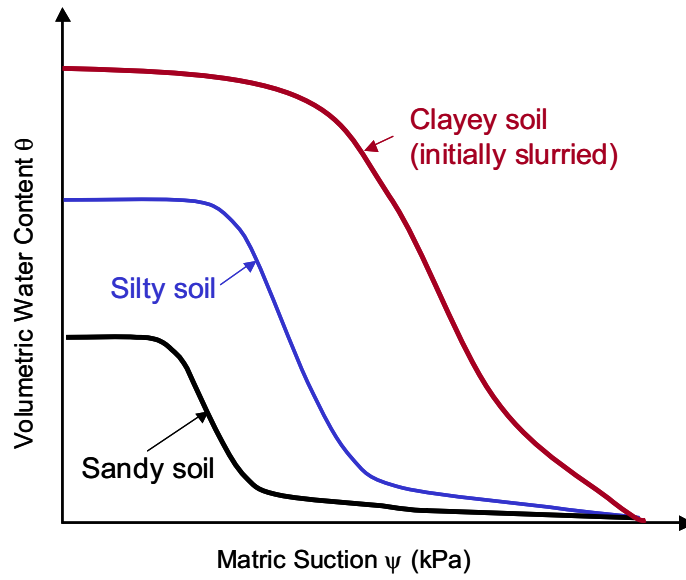


Figure 2.16 Water retention curves for sandy soil, silty soil, and clayey soil (after Fredlund and Xing 1994)

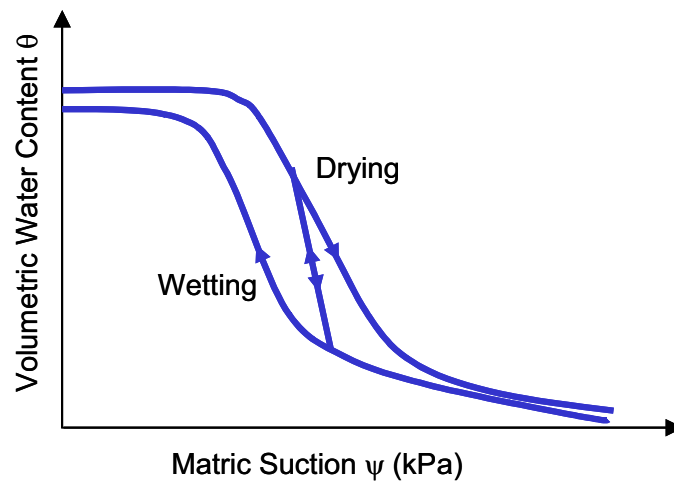


Figure 2.17 Conceptual illustration of hysteresis in water retention curve.

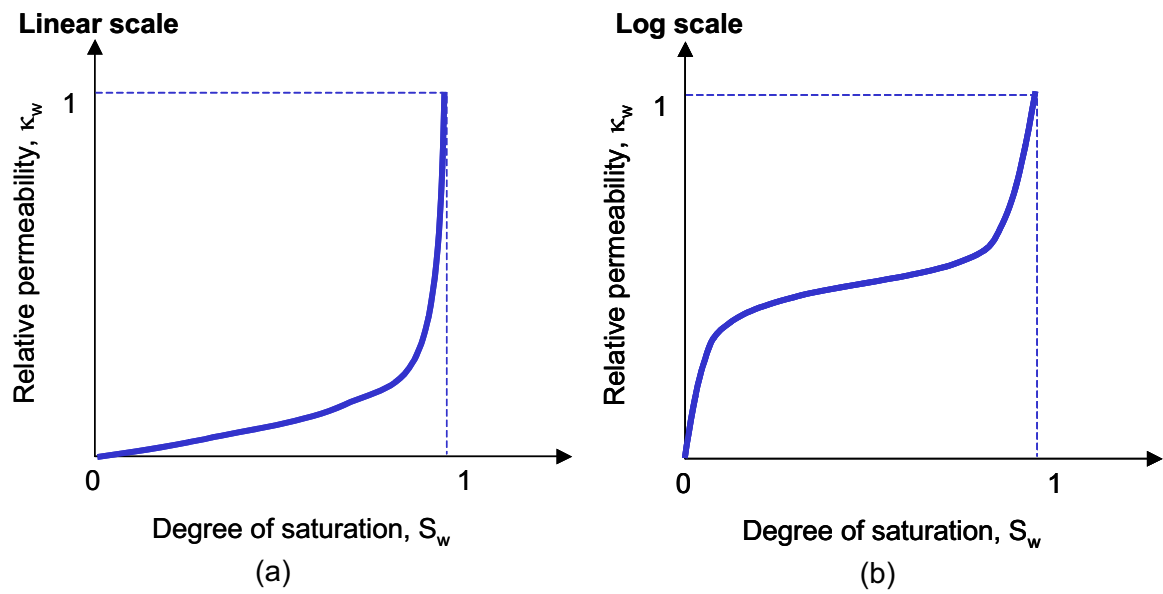


Figure 2.18 Water relative permeability curve in: (a) linear scale; and (b) log scale

PART 3:

DEVELOPMENT AND IMPLEMENTATION

CHAPTER 3

IMPLEMENTATION OF MECHANICAL CONSTITUTIVE MODELS

3.1 Summary

Prior to proposing new developments in constitutive models, it is important to first examine the most widely accepted existing models. This will allow providing comparisons between newly developed models against the current state of knowledge and suggest demonstrating any improvements over the available models. Numerical implementation of two elasto-plastic mechanical constitutive models is discussed in this chapter. The detailed mathematical formulations are also presented. Constitutive models are implemented in FLAC (Itasca 2000a). Some example analyses are provided to verify the proposed formulation.

3.2 The BBM (Alonso et al. 1990) and the BGM (Blatz and Graham 2003)

The critical state mechanical constitutive models considered in this thesis are the BBM (Basic Barcelona Model) (Alonso et al. 1990) and the BGM (Blatz and Graham 2003). The BBM is widely considered to be the first comprehensive critical state model for unsaturated clays, while the BGM is developed based on the results of triaxial tests

conducted with controlled suction and suction measurements at the University of Manitoba (Blatz 2000). Both models employ three stress-state variables: mean stress (p), deviatoric stress (q), and suction (s) to describe the state of stress in a three-phase soil material (Fredlund and Morgenstern 1977). A general review of these constitutive models is provided in Chapter 2.

Comparison of the yield loci and critical state line of the BBM and the BGM is illustrated in Figures 3.1 and 3.2. Comparison of the yield loci and critical state lines at constant suction in p - q space of the two constitutive models indicates some key differences in the definition of these material parameters (Figure 3.1). Unlike the critical state slope (M) for the BBM, the critical state slope (N) for the BGM increases when suction (s) increases (Figure 3.1).

Figure 3.2 shows the yield loci in p - s space for the isotropic condition due to the BBM and the BGM. The yield surface for the BBM is limited by the SI-line (Suction Increase), 'cohesion' line, and LC-line (Loading Collapse) (Figure 3.2a). The suction measurement to develop the BGM is higher than that of the BBM. Collapse due to suction increase has not been observed in laboratory tests on high plastic clays even for high values of suction (12 MPa) (Blatz and Graham 2003) or 80 MPa (Anderson 2003). The SI-line is not considered in the BGM, although it is still postulated to exist at some position (Figure 3.2b). Further investigation is still required to determine the location of this SI line. The yield surface is controlled by the LY-line and T-line that are both simplified to be linear.

Figures 3.3 and 3.4 illustrate the stress-volume relationship of the BBM and the BGM. Parameters κ and λ control deformation due to changes in mean stress (p). The parameter κ is consistent for both models (Figure 3.3). The parameter λ for the BBM

decreases with suction increase (Figure 3.3a), while it is constant for the BGM. The parameters κ_s and λ_s control the deformation due to change in suction (s) for the BBM (Figure 3.4a). These parameters κ_s and λ_s are independent of the suction. Since the SI-line does not exist for the BGM, deformation due to change in suction (s) for the BGM is controlled only by the parameter κ_s . The equations of the yield surface for the BBM and the BGM are summarized in Table 3.1.

3.3 Mathematical Formulation

3.3.1 Implementation Method

This research uses FLAC-2D (Fast Lagrangian Analysis of Continua) (Itasca 2000b) to implement the constitutive models. FLAC-2D is a 2-dimensional finite difference analysis software package that can be used to solve hydro-mechanical analysis. Using the “FISH” (Itasca 2000a), a built-in programming language in FLAC, the user can implement user-defined constitutive models relating stress and strain increments using an iterative process.

3.3.2 Constant Suction

Implementation of the BBM and the BGM for constant suction follows the method used in the implementation of the Modified Cam-Clay Model (Roscoe and Burland 1968) into the FLAC (Itasca 2000b) using different yield surfaces and hardening laws. This implementation process uses an incremental elastic law, yield and potential functions, plastic corrections, and hardening laws. In this section, the discussion focuses on the implementation of algorithms for the BBM. The algorithm to implement the BGM follows afterward.

3.3.2.1 Incremental Elastic Law

When considering a constant suction plane, the BBM is expressed in terms of three variables: the mean stress (p), the deviatoric stress (q) and the specific volume (v). In the FLAC implementation of this model, principal stresses ($\sigma_1, \sigma_2, \sigma_3$) are used, the out-of-plane stress (σ_{zz}) being recognized as one of these (by convention, traction and dilation are positive).

The generalized stress components (p and q) are expressed in terms of principal stresses as follows:

$$p = -\frac{1}{3}(\sigma_1 + \sigma_2 + \sigma_3) \quad [3.1]$$

$$q = \frac{1}{\sqrt{2}}\sqrt{(\sigma_1 - \sigma_2)^2 + (\sigma_2 - \sigma_3)^2 + (\sigma_3 - \sigma_1)^2} \quad [3.2]$$

Incremental strain variables associated with p and q are the volumetric strain increment ($\Delta\varepsilon_{vp}$) and distortional strain increment ($\Delta\varepsilon_q$).

$$\Delta\varepsilon_{vp} = \Delta\varepsilon_1 + \Delta\varepsilon_2 + \Delta\varepsilon_3 \quad [3.3]$$

$$\Delta\varepsilon_q = \frac{\sqrt{2}}{3}\sqrt{(\Delta\varepsilon_1 - \Delta\varepsilon_2)^2 + (\Delta\varepsilon_2 - \Delta\varepsilon_3)^2 + (\Delta\varepsilon_3 - \Delta\varepsilon_1)^2} \quad [3.4]$$

where $\Delta\varepsilon_i$, $i = 1,3$ are principal strain increments.

By assumption, the principal strain increments may be decomposed into elastic and plastic parts, so that:

$$\Delta\varepsilon_i = \Delta\varepsilon_i^e + \Delta\varepsilon_i^p, \quad i = 1,3 \quad [3.5]$$

The specific volume is defined as:

$$v = \frac{V}{V_s} \quad [3.6]$$

where V_s is the volume of solid particles, assumed incompressible, contained in a volume (V) of soil. The incremental relation between volumetric strain ε and specific volume has the form:

$$\Delta\varepsilon = \frac{\Delta v}{v} \quad [3.7]$$

Starting with an initial specific volume (v_0), for small volumetric increments:

$$v = v_0 (1 + \varepsilon) \quad [3.8]$$

where ε is the current accumulated volumetric strain.

The incremental expression of Hooke's law in principal axes may be expressed in the form

$$\begin{aligned}\Delta\sigma_1 &= \alpha_1\Delta\varepsilon_1^e + \alpha_2(\Delta\varepsilon_2^e + \Delta\varepsilon_3^e) \\ \Delta\sigma_2 &= \alpha_1\Delta\varepsilon_2^e + \alpha_2(\Delta\varepsilon_1^e + \Delta\varepsilon_3^e) \\ \Delta\sigma_3 &= \alpha_1\Delta\varepsilon_3^e + \alpha_2(\Delta\varepsilon_1^e + \Delta\varepsilon_2^e)\end{aligned}\quad [3.9]$$

where $\alpha_1 = K + 4G/3$ and $\alpha_2 = K - 2G/3$

Alternatively, using deviatoric parts of the incremental stress and strain tensors, we may write:

$$\begin{aligned}\Delta s_i &= 2G\Delta\varepsilon_{si}^e \quad i = 1, 3 \\ -\Delta p &= K\Delta\varepsilon^e\end{aligned}\quad [3.10]$$

where:

$$\begin{aligned}\Delta s_i &= \Delta\sigma_i + \Delta p; \\ \Delta\varepsilon_{si}^e &= (\Delta\varepsilon_i^e - \Delta\varepsilon^e)/3; \\ \Delta\varepsilon^e &= \Delta\varepsilon_1^e + \Delta\varepsilon_2^e + \Delta\varepsilon_3^e\end{aligned}\quad [3.11]$$

3.3.2.2 Yield and Potential Function

Yield surfaces in p-q and p-s spaces for the BBM are illustrated in Figure 3.5

The yields function from Table 3.1:

$$f = q^2 - M^2(p + p_s)(p_0 - p) \quad [3.12]$$

Using associated flow rule such as discussed by Davis and Selvadurai (2002), potential function $g = f$,

$$g = q^2 - M^2(p + p_s)(p_0 - p) \quad [3.13]$$

where:

$$M = \text{constant} \quad [3.14]$$

$$p_0 = p_1 \left(\frac{p_0^*}{p_1} \right)^{\frac{\lambda(0)-\kappa}{\lambda(s)-\kappa}} \quad [3.15]$$

$$p_s = k.s \quad [3.16]$$

$$\lambda(s) = \lambda(0) [(1 - r) \exp(-\beta s) + r] \quad [3.17]$$

In the case of the BGM, the slope of the critical state line is not constant (Figure 3.1b). The slope of the critical state line (M) is substituted as the N-parameter in Equations 3.12 and 3.13, which is defined as:

$$N = \frac{q_{cs}}{p_0 + p_s} \quad [3.18]$$

where p_s and p_0 in Equations 3.12 and 3.13 are defined from the T-line and LY-line (Figure 3.2b) as:

$$p_s = k \cdot s \quad [3.19]$$

$$p_0 = p_0^* + r \cdot s \quad [3.20]$$

Since compression has positive sign (+), from Equations 3.1 and 3.2:

$$q^2 = \frac{1}{2} \left[(\sigma_1 - \sigma_2)^2 + (\sigma_2 - \sigma_3)^2 + (\sigma_3 - \sigma_1)^2 \right] \quad [3.21]$$

$$p^2 = \frac{1}{9} \left[\sigma_1^2 + \sigma_2^2 + \sigma_3^2 + \sigma_1\sigma_2 + \sigma_2\sigma_3 + \sigma_3\sigma_1 \right] \quad [3.22]$$

Substitution of Equations 3.21 and 3.22 into Equation 3.13, the potential function is:

$$\begin{aligned}
g &= q^2 + M^2(\mathbf{p} + \mathbf{p}_s)(\mathbf{p} - \mathbf{p}_0) \\
&= q^2 + M^2(\mathbf{p}^2 + (\mathbf{p}_s - \mathbf{p}_0)\mathbf{p} - \mathbf{p}_s \cdot \mathbf{p}_0) \\
&= \frac{1}{2}[(\sigma_1 - \sigma_2)^2 + (\sigma_2 - \sigma_3)^2 + (\sigma_3 - \sigma_1)^2] + M^2 \left\{ \begin{array}{l} \frac{1}{9}(\sigma_1 + \sigma_2 + \sigma_3)^2 \\ + \frac{1}{3}(\sigma_1 + \sigma_2 + \sigma_3)(\mathbf{p}_s - \mathbf{p}_0) \\ - \mathbf{p}_s \cdot \mathbf{p}_0 \end{array} \right\}
\end{aligned} \tag{3.23}$$

3.3.2.3 Plastic Correction

The plastic correction to avoid strain increments from overstepping the yield function by a degree greater than a set limit is given by:

$$\Delta \varepsilon_i^p = \lambda^s \frac{\partial g}{\partial \sigma_i} \quad ; i = 1, 3 \tag{3.24}$$

$$\Delta \varepsilon_1^p = \lambda^s(\mathbf{c}_a); \quad \Delta \varepsilon_2^p = \lambda^s(\mathbf{c}_b); \quad \Delta \varepsilon_3^p = \lambda^s(\mathbf{c}_c) \tag{3.25}$$

where:

$$\mathbf{c}_a = \frac{\partial g}{\partial \sigma_1}; \quad \mathbf{c}_b = \frac{\partial g}{\partial \sigma_2}; \quad \mathbf{c}_c = \frac{\partial g}{\partial \sigma_3} \tag{3.26}$$

Finally, \mathbf{c}_a , \mathbf{c}_b , and \mathbf{c}_c can be summarized as follows:

$$\begin{aligned}
\mathbf{c}_a &= \frac{M^2}{3}(2\mathbf{p} + \mathbf{p}_s - \mathbf{p}_0) + (\sigma_1 - \sigma_2) + (\sigma_1 - \sigma_3) \\
\mathbf{c}_b &= \frac{M^2}{3}(2\mathbf{p} + \mathbf{p}_s - \mathbf{p}_0) + (\sigma_2 - \sigma_1) + (\sigma_2 - \sigma_3) \\
\mathbf{c}_c &= \frac{M^2}{3}(2\mathbf{p} + \mathbf{p}_s - \mathbf{p}_0) + (\sigma_3 - \sigma_1) + (\sigma_3 - \sigma_2)
\end{aligned} \tag{3.27}$$

The elastic strain increments may be expressed from Equation 3.5 as total strain increment minus plastic strain increments. In further using Equation 3.25, the elastic laws in Equation 3.9 become:

$$\begin{aligned}\Delta\sigma_1 &= \alpha_1\Delta\varepsilon_1^e + \alpha_2(\Delta\varepsilon_2^e + \Delta\varepsilon_3^e) - \lambda^s[\alpha_1c_a + \alpha_2(c_b + c_c)] \\ \Delta\sigma_2 &= \alpha_1\Delta\varepsilon_2^e + \alpha_2(\Delta\varepsilon_1^e + \Delta\varepsilon_3^e) - \lambda^s[\alpha_1c_b + \alpha_2(c_a + c_c)] \\ \Delta\sigma_3 &= \alpha_1\Delta\varepsilon_3^e + \alpha_2(\Delta\varepsilon_1^e + \Delta\varepsilon_2^e) - \lambda^s[\alpha_1c_c + \alpha_2(c_a + c_b)]\end{aligned}\quad [3.28]$$

Let the new and old stress-states be referred to by superscripts N and O respectively.

Then, by definition,

$$\sigma_i^N = \sigma_i^O + \Delta\sigma_i \quad ; i = 1,3 \quad [3.29]$$

Substitution of Equation 3.23 gives:

$$\begin{aligned}\sigma_1^N &= \sigma_1^l - \lambda^s[\alpha_1c_a + \alpha_2(c_b + c_c)] \\ \sigma_2^N &= \sigma_2^l - \lambda^s[\alpha_1c_b + \alpha_2(c_a + c_c)] \\ \sigma_{31}^N &= \sigma_3^l - \lambda^s[\alpha_1c_c + \alpha_2(c_a + c_b)]\end{aligned}\quad [3.30]$$

where:

$$\begin{aligned}\sigma_1^l &= \sigma_1^O + \alpha_1\Delta\varepsilon_1^e + \alpha_2(\Delta\varepsilon_2^e + \Delta\varepsilon_3^e) \\ \sigma_2^l &= \sigma_2^O + \alpha_1\Delta\varepsilon_2^e + \alpha_2(\Delta\varepsilon_1^e + \Delta\varepsilon_3^e) \\ \sigma_3^l &= \sigma_3^O + \alpha_1\Delta\varepsilon_3^e + \alpha_2(\Delta\varepsilon_1^e + \Delta\varepsilon_2^e)\end{aligned}\quad [3.31]$$

p^N and $(p^N)^2$ are:

$$\begin{aligned}
p^N &= \frac{1}{3} \{ \sigma_1^N + \sigma_2^N + \sigma_3^N \} \\
&= \frac{1}{3} \left\{ (\sigma_1^I + \sigma_2^I + \sigma_3^I) - \lambda^s \left\{ \begin{array}{l} \alpha_1 (c_a + c_b + c_c) \\ + 2\alpha_2 (c_a + c_b + c_c) \end{array} \right\} \right\}
\end{aligned} \tag{3.32}$$

$$\alpha_1 + 2\alpha_2 = 3K \tag{3.33}$$

$$p^N = p^I + \lambda^s [-K(c_a + c_b + c_c)] \tag{3.34}$$

$$(p^N)^2 = (p^I)^2 + \lambda^s \{-2Kp^I(c_a + c_b + c_c)\} + \lambda^{s^2} \{K^2(c_a + c_b + c_c)^2\} \tag{3.35}$$

q^N and $(q^N)^2$ are:

$$q^{N^2} = \frac{1}{2} \left\{ (\sigma_1^N - \sigma_2^N)^2 + (\sigma_2^N - \sigma_3^N)^2 + (\sigma_3^N - \sigma_1^N)^2 \right\} \tag{3.36}$$

$$\sigma_1^N - \sigma_2^N = (\sigma_1^I - \sigma_2^I) - \lambda^s (\alpha_1 - \alpha_2)(c_a - c_b) \tag{3.37}$$

Substitute $\alpha_1 - \alpha_2 = 2G$ gives:

$$\begin{aligned}
\sigma_1^N - \sigma_2^N &= (\sigma_1^I - \sigma_2^I) - \lambda_s [2G(c_a - c_b)] \\
\sigma_2^N - \sigma_3^N &= (\sigma_2^I - \sigma_3^I) - \lambda_s [2G(c_b - c_c)] \\
\sigma_3^N - \sigma_1^N &= (\sigma_3^I - \sigma_1^I) - \lambda_s [2G(c_c - c_a)]
\end{aligned} \tag{3.38}$$

$$(q^N)^2 = (q^I)^2 + \lambda^s \left[-2G \left\{ \begin{array}{l} (c_a - c_b)(\sigma_1^I - \sigma_2^I) \\ (c_b - c_c)(\sigma_2^I - \sigma_3^I) \\ (c_c - c_a)(\sigma_3^I - \sigma_1^I) \end{array} \right\} \right] + \lambda^{s^2} \left[2G^2 \left\{ \begin{array}{l} (c_a - c_b)^2 \\ (c_b - c_c)^2 \\ (c_c - c_a)^2 \end{array} \right\} \right] \tag{3.39}$$

Substitution of Equations 3.31, 3.35, and 3.39 into potential function in Equation 3.13 gives:

$$g = q^{N^2} + M^2 [p^{N^2} + (p_s - p_0)p^N - p_s \cdot p_0] \tag{3.40}$$

$$\begin{aligned}
g &= \underbrace{(q^I)^2 + \lambda^s \left[-2G \left\{ \begin{array}{l} (c_a - c_b)(\sigma_1^I - \sigma_2^I) \\ (c_b - c_c)(\sigma_2^I - \sigma_3^I) \\ (c_c - c_a)(\sigma_3^I - \sigma_1^I) \end{array} \right\} \right]}_{(q^N)^2} + \lambda^{s^2} \left[2G^2 \left\{ \begin{array}{l} (c_a - c_b)^2 \\ (c_b - c_c)^2 \\ (c_c - c_a)^2 \end{array} \right\} \right] \\
&+ \underbrace{M^2 (p^I)^2 + \lambda^s [-2M^2 K p^I (c_a + c_b + c_c)]}_{M^2 p^{N^2}} + \lambda^{s^2} [M^2 K^2 (c_a + c_b + c_c)^2] \\
&+ \underbrace{M^2 (p_s - p_0) p^I + \lambda^s [-M^2 K (p_s - p_0) (c_a + c_b + c_c)]}_{(p_s - p_0) p^N} \\
&- M^2 p_s \cdot p_0
\end{aligned} \tag{3.41}$$

For $g = 0$, Equation 3.41 can be written as follows:

$$A\lambda^{s^2} + B\lambda^s + C = 0 \quad [3.42]$$

where:

$$A = 2G^2 \left\{ \begin{array}{l} (c_a - c_b)^2 \\ + (c_b - c_c)^2 \\ + (c_c - c_a)^2 \end{array} \right\} + M^2 K^2 (c_a + c_b + c_c)^2$$

$$B = -2G \left\{ \begin{array}{l} (c_a - c_b)(\sigma_1^1 - \sigma_2^1) \\ + (c_b - c_c)(\sigma_2^1 - \sigma_3^1) \\ + (c_c - c_a)(\sigma_3^1 - \sigma_1^1) \end{array} \right\} - M^2 K (c_a + c_b + c_c) (2p^1 + p_s - p_0)$$

$$C = (q^1)^2 + M^2 (p^1)^2 + M^2 p^1 (p_s - p_0) - M^2 p_s p_0$$

$$= (q^1)^2 + M^2 (p^1 + p_s) (p^1 - p_0)$$

$$= f(p^1, q^1)$$

[3.43]

3.3.2.4 Hardening Law

The hardening law algorithm is illustrated in Figures 3.6-3.9. Figure 3.6 illustrates the current state plotted in three-dimensional $(\ln(p); \ln(s); v)$ space. The normal consolidation surface and swelling surface are also presented in Figure 3.6. The three-dimensional $\ln(p)$ - $\ln(s)$ - v space is extracted into four 2-dimensional spaces $(v-\ln(p))$ at $s=0$ and at $s=s_1$; $v-\ln(s)$; and $p-s$ in Figures 3.7 and 3.8. Initially the following parameters and initial conditions are predetermined for the analysis:

$p_0(0)$ = initial overconsolidation pressure at suction equal to zero

p_1 = reference pressure

$v_{\lambda}(0)$ = the specific volume related to reference pressure p_1 at normal consolidation line at the suction equal to zero ($s=0$)

From Figure 3.8, we can calculate

$$v_{\lambda}(s) = v_{\lambda}(0) - \kappa_s \ln\left(\frac{s + p_{\text{atm}}}{p_{\text{atm}}}\right) \quad [3.44]$$

Figure 3.7a shows the following relationship:

$$v = v_{\kappa(s)} - \ln\left(\frac{p}{p_1}\right) \rightarrow v_{\kappa(s)} = v + \ln\left(\frac{p}{p_1}\right) \quad [3.45]$$

From Figure 3.7a, the specific volume corresponding to the current suction ($v_{pc}(s)$) can be calculated as:

$$v_{pc}(s) = v_{\lambda(s)} - \lambda(s) \ln\left(\frac{p_0(s)}{p_1}\right) \quad [3.46]$$

$$v_{pc}(s) = v_{\kappa(s)} - \kappa \ln\left(\frac{p_0(s)}{p_1}\right) \quad [3.47]$$

where:

$$\lambda(s) = \lambda(0) \left[(1-r)e^{-\beta s} + r \right] \quad [3.48]$$

Elimination of $v_{pc}(s)$ in Equations 3.47 and 3.48 gives:

$$p_0(s) = p_1 e^{\left(\frac{v_\lambda(s) - v_\kappa(s)}{\lambda(s) - \kappa} \right)} \quad [3.49]$$

Equation 3.49 is used to calculate the current preconsolidation pressure $p_0(s)$ at $s = s_1$ after yielding occurs. Finally, the new saturated consolidation pressure $p_c(0)$ can be calculated using LC-curve relationship in Figure 3.9 as follows:

$$p_c(0) = p_1 \left[\frac{p_c(s)}{p_1} \right]^{\left[\frac{\lambda(0) - \kappa}{\lambda(s) - \kappa} \right]} \quad [3.50]$$

3.3.3 Suction Changes

3.3.3.1 Methodology

Hydro-mechanical analysis using 2-phase flow in FLAC (Itasca 2001) is used to incorporate the influence of suction on the performance. Suction is defined as the difference between pore air pressure and pore water pressure ($u_a - u_w$). The algorithm to incorporate suction changes is illustrated in Figure 3.10 and Figure 3.11. The yield surface, critical state surface, and coefficients of compressibility are updated due to the change of suction (Figure 3.10).

For two-phase flow with constitutive models involving plasticity, Bishop effective stress is used to detect failure (Dangla 1999, Itasca 2001). This effective stress is defined as (Itasca 2001):

$$\sigma'_{ij} = \sigma_{ij} + \bar{P} \delta_{ij} \quad [3.51]$$

and

$$\bar{P} = S_w u_w + S_a u_a \quad [3.52]$$

The implementation of elasto-plastic models (i.e., the BBM and the BGM) with suction change requires translation of the axis of the constitutive models mean stress ($p-u_a$) to

$$p' = (p-u_a) + S_w(u_a - u_w) \quad [3.53]$$

Using mean stress in the Equation 3.53, the algorithm for constant suction can be used to implement suction changes by updating the coefficients of compressibility, yield surface, and critical state surface with suction changes.

3.3.3.2 Updating Suction

Two types of variables are included in FLAC calculations. They are grid variables and zone variables (Itasca 2000b). The analysis in the user-defined constitutive model (UDM) in FLAC is calculated within zone variables (Itasca 2000b). Pore water pressure (u_w) and pore air pressure (u_a) in FLAC are grid variables, consequently the average of the grid variables to get zone variables is required to incorporate suction changes in the

analysis. Referring to a reference zone and grid in Figure 3.12, the suction for each grid point is:

$$s_{(i,j)} = u_{a(i,j)} - u_{w(i,j)} \quad [3.54]$$

The suction for the zone i,j is:

$$\bar{s}_{(i,j)} = \frac{s_{i,j} + s_{i+1,j} + s_{i,j+1} + s_{i+1,j+1}}{4.0} \quad [3.55]$$

3.3.3.3 Coefficients of Compressibility

Implementation of the mean stress in Equation 3.53 requires determination of the equivalent coefficient of compressibility. The transformation of coefficient of compressibility in the 'original' mean stress $(p-u_a)$ to the mean stress in Equation 3.53 is illustrated in Figure 3.13. In this discussion the $(p-u_a)$ vs s space is addressed as 'original' space, while the $[(p-u_a)+S_w.s]$ vs s is the 'equivalent' space.

In the 'original' space, the volume change (dv_{tot}) due to the changes in mean stress $(d(p-u_a))$ and suction (ds) is:

$$\begin{aligned} dv_{tot} &= dv_s + dv_p \\ &= \kappa_s \frac{ds}{s} + \kappa \frac{d(p-u_a)}{(p-u_a)} \end{aligned} \quad [3.56]$$

where κ_s is the coefficient of compressibility due to the changes of suction (ds), and κ is the coefficient of compressibility due to the changes of mean stress (dp).

For a small suction increment ($ds \rightarrow 0$), the volume change due to the changes of 'equivalent' mean stress is:

$$dv_{\text{tot}} = \kappa' \frac{d[(p - u_a) + S_w(u_a - u_w)]}{[(p - u_a) + S_w(u_a - u_w)]} \quad [3.57]$$

where κ' is the equivalent coefficient of compressibility, that can be determined by substitution of Equation 3.57 into 3.56:

$$\kappa' = \left[\kappa_s \frac{ds}{s} + \kappa \frac{dp'}{p'} \right] \frac{p' + S_w \cdot s}{dp' + S_w \cdot ds} \quad [3.58]$$

where $p' = p - u_a$.

For a special case where $ds = d(p - u_a) = 1$, Equation 3.58 is simplified into:

$$\kappa' = \left[\frac{\kappa_s}{s} + \frac{\kappa}{p'} \right] \frac{p' + S_w \cdot s}{1 + S_w} \quad [3.59]$$

Using the Equations 3.58 and 3.59, the equivalent coefficients of compressibility for the BBM can be categorized into 4 zones such as illustrated in Figure 3.14. These equivalent coefficients of compressibility are summarized in Table 3.2. Since the SI-line does not exist in the BGM, only two of the coefficients of compressibility ($\kappa'_{(1)}$, $\lambda'_{(1)}$) in Table 3.2 are required. These coefficients of compressibility are updated with each incremental change of suction.

3.3.3.4 Yield Surface on p-s Space

Figure 3.15 illustrates the changes of the yield lines (T-line and LY-line) from the 'original' space to the modified space. These lines are shifted to the right as their magnitude increased by $S_w \cdot s$ (Figure 3.15). The magnitude of $S_w \cdot s$ can be determined from the water retention curve (WRC) that relates the degree of saturation (S_w) to suction (s).

3.3.3.5 Critical State Slope (M)

The critical state surface of the BGM is illustrated in Figure 3.16 (left) is developed from:

$$q_{cs}(s) = M^p \cdot p_0(s) + M^b \cdot s \quad [3.60]$$

The equivalent critical state slope (M^{ps}) is

$$M^{ps} = \frac{M^p \cdot (p - u_a) + M^b \cdot s}{p + S_w \cdot s} \quad [3.61]$$

The change of this critical state slope results in the changes of the yield ellipse in p-q space.

3.4 Verification

The constant suction algorithm combined with the updated parameters are used to implement the BBM (Alonso et al. 1990) and the BGM (Blatz and Graham 2003). The comparison of FLAC simulations for constant suction using the BBM and the results from the original publication (Alonso et al. 1990) in Figure 3.17b validates the implementation of the BBM in FLAC. The input data used in this analysis are presented in Appendix 1. The effects of the overconsolidation ratio (OCR) for different suction (s) are illustrated in Figures 3.18-3.21. The results of the analysis for lightly overconsolidated clay (LOC) are illustrated in Figures 3.18-3.19, while for highly overconsolidated clay (HOC) are illustrated in Figures 3.20-3.21.

For changes in suction, the algorithm in Figure 3.10 is implemented in FLAC using the FISH language. The FISH file used to implement the BBM and the BGM are presented in Appendices 1 and 2. These files consist of 4 functions:

1. **set_sn** : to define initial suction.
2. **set_v0** : to define initial yield surface, critical state surface, coefficients of compressibility, and reference volume.
3. **bbmtp** or **bgmtp** : to implement elasto-plastic constitutive models in p-q space with constant suction.
4. **set_sn** : to update suction, yield surface, critical state surface, coefficients of compressibility, and reference volume.

Application of this FISH file follows the algorithm show in Figure 3.11. Examples of applications that use these files (bbmtp.fis and bgmtp.fis) are illustrated in Appendices 1-2.

3.5 Concluding Remarks

The constant suction algorithm using updated parameters as a function of incremental changes of stress-states as presented in this chapter can be used to implement elasto-plastic constitutive models (the BBM (Alonso et al. 1990) and the BGM (Blatz and Graham 2003)) in H-M analysis using FLAC-2D for unsaturated swelling clay soils.

Table 3.1. Yield surface due to the BBM and the BGM

Basic Barcelona Model (BBM) (Alonso et al. 1990)	Blatz and Graham Model (BGM) (Blatz and Graham 2003)
<u>Yield function</u>	
$f = q^2 - M^2 (p + p_s) (p_0 - p)$	$f = q^2 - N^2 (p + p_s) (p_0 - p)$
where:	
<u>Slope of Critical State Line</u>	
$M = \text{constant}$	$N = \frac{q_{cs}}{p_0 + p_s}$
	$q_{cs}(s) = M^p \cdot p_0(s) + M^b \cdot s$
<u>T-line</u>	
$p_s = k \cdot s$	$p_s = k \cdot s$
<u>LY-line</u>	
$p_0 = p_1 \left(\frac{p_0^*}{p_1} \right)^{\frac{\lambda(0)-\kappa}{\lambda(s)-\kappa}}$	$p_0 = p_0^* + r \cdot s$
<u>Coefficients of compressibility</u>	
$\lambda(s) = \lambda(0) [(1 - r) \exp(-\beta s) + r]$	$\kappa, \lambda, \kappa_s, \lambda_s \text{ are constants.}$
$\kappa, \kappa_s, \lambda_s \text{ are constants.}$	

Table 3.2. Equivalent coefficients of compressibility of the BBM and the BGM for FLAC formulation

	$p < p_c$	$p < p_c$
$s < s_0$	<u>Zone I (BBM & BGM)*</u> $\kappa'_{(1)} = \left[\kappa_s \frac{ds}{s} + \kappa \frac{d(p - u_a)}{(p - u_a)} \right] \cdot D$	<u>Zone II (BBM & BGM) *</u> $\lambda'_{(1)} = \left[\kappa_s \frac{ds}{s} + \lambda \frac{d(p - u_a)}{(p - u_a)} \right] \cdot D$
$s > s_0$	<u>Zone III (BBM only)*</u> $\kappa'_{(1)} = \left[\lambda_s \frac{ds}{s} + \kappa \frac{d(p - u_a)}{(p - u_a)} \right] \cdot D$	<u>Zone IV (BBM only) *</u> $\kappa'_{(1)} = \left[\lambda_s \frac{ds}{s} + \lambda \frac{d(p - u_a)}{(p - u_a)} \right] \cdot D$
Where $D = \frac{(p - u_a) + S_w \cdot s}{d(p - u_a) + S_w \cdot ds}$		
* Locations of the zone refer to Figure 3.14		

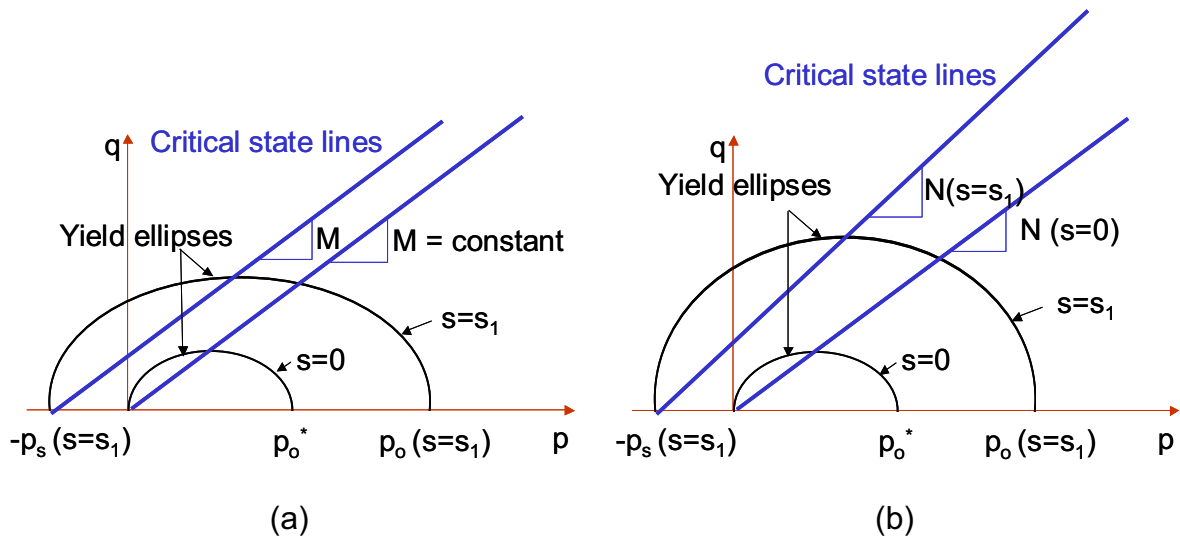


Figure 3.1 Yield loci and critical state lines at constant suction in p - q space due to:
(a) the BBM and (b) the BGM

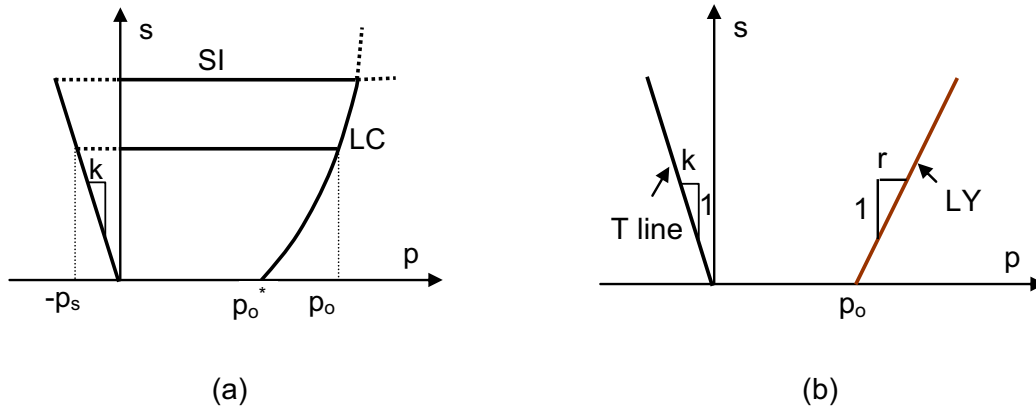


Figure 3.2 Yield loci in p - s space in isotropic conditions ($q=0$) due to:
(a) the BBM; and (b) the BGM

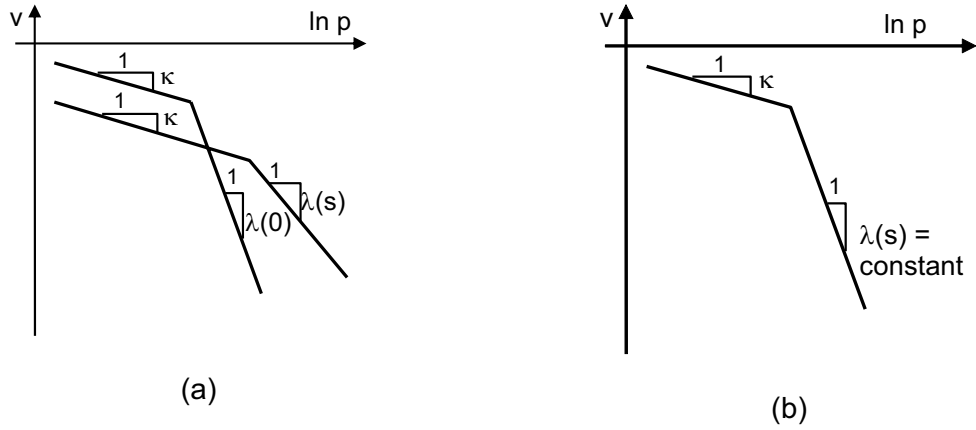


Figure 3.3 Stress-volume relationship ($\ln p$ - v) due to:
(a) the BBM; and (b) the BGM

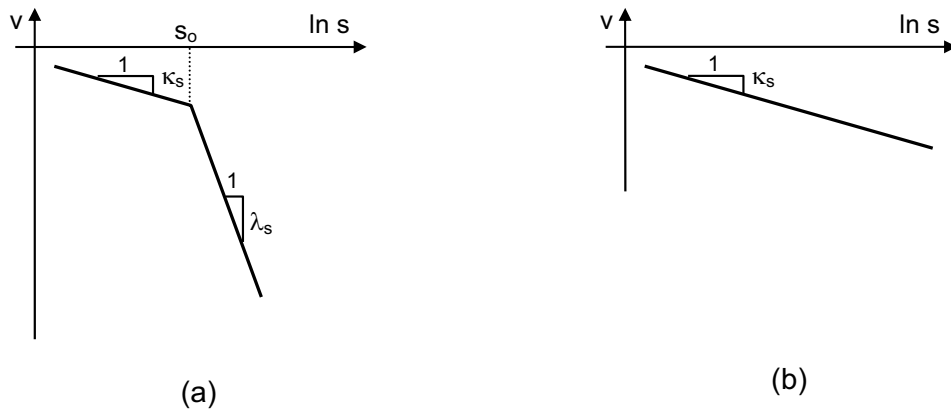


Figure 3.4 Stress-volume relationship ($\ln s$ - v) due to:
(a) the BBM; and (b) the BGM

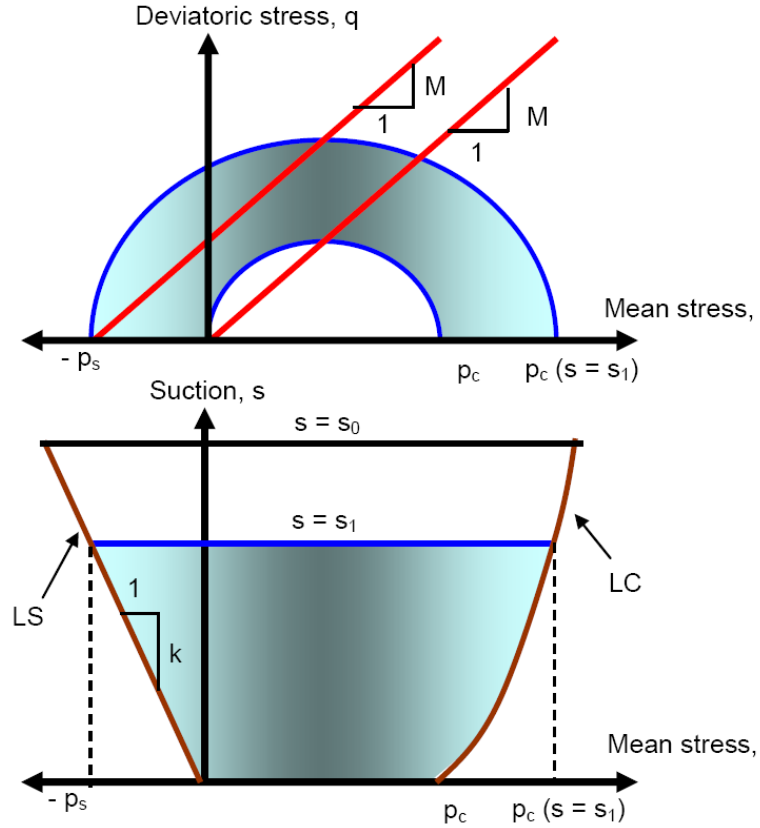


Figure 3.5 Yield surfaces in p-q and p-s spaces for the BBM (after Alonso et al. 1990)

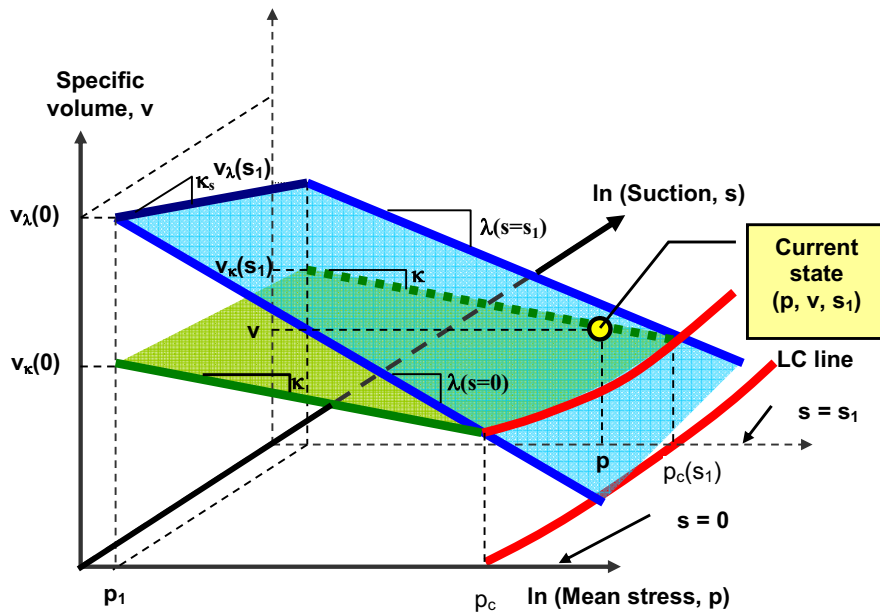
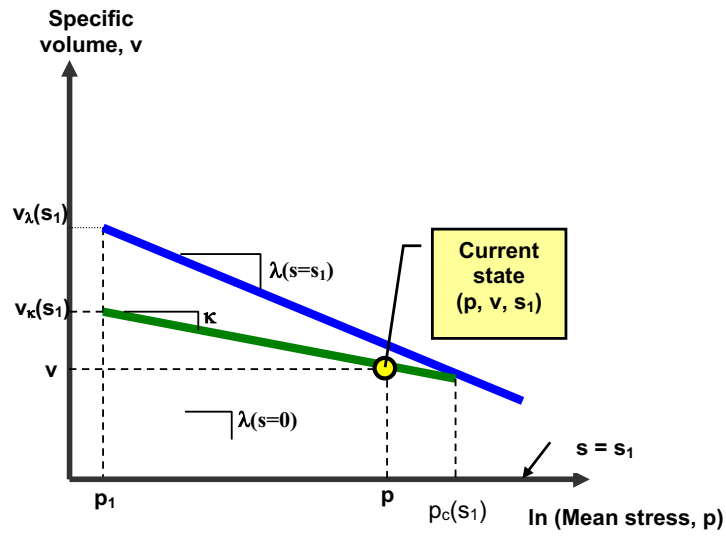


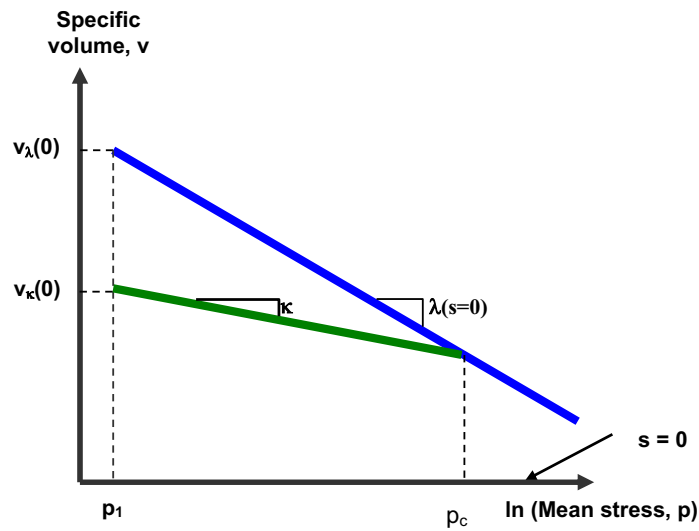
Figure 3.6 Hardening laws algorithm plotted in 3D p-s-v space

$s = s_1$



(a)

$s = 0$



(b)

Figure 3.7 Hardening laws algorithm plotted in $\ln p$ - v space

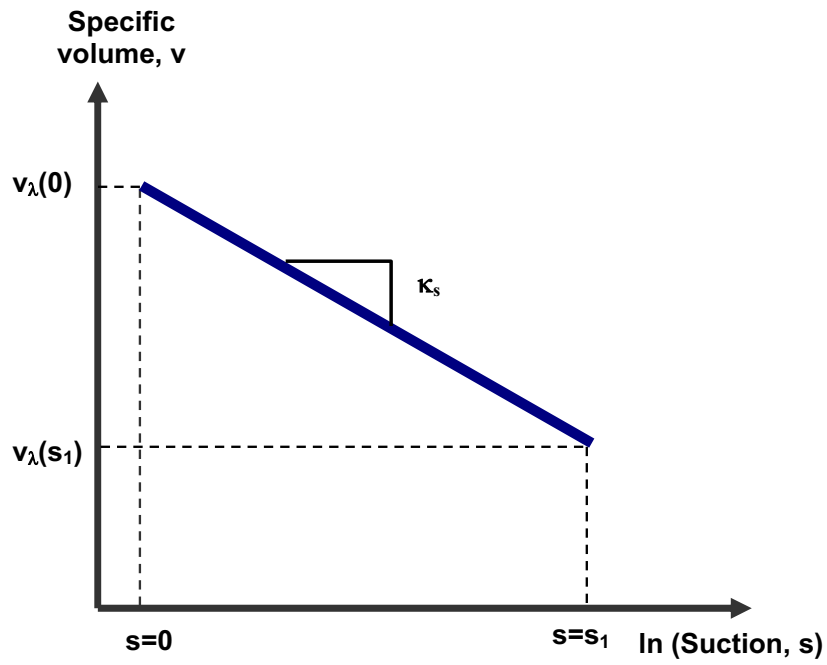


Figure 3.8 Hardening laws algorithm plotted in $\ln s$ - v space

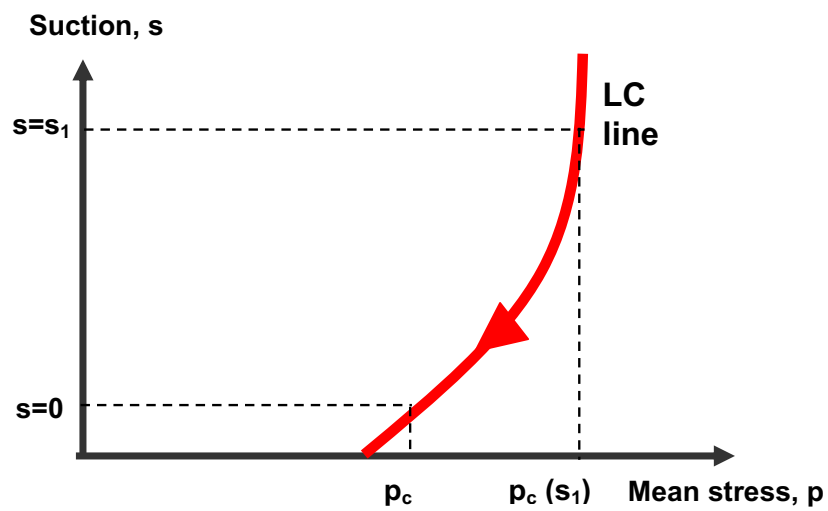


Figure 3.9 Hardening laws algorithm plotted in p - s space

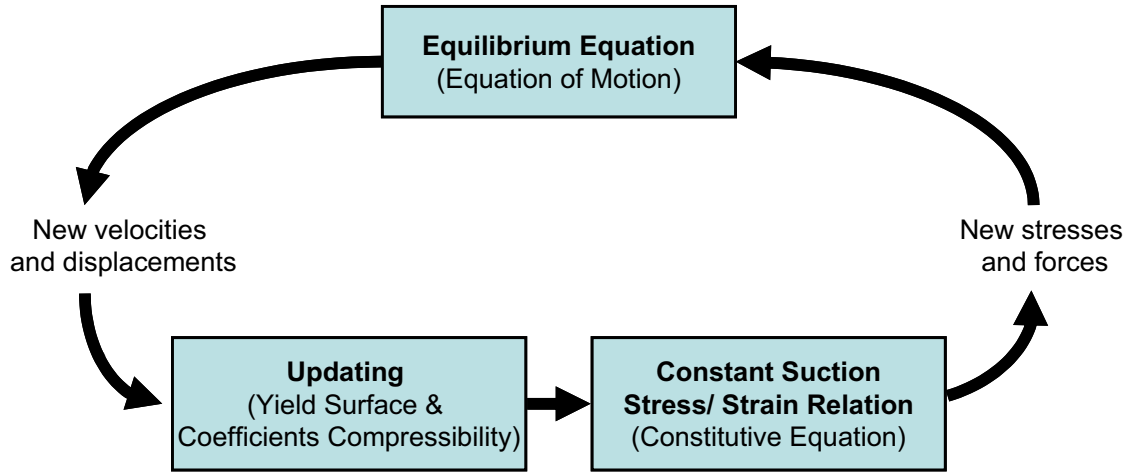


Figure 3.10 Algorithm to implement elasto-plastic model with suction changes in FLAC

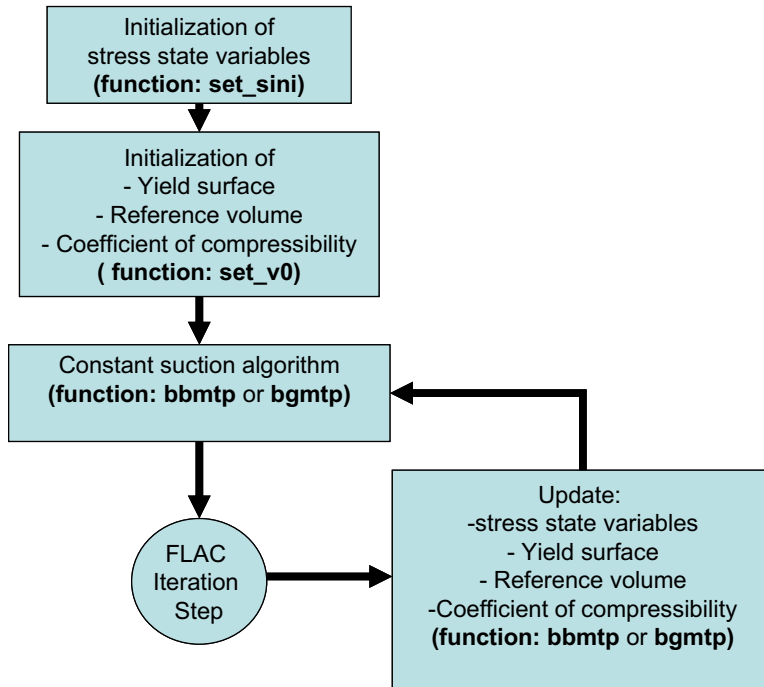


Figure 3.11 Algorithm to use FISH function for the BBM and the BGM

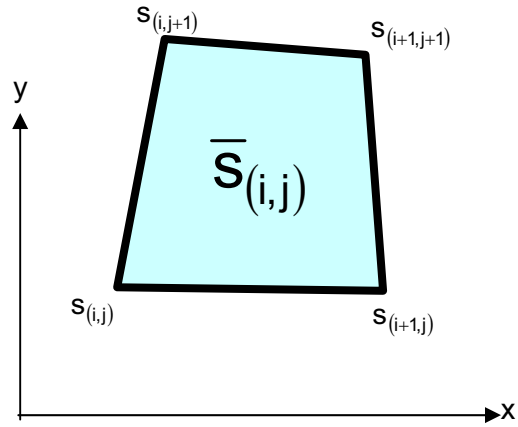


Figure 3.12 Grid variables and zone variables

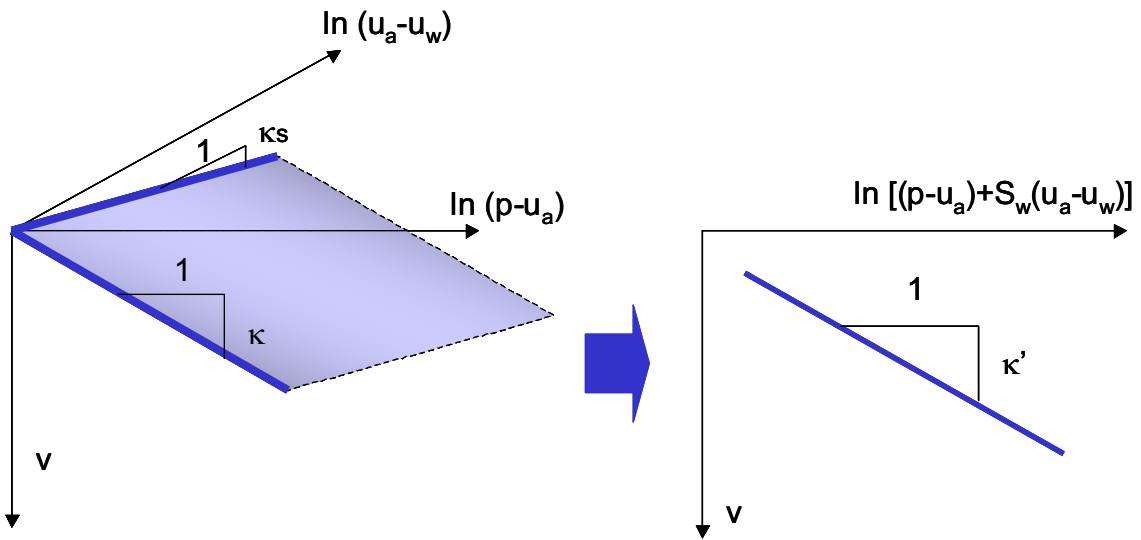


Figure 3.13 Equivalent coefficients of compressibility

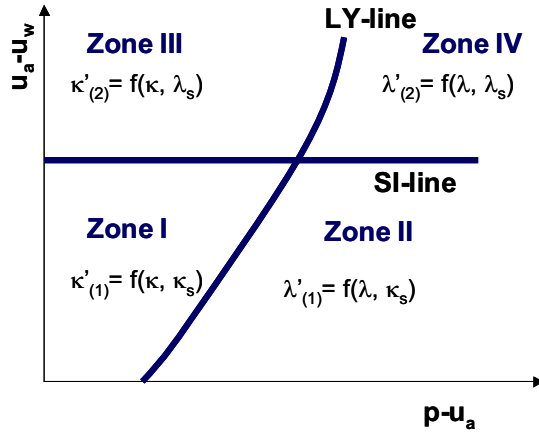


Figure 3.14 Equivalent coefficients of compressibility for the BBM

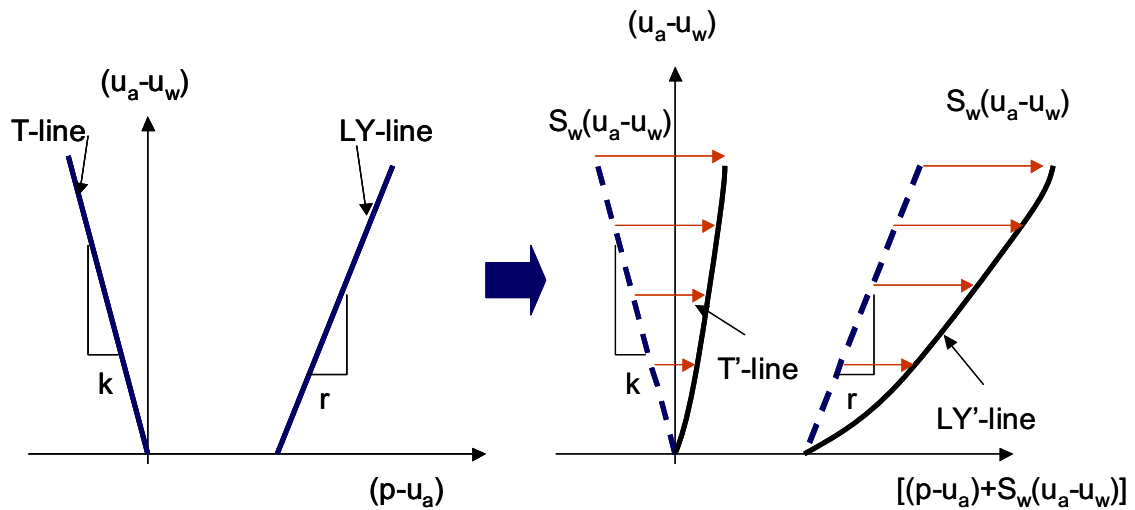


Figure 3.15 Equivalent yield lines (T-line and LY-line) on p-s space

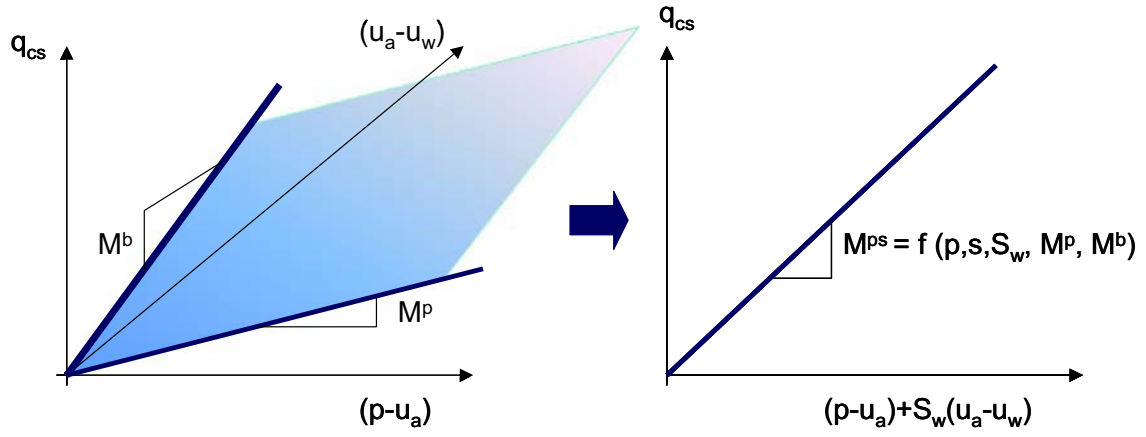
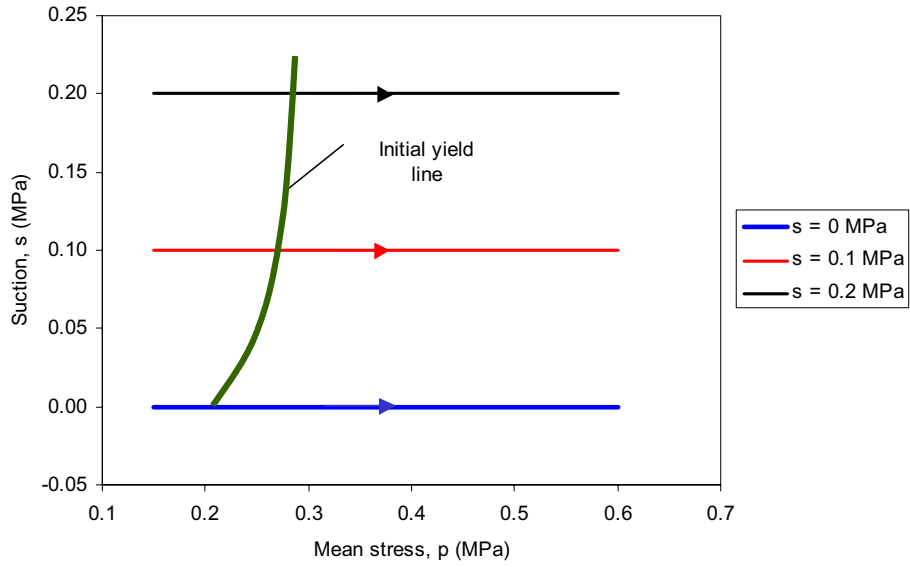
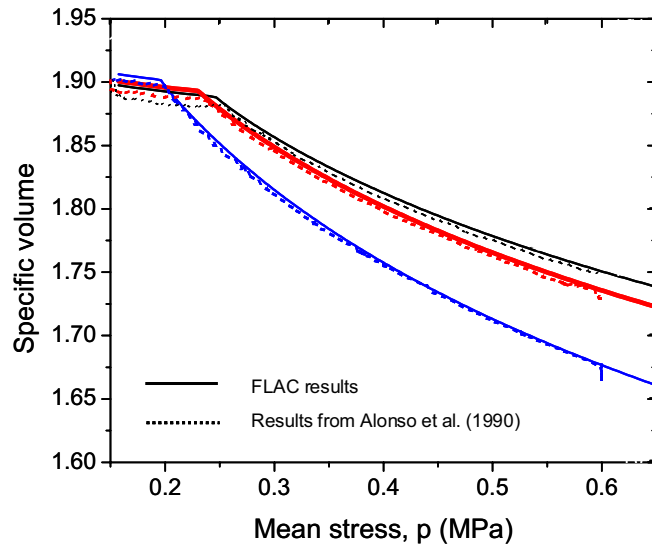


Figure 3.16 Equivalent slope of the critical state surface



(a)



(b)

Figure 3.17 The FLAC simulation results using the BBM compared with the results from Alonso et al. (1990) in: (a) p - s space; and (b) p - v space

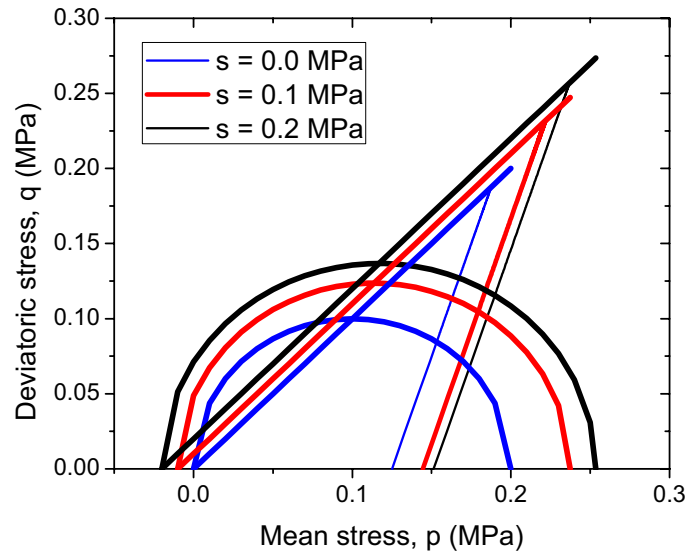


Figure 3.18 Mean stress, p vs deviatoric stress, q and the yield loci for Lightly Over Consolidated clay (LOC)

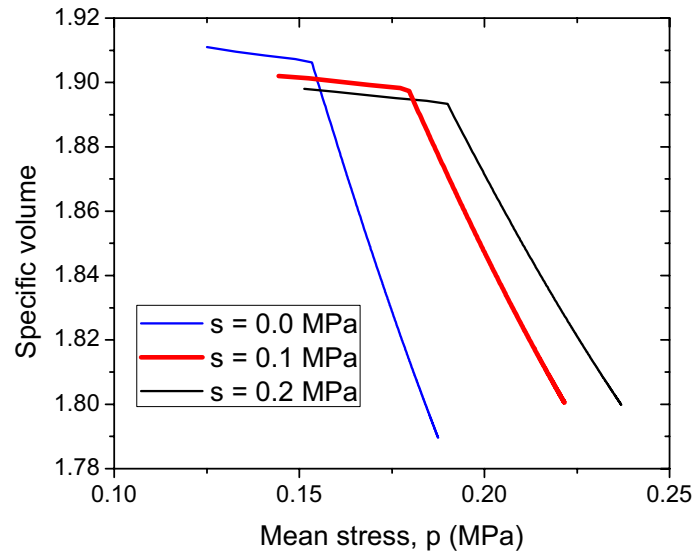


Figure 3.19 Mean stress, p vs specific volume, v for Lightly Over Consolidated (LOC) clay

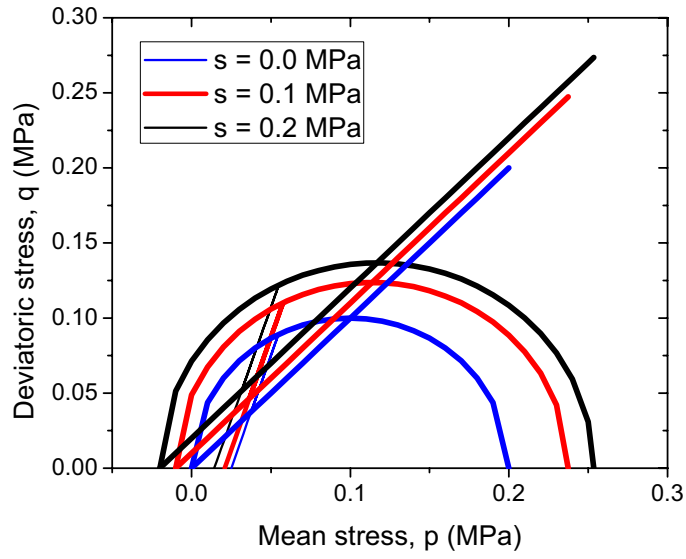


Figure 3.20 Mean stress, p vs deviatoric stress, q and the yield loci for Highly Over Consolidated (HOC) clay

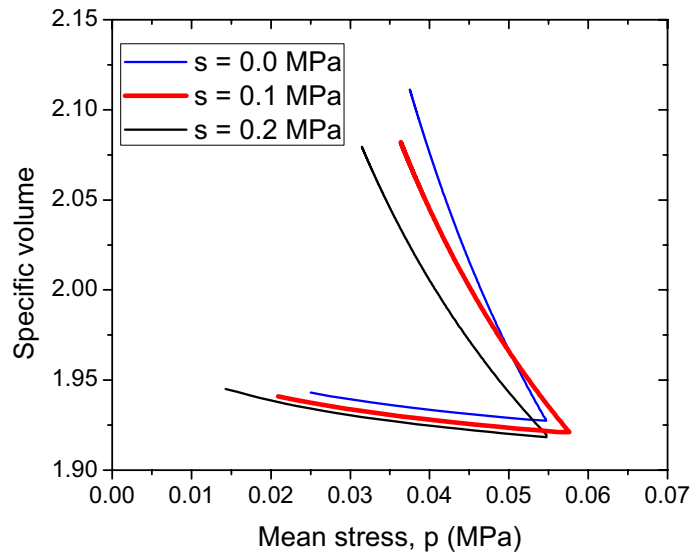


Figure 3.21 Mean stress, p vs specific volume, v for Highly Over Consolidated (HOC) clay

CHAPTER 4

NEW 3-D PERMEABILITY MODEL AND WATER RETENTION SURFACE

4.1 Introduction

A permeability model and a water retention curve (WRC) are required as the hydraulic constitutive models for Hydraulic-Mechanical (H-M) analysis for the interpretation of the H-M behaviour of unsaturated swelling clay (USC). This chapter proposes a new three-dimensional water permeability model and water retention surface (WRS). Experimental evidence is used to justify additional features of the new constitutive models. Conceptual models explaining the characteristics of the new constitutive models are also discussed. Finally, this chapter provides mathematical formulation of the constitutive models, as well as the algorithm to implement these constitutive models.

4.2 Theoretical Background

4.2.1 Conceptual Models to Illustrate the Mechanisms of the Constitutive Models

Figures 4.1 to 4.3 illustrate three mechanisms that may occur in the Hydraulic-Mechanical (H-M) processes of USC. All three mechanisms can be simulated using the

new constitutive models presented in this chapter. The first mechanism (Figure 4.1) illustrates the typical permeability function (Figure 4.1a) and water retention curve (WRC) (Figure 4.1b). Suction (s) increases due to a decrease in the degree of water saturation (S_w) under a drying cycle (Figures 4.1a and b). Figure 4.1c illustrates conceptual distributions of pore water pressure (u_w) and pore air pressure (u_a) in a cross-sectional area of rigid soil matrix corresponding to the points 1-4 in Figures 4.1a and 4.1b (after Lu and Likos 2004). An assumption of constant porosity (n) is made in this conceptual model (Lu and Likos 2004).

The assumption of constant porosity (n) in Figure 4.1 is not fully valid for the case of USC, where volume change due to a change of water content can be significant. The second mechanism illustrated in Figure 4.2 shows that for constant degree of water saturation (S_w), the water permeability (k_w) increases due to increases in total porosity (n) (Figure 4.2a), while suction (s) decreases due to an increase in total porosity (n) (Figure 4.2b). This constant degree of water saturation (S_w) can be obtained in the non-constant volume (v) laboratory test in the saturated condition to measure the water permeability (k_w). However, the constant degree of water saturation (S_w) is almost impossible to achieve in the laboratory test within unsaturated conditions. The conceptual cross-sectional area and capillary rise corresponding to points a and b in Figures 4.2a and 4.2b are illustrated in Figures 4.2c and 4.2d.

Figure 4.3 illustrates the third mechanism. Typical results of Mercury Intrusion Porosimetry (MIP) tests on compacted swelling clay shows they have bi-modal or three-modal distributions (Figure 4.3b) (Dixon et al. 2002). Based on this result the porosity can be considered as micropores and macropores (Dixon et al. 2002, Siemens 2006).

Due to the two modes of porosity, it is possible to have a different total suction (s) and water permeability (k_w) for a constant degree of water saturation (S_w) and a constant total porosity (n). The water permeability (k_w) decreases with an increase in total suction rate as illustrated in Figure 4.3a. Points a and b in Figure 4.3a correspond to two pipes that have the same area A , but of different types (Figure 4.3c). Point a in Figure 4.3a corresponds to the single pipe that has total area A (Figure 4.3c), which represents the macropores. Point b is analogous to combination of smaller pipes that has the same total area A (Figure 4.3c), which represents the micropores. The height of capillary rise can represent the magnitude of suction. Figure 4.3d illustrates the corresponding capillary rises of points a and b in Figure 4.3a.

4.2.2 Permeability Surface

Several large-scale experiments were conducted at the Atomic Energy of Canada Limited (AECL)'s Underground Research Laboratory (URL) in Canada (Dixon et al. 2002). One of them was the large-scale isothermal test (ITT) (Dixon et al. 2002) that monitored infiltration into swelling clay barrier materials from surrounding bedrock. An attempt to model this behaviour (Thomas et al. 2003) resulted in an 'exponential relationship' (Figure 4.4) demonstrates a decrease of water permeability (k_w) with an increase in the degree of water saturation (S_w) for $S_w > 90\%$, that is contradictory to the conventional permeability functions accepted in the literature (e.g. Brook and Corey 1964, van Genuchten 1980, Fredlund and Xing 1994).

This 'exponential relationship' (Figure 4.4) indicates the need for a 3-D permeability surface such as the example illustrated in Figure 4.5. Using this conceptual 3-D permeability surface in Figure 4.5, the water permeability (k_w) is not only dependent on

the degree of water saturation (S_w), but also the total porosity (n). This 3-D permeability surface in Figure 4.5 maintains the original characteristic of the conventional water permeability function, where water permeability (k_w) increases with an increase in the degree of water saturation (S_w). Water permeability (k_w) also increases due to an increase in total porosity (n) (Figure 4.5) for a constant degree of water saturation (S_w). Consequently, the exponential relationship shown in Figure 4.1 can be drawn in this 3-D permeability surface as illustrated in Figure 4.2.

4.2.3 Experimental Evidence and Calibration

Dixon et al. (1999) conducted water permeability (k_w) measurements for various types of swelling clay under various hydraulic gradients. Dixon et al. (1999) showed that the water permeability (k_w) increases with an increase of effective porosity (n_e) even under various hydraulic gradients (Figure 4.6a). Figure 4.6b shows the relationship of total porosity (n) and water permeability (k_w).

Total porosity (n) is defined as a measure of the proportion of the soil volume not occupied by soil solids particles and is commonly derived by calculation of the fractional volumes occupied by solids (n_s), liquids (n_w) and gas (n_g) (Dixon 1999). In a swelling clay having a high specific surface area, the potential for at least a portion of the pore volume to be occupied by structured water has led to the development of a parameter defined as the effective porosity (n_e) (Gray et al. 1984) or the porosity available for flow (n_w) (Yong and Warkentin 1975). This effective porosity (n_e) or the porosity available for flow (n_w) will be less than the total porosity (n), because the some water particle retained within the solids particle that due to the Gouy-Chapman diffuse-double layer effect for unsaturated swelling clay (Gouy 1910; Chapman 1913).

The relationship of the effective porosity (n_e) and the water permeability (k_w) can be generated using this laboratory test data showing an increase in water permeability (k_w) with an increase in effective porosity (n_e). The laboratory test results in Figure 4.6a are used to calibrate the relationship between the saturated water permeability (k_w^{sat}) and effective porosity (n_e). This first trial of this relationship is drawn in Figure 4.6a. Further statistical analysis of this model is required to improve the reliability of this model. Combination of the relationship of water permeability (k_w) as a function of effective porosity (n_e) (Figure 4.6a) and the conventional permeability function defining the relationship of water permeability (k_w) as a function of degree of water saturation (S_w) (Figure 4.4) supports the existence of the conceptual 3-D permeability surface.

4.2.4 Boundary Conditions Effects

A triaxial apparatus with controlled suction and suction measurements (Blatz and Graham 2000, Siemens and Blatz 2006) has the capability of simulating various boundary conditions, so that the effect of the boundary conditions on material behaviour can be investigated. Total suction, volume of water added to the specimen, confining pressure, and displacement were measured during experiments conducted by Siemens (2006). Constant volume, constant stiffness, constant confining pressure, and radial flow tests were performed using this apparatus (Siemens 2006).

These tests were conducted on specimens with the same initial as-compacted target conditions of gravimetric water content (w) of 19.4% and dry density (ρ_{dry}) of 1.67 Mg/m³ to achieve a degree of water saturation (S_w) of approximately 85% (Siemens 2006). Figure 4.7 summarizes the test results in p - w - v space, where p is mean stress, v is specific volume, and w is the gravimetric water content. The line 'fitted limit' (Figure 4.7)

indicates the end of the test condition, where no further volume of water can be added to specimens. Typical results of infiltration test using triaxial cell with controlled suction and suction measurements are illustrated in Figure 4.8. The projection of these measurements on a gravimetric water content (w) versus end-of-test specific volume (v) space for all infiltration tests provides a linear relationship as shown in Figure 4.9a:

$$w_{\max} \text{ (in \%)} = 38.05 v - 41.398 \quad [4.1]$$

(after Siemens 2006)

where w_{\max} is the maximum gravimetric water content (in percent, %) and v is the specific volume of the soil. This line is called the 'maximum water content line'. The line separates the region where flow can occur (zone 1) and where flow will not occur (zone 2). Assuming relative density (G_s) of 2.7 (Graham et al. 1997) the maximum degree of water saturation (S_{\max}) can be calculated as:

$$S_{\max} \text{ (\%)} = \frac{G_s}{v - 1} (38.05v - 41.398) \quad [4.2]$$

The relationship between maximum degree of water saturation (S_{\max}) and specific volume (v) in Equation 4.2 is illustrated in Figure 4.9b. This relationship is used to incorporate the boundary condition effects within the permeability models. Some statistical analysis may be required for further development of this model.

Assuming that the volume of the solids is constant, two types of porosity can be determined using the relationship presented in Figure 4.9b. Figure 4.10 describes the conceptual model to illustrate the composition of volume of the soil, assuming the volume of solids as a constant. Two types of porosity can be indicated from the maximum degree of water saturation measurement, which are flow-porosity (n_F) and non-flow porosity (n_{NF}). The flow porosity (n_F) is defined as porosity available for flow, while non-flow porosity (n_{NF}) is defined as:

$$n_{NF} = n_{total} - n_F \quad [4.3]$$

where n_{total} is the total porosity.

The flow porosity (n_F) increases with an increase in specific volume (v) and decrease in dry density (ρ_{dry}) as illustrated in Figures 4.11a and 4.11b. In contrast, non-flow porosity (n_{NF}) decreases with an increase of specific volume (v) and a decrease of dry density (ρ_{dry}) (Figures 4.11a and 4.11b).

4.2.5 Three-dimensional Water Retention Surface

Siemens (2006) presented a three-dimensional water retention curve for bentonite-sand buffer (BSB) material as illustrated in Figure 4.12. The results of infiltration tests using a triaxial cell with controlled suction and suction measurements were plotted as specific volume (v) versus suction (s) versus gravimetric water content (w) (Figure 4.12) (Siemens 2006). The transformation from gravimetric water content (w) to degree of saturation (S_w) is required for implementation of the constitutive model in the hydraulic-mechanical analysis.

Based on this experimental evidence (Figure 4.12) (Siemens 2006), the water retention surface can be drawn as illustrated in Figure 4.13 as the relationship between specific volume (v) versus degree of saturation (S_w) versus suction (s). Three lines on this surface (Figure 4.13) can be used to generate the mathematical equation of this water retention surface. These lines are the water retention curve (WRC) for constant specific volume, an iso-saturation line, and a maximum degree of saturation line. The constant specific volume (v) line defines the relationship of the total suction as a function of degree of water saturation (S_w) under constant volume condition. The iso-saturation line describes the relationship of the total suction as a function of specific volume (v) under constant degree of water saturation (S_w). The maximum saturation line describes the relationship of maximum degree of water saturation (S_{max}) as a function of specific volume (v).

The mathematical representation of the water retention curve (WRC) for constant specific volume can be determined from the existing WRC models (e.g., van Genuchten 1980 or Fredlund and Xing 1994 model). The maximum degree of water saturation (S_w) is determined from measurement of gravimetric water content (w) and specific volume (v) at the end-of-test, such as illustrated in Figure 4.9. The iso-saturation line (Figure 4.13) defines the change of suction due to a change of specific volume (v) at a constant degree of water saturation (S_w) condition; such as defined by the second mechanism in Figure 4.3.

The existence of hysteretic nature in the water retention curve (WRC) during drying and wetting cycles has also been investigated as discussed in Chapter 2. This hysteretic behaviour can be depicted on the 3-D water retention surface (WRS) as illustrated in Figure 4.14. Consequently implementation of this surface using a finite element (FE) or

finite difference (FD) methods can potentially be used to incorporate the hysteretic behaviour of the water retention curve (WRC). The implementation algorithm of the water retention surface is discussed in Chapter 5.

4.3 Permeability Surface

4.3.1 Mathematical Formulation

The permeability surface shown in Figure 4.5 can be generated using:

$$k_w = f(S_w, n) \quad [4.4]$$

where, k_w is the water permeability; S_w is the degree of water saturation (S_w); and n is the total porosity.

The water permeability follows the van Genuchten (1980) model for constant porosity (n), such as:

$$k_w = k_{sat}(n) \cdot \kappa_{rw} \quad [4.5]$$

$$\kappa_{rw} = S_e^b [1 - (1 - S_e^{1/a})^2] \quad [4.6]$$

where κ_{rw} is the relative water permeability; a is the fitting parameter, S_e is the effective degree of water saturation, which is defined as:

$$S_e = \frac{S_w - S_{res}}{S_{max} - S_{res}} \quad [4.7]$$

The saturated water permeability (k_{sat}) is a function of total porosity (n). The relationship of the saturated water permeability (k_{sat}) as a function of the porosity (n) is described as:

$$\kappa_r^{sat}(n) = n_e^{na} \left[1 - \left(1 - n_e^{1/na} \right)^{na} \right]^2 \quad [4.8]$$

where n_e is the effective porosity, which is defined as the porosity available for water to flow. This can be defined as a function of total porosity (n), minimum porosity (n_{min}), and maximum porosity (n_{max}), such as:

$$n_e = \frac{n - n_{min}}{n_{max} - n_{min}} \quad [4.9]$$

$$k_{sat}(n) = k_{max} \cdot \kappa_r^{sat}(n) \quad [4.10]$$

where k_{max} is the maximum water permeability correlated with the maximum porosity (n_{max}).

Equation 4.8 can be simplified by substitution of $a=1$ to reduce the number of parameters required for this model,

$$\kappa_r^{\text{sat}}(n) = n_e^{nb+2} \quad [4.11]$$

Thus, only two more additional parameters are required to define the permeability surface illustrated in Figure 4.5.

4.3.2 Calibration of Parameters

Parameters of the permeability surface (Figure 4.5) for the BSB material can be calibrated using permeability measurements (Graham et al. 1997, Dixon et al. 2002) and end-of-test measurements from infiltration tests using controlled suction and suction measurements (Siemens 2006).

Parameter (a) in Equation 4.6 is equal to 0.2, parameters (na) in Equation 4.8 is 1.0, while parameter (nb) in Equation 4.11 is equal to 2.5. The maximum porosity (n_{max}) is 0.45, while minimum porosity (n_{min}) is 0.30. This produces a saturated hydraulic conductivity (k_{sat}) of 5×10^{-12} m/s (Graham et al. 1997) correlated with an initial porosity of 0.38 and an effective porosity of 0.53. The relationship of the permeability (k_w) as a function of effective porosity (n_e) and total porosity (n) is illustrated in Figures 4.6a and 4.6b.

4.3.3 Implementation Algorithm

This permeability surface can be implemented in FLAC (Itasca 2001) by creating a FISH function (Itasca 2000a). The porosity is calculated for each time increment and the saturated hydraulic conductivity is updated using the relationship in Equation 4.10 with parameters defined previously. The algorithm to calculate the porosity in FLAC (Itasca 2001) is presented in Appendix 3.

4.4 Water Retention Surface (WRS)

4.4.1 Mathematical Formulation of the Surface and the Parameters

The water retention surface (WRS) in Figure 4.13 can be generated using the following equations:

$$s = f(S_w, v) \quad [4.12]$$

For constant specific volume (v),

$$s(S_w) = P_o \left(S_e^{-1.5} - 1 \right)^{1.5} \quad [4.13]$$

where s is the total suction that is the difference between the pore air pressure and the pore water pressure ($u_a - u_w$); P_o is the threshold pressure or air entry value; and S_e is the effective degree of water saturation, which is defined as:

$$S_e = \frac{S_w - S_{res}}{S_{max}(v) - S_{res}} \quad [4.14]$$

where S_w is the degree of water saturation; S_{res} is the residual degree of water saturation; while S_{max} is the maximum degree of water saturation, which is dependent on the magnitude of the specific volume, $S_{max} = f(v)$.

$$S_{max}(\%) = \frac{G_s}{v-1}(A \cdot v - B) \quad [4.15]$$

where A and B are the fitting parameters that can be estimated from the infiltration tests with various voundary conditions such as triaxial cell with controlled suction and suction measurement (i.e., Siemens 2006).

4.4.2 Calibration

Substitution of the S_{max} equal to 1 in Equations 4.13 and 4.14 results in water retention curve equation (WRC) of van genuchten (1980). The laboratory measurements of water retention curve (WRC) describing the relationship of gravimetric water content (w) and suction of BSB material using various measurement methods (Wan 1996, Wiebe 1996, Tang 1999, Blatz 2000, Anderson 2003) are illustrated in Figure 4.15. Several WRC equations proposed by Wan (1996) and Blatz (2000) are also shown in Figure 4.15. These equations are summarized in Table 4.1. The material properties for the WRC models are summarized in Table 4.2.

Most H-M (hydraulic-mechanical) analysis formulations (e.g. FLAC (Itasca 2001)) use a degree of saturation vs suction relationship to describe the water retention curve. The gravimetric water content (w) in Figure 4.15 is used to calculate the degree of water saturation (S_w) using specific gravity (G_s) of 2.7 and porosity (n) of 0.38. The results of the infiltration tests using various boundary conditions (Siemens 2006) are also shown in Figure 4.15. The van Genuchten (1980) model is used to describe the best-fit curve. The van Genuchten (1980) model can be described using Equation 4.13 and 4.14 by substituting a constant S_{max} equal to 1. The fitting parameters used to generate curves for each model in Figure 4.16 are summarized in Table 4.3.

Parameters A and B in Equation 4.15 can be determined from the end-of-test measurements of volume-mass relationships of soil from infiltration tests using the triaxial cell with controlled suction and suction measurements (Siemens 2006). Parameters A and B for BSB material are 38.1 and 41.5 such as in Equation 4.2 (Siemens 2006).

4.4.3 Limitation of the Volume-Mass Relationship for Unsaturated Swelling Clay

The transformation from w - v space (Figure 4.9a) into S - v space (Figure 4.9b) using Equation 4.2 produces the scatter of the data in S - v space. This indicates the limitation of the general volume-mass relationships using Equation 4.2.

Villar (2002) proposed that the density of water could change during testing causing the degree of water saturation S_w greater than 100%. Various authors suggested that in the vicinity of clay laminae, the structure of water molecules is disturbed, their properties differing from those of free water (Sposito and Prost 1982). This modification of the

properties of the adsorbed water becomes more noteworthy with low contents of water such as within the unsaturated swelling clay with high dry density in this thesis. Martin (1962) showed the variation of the water density adsorbed in montmorillonite as a function of clay water content obtained by means of pycnometers and X-ray diffraction. He also presented the water density calculated to maintain the degree of saturation of the clay at 100 % for different types of test. The variation of the water density adsorbed in montmorillonite is within the range of 1.37 g/cm^3 to 1.41 g/cm^3 for 12% to 28% of clay water content (Martin 1962).

Push et al. (1990) find that the density of water in sodium montmorillonite depend on the degree of ordering and the presence of molecules of interstitial water. Consideration of clay and pore fluid chemistry and mineralogy to describe the behaviour of unsaturated swelling clay may be required. The non-constant water density (ρ_w) results in a non-constant specific gravity (G_s). The assumption of constant specific gravity (G_s) may not be adequate as indicated by the scatter in the measurement points shown in Figure 4.9b.

Another explanation is due to the effect of two types of porosity and the diffuse double layer effects in swelling clay. Some possible methods that may improve this volume-mass relationship for swelling clay is to consider two types of degree of saturation (S_w), for each of the micropores and macropores. Alonso et al. (1999) presented a model considering independent micro- and macro- structure for swelling clay, called the Barcelona Expansive Model (BExM).

The calibration of the parameters of this model is challenging. The effective clay dry density (ECDD) concept (Dixon and Miller 1995) and the effective monmorillonite dry

density (EMDD) (Baumgartner and Snider 2002) consider the behaviour of clay to be dominated by clay content (for ECDD) or montmorillonite content (EMDD). Other materials are considered as aggregate. These concepts may be used to define this volume-mass relationship for swelling clay and be used to calibrate the BExM model (Alonso et al. 1999). Consideration of two independent structures of the soil is beyond the scope of this research and will be incorporated as a suggestion for future research.

4.5 Concluding Remarks

This chapter proposes a new set of hydraulic constitutive models for unsaturated swelling clay based on the results of infiltration tests using a triaxial apparatus with controlled suction and suction measurements (Siemens 2006, Blatz 2000). The mathematical equations to generate a permeability surface and water retention surface are presented in this chapter. The parameters of these equations can be determined through surface fitting techniques using the laboratory test results.

The algorithm to implement the permeability surface in FLAC (Itasca 2001) is presented, and will be used to model the barrier systems in the following chapters. Implementation of the water retention surface in FLAC (Itasca 2001) requires modification of the mathematical formulation. The mathematical formulation to implement this water retention surface (WRC) is discussed in Chapter 5.

Table 4.1 Proposed equations of WRC for BSB materials from various tests

Author	Equations
Wan (1996)	$\text{Log } S = 2.729 - 0.142 w$; for $w = 1$ to 11% ; $R^2 = 0.99$ $\text{Log } S = 1.983 - 0.074 w$; for $w = 11$ to 25% ; $R^2 = 0.91$
Blatz (2000)	Wetting curve: $S = -4.9 + 275 \exp(-wc/5.4)$; for $S = 3.5$ MPa to 93 MPa Drying Curve $S = 398.1^{(-w/4.3)}$

Table 4.2. Summary of material properties of WRC measurements

Author	Soil type	Preparation methods	Ratio (Bentonite: Sand)	Atterberg Limit		Initial Volume-mass Relationship					Range	
				Liquid Limit (W_L) (%)	Plasticity Index (I_p) (%)	Water Content (wc)	Dry Density (γ_{dry}) (Mg/m^3)	Degree of Saturation (S_w) (%)	Specific Gravity (G_s)	Porosity, n	Water Content (wc) (%)	Suction (MPa)
Anderson (2003)	Saskatchewan Bentonite	Compacted to RBM Parameter	50:50	222	176	19.4	1.67	85	2.7	0.38	4 – 19.4	10 – 130
	Wyoming Bentonite	Compacted to RBM Parameter	50:50	605	561	19.4	1.67	85	2.7	0.38	4 – 19.4	10 – 130
Blatz (2000)	Avonlea Bentonite	Compacted to RBM Parameter	50:50	211	167	19.42	1.67	85	2.7	0.38	7 – 23	2 – 75
Tang (1999)	Avonlea Bentonite	Compacted at a "saturated" condition ($S_r = 98\%$)	50:50	230-250	200	22.4	1.67	95	2.7	0.39	5 – 23	2 – 126
Wiebe (1996)	Avonlea Bentonite	Compacted at different water contents	50:50	N/A	N/A	23	1.67	N/A	2.7			
Wan (1996)	Avonseal, Saskatchewan (Dixon et al. 1992)	Compacted at different water contents	50:50	250	200	17-24	1.41-1.67				0-26	2-500

Table 4.3 vanGenuchten parameters used to generate curve in Figure 4.15

Curve	Parameter-a	Parameter-Po (MPa)	Residual degree of saturation, S_{res}
Lower-bound	0.3	0.5	0.1
Upper-bound	0.3	5.0	0.1
Modelling infiltration test (Siemens 2006)	0.12	1.0	0.1
Modelling Large Scale Isothermal test (Dixon et al. 2002)	0.20	3.5	0.1

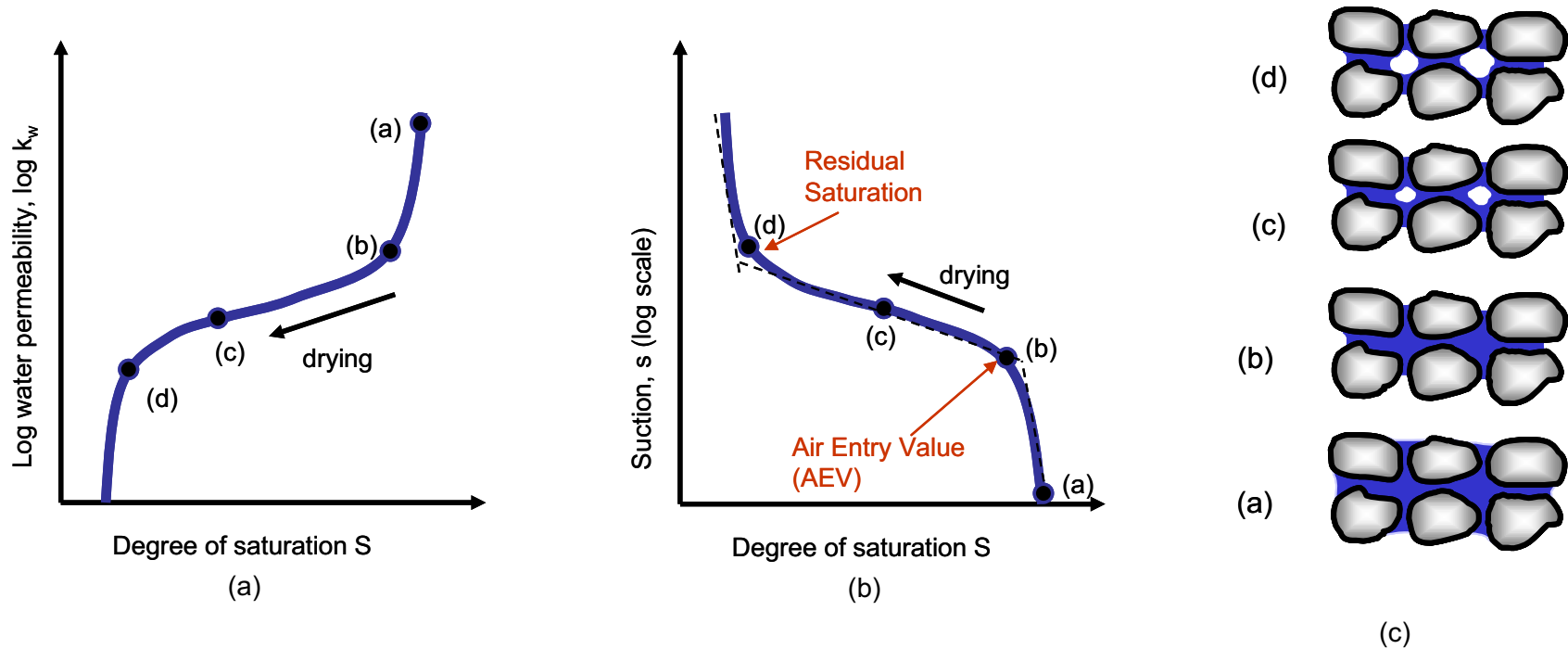


Figure 4.1 (a) Permeability Function, (b) Water retention Curve, (c) Conceptual distributions of pore water and pore air in a cross-sectional area of rigid soil matrix (constant porosity)

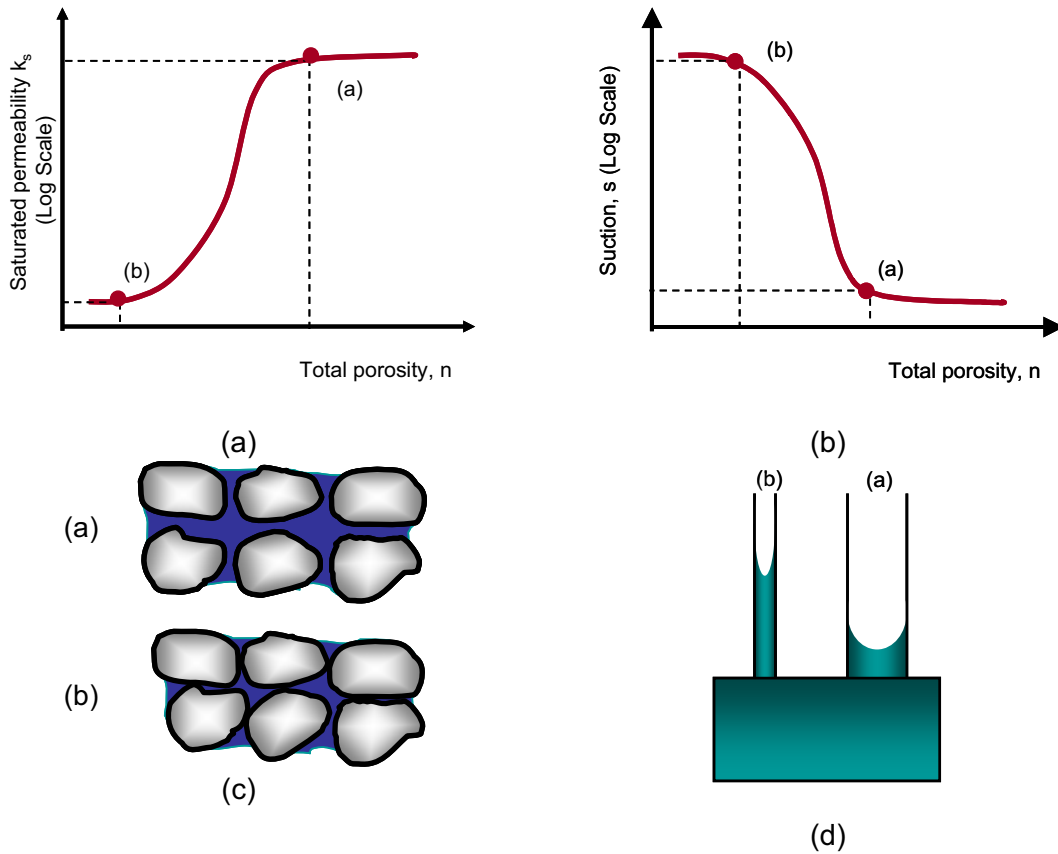


Figure 4.2 (a) Water permeability versus total porosity; (b) Suction versus total porosity; (c) Cross-sectional area of related points; (d) Capillary rise corresponding to the two points

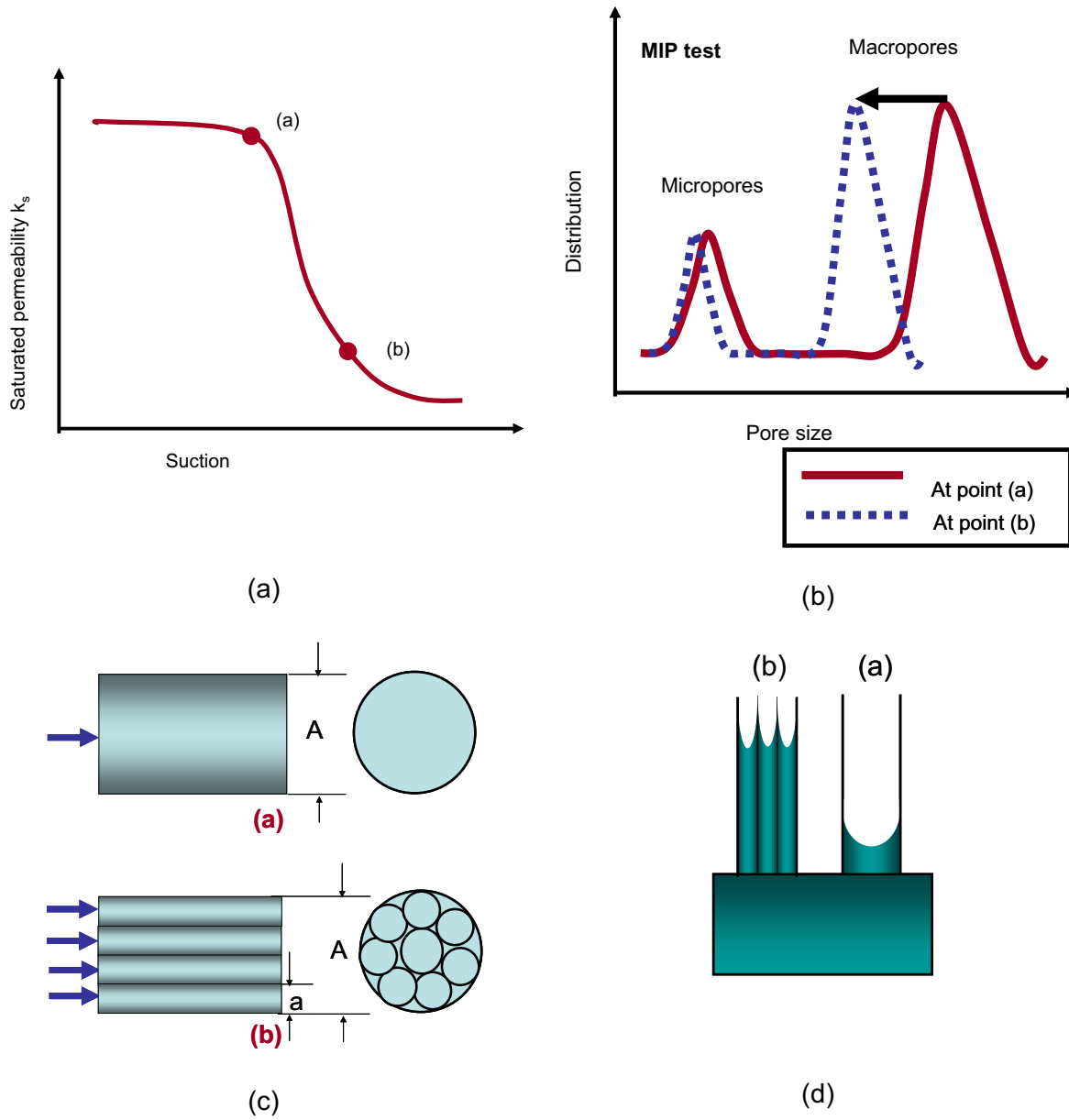


Figure 4.3 (a) Suction versus water permeability for constant total specific volume; (b) Corresponding MIP test results; (c) Corresponding cross-sectional area; (d) Corresponding capillary rise

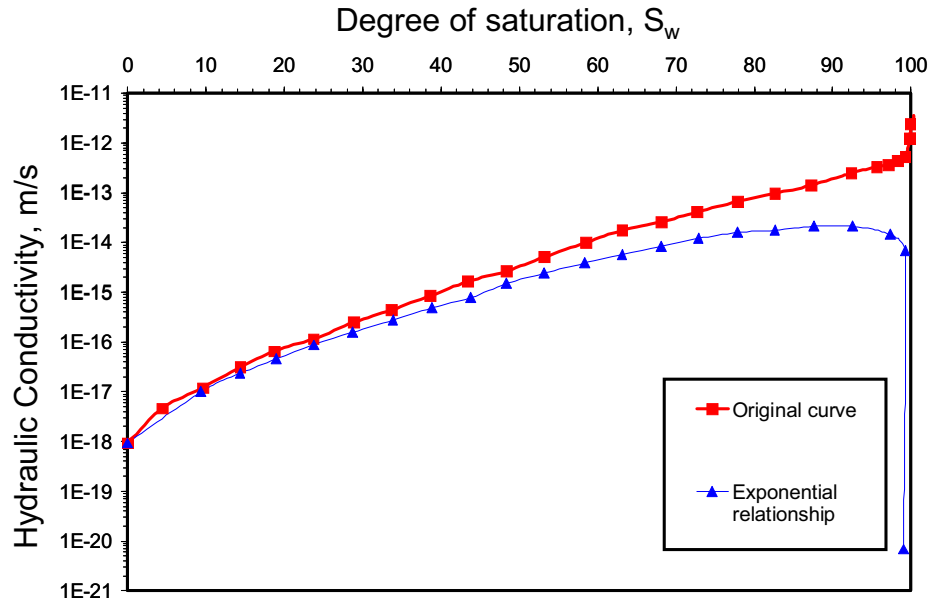


Figure 4.4 Hydraulic conductivity curves for the BSB (bentonite sand buffer) (after Thomas et al. 2003)

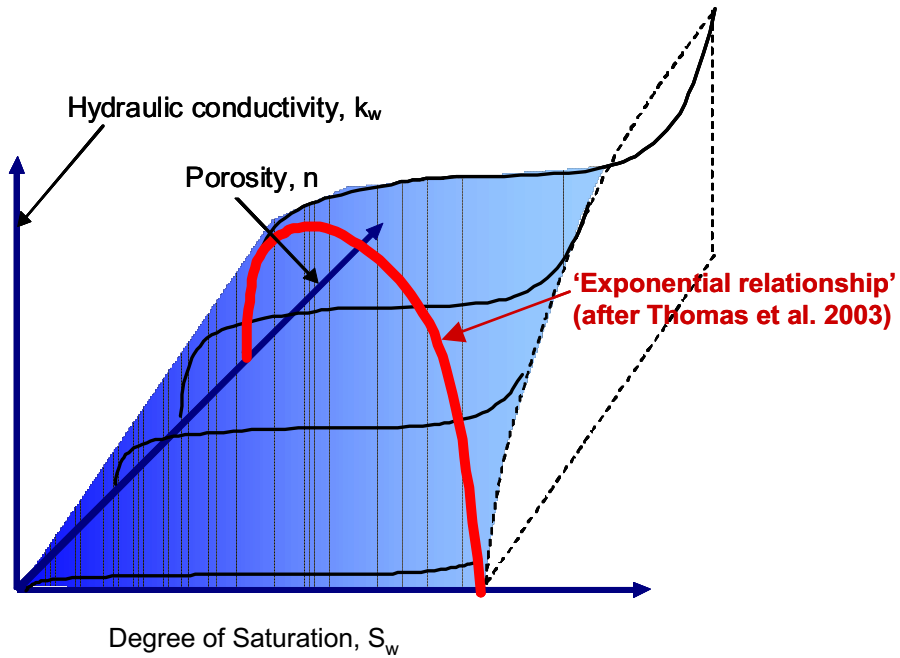


Figure 4.5 Hypothetical hydraulic conductivity surface

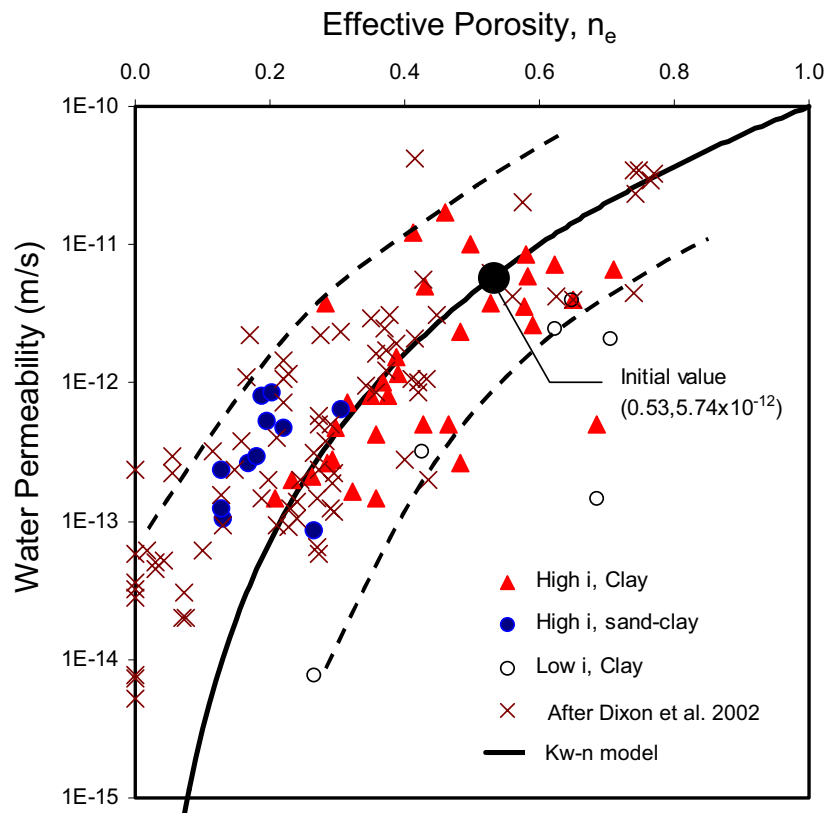


Figure 4.6 a. Water permeability vs effective porosity (data after Dixon et al. 2002)

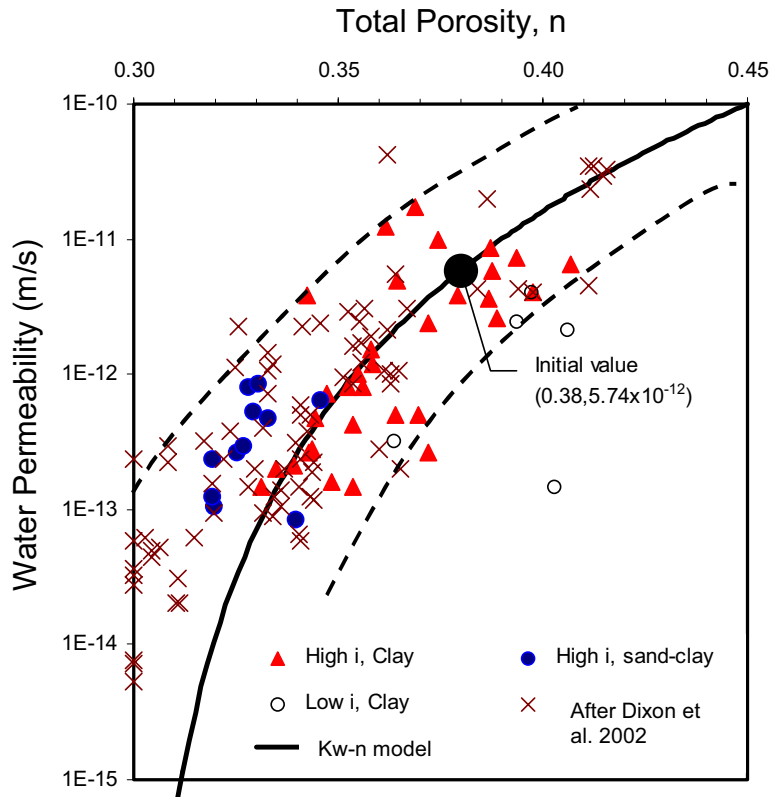


Figure 4.6.b. Water permeability vs total porosity (data after Dixon et al. 2002)

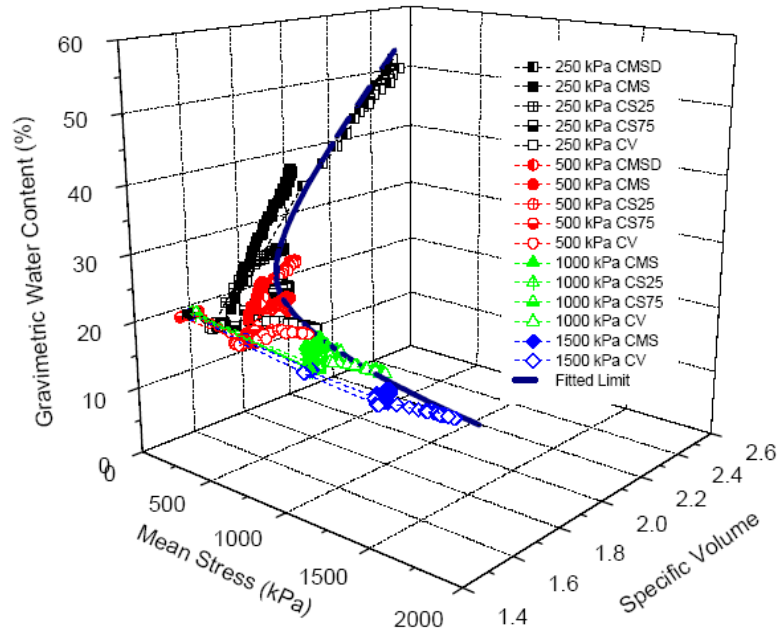


Figure 4.7 Results of infiltration test on compacted Bentonite-Sand-Buffer (BSB) on p-w-v space (Siemens 2006)

Used with permission by Siemens, July 23, 2007.

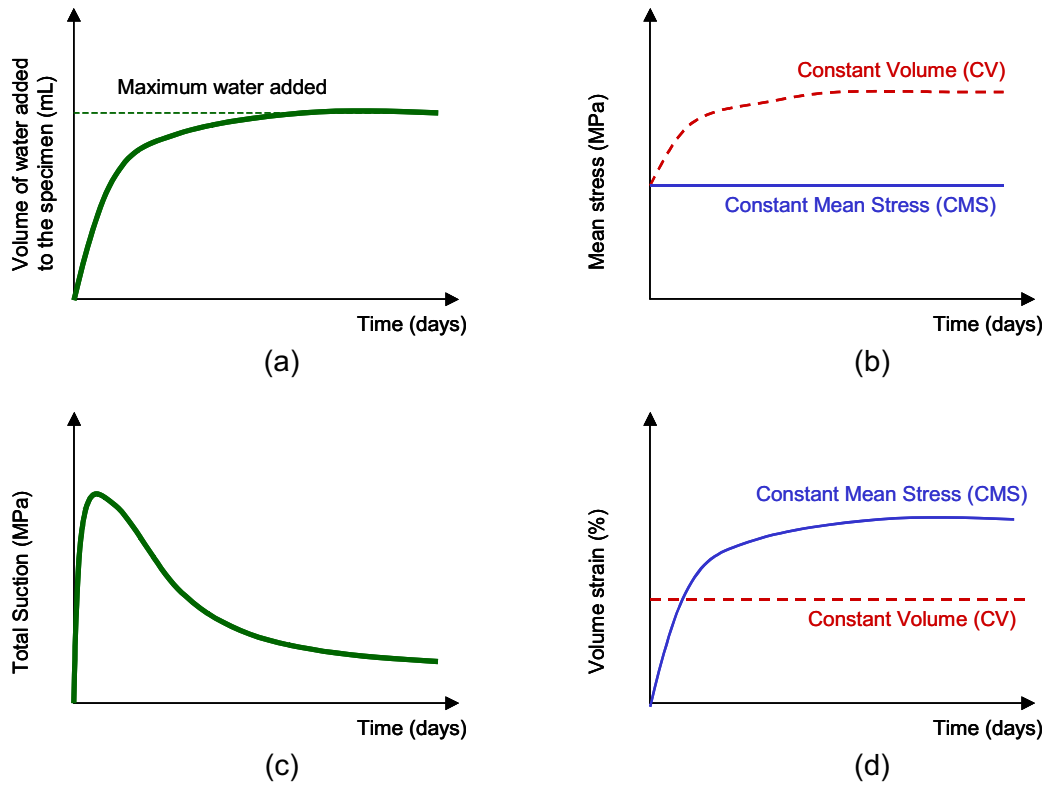
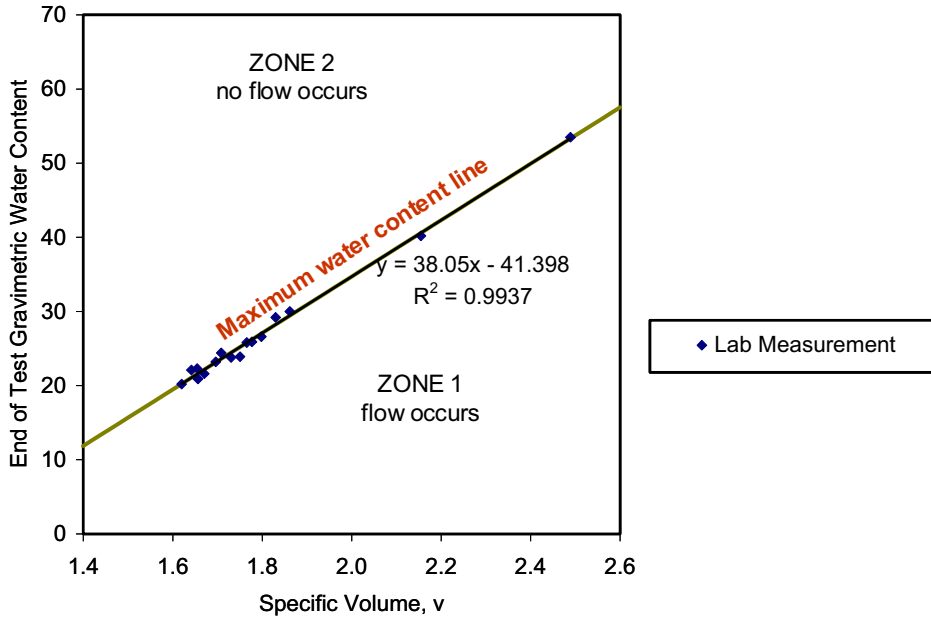
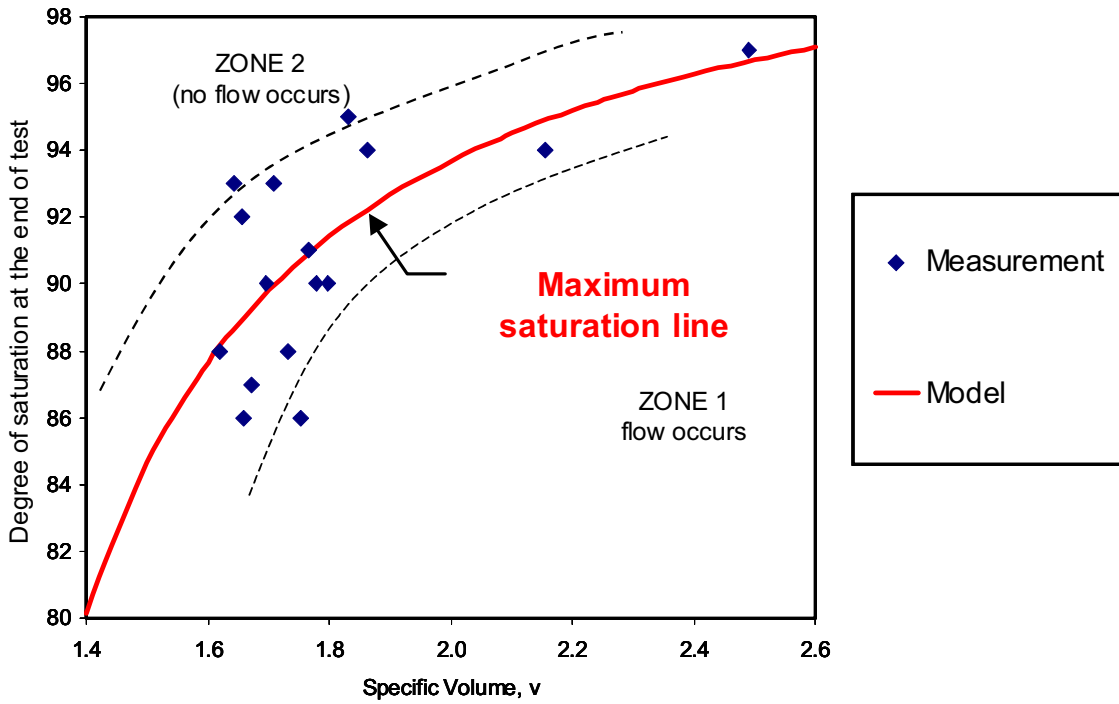


Figure 4.8 Typical results of infiltration test using triaxial cell with controlled suction and suction measurements (after Siemens 2006)

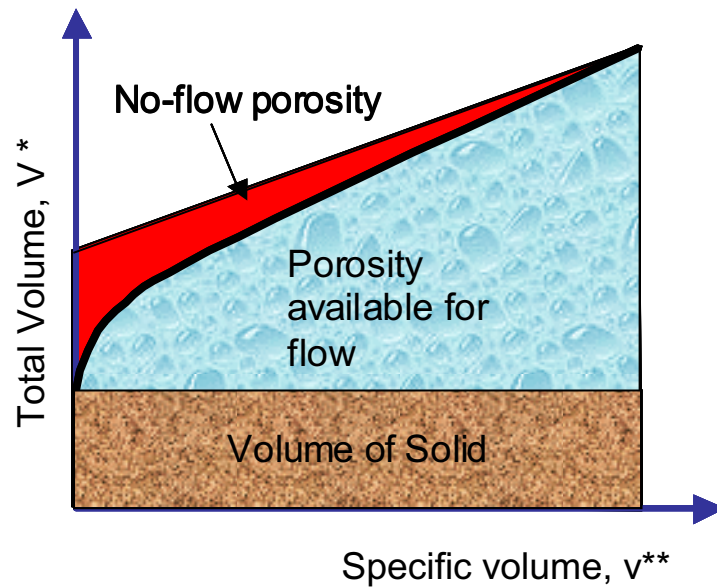


(a)



(b)

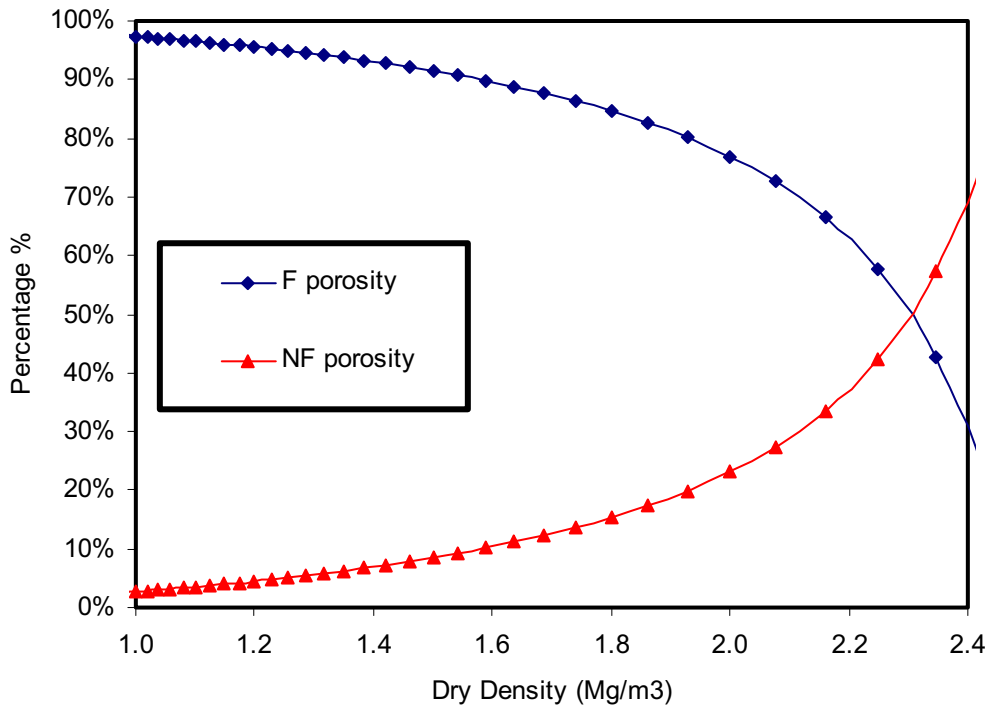
Figure 4.9 End-of test gravimetric water content (w) and degree of saturation (S_w) as a function of specific volume v (data after Siemens 2006)



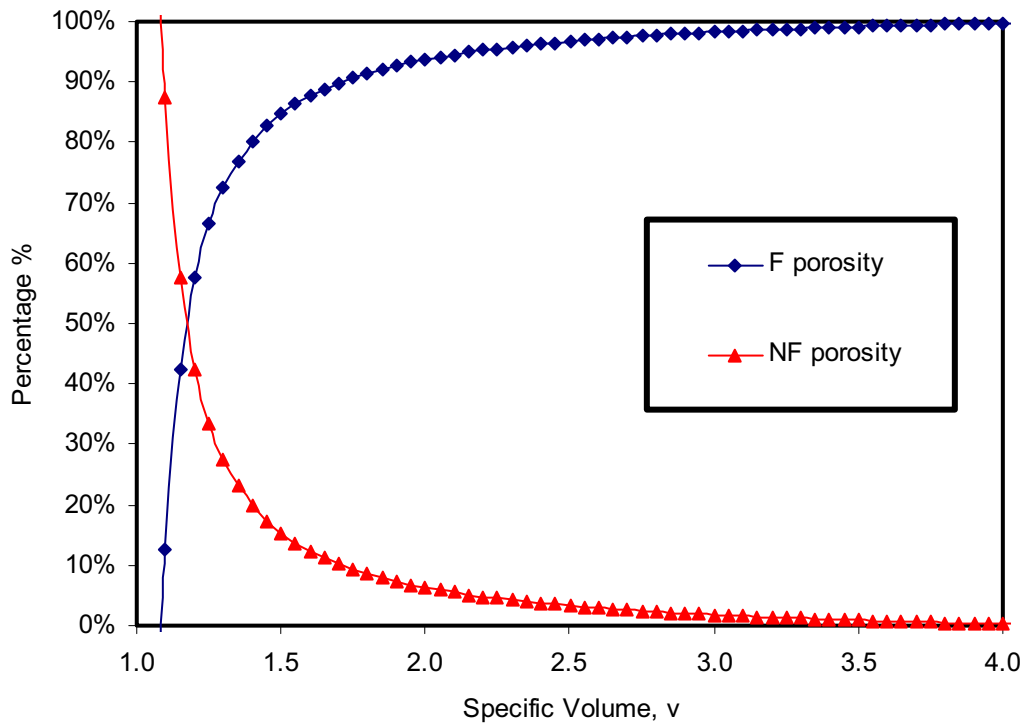
Notes:

- *) Total volume (V) is the total volume of soil with a unit of m^3 . (Volume = Volume of soil solids + Volume of void);
- **) Specific volume (v) has no unit, $v = 1+e$, where e is the void ratio.

Figure 4.10 Conceptual model illustrated end-of test degree of saturation measurements



(a)



(b)

Figure 4.11 Relationship of flow porosity and : (a) dry density; (b) specific volume

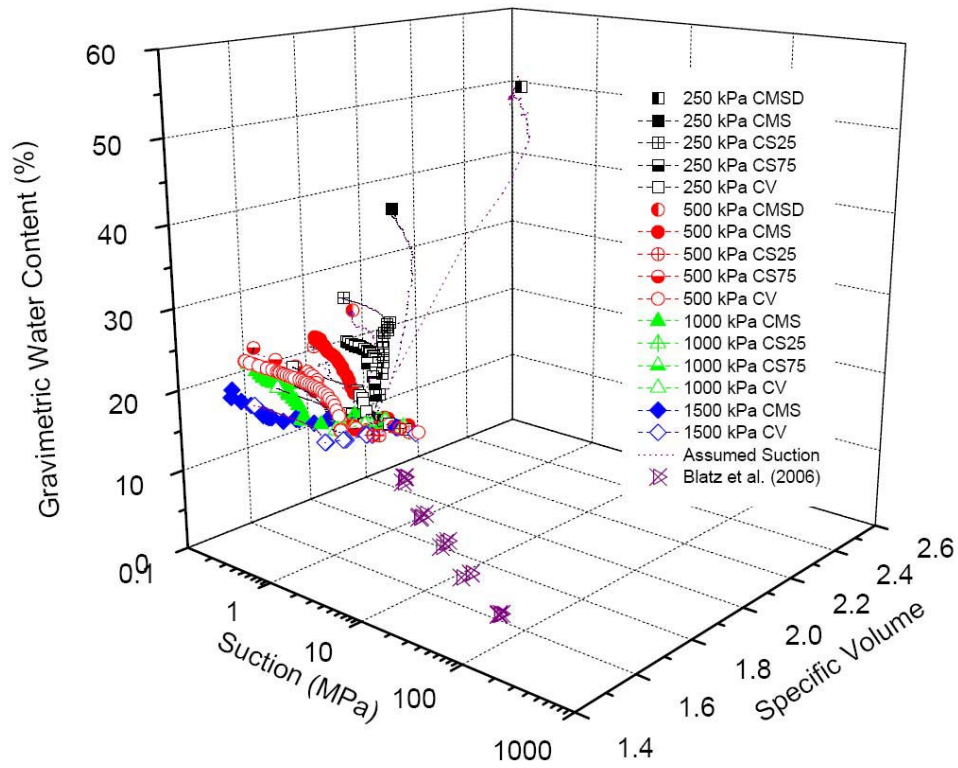


Figure 4.12 Three-dimensional water retention curve – specific volume versus suction versus gravimetric water content (Siemens 2006)

Used with permission by Siemens, July 23, 2007.

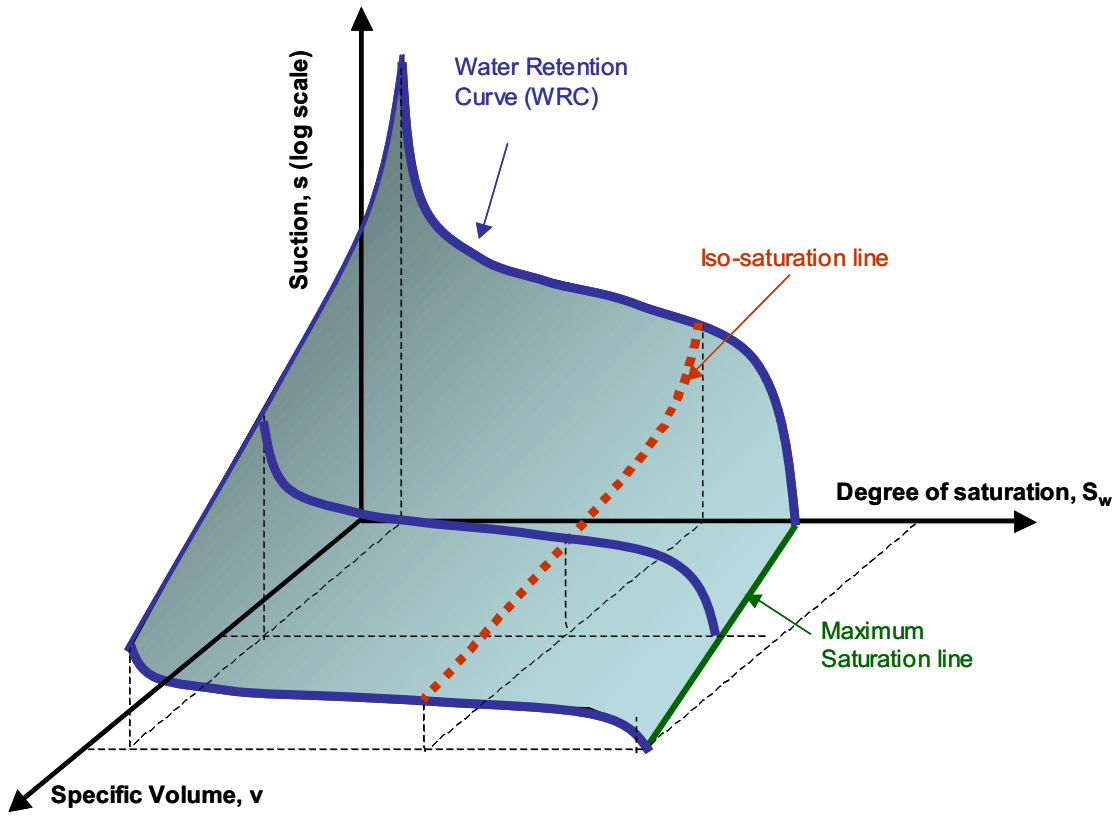


Figure 4.13 Water retention surface

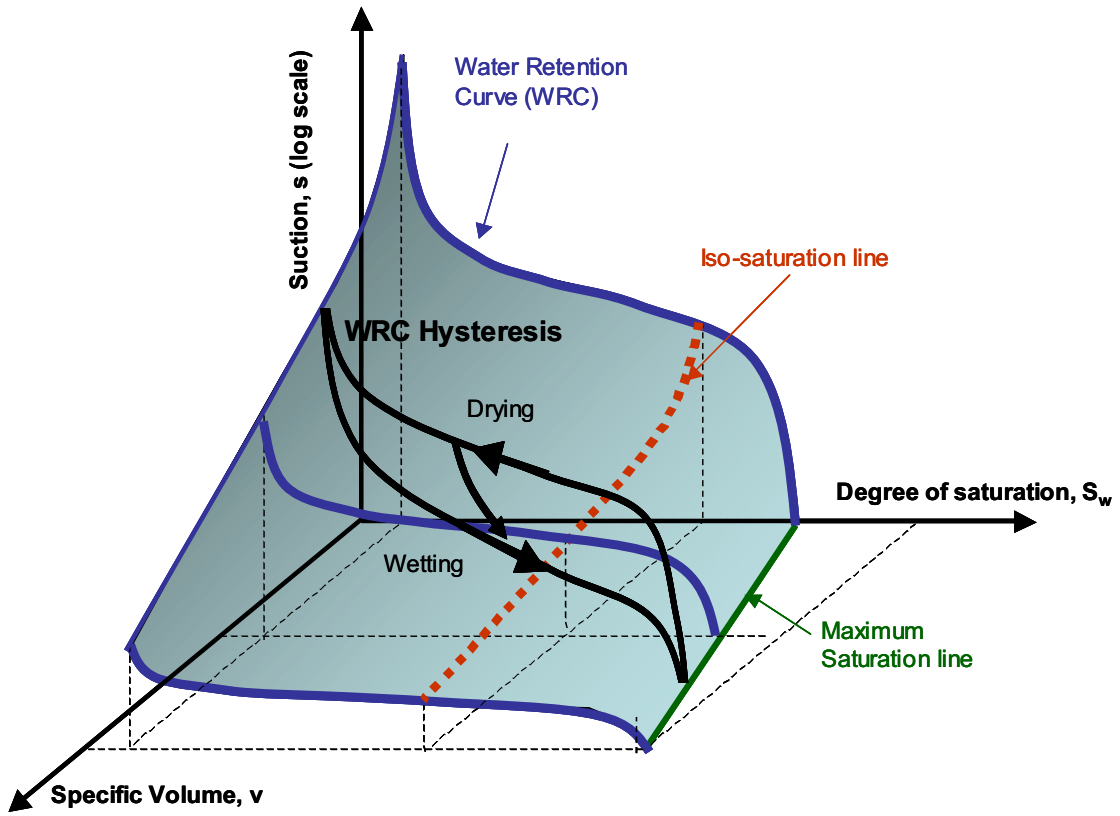


Figure 4.14 Hysteresis of water retention curve (WRC) located on the water retention surface

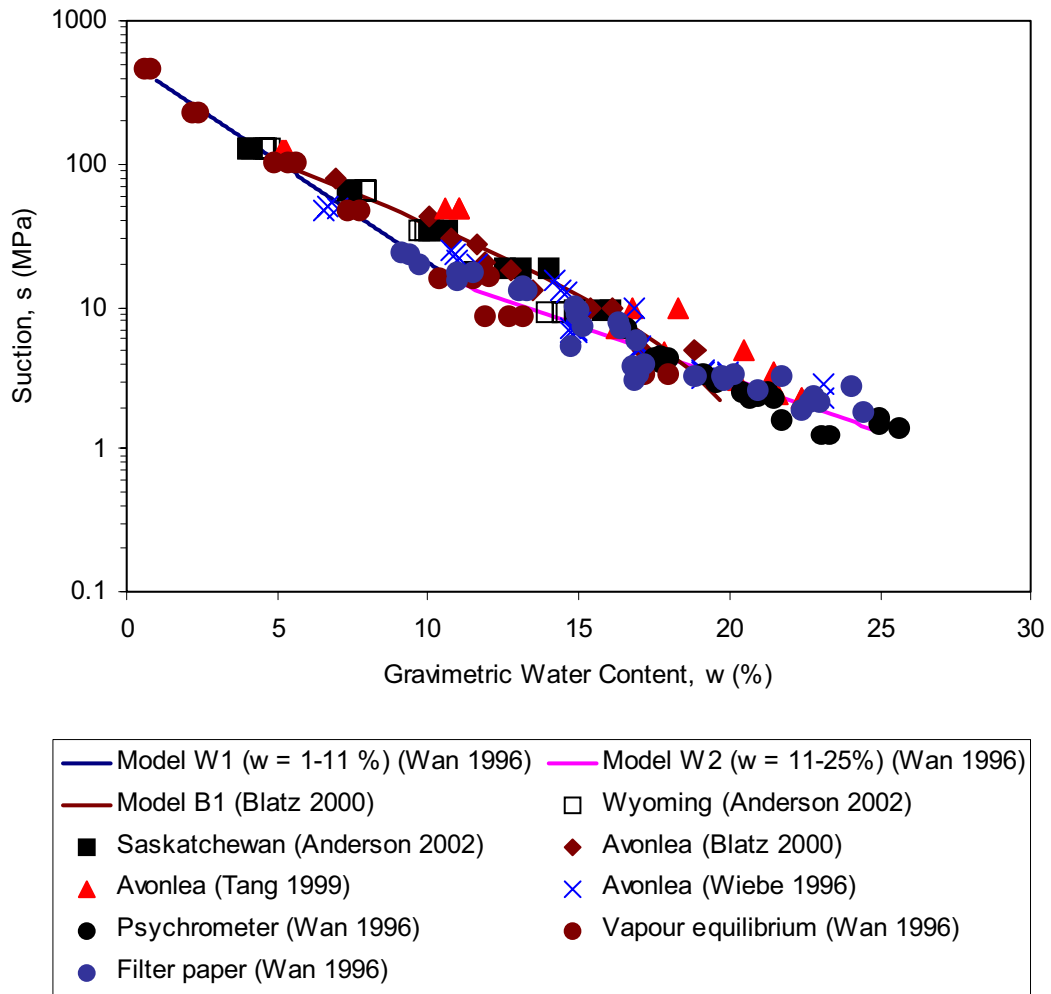


Figure 4.15 Laboratory measurements of WRC of BSB material (w vs suction) (without data from Siemens 2006)

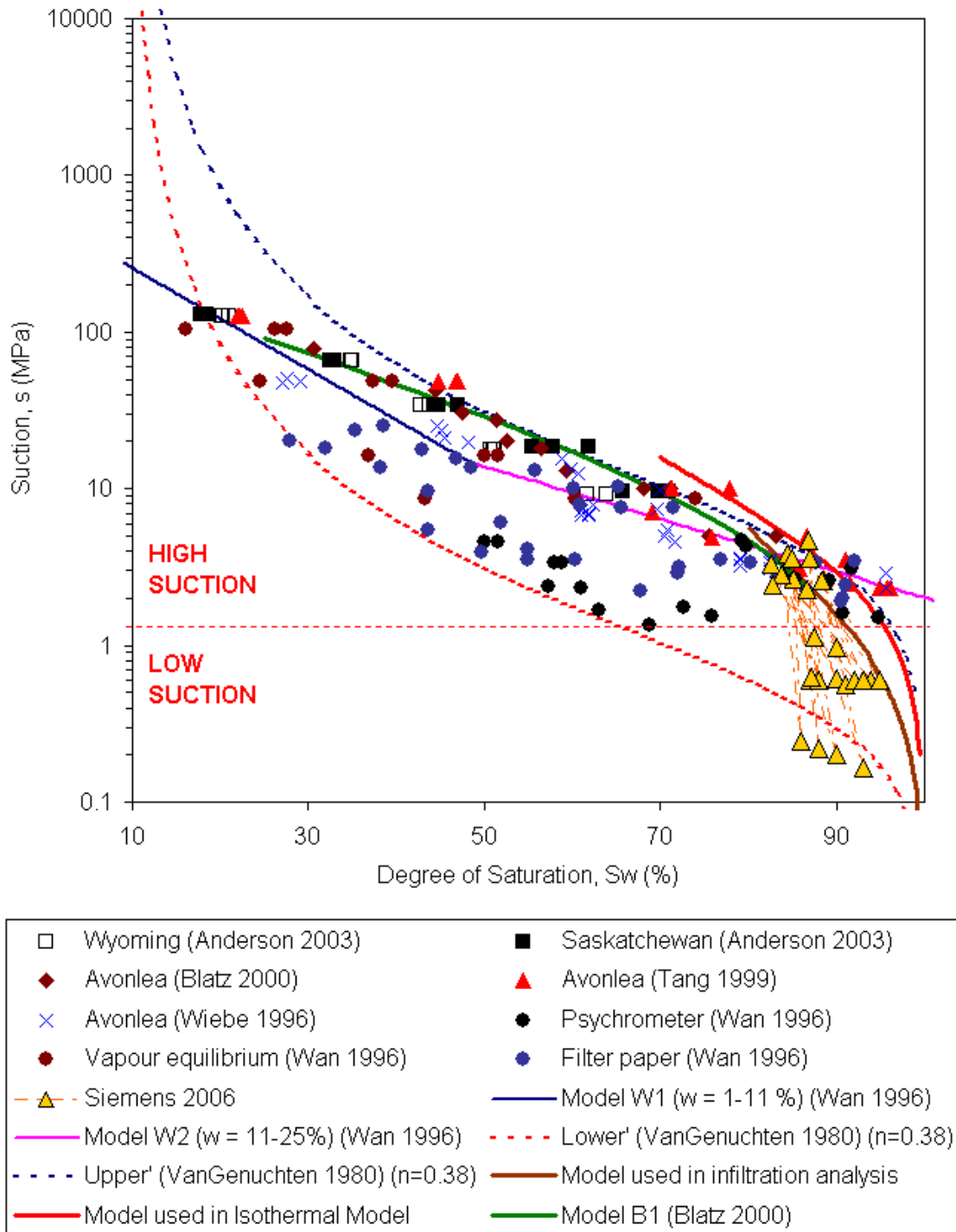


Figure 4.16 Laboratory measurements of WRC of BSB material (S_w vs suction)

CHAPTER 5

IMPLEMENTATION OF NEW 3D WATER RETENTION SURFACE

5.1 Introduction

The water retention curve for swelling clay is dependent on gravimetric water content (w) or degree of water saturation (S_w) and specific volume (v), so that it creates a surface such as discussed in Chapter 4. This chapter will discuss the mathematical formulations to implement this surface. The governing equations and the numerical formulation to implement the 3-D water retention surface using finite differences is presented in this chapter.

5.2 Water Retention Surface

The water retention surface in Figure 5.1 can be described using the following equations.

$$s(S_w, v) = P_o \left(S_e^{-1/a} - 1 \right)^{1-a} \quad [5.1]$$

$$S_e = \frac{S_w - S_{res}}{S_{max}(v) - S_{res}} \quad [5.2]$$

$$S_{\max}(\%) = \frac{G_s}{v-1}(A \cdot v - B) \quad [5.3]$$

where

S_w is the water degree of saturation;

v is the specific volume;

s is total suction. In most geotechnical engineering applications the osmotic suction (π) is much smaller than the matric suction ($u_a - u_w$), such that the total suction (s) is the same as the matric suction ($u_a - u_w$) (Fredlund and Rahardjo 1993);

a is the fitting parameter;

P_0 is air entry pressure (Pa);

S_e is effective water degree of saturation, which is defined using Equation 5.2.

S_{\max} is the maximum degree of saturation as a function of the specific volume and defined by Equation 5.3.

G_s is the specific gravity;

A is fitting first parameter to define maximum degree of saturation;

B is fitting second parameter to define maximum degree of saturation.

The Equations 5.1 to 5.3 are modified from van Genuchten (1980) model by incorporating the effect of the boundary condition based on the laboratory results on the Bentonite Sand Buffer (BSB) material using triaxial cell with controlled suction and suction measurement (Siemens 2006). The detail derivation and justification of these equations are presented in Chapter 4. Figure 5.2 illustrated the relationship of maximum degree of water saturation (S_w) as a function of specific volume (v) generated from Equation 5.3. This relationship is illustrated in Figure 5.1 as maximum saturation line.

5.3 Mathematical Formulation

The implementation of this water retention surface follows the formulation of multi-phase flow in porous media (Peaceman 1977). In this case, a two-phase flow formulation is used. This approach is also used in a two-phase flow option in FLAC (Itasca 2001).

The void space is completely filled by the two fluids, comprising water (w) and air (a). The two-phase flow option allows numerical modelling of the flow of two immiscible fluids. One fluid displaces the other and simultaneous flow of the two fluids takes place in the porous medium with no mass transfer between them. One of the fluids (water, w) wets the porous medium more than the other (air, a), so that the air pressure (u_a) will be higher than the water pressure (u_w).

The suction (s) is defined as the difference of the air pressure (u_a) and water pressure (u_w). It is a function of water degree of saturation (S_w) and specific volume (v) defined by Equations 5.1 to 5.3. Darcy's law is used to describe the flow of each fluids (water, w and air, a). In this formulation, the water permeability is only dependent on the degree of water saturation (S_w). However, the algorithm to implement the permeability surface presented in Chapter 4 can be combined with this formulation to introduce the effects of changing porosity.

The governing equations of this two-phase flow formulation consist of transport laws, relative permeability laws, the water retention surface, the degree of saturation, fluid balance laws, fluid constitutive laws, balance of momentum, mechanical constitutive laws, and compatibility equations.

5.3.1 Governing Equations

The governing equations used in this Chapter is based on the modification of the governing equations for two-phase flow formulation by Peaceman (1977) and Itasca (2001). The two-phase flow formulation embodies the following laws: transport laws; permeability laws; capillary pressure laws; saturation; fluid balance laws; fluid constitutive laws; balance of momentum; mechanical constitutive laws; and compatibility equations.

5.3.1.1 Transport Laws

Darcy's law describes transport of water (w) and air (a) in porous medium as:

$$q_i^w = -k_{ij}^w \kappa_r^w \frac{\partial}{\partial x_j} (u_w - \rho_w g_k x_k) \quad [5.4]$$

$$q_i^a = -k_{ij}^a \frac{\mu_w}{\mu_a} \kappa_r^a \frac{\partial}{\partial x_j} (u_a - \rho_a g_k x_k) \quad [5.5]$$

where κ_r is the relative permeability for the fluids, which is a function of degree of water saturation (S_w) and specific volume (v); μ is dynamic viscosity of the fluids; u_w and u_a are pore water pressure and pore air pressure respectively (e.g., in Pa); ρ is the fluid density (e.g., in kg/m^3); g is the gravity acceleration (e.g., in m/s^2); and k_{ij} is the saturated mobility coefficient, which is a tensor (e.g., in $\text{m}^2/(\text{Pa}\cdot\text{s})$), which is defined as:

$$k = \frac{k_H}{g \cdot \rho_w} = \frac{\kappa}{\mu} \quad [5.6]$$

where k_H is the hydraulic conductivity (e.g., in m/s); g is the gravitational acceleration (e.g., in m/s²); ρ_w is the fluid density; κ is the intrinsic permeability (e.g., in m²); and μ is the dynamic viscosity (e.g., units of N-sec/m²).

5.3.1.2 Permeability Laws

The permeability laws used in the formulation follow the 3-D permeability surface presented in Chapter 4. The relative permeabilities are related to degree of water saturation (S_w) by empirical laws modified from the van Genuchten (1980) model to incorporate the effect of boundary conditions for constant porosity (n):

$$\kappa_r^w = S_e^b \left[1 - (1 - S_e^{1/a})^a \right]^2 \quad [5.7]$$

$$\kappa_r^a = (1 - S_e)^c \left[1 - S_e^{1/a} \right]^{2a} \quad [5.8]$$

In Equations 5.7 and 5.8, a , b , c are constant parameters and S_e is the effective degree of water saturation. The effective degree of water saturation (S_e) is defined as:

$$S_e = \frac{S_w - S_r^w}{S_{\max} - S_r^w} \quad [5.9]$$

where S_w is the degree of water saturation; S_r^w is residual degree of water saturation; and S_{max} is the maximum degree of water saturation, which is a function of porosity (n) or specific volume (v). The maximum degree of water saturation S_{max} is defined in Equation 5.3. The relationship between the relative permeabilities (κ_r^w, κ_r^a) and the effective degree of water saturation (S_e) is illustrated in Figure 5.3.

The saturated hydraulic permeability is a function of specific volume (v) or total porosity (n) for unsaturated swelling clay. The function relating the saturated water permeability (k_{sat}) and total porosity (n) can be defined as:

$$k_{sat}(n) = k_{max} \cdot \kappa_r^{sat}(n) \quad [5.10]$$

$$\kappa_r^{sat}(n) = n_e^{nb+2} \quad [5.11]$$

$$n_e = \frac{n - n_{min}}{n_{max} - n_{min}} \quad [5.12]$$

where κ_r^{sat} is relative saturated water permeability; n_e is the effective porosity, which is defined as the porosity available for water to flow; n_{max} is the maximum porosity; n_{min} is the minimum porosity; nb is the constant parameter; and k_{max} is the maximum water permeability correlated with the maximum porosity (n_{max}). Combination of Equations 5.7

and 5.12 defines the permeability surface as illustrated in Figure 5.4. Four additional parameters (nb , k_{max} , n_{max} , and n_{min}) are required to create the complete permeability surface in Figure 5.4.

5.3.1.3 Capillary Pressure Laws

The capillary pressure law relates the difference in fluid pressure ($u_a - u_w$) to the degree of saturation (S_w) and specific volume (v). The capillary pressure law follows the 3-dimensional water retention surface presented previously.

5.3.1.4 Saturation

Assuming that water (w) and air (a) completely fill the pore space, and we have:

$$S_w + S_a = 1 \quad [5.13]$$

where S_w and S_a are the degrees of water and air saturation respectively.

5.3.1.5 Fluid Balance Laws

Assuming slightly compressible fluids, the fluid balance relations are

$$\frac{\partial \zeta_w}{\partial t} = -\frac{\partial q_i^w}{\partial x_i} + q_v^w \quad [5.14]$$

$$\frac{\partial \zeta_a}{\partial t} = -\frac{\partial q_i^a}{\partial x_i} + q_v^a \quad [5.15]$$

where ζ is the variation of fluid content (variation of fluid volume per unit volume of porous material), and q_v is the volumetric fluid source intensity.

5.3.1.6 Fluid Constitutive Laws

The constitutive laws for the fluids are:

$$S_w \frac{\partial u_w}{\partial t} = \frac{K_w}{n} \left[\frac{\partial \zeta_w}{\partial t} - n \frac{\partial S_w}{\partial t} - S_w \frac{\partial \epsilon}{\partial t} \right] \quad [5.16]$$

$$S_a \frac{\partial u_a}{\partial t} = \frac{K_a}{n} \left[\frac{\partial \zeta_a}{\partial t} - n \frac{\partial S_a}{\partial t} - S_a \frac{\partial \epsilon}{\partial t} \right] \quad [5.17]$$

where K_w and K_a are water and air bulk moduli and ϵ is volumetric strain.

Finally, the substitutions of Equation 5.14 into Equation 5.16 and Equation 5.15 into Equation. 5.17, and some rearrangement of terms results in:

$$n \left[\frac{S_w}{K_w} \frac{\partial u_w}{\partial t} + \frac{\partial S_w}{\partial t} \right] = - \left[\frac{\partial q_i^w}{\partial x_i} + S_w \frac{\partial \epsilon}{\partial t} \right] \quad [5.18]$$

$$n \left[\frac{S_a}{K_a} \frac{\partial u_a}{\partial t} + \frac{\partial S_a}{\partial t} \right] = - \left[\frac{\partial q_i^a}{\partial x_i} + S_a \frac{\partial \epsilon}{\partial t} \right] \quad [5.19]$$

In hydraulic only analysis, the change in volume strain with time $\left(\frac{\partial \epsilon}{\partial t} \right)$ is omitted, so that the permeability functions and water retention surface are only dependent on the degree of water saturation (S_w). In this case, the formulation will be the same as the original two-phase flow formulations of FLAC2D (Itasca 2001) using van Genuchten

(1980) model. The Equations 5.18, 5.19, 5.13, and 5.1 for constant v form a nonlinear system of four equations that needs to be solved for the four unknowns (u_w , u_a , S_w , and S_a).

The implementation of the permeability surface and the water retention surface presented previously requires a coupled hydro-mechanical (H-M) analysis. The additional equations for a coupled hydro-mechanical analysis are the balance of momentum, mechanical constitutive laws, and compatibility equations.

5.3.1.7 Balance of Momentum

The balance of momentum equation is:

$$\frac{\partial \sigma_{ij}}{\partial x_j} + \rho g_i = \rho \frac{dy_i}{dt} \quad [5.20]$$

where, ρ is the bulk density, and \dot{y} is velocity. The bulk density can be calculated as:

$$\rho = \rho_d + n(S_w \rho_w + S_a \rho_a) \quad [5.21]$$

where ρ_w and ρ_a are water and air densities; and ρ_d is the dry density of soil.

5.3.1.8 Mechanical Constitutive Laws

The incremental constitutive response for the porous solid has the general form of:

$$\Delta\sigma'_{ij} = H(\sigma_{ij}, \Delta\epsilon_{ij}, \kappa) \quad [5.22]$$

where $\Delta\sigma'_{ij}$ is the change in effective stress, H is the functional form of the constitutive law, and κ is a history parameter. The change of effective stress follows 2-phase flow formulation in FLAC (Itasca 2001) and it is defined as:

$$\Delta\sigma'_{ij} = \Delta\sigma_{ij} + \overline{\Delta u} \delta_{ij} \quad [5.23]$$

where Dangla (1999) shows:

$$\overline{\Delta u} = S_w \Delta u_w + S_a \Delta u_a \quad [5.24]$$

As may be seen from this formulation, provided the total stress remains constant, deformation will only occur if a change of pore pressure takes place. The Bishop (1959) effective stress is used to detect the stress-state for constitutive models involving plasticity. The Bishop (1959) effective stress is defined as:

$$\sigma'_{ij} = \sigma_{ij} + \bar{u} \delta_{ij} \quad [5.25]$$

$$\bar{u} = S_w u_w + S_a u_a \quad [5.26]$$

5.3.1.9 Compatibility Equation

The compatibility equation relates strain rate and velocity gradient and it is defined as:

$$\dot{\epsilon}_{ij} = \frac{1}{2} \left[\frac{\partial \dot{y}_i}{\partial x_j} + \frac{\partial \dot{y}_j}{\partial x_i} \right] \quad [5.27]$$

5.3.2 Boundary and Initial Conditions

The initial values of the water degree of saturation (S_w), pore water pressure (u_w) and specific volume of the specimen (v) or porosity (n) are specified in the analysis. The air degree of saturation (S_a) and pore air pressure (u_a) can be derived from the saturation relationship in Equation 5.13 and the water retention surface in Equations 5.1 to 5.3.

5.4 Numerical Formulation

The fluid balance equations (Equations 5.14 to 5.15) can be solved using a discretization and finite difference method such as used in FLAC (Itasca 2001). In two-phase flow calculations, two pore pressures (u_w , u_a) and one value of the saturation (S_w) are defined at each node. It is assumed that these variables (u_w , u_a , and S_w) vary linearly within triangular regions corresponding to the zones in the FLAC formulation (Itasca 2001), which will be discussed briefly later. The numerical scheme rests on a nodal formulation of the fluid continuity equations. The nodal flow contributions are calculated on a zone basis, using an upstream weighting technique. The resulting system of ordinary

differential equations is solved using an explicit formulation stepping forward in time. This section derives the numerical formulation of the water retention surface $[(u_a - u_w) = f(S_w, v)]$.

5.4.1 Derivation of Element “Stiffness Matrix”

The element “stiffness matrix” defined in this section corresponds to the fluid mobility coefficient (k) that is required in the 2-phase flow calculation. This stiffness matrix derivation follows FLAC (Itasca 2001) analysis.

Neglecting gravity for the moment, Darcy’s law (in Equations. 5.4 and 5.5) for anisotropic porous medium is reduced to:

$$q_i = -k_{ij} \frac{\partial u}{\partial x_j} \quad [5.28]$$

A mixed discretization method (Marty and Cundall 1982), such as used in FLAC (Itasca 2001), is used in this formulation. Each quadrilateral element is divided into triangles in two different ways as illustrated in Figure 5.4a. Pore pressure is assumed to vary linearly within a triangle, and the vector q_i is derived for a generic triangle of area A by application of the Gauss divergence theorem. The form of Gauss’ divergence theorem is (e.g., Malvern 1969):

$$\int_s n_i f ds = \int_A \frac{\partial f}{\partial x_i} dA \quad [5.29]$$

where

\int_s is the integral around the boundary of a closed surface;

n_i is the unit normal to the surface, s ;

f is a scalar, vector, or tensor;

x_i are position vectors;

ds is an incremental arc length; and

\int_A is the integral over the surface area, A .

Defining the average value of the gradient over the area A as

$$\left[\frac{\partial f}{\partial x_i} \right] = \frac{1}{A} \int_A \frac{\partial f}{\partial x_i} dA \quad [5.30]$$

Substitution of Equation 5.30 into Equation 5.29 results in:

$$\left[\frac{\partial f}{\partial x_i} \right] = \frac{1}{A} \int_s n_i f ds \quad [5.31]$$

For a triangular sub-element, the finite difference form of Equation 5.29 becomes

$$\left[\frac{\partial f}{\partial x_i} \right] = \frac{1}{A} \sum_s \langle f \rangle n_i \Delta s \quad [5.32]$$

where Δs is the length of a side of the triangle, the summation occurs over the three sides of the triangle. The value of $\langle f \rangle$ is taken to be the average over the side.

Using the general form of the Gauss divergence theorem for a triangular sub-element in Equation 5.32, Darcy's law in Equation 5.28 can be written as:

$$q_i \cong \frac{k_{ij}}{A} \sum un_i s \quad [5.33]$$

where Σ is the summation over the three sides of the triangle (Figure 5.5); n is the unit normal to the side, and s is the length of the side.

The two components of q are:

$$q_1 = \frac{1}{A} [k_{11} \sum un_1 s + k_{12} \sum un_2 s] \quad [5.34]$$

$$q_2 = \frac{1}{A} [k_{21} \sum un_1 s + k_{22} \sum un_2 s] \quad [5.35]$$

Considering, for example, the contribution of side (ab) of the triangle to the simulations:

$$q_1^{(ab)} = \frac{1}{2A} [-k_{11}(u^{(b)} + u^{(a)})(x_2^{(b)} - x_2^{(a)}) + k_{12}(u^{(b)} + u^{(a)})(x_1^{(b)} - x_1^{(a)})] \quad [5.36]$$

$$q_2^{(ab)} = \frac{1}{2A} \left[-k_{21} (u^{(b)} + u^{(a)}) (x_2^{(b)} - x_2^{(a)}) + k_{22} (u^{(b)} + u^{(a)}) (x_1^{(b)} - x_1^{(a)}) \right] \quad [5.37]$$

The other two sides, (bc) and (ca), provide similar contributions to q_i . The specific discharge vector contribution is then converted to scalar volumetric flow rates at the nodes by making dot products with the normals to the three sides of the triangles. The general expression is

$$Q = q_i n_i s \quad [5.38]$$

For example, the flow rate into node (a) is

$$Q^{(a)} = \left\{ -q_1 (x_2^{(b)} - x_2^{(c)}) + q_2 (x_1^{(b)} - x_1^{(c)}) \right\} / 2 \quad [5.39]$$

The factor 2 in Equation 5.38 accounts for the fact that the node only captures half the flow crossing a neighbouring edge (since the other half goes to the other node of the edge). Similar expressions apply to nodes (b) and (c).

Nodal flow rates are added from the three triangles meeting at the node and divided by 2, since the flow sum comes from two overlaid grids. The “stiffness” matrix $[M]$ of the whole quadrilateral element is defined in terms of the relation between the pressures at the four nodes and the four nodal flow rates, as derived above:

$$\{Q\} = [M]\{u\} \quad [5.40]$$

For a special case of a square zone, aligned with the coordinate axes, the stiffness matrix has the form:

$$[M] = -\frac{k}{2} \begin{bmatrix} 2 & -1 & 0 & -1 \\ -1 & 2 & -1 & 0 \\ 0 & -1 & 2 & -1 \\ -1 & 0 & -1 & 2 \end{bmatrix} \quad [5.41]$$

where k is the isotropic mobility coefficient. This matrix is identical to the one that would be obtained in a classical finite difference or finite volume method.

5.4.2 Nodal Formulation of the Fluid Balance Laws

For a finite volume V , the balance laws take the form:

$$\frac{S_w}{K_w} \Delta u_w + \Delta S_w = -\frac{1}{nV} [Q_w \Delta t + S_w \Delta V] \quad [5.42]$$

$$\frac{S_a}{K_a} \Delta u_a + \Delta S_a = -\frac{1}{nV} [Q_a \Delta t + S_a \Delta V] \quad [5.43]$$

where V is nodal volume, and Q is nodal flow rate.

The water retention surface (WRS) in Equations 5.1 to 5.3 can be re-written as:

$$s = f(S_w, v) \quad [5.44]$$

This results in the incremental form of the suction as a function of degree of saturation increments (ΔS_w) and specific volume (ΔV)

$$\Delta s = \left(\frac{\partial s}{\partial S_w} \right) \Delta S_w + \left(\frac{\partial s}{\partial V} \right) \Delta V \quad [5.45]$$

where $\left(\frac{\partial s}{\partial S_w} \right)$ and $\left(\frac{\partial s}{\partial V} \right)$ are the derivative of the water retention surface (Equations 5.1 to 5.3) with respect to water degree of saturation (S_w) and specific volume (V). This function will be discussed later.

The incremental form of saturation in Equation 5.13 is

$$\Delta S_w + \Delta S_a = 0 \quad [5.46]$$

Substitutions of Equations 5.45 to 5.46 into Equations 5.42 to 5.43 to eliminate Δu_a and ΔS_a and some rearrangement of terms results in:

$$\frac{S_w}{K_w} \Delta u_w + \Delta S_w = -\frac{1}{nV} [Q_w \Delta t + S_w \Delta V] \quad [5.47]$$

$$\frac{S_a}{K_a} \Delta u_w + \left[\frac{S_a \left(\frac{\partial s}{\partial S_w} \right)}{K_a} - 1 \right] \Delta S_w = -\frac{1}{nV} Q_a \Delta t - S_a \left[\frac{1}{nV} + \frac{nV \left(\frac{\partial s}{\partial V} \right)}{K_a} \right] \Delta V \quad [5.48]$$

Finally, solving for Δu_w and ΔS_w , we obtain:

$$\Delta u_w = \frac{E - B \cdot D}{C - A \cdot D} \quad [5.49]$$

$$\Delta S_w = B - A \left[\frac{E - B \cdot D}{C - A \cdot D} \right] \quad [5.50]$$

where

$$A = \frac{S_w}{K_w}$$

$$B = -\frac{1}{n \cdot V} [Q_w \cdot \Delta t + S_w \cdot \Delta V]$$

$$C = \frac{S_a}{K_a}$$

$$D = \left[\frac{S_a \left(\frac{\partial s}{\partial S_w} \right)}{K_a} - 1 \right]$$

$$E = -\frac{1}{n \cdot V} Q_a \Delta t - S_a \left[\frac{1}{n \cdot V} + \frac{n \cdot V \left(\frac{\partial s}{\partial V} \right)}{K_a} \right] \Delta V$$

Using the explicit numerical scheme, the new nodal pore water pressure and degree of water saturation (S_w) at $t + \Delta t$ are evaluated from those at time t by adding the increments in Equations 5.49 and 5.50, evaluated from known quantities at time t . The volume increments (ΔV) are calculated from the mechanical cycle. The new value of pore air pressure (u_a) at a node is derived from the new values of u_w and s_w with current volume V , using the water retention surface equations (Equations 5.1 to 5.3).

5.4.3 Derivative of Water Retention Surface (WRS)

The derivative of the water retention surface in Equations 5.1 to 5.3 with respect to the

degree of water saturation $\left(\frac{\partial s}{\partial S_w}\right)$:

$$\frac{\partial s}{\partial S_w} = -\frac{1-a}{a} \cdot P_o \frac{S_e^{-1/a}}{S_{\max} - S_{\text{res}}} \left(1 - S_e^{1/a}\right)^{-a} \quad [5.51]$$

where S_{\max} is defined using Equation 5.3.

The derivative of the water retention surface in Equations. 5.1-5.3 with respect to the

specific volume $\left(\frac{\partial s}{\partial v}\right)$:

$$\frac{\partial s}{\partial v} = -\frac{1-a}{a} \cdot P_o \left(U^{-1/a}\right) \left(1 - U^{1/a}\right)^{-a} \left(\frac{\partial U}{\partial v}\right) \quad [5.52a]$$

where

$$U = \frac{(S_w - S_{\text{res}})v - (S_w - S_{\text{res}})}{(G_s A - S_{\text{res}})v - (G_s B - S_{\text{res}})} \quad [5.52b]$$

$$\frac{\partial U}{\partial v} = \frac{G_s(S_w - S_{res})(A - B)}{\{(G_s A - S_{res})v - (G_s B - S_{res})\}^2} \quad [5.52c]$$

5.4.4 Nodal Flow Rate

The zone contributions to nodal flow rates Q_w and Q_a are calculated using the element “stiffness matrix” $[M]$, which was discussed previously.

For two-phase flow, the nodal volumetric flow rates in a zone Q_w , Q_a are related to nodal pore pressures u_w and u_a by the matrix expressions:

$$Q_w = \hat{\kappa}_r^w [M_w] \{u_w - \rho_w x_i g_i\} \quad [5.53]$$

$$Q_a = \hat{\kappa}_r^a \frac{\mu_w}{\mu_a} [M_w] \{u_w - \rho_w x_i g_i\} \quad [5.54]$$

where $\hat{\kappa}_r$ is relative permeability for the zone. The current relative permeabilities are evaluated from the permeability function, such as presented in Equations 5.7 to 5.12 by inputting the current zone degree of water saturation (\bar{S}) and current specific volume (v).

5.4.5 Time Step

The stable time step for numerical stability can be calculated on the basis of fluid diffusivity (Itasca 2001). An estimation of the timestep magnitude may be obtained using the formula (Itasca 2001):

$$\Delta t = L_z^2 n \min\left(\frac{1}{k_w \cdot K_w}, \frac{1}{k_a \cdot K_a}\right) \quad [5.55]$$

where L_z is the smallest zone size in the simulation, and k_a is the saturated mobility coefficient for the non-wetting fluid:

$$k_a = k_w \cdot \frac{\mu_w}{\mu_a} \quad [5.56]$$

The effect of increased mechanical stiffness can be incorporated in quasi-static analysis in the density-scaling scheme (Itasca 2001); the apparent mechanical bulk modulus of a zone is modified by the presence of fluids as follows:

$$K \cong K + \frac{S_w K_w + S_a K_a}{n} \quad [5.57]$$

where n is the porosity of the zone.

5.4.6 Mechanical Coupling

The mechanical coupling can be made by incorporating changes in effective stress induced deformation. Any mechanical constitutive models, such as elasto-plastic models presented in Chapter 3 can be used in conjunction with this formulation.

The mechanical constitutive model (Chapter 3) calculates an effective stress change using a law of functional form in Equation 5.22. The corresponding total stress change is then derived from Equation 5.23. The mean zone pressure in this formula is evaluated from Equation 5.24, using mean zone values for saturations and pressure increments.

In transient hydraulic-mechanical calculations, volumetric deformations generate pore pressures and saturation changes. This additional coupling effect is taken into consideration by incorporation of the terms with ΔV in Equations 5.49 and 5.50 in the numerical scheme. The nodal contributions of those terms are calculated after distribution of zonal volumetric strains to the nodes.

5.5 Concluding Remarks

The new set of hydraulic constitutive models used to define the water retention surface and permeability surface is presented in this Chapter. Each is a function of the degree of water saturation (S_w) and specific volume (v).

The governing equations to implement these constitutive models into a two-phase flow formulation are summarized. These governing equations can be solved using a

discretization and finite-difference method and the numerical formulation using these methods has been presented.

These sets of numerical formulations can be used to implement a new set of three-dimensional hydraulic constitutive models. They also can be combined with the mechanical constitutive models, such as elasto-plastic models presented previously to provide fully coupled hydraulic-mechanical behaviour.

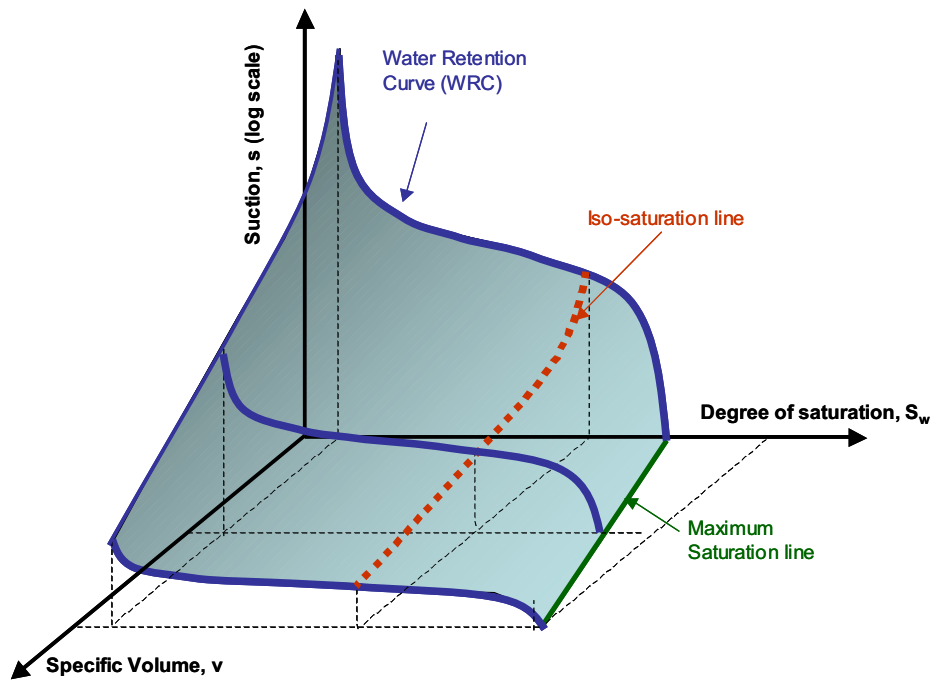


Figure 5.1 The water retention surface

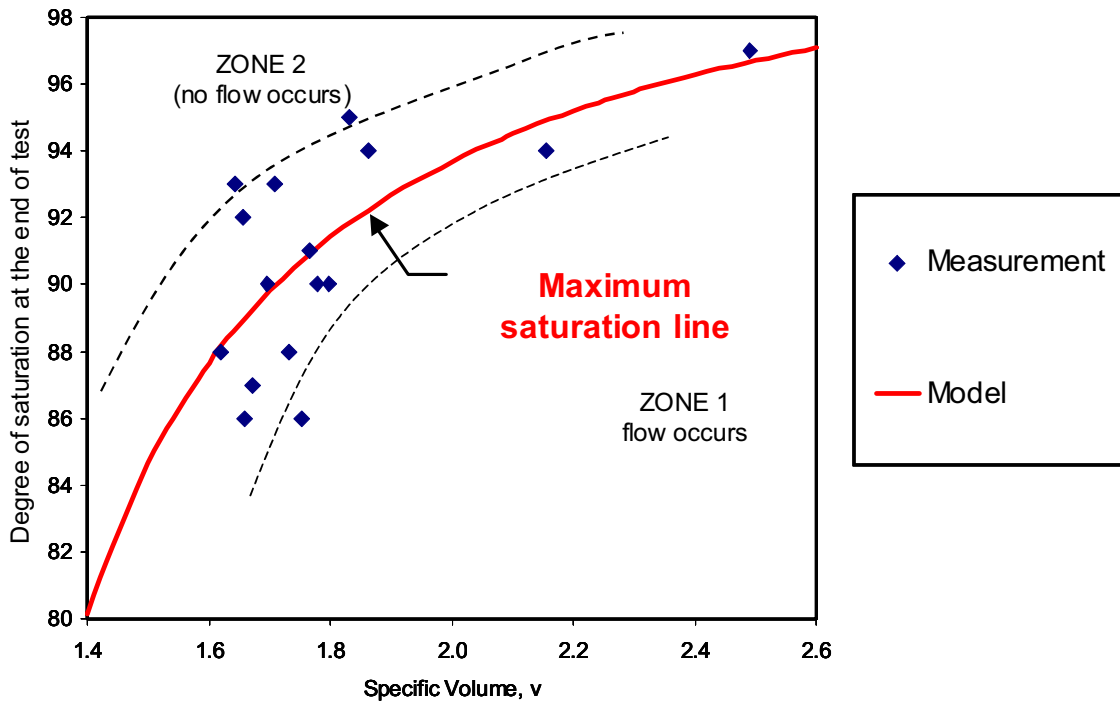


Figure 5.2 End-of test gravimetric water content (w) and degree of saturation (S_w) as a function of specific volume v (data after Siemens 2006)

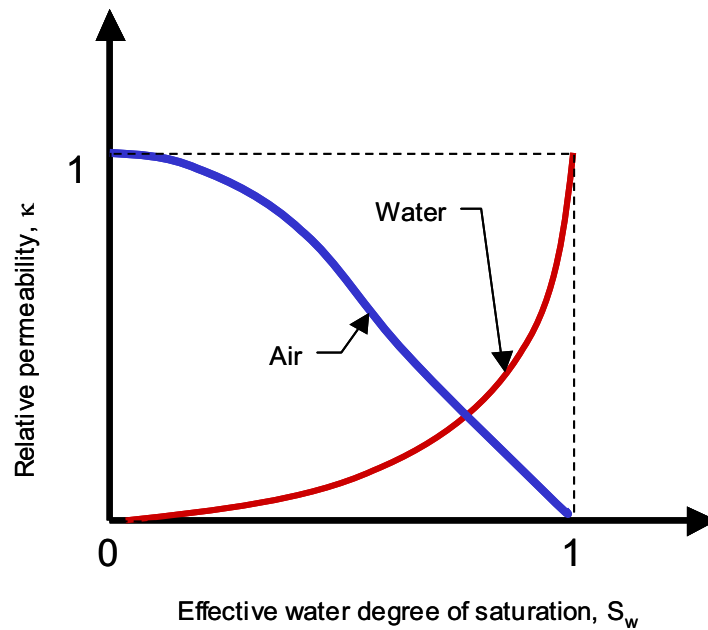


Figure 5.3 The relationship between the relative permeabilities (κ_r^w, κ_r^a) and the effective degree of saturation (S_e)

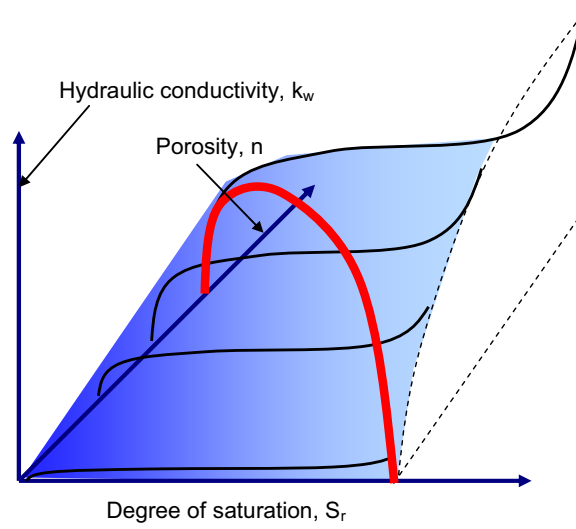


Figure 5.4 The permeability surface

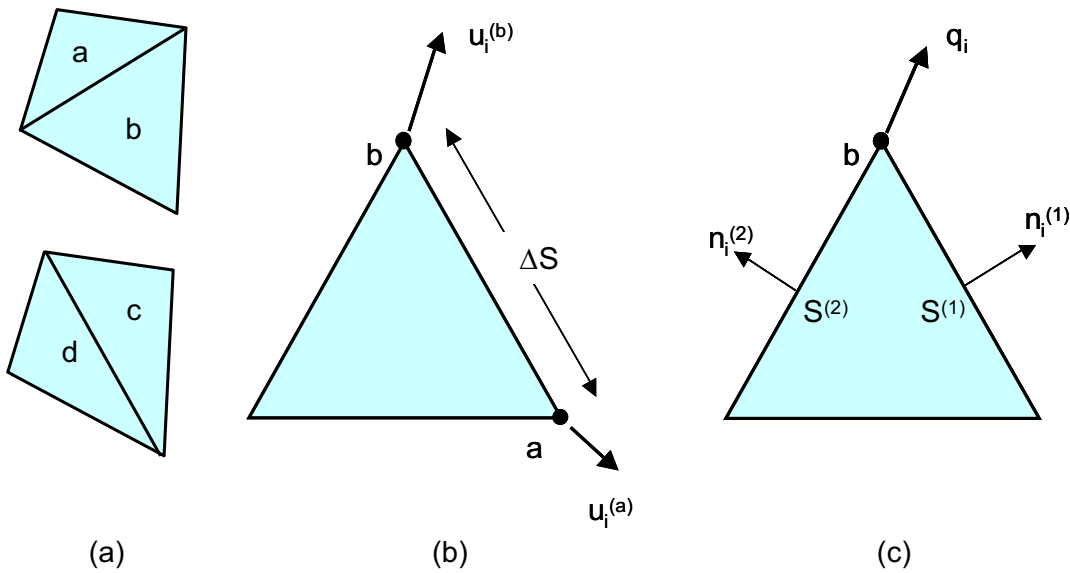


Figure 5.5 (a) Overlaid quadrilateral elements used in FLAC; (b) Typical triangular element with velocity vectors; (c) Nodal flow vector

PART 4:

PROPOSED CALIBRATION METHOD

CHAPTER 6

PARAMETER EVALUATION METHOD (PEM)

6.1 Introduction

This chapter provides a calibration method relating the results of laboratory test to the numerical constitutive model. This chapter proposes a new method to evaluate the parameters of rigorous mechanical constitutive models for unsaturated swelling clay, called the 'Parameter Evaluation Method' (PEM). The PEM is used to evaluate two mechanical constitutive models: the BBM (Basic Barcelona Model) (Alonso et al. 1990); and the BGM (Blatz and Graham 2003).

The main objective of this chapter is to introduce the application of the PEM to assess the ability of the two constitutive models to simulate the behaviour of unsaturated swelling clay. The limitations of the two existing constitutive models and some recommendations to modify these models are also summarized. The application of the PEM can reduce the difficulty in the calibrations of rigorous constitutive models. This chapter summarizes publications of the PEM by the author of this thesis along with other co-authors (Priyanto et al. 2004, Priyanto et al. 2005, and Priyanto et al. 2006).

6.2 Background

The characterization of unsaturated swelling clay is more difficult compared with other engineering materials (Lade 2005). Characterization of unsaturated swelling clay can be done by means of laboratory testing combined with numerical modelling. The focus of this thesis is toward the characterization of unsaturated swelling clay through numerical modelling.

Priyanto et al. (2005) summarized several challenges in numerical modelling of unsaturated swelling clay. Due to the complexity of unsaturated clay behaviour, a simple constitutive model may not be sufficient to describe the general response to all possible stress paths. Consequently, more comprehensive constitutive models (such as those referred to as critical state models) are required. Unlike critical state soil mechanics (Roscoe and Burland 1968) for saturated soils, a widely accepted constitutive model for unsaturated high plastic clay is not clearly established at this time. There are many constitutive models proposed that are developed for various types of clay materials and varying stress-state and environmental conditions using different laboratory test methods (e.g. Alonso et al. 1990, Wheller and Sivakumar 1995, Alonso et al. 1999, Tang and Graham 2002, Blatz and Graham 2003). Selection of the most suitable constitutive model to simulate a particular type of material forms a considerable challenge.

It is also possible that a specific constitutive model is only adequate to simulate a specific clay mineral or soil type. When such a constitutive model is applied to different types of material and conditions, modifications of the model are required. The BBM (Alonso et al. 1990) was originally calibrated based on clay with low-to-medium

plasticity. Additional features are required to capture the swelling behaviour when used for high plastic clay as outlined in Alonso et al. (1999). Consequently, assessment of the capability of existing constitutive models is important. In this discussion, the BBM and the BGM are selected in the analysis based on the following reasons. The BBM is the first critical state soil model for unsaturated clay, while the BGM is developed based on the laboratory test results using a similar clay material as used in this thesis. The BGM was developed on the foundation of the BBM and added some new features of behaviour for the specific clay and preparation procedure used.

The PEM is used to assess of the numerical simulations using the BBM and the BGM of three specimens. This assessment allows comparison of the two constitutive models based on three PEM criteria. The application of the PEM also shows some limitation of both constitutive models (i.e. the BBM and the BGM). The recommendations to modify both constitutive models are also provided. The PEM analysis is used to justify the selection of the mechanical constitutive model and its parameters in Chapters 7 and 8.

6.3 Parameter Evaluation Method (PEM)

6.3.1 General Overview

The Parameter Evaluation Method (PEM) was developed based on the assumption when a constitutive model is representative to simulate the general behaviour of a particular material, its parameters are independent of the magnitude and direction of the stress paths and other conditions applied to this material (Priyanto et al. 2004).

The application of the PEM requires both laboratory testing, numerical simulation, and iteration process. The following assumptions are made in the application of the PEM:

- The parameters of the numerical constitutive model are calibrated with the laboratory testing results; and
- The accuracy of both the numerical simulations and the laboratory tests are within an acceptable range.

The first idea in the development of the PEM was to estimate the parameters of elasto-plastic mechanical constitutive models. However, the PEM can also be used: to assess and compare the existing constitutive models; to select the existing constitutive models; and as a tool to develop a new constitutive model.

6.3.2 Process

The overall process involved in the PEM is illustrated in Figure 6.1. The process starts after the completion of laboratory testing program. The magnitude and direction of the stress paths, boundary conditions, and other conditions (e.g., temperature, initial condition, pore fluid salinity, etc) for the laboratory testing program are planned based on the possible processes and conditions that may occur in the engineered systems in which the laboratory testing results will be applied. At the end of the laboratory testing program, all of the magnitude and direction of the stress paths involved in the application are characterized using laboratory testing.

Following the end of the laboratory testing program, a possible constitutive model is selected. Initial parameters of the constitutive models are determined to start the iteration process. The reasonable range of initial parameters can be verified using available database from previous laboratory testing results. If a database is not available, any values of parameters that do not result in imaginary numbers in the

simulations can be used. The overall process of the PEM consists of multiple iteration processes for many stress paths ((p-s) 1, 2, 3, ...n) and responses ((p-v) 1, 2, 3, ...n) (Figure 6.1).

The iteration process for a single stress path is illustrated in Figure 6.2. The steps used in the iteration process are as follows. generating laboratory test results; discretization of laboratory test results; simulation; and iteration. The laboratory test of unsaturated soil results in the stress paths and responses in p-s space and p-v space. These laboratory testing results (i.e., $(p-s)_{lab}$) and $(p-v)_{lab}$) are discretized to provide sufficient data points in the simulation and iteration process. The iteration process in the PEM requires the development of a simulation program that is coupled with an automated iteration. The simulation program has to be relatively simple to allow the iteration process. In this thesis, the simulation program was developed using finite different method using MS-Excel and the iteration process was conducted using solver-function within MS-Excel. In this thesis approximately 250 data points are used in the simulation of the constitutive model and iteration process.

The $(p-s)_{lab}$ data points are used as an input in the simulation, while $(p-v)_{lab}$ data points are used as target response in the simulations. Using the constitutive model with initial parameters the $(p-v)_{sim}$ are calculated using the simulation program. This initial response may not be the same as the target ($(p-v)_{lab}$). The absolute difference (AD) of the simulation response ($(p-v)_{sim}$) and the target ($(p-v)_{lab}$) are calculated.

The calculation of the total absolute difference (TAD) is illustrated in Figure 6.3. After the discretization process, the simulation response ($(p-v)_{sim}$) and target response ($(p-v)_{lab}$) have similar increment. The absolute difference (AD) value for each point is then

calculated. The summation of this AD value for the entire stress path will be termed as the total absolute difference (TAD). All relevant model parameters are altered within physically meaningful ranges to minimize the TAD value. This new set of parameters will be called 'iterated parameters' corresponding to one stress path. The iteration process (Figure 6.2) is then repeated for the rest of stress paths (stress paths (p-s) 1, 2, 3, ... n in Figure 6.1). At the end of the iteration process for all the stress paths, several sets of parameters corresponding to the each stress paths are obtained (Figure 6.1). These sets of parameters are then used to calculate the simulated response and the yield surface corresponding to each set of parameters.

The PEM criteria are then examined. The three (3) PEM criteria are as follows.

1. The simulated response and laboratory response for each of the stress path and response must be relatively similar in the magnitude and direction.
2. The variation of the parameters generated from different stress paths is relatively small.
3. The locations of the yield surface should not alter with various stress paths.

If these criteria cannot be met, the process is back in the selection or modification of the constitutive model (Figure 6.1). When these 3 criteria are sufficient, the PEM parameters can be generated from the average of the fitting parameters from various stress paths.

6.3.4 The Difference Between the PEM and 'Conventional' Curve Fitting

The primary principle difference between the PEM and the 'conventional' curve fitting exercise is in the criteria introduced in the PEM. The 'conventional' curve fitting only aims to generate the simulation response that is similar to the target, but the stress path

dependency of the constitutive model is not examined. The 'conventional' curve fitting process will only use the 1st PEM criterion that only considers each stress path independently, but does not consider the 2nd and 3rd PEM criteria that measure the dependency of the constitutive model parameters to the stress paths. The variation of constitutive model parameters due to different stress paths indicates that this constitutive model is not sufficient for a particular behaviour. It also indicates that parameters of the constitutive model generated are only sufficient within a limited range. The PEM algorithm uses the dependency of the constitutive model parameters to indicate the limitation of the constitutive model. Such information is useful to provide interpretation of the numerical modelling results and recommendations to improve or modify the existing constitutive model.

The possibility to apply various constitutive models for the same laboratory testing results creates the possibility to iterate not only constitutive model parameters, but also the constitutive model itself in the surface fitting process, when multiple constitutive models are included in the PEM algorithm (Figure 6.1).

The main objective of the PEM application in this chapter is not the 'estimation' of constitutive model parameters, but the 'evaluation' of the existing constitutive models (the BBM and the BGM). The variation of the constitutive model parameters generated from different stress paths will be used to identify the limitation of the existing constitutive model and to provide the recommendations improving the existing constitutive models.

6.4 Stress Paths

The discussion in this chapter includes three stress paths from the laboratory testing, which consist of: two stress paths from the triaxial testing with controlled suction and suction measurement (i.e., specimens JB104 and JB105, Blatz 2000); and a stress path from constant volume infiltration test (i.e., specimen GS041, Siemens 2006). The plot of JB104 and JB105 stress path in p - s space are depicted in Figure 6.4, the stress path of specimen GS041 is shown in Figure 6.10a.

All of the three specimens (JB104, JB105, and GS041) are of the bentonite sand buffer (BSB) material, which is 50:50 (mixture by dry mass) of well graded silica sand and Na-bentonite. They all have an initial 'as-compacted' suction of 3 to 4 MPa. Careful sampling preparation procedures were also followed for all the specimens to achieve identical as-compacted conditions. The Avonlea bentonite was used to prepare the specimens JB104 and JB105 and the Wyoming bentonite was used to prepare the specimen GS041. Anderson et al. (2002) concluded that the comparison of the two types of bentonite (i.e., Avonlea and Wyoming) is reasonable within experimental accuracy.

Specimens JB104 and JB105 followed stress paths a-b-c-d-e and a-b-c-f-g respectively in the p '- s space (Figure 6.4). These specimens were loaded isotropically ($q=0$) until yielding was observed, indicating that they had exceeded the loading collapse (LC) curve of the BBM or the LY-line of the BGM. Figure 6.4 showed that increasing mean stress p' was accompanied by a decrease in suction. The results were consistent with those reported by Tang et al. (2002). After yielding occurred, these specimens were unloaded to achieve an overconsolidation ratio of approximately 2.0 (path b-c in Figure

6.4). These specimens were then dried while still in the triaxial cell to a target suction value using a vapour circulation system (Blatz and Graham 2003) and the mean stress (p') was constant. These resulted in the suction increase as shown by path c-d for specimen JB104 and path c-f for specimen JB105 in Figure 6.4. Once equilibrium was achieved, an isotropic loading was applied to the specimens and the volume and suction were measured (paths d-e and f-g in Figure 6.4).

Specimen GS041 was subjected to constant volume infiltration in the triaxial cell (Siemens 2006). The stress path f-g of the specimen GS041 is shown in Figure 6.10a. An isotropic loading of 0.5 MPa was initially applied in this specimen. The specimen was then given access to water (wetting) under controlled constant volume boundary condition until equilibrium condition. At the equilibrium condition, the volume of water added to the specimen, the suction, mean stress, and volume were constant. The constant volume boundary condition was achieved by an automated cell pressure controlled.

Three comparisons are considered in the discussion:

1. Comparison of specimens JB104 and JB105 (Figure 6.4).

Specimens JB104 and JB105 follow the same direction of stress paths, but they have different magnitude. Comparisons of these two specimens (JB104 and JB105) allow the evaluation of the ability of constitutive model to simulate two stress paths that have the similar direction, but different magnitude. The suction changes of both specimens are relatively small.

2. Comparison of specimens JB104 and GS041 (Figure 6.10a).

Specimens JB104 and GS041 are within relatively similar magnitude of stress path, but they have different direction. Specimen JB104 experienced loading-unloading-loading process with a relatively small change in suction. Due to the infiltration process in the specimen GS041, suction changes of specimen GS041 is much greater than specimen JB104. The comparison of these two specimens (JB104 and GS041) allows comparison of two stress paths within the similar range of magnitude, but of different direction.

3. Comparison of the simulation of the specimen GS041 using the BBM, the BGM, and FLAC2D.

FLAC2D with 2-phase flow option is used to simulate specimen GS041 which experienced constant volume infiltration test. The purpose of this comparison is to evaluate the role of the hydraulic constitutive model in the simulation of specimen GS041.

6.5 Discussion

6.5.1 Specimens JB104 and JB105 (After Priyanto et al. 2005)

6.5.1.1 Laboratory Results versus Simulation Response (Criteria 1)

The simulation responses using the BBM and the BGM to simulate specimens JB104 and JB105 are illustrated in Figure 6.5. Simulation responses of both specimens using the BGM are marginally closer to the laboratory testing results than those using the BBM. However the directions of the simulation responses using the BGM are slightly opposite to the laboratory testing results along the stress paths b-c and f-g for specimen JB105 (Figure 6.5b). The suction increase results in volume decrease, while the decrease in mean stress (p') results in volume increase. The volume changes due to

the changes of mean stress (p') and suction (s) are controlled by parameters κ and κ_s respectively. Table 6.1 indicates that the iterated parameter κ of the BGM for specimen JB105 is less than that for specimen JB104, while parameter κ_s is greater for specimen JB105 than that for specimen JB104. Consequently, total volume change for specimen JB105 results in a slight volume decrease (paths b-c and f-g due to the BGM in Figure 6.5b).

The BBM created a coupling of the LC-line with the coefficients of compressibility. This coupling has caused the simulation response due to the BBM cannot be closer to the laboratory response after iteration process (Figure 6.5). Considering that the BBM was developed for kaolin clay (e.g., low to moderate plasticity clay) (Alonso et al. 1990), the coupling of the yield line (LC-line) with the coefficients of compressibility in the BBM may not be sufficient for the high plastic clay.

The simulation response due to the BBM for specimen JB104 is closer than that for specimen JB105 (Figure 6.5). The volume change due to suction of specimen JB104 has smaller effect on the total volume change than that of specimen JB105. The comparison of the simulation response using the BBM for specimens JB104 and JB105 indicates that the BBM is better for the stress paths with smaller suction changes (Figure 6.5).

6.5.1.2 Parameters Variation (Criteria 2)

Figure 6.5 shows that simulation using the BGM is better than that of the BBM. The variations of the iterated parameters for both models (the BBM and the BGM) in Table 6.1 are relatively small. However, the variation of the of compressibility coefficients (κ , κ_s , and λ) of the BGM differs more notably between the specimens JB104 and JB105.

Both of the constitutive models (the BBM and the BGM) consider constant parameter (κ) for different suction. The variations of these coefficients indicates the dependency of the coefficient of compressibility on suction and mean stress. The possible modifications of the existing constitutive models is to create the coefficient of compressibility (κ) as a function of suction (s).

6.5.1.3 Yield Line (Criteria 3)

The last PEM criterion is to evaluate the location and shape of the predicted yield surface. The plots of the BBM's LC-curve and the BGM's LY-line are shown with the stress paths of JB104 and JB105 in Figure 6.6. Both the LY-line and LC-curve are relatively similar. The non-linearity of the LC-curve is not significant within the suction (s) range of 0-12MPa, the linear LY-line is sufficient to describe the yield surface of the material.

The plots of LC-curve and LY-curve with yield points interpreted from the laboratory testing are shown in Figures 6.7 and 6.8. The laboratory yield points in Figures 6.7 and 6.8 are taken from Anderson (2003) and Blatz (2000). Although they are from different types of bentonite (i.e., Avonlea (Blatz 2000) and Wyoming (Anderson 2002)), the assumption that the specimens have relatively similar material properties can still be made (Anderson et al. 2002), so the plot of these data points in the same p' - s space can be made. Figure 6.7 shows that the LC-curve and LY-curve show good agreement with the laboratory yield points.

However if a wider range of suction is examined (0-120 MPa) (Figure 6.8), the LC-curve is more suitable than the LY-curve to determine the yield points. It indicates that the

coupling of the LC-curve with the coefficient of compressibility allows extrapolation of the yield line, but it causes the simulation response of specimen JB105 cannot be closer to the laboratory test results (Figure 6.5b). The LC-line in Figure 6.8 shows that the application of the constitutive model can be extended beyond the magnitude of laboratory testing results.

The LY-line of the BGM is only sufficient to represent the yield line up to 12 MPa. The LY-line of the BGM overestimates the yield surface for suction greater than 12 MPa, which indicates that if the constitutive model is calibrated for low suction, it may not be suitable for higher suction. This agrees with Blatz et al. (2005) who showed that a threshold exist in the BSB material at suction of approximately 30 MPa. The mechanical behaviour of the BSB is clay dominated for suction less than 30 MPa, while it is sand dominated for suction greater than 30 MPa. The explanation is that as suction increases, the clay structure shrinks which brings the sand particles in contact.

6.5.1.4 Modifications and Limitations of Constitutive Models

Modifications

Possible modification of the LY-line of the BGM is shown in Figure 6.9. The linear LY-line of the BGM can be changed into a bilinear LY-line. Two additional parameters are required to define this bi-linear LY-lines (e.g., LY₁-line and LY₂-line). The LY₁-line is defined by parameters p_0^* and the slope r_1 . The parameter p_0^* is the preconsolidation pressure at saturated conditions and parameter r_1 is the slope of the LY₁-line. Two additional parameters are required to define LY₂-line, which are parameters s_1 and r_2 . Parameter s_1 defines the maximum suction where the line LY₁ is still suitable to describe

the yield surface and parameter r_2 is the slope of the LY_2 line. This modifications can prevent the BGM from overestimating the yield surface at higher suction value.

Limitations

The parameters presented in Table 6.1 were only limited for suction less than 12 MPa with relatively small suction changes, due to the limitation of the constitutive models (e.g., the BBM and the BGM). The application of these parameters for greater range magnitude and type of stress paths will require further analysis. Considering the limitation of the constitutive models and the number of the specimens used in the analysis, the PEM parameters for various stress paths are not calculated.

6.5.2 Simulation of the Specimen GS041 (After Priyanto et al. 2006)

Two types of simulation can be used in the iteration process for a single stress path as shown in Figure 6.2, which are:

- 1) stress-volume (s-v) analysis; and
- 2) volume-stress (v-s) analysis.

The difference between the two analyses are in the input and output in the simulation process and the target in the iteration process. The s-v analysis is shown in Figure 6.2, where the input in the simulation process is the laboratory testing stress path $(p-s)_{lab}$, while the target in the iteration process is the laboratory response $(p-v)_{lab}$. The v-s analysis is the opposite of the s-v analysis, where the laboratory response $(p-v)_{lab}$ is used as an input in the simulation and the stress path from the laboratory testing $(p-s)_{lab}$ is used as the target of the iteration.

6.5.2.1 Stress-Volume (s-v) Analysis

Comparison of the stress path of specimen GS041 and specimen JB104 in p-s space is illustrated in Figure 6.10a. The parameters used in this analysis are summarized in Table 6.2. Both specimens GS041 and JB104 are within relatively similar suction range, but they are of different type. The parameters BBM and the BGM for the specimen JB104 in Table 6.1 are used in the s-v analysis for specimen GS041 to evaluate if the constitutive models are able to simulate different type of stress path within relatively similar suction range. The specific volume responses for both constitutive models are illustrated in Figure 6.10b as BBM1 and BGM1. The plot of yield lines generated from these parameters is also illustrated in Figure 6.10a. Based on these analyses, the specimen GS041 experiences yield such that a notable transition exists in the specific volume v for both constitutive models (BBM1 and BGM1 in Figure 6.10b). It is not the case of the laboratory test results of specimen GS041, which the yielding is not indicated in the laboratory test result.

Considering that the yielding is not reported in the laboratory test, the specimen GS041 is assumed within elastic range at all time in BBM2 and BGM2 (Figure 6.10b). Assuming that parameters p_o and p_o^* equal to 1 MPa results in the shifting of the yield line of the BBM and the BGM, so the specimen GS041 is within elastic range at all time. The s-v analysis responses for the BBM and the BGM are illustrated in Figure 6.10b. It indicates that constant volume conditions cannot be obtained by either constitutive models. The parameters of the BBM and the BGM that were suitable for specimen JB104 cannot be used to simulate constant volume infiltration test in specimen GS041.

6.5.2.2 Volume-Stress (v-s) Analysis

The parameters of the BBM2 and the BGM2 are used in the v-s analysis. The result of this analysis is shown in Figure 6.11 as BBM3 and BGM3 in p-s space. These results show that both constitutive models highly overestimate the mean stress (p) compared with the laboratory results (Figure 6.11).

The differences of the BBM3 and BGM3 with the laboratory results are minimized by iteration of parameters κ and κ_s , the new set of parameters are summarized in Table 6.2 as BBM-BGM4. The plot of the BBM-BGM4 is illustrated in Figure 6.11. The results are the same for both constitutive models (the BBM and the BGM), because the coefficients of compressibility (κ and κ_s) are constant within the elastic range.

Although the BBM-BGM4 are relatively close to the laboratory response (Figure 6.11), the limitation of both constitutive models in capturing the behaviour of specimen GS041 is still indicated. Comparison of the parameters of the JB104 and the BBM-BGM4 in Table 6.2 indicates that the dependency of parameters of both constitutive models to simulate two different specimens (JB104 and GS041) that have similar range of stress path magnitude, but of different type. Coefficients of compressibility (κ and κ_s) for specimen GS041 are much greater than those for specimen JB104. The different shape of BBM-BGM4 compared with the laboratory results is also indicated in Figure 6.11.

6.5.2.3 Modifications of Constitutive Models

Modification of both constitutive models (the BBM and the BGM) to capture this behaviour can be made by introducing a parameter κ_{rat} , which is the ratio of coefficients of compressibility due to the change in mean stress to that of suction (κ/κ_s) as shown in

Table 6.2. The parameter κ_{rat} increases with the swelling induced pressure. This value is greater for stress paths involving wetting (e.g., specimen GS041) than for stress paths involving drying (e.g., specimen JB104). The parameter κ_{rat} can be used as an additional parameter to modify the existing constitutive models to more accurately simulate the behaviour of specimen GS041. Further investigation of the rationale for this parameter is still required.

6.5.2.4 Modelling Specimen GS041 using FLAC2D

Finite difference analysis using FLAC2D (Itasca 2001) has been used to model the constant volume infiltration test of specimen GS041. Two-phase flow with hydraulic-mechanical interaction is utilized in the analysis to incorporate the water retention curve (WRC) and permeability function. The main objective of this analysis is to investigate the role of hydraulic constitutive model. The WRC and permeability function are defined using the van Genuchten (1980) model with parameters $a=0.20$, $b=0.50$, $c=0.50$, $P_o=2.0$ MPa, and residual degree of saturation $S_r = 0.01$. These parameters are obtained from fitting laboratory results from Blatz (2000). The saturated hydraulic conductivity (k_h) of 5×10^{-12} m/s (Graham et al. 1997) as used by Thomas et al. (2003) to model the BSB material is used in the analysis. The mechanical behaviour is described by means of a linear-elastic model with bulk modulus (K) of 42 MPa and shear modulus (G) of 34 MPa (Graham et al. 1997). The input and output of the analysis are shown in Figure 6.12.

The mechanical and hydraulic boundary conditions, initial condition, and the grid used in the FLAC analysis are illustrated in Figure 6.12a. The model uses 5x20 axisymmetric grids (Figure 6.12a). The initial mean stress of 500 kPa and degree of saturation of 82.5% are applied as initial conditions (Figure 6.12a). The constant porosity (n) of 0.38

is used in the FLAC analysis (Itasca 2001) taken from the as-compacted laboratory measurement (Siemens 2006). Fixed displacement in the x and y directions are applied along the boundaries (Figure 6.12a). Once the model is started, the pore water pressure of 200 kPa is applied along the perimeter boundary, while impermeable boundary conditions are applied at the top, bottom, and center line (Figure 6.12a).

The suction, volume of water added to the specimen, and total mean stress from FLAC simulation compared with the laboratory test results are illustrated in Figures 6.12b to 6.12d. The FLAC analysis underestimates the volume of water added to the specimen (Figure 6.12c), but it overestimates the mean stress (Figure 6.12d). The suction from FLAC analysis underestimates the laboratory results after 3 days (Figure 6.12b). Figures 6.12b to 6.12d indicate that FLAC analysis has reached equilibrium after 4 days, which is much faster than that of the laboratory test (approximately 12 days). Improvement in the FLAC analysis is discussed in Chapters 7 to 9.

Although a linear-elastic model is used in the FLAC analysis, the plot of the stress paths of the FLAC analysis compared with the laboratory test indicates relatively similar shape (Figure 6.11). Compared with previous analyses in Tables 6.1 and 6.2 that consider the mechanical constitutive model independently, the FLAC analysis using coupled hydraulic-mechanical constitutive model has demonstrated that considerable improvement in the magnitude and shape of the stress path (Figure 6.12). It demonstrates that the hydraulic constitutive models (WRC and permeability laws) are very important to simulate the behaviour of the infiltration process such as in specimen GS041.

6.6 Concluding Remarks

This research proposes a method called the 'Parameter Evaluation Method' (PEM) that has an ability to estimate the parameters of constitutive models and to evaluate the performance of constitutive models. This algorithm has an ability to estimate the constitutive model parameters and to reduce the difficulty of calibrations of constitutive models with many parameters, so that the numbers of the parameters should not be a measure to define the complexity of constitutive models. The principal that 'when constitutive models are adequate to simulate the general behaviour of a material, their parameters should not change due to various input' is used to generate the criteria to evaluate the constitutive models.

In the case of mechanical elasto-plastic constitutive models, the criteria that should be used to evaluate their performance are:

- 1) The simulated response and laboratory response for each of the stress path and response must be relatively similar in the magnitude and direction.
- 2) The variation of the parameters generated from different stress paths is relatively small.
- 3) The locations of the yield surface should not alter with various stress paths.

This PEM algorithm is used to simulate the mechanical behaviour of unsaturated swelling clay using two elasto-plastic mechanical constitutive models (e.g. the BBM and the BGM). The results indicate some limitations of both constitutive models and modifications of the BGM have been made based on this evaluation.

6.7 Justification of Mechanical Constitutive Model and Its Parameters

The discussion in this chapter is used to justify the selection of the mechanical constitutive model and its parameters used in the analysis in Chapters 7 and 8.

1. Selection of the Mechanical Constitutive Model for Application in Chapters 7 and 8.

Considering the better simulation response of the BGM compared with the BBM in Figure 6.5, the BGM is preferred in the simulation of the unsaturated swelling clay in Chapters 7 and 8 in which the small suction changes is considered. Chapters 7 and 8 describes the modelling of the small scale infiltration test and large scale isothermal test respectively. Considering the limitation fo the BBM to simulate the behaviour of unsaturated swelling clay, the BGM is preferred as the starting point of the development of the constitutive model for unsaturated swelling clay due to its simplicity. The hydraulic constitutive models are very significant to simulate the infiltration process in Chapters 7 and 8 as shown by FLAC analysis.

Selection of the Parameters

Chapter 3 has discussed that the difference of the stress state variable used in the implementation of the BGM results in the modification of the parameter of the constitutive models. This modification is applied to the BGM parameters related to the yield surface for specimen JB104 (Table 6.1) and applied in the analysis in Chapters 7 and 8. The coefficient of compressibility within the elastic range (κ and κ_s) in Chapters 7 and 8 are calculated using the fitting process of specimen GS041 (BBM-BGM4 in Figure 6.11) after the stress state variable modification (Chapter 3). The specimens JB104 and GS041 are selected because: they are within same magnitude as the application in

Chapters 7 and 8; and the applications in Chapters 7 and 8 are within small suction changes.

6.8 Suggestions of Future Research

The suggestions of Future Research include: creating computer software to generate parameters of rigorous constitutive model; coupling hydro-mechanical constitutive models in the PEM; and 'Parameter Generator Concept'.

1. Creating computer software to generate parameters of rigorous constitutive model

The 3 PEM criteria have been assessed qualitatively in this chapter by comparison of the plots of the simulation response and laboratory response. The quantitative assessment of these 3 PEM criteria can be made by calculation of the Total Absolute Difference (TAD) value and standard deviation of the iterated parameters. The quantitative assessment of the PEM criteria can be included in the computer algorithm to create a computer software to generate the parameters of a rigorous constitutive model.

2. Coupling hydro-mechanical constitutive models in the PEM.

The simulation program used to implement the PEM algorithm only considers the mechanical constitutive model independently. The infiltration process in unsaturated swelling clay includes both fluid and mechanical behaviour. Considering mechanical constitutive models independently is not adequate to simulate this behaviour. The recommendation is made to incorporate the hydraulic-mechanical constitutive models in the simulation program to implement the PEM.

3. *Parameter Generator Concept.*

Rigorous constitutive models require more laboratory results to calibrate the necessary parameters that can be expensive and time consuming. At present much of focus of numerical modelling in geotechnical engineering is intended to understand the physical behaviour of the engineered system. The 'parameter generator concept' in Figure 6.13 extend the application of numerical modelling to estimate constitutive model parameters including both mechanical and hydraulic aspects of behaviour.

The triaxial testing with controlled and measured suction (Blatz 2000, Siemens 2006) the ability to measure the history of: stress variables (mean stress p , deviatoric stress q , and suction s); strains (inferred in volume strain ε_v and shear strain ε_s), as well as the volume of water added into the specimen. The choice of stress paths can then be directed to resemble the expected behaviour of the engineered structure (Figure 6.13).

Similarly, the boundary and initial conditions, stress paths, and initial parameters are predetermined in the numerical model of this laboratory specimen also produces all the histories of the stress, strain, and volume of water added to the specimen. Using the initial parameters, numerical responses that may not be close to the laboratory responses can be calculated. Minimizing the difference between the history of numerical and laboratory results (stress versus time, strain versus time, and water added to specimen versus time in Figure 6.13) will produce the PEM parameters of constitutive model simultaneously. These parameters can then be applied for numerical modelling of engineered structures. Since the numerical model incorporates both mechanical and hydraulic constitutive models, it will results in both parameters of the mechanical and hydraulic constitutive models (WRC and permeability laws). Therefore, when this type of test is used together with the PEM algorithm, it can reduce the necessity for independent

permeability testing that is very difficult to have higher accuracy (variations over an order of magnitude). The dependency of the permeability coefficient of the stress-state variables can also indirectly measured using this method. This concept is suggested as future research.

Table 6.1 Parameters used in the numerical simulation stress paths #1
(after Priyanto et al. 2005)

Blatz and Graham Model (BGM) (2003)			BBM (Alonso et al. 1990)		
	JB-104	JB-105		JB-104	JB-105
Compressibility Coefficient					
λ	0.1092	0.0946	$\lambda(0)$	0.1276	0.1136
κ	0.0212	0.0176	κ	0.0161	0.0107
κ_s	0.0669	0.0820	κ_s	0.0179	0.0171
LY-Line			LC-curve		
p_o (MPa)	0.50	0.50	p_o^* (MPa)	0.50	0.50
r	0.225	0.225	p^c (MPa)	0.0140	0.0154
			R	0.6839	0.6832
			β (MPa ⁻¹)	0.2310	0.2324

Table 6.2 Parameters used in the numerical simulation stress paths #2
(after Priyanto et al. 2006)

Blatz and Graham Model (BGM) (2003)				BBM (Alonso et al. 1990)			
Parameters	JB104	BGM2	BGM4	Parameters	JB104	BBM2	BBM4
	BGM1	BGM3			BBM1	BBM3	
Compressibility Coefficient							
λ	0.11	0.11	n/a	$\lambda(0)$	0.13	0.13	n/a
κ	0.021	0.021	0.010	κ	0.016	0.012	0.010
κ_s	0.067	0.067	0.052	κ_s	0.018	0.018	0.052
LY-Line				LC-curve			
p_o (MPa)	0.50	1.00	n/a	p_o^* (MPa)	0.50	1.00	n/a
r	0.23	0.23	n/a	p^c (MPa)	0.014	0.014	n/a
				r	0.70	0.70	n/a
				β (MPa ⁻¹)	0.23	0.23	n/a
$\kappa_{rat} = \kappa / \kappa_s$	0.31	0.31	0.19		0.67	0.67	0.19

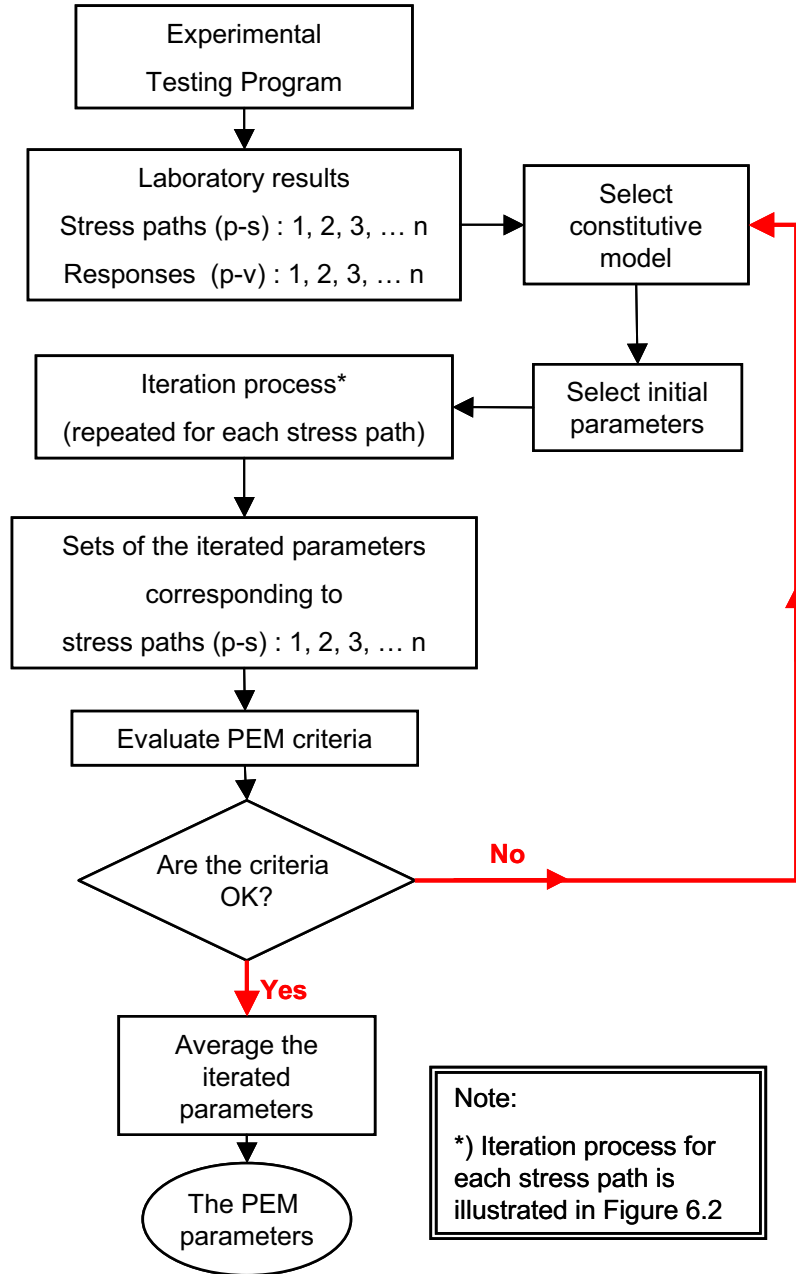


Figure 6.1 Parameter Evaluation Method (PEM)

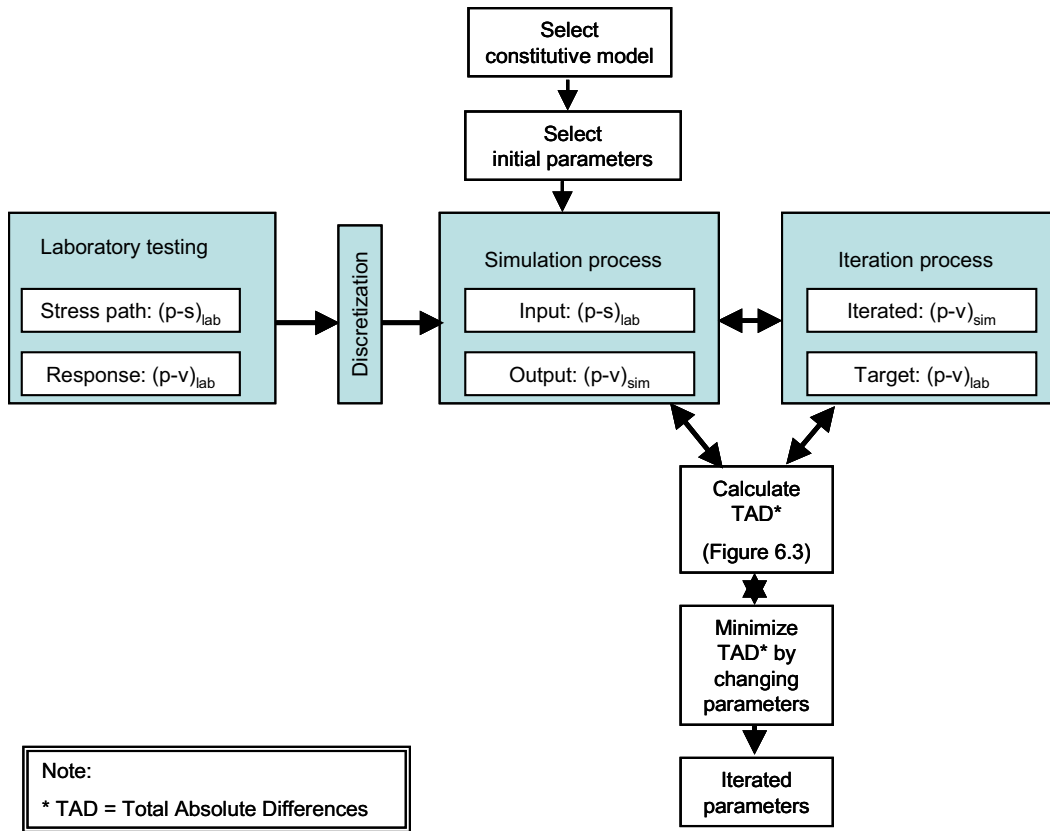


Figure 6.2 Iteration Process for a Single Stress Path

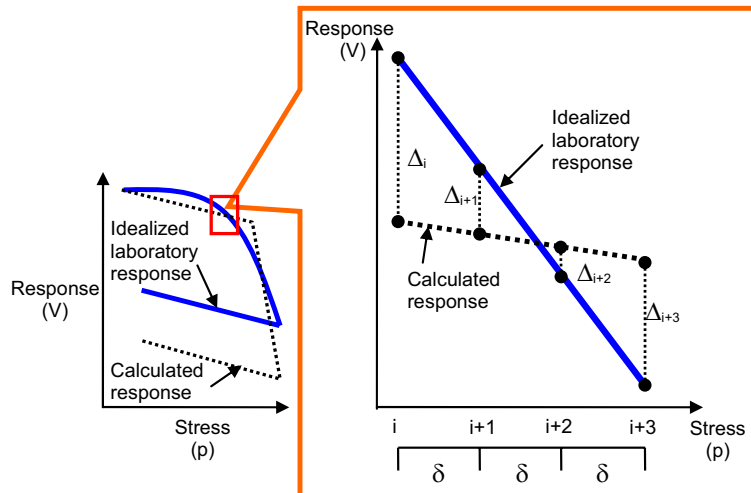


Figure 6.3 The Calculation of Total Absolute Difference (TAD) (after Priyanto et al. 2004)

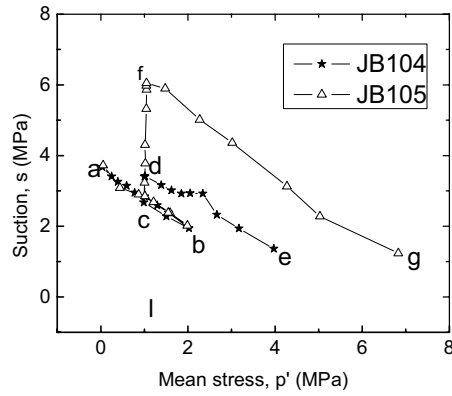


Figure 6.4 Stress paths in p' - s stress space (after Blatz 2000)

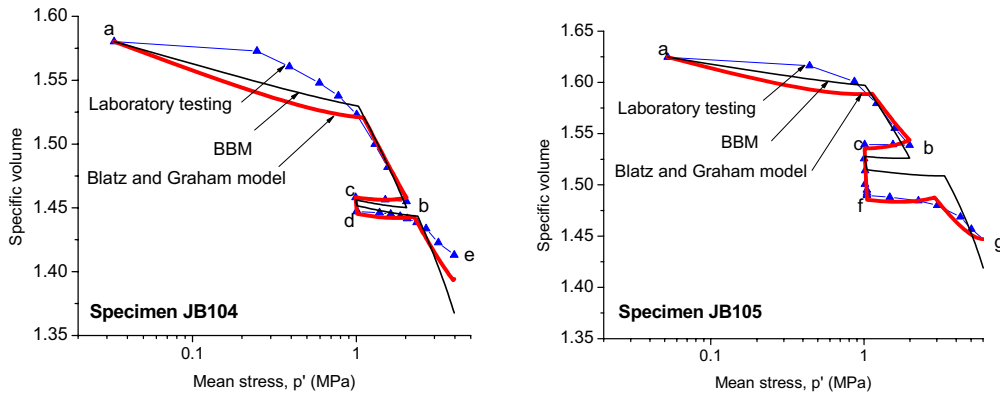


Figure 6.5 Experimental results and simulation responses using the two models in V - $\ln(p')$ space (after Priyanto et al. 2005)

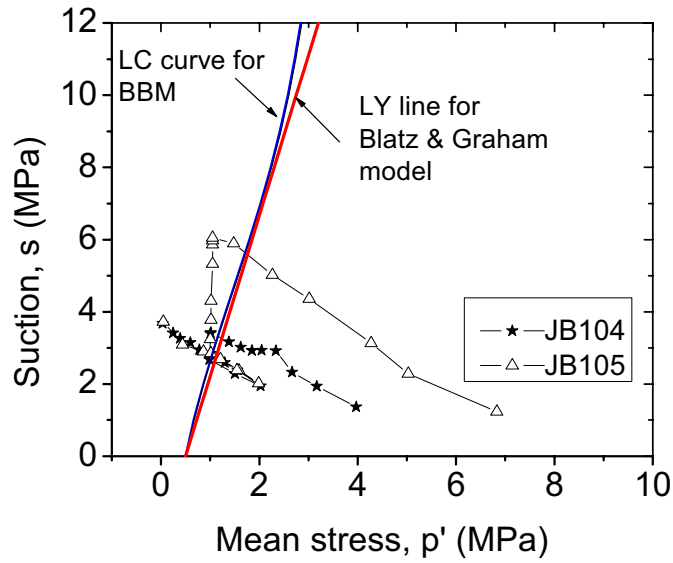


Figure 6.6 Experimental stress paths and LC-curve of the BBM and the BGM (after Priyanto et al. 2005)

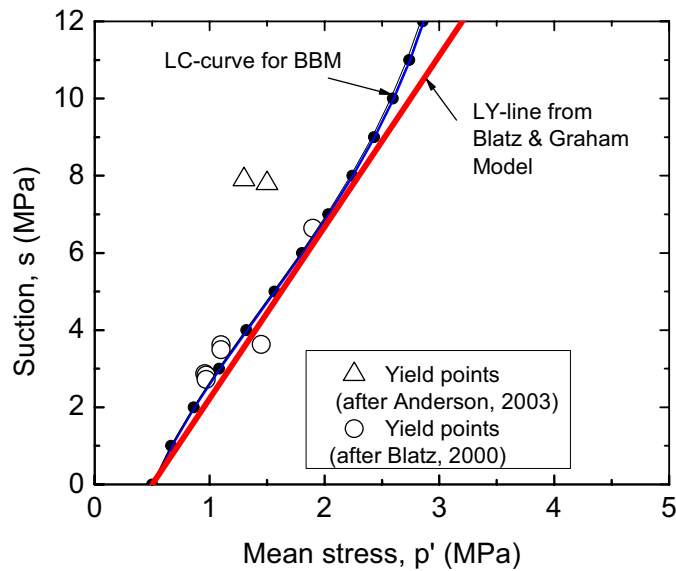


Figure 6.7 Experimental yield point and LC-curve calculated with PEM parameters for the BBM and the BGM for suction of 0 to 12MPa (after Priyanto et al. 2005)

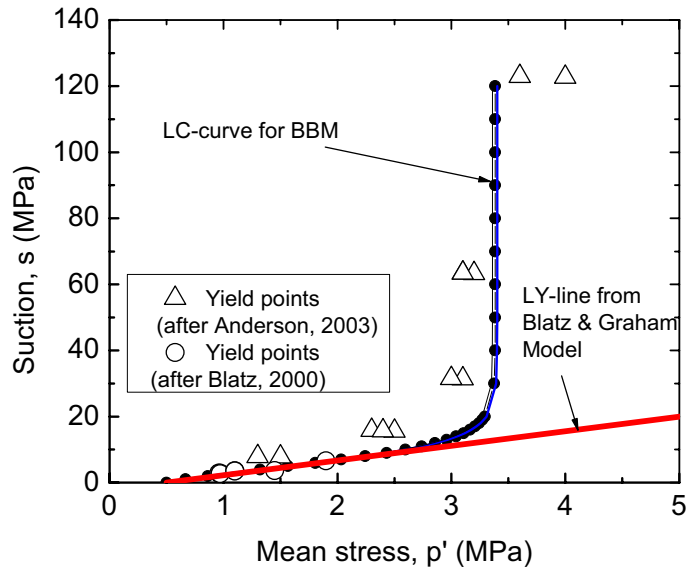


Figure 6.8 Experimental yield point and LC curve calculated with PEM parameters for the BBM and the BGM for suction of 0 to 120MPa (after Priyanto et al. 2005)

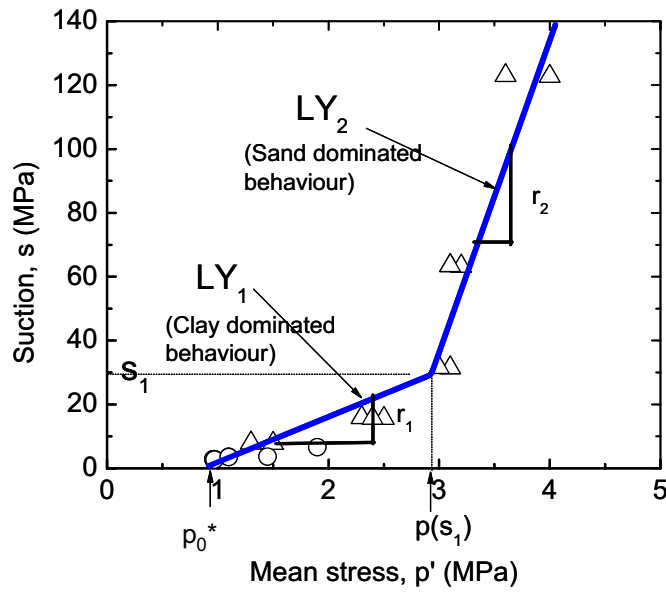


Figure 6.9 Possible modification of LC-line for the BGM (after Priyanto et al. 2005)

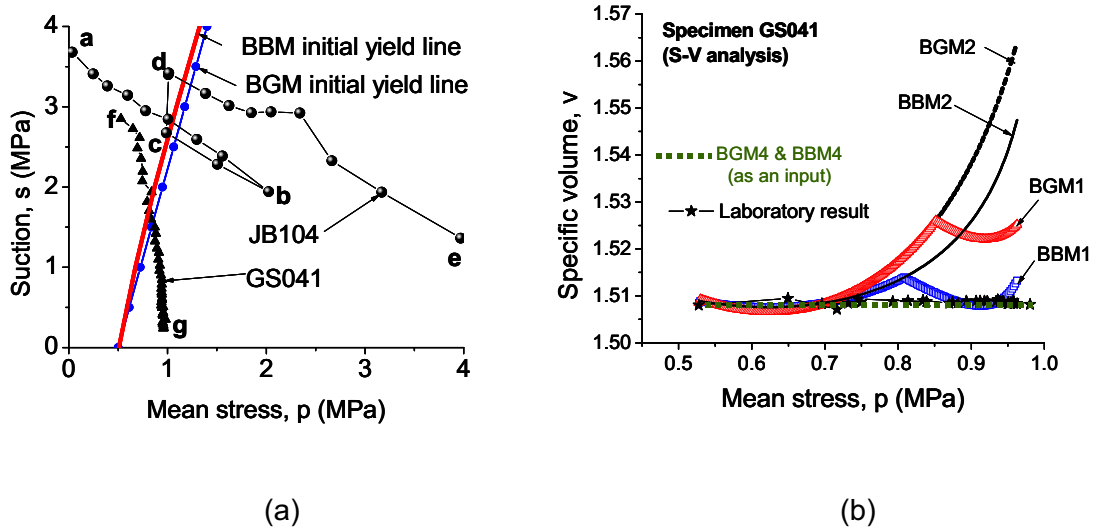


Figure 6.10 (a) Laboratory stress paths of specimens JB104 and GS041 plotted in p-s space with the initial yield lines; (b). Results of s-v analysis for specimen GS041 plotted in v-p space with the laboratory test results (after Priyanto et al. 2006)

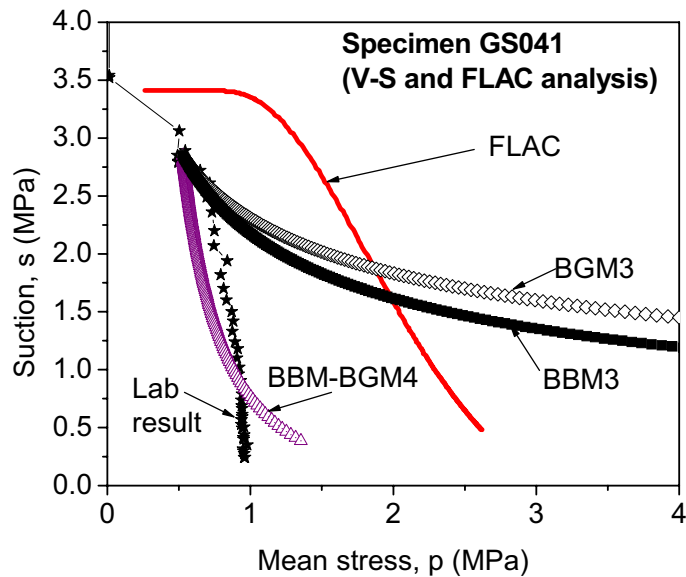


Figure 6.11 Stress paths calculated from the v-s analysis and stress path generated from FLAC (after Priyanto et al. 2006)

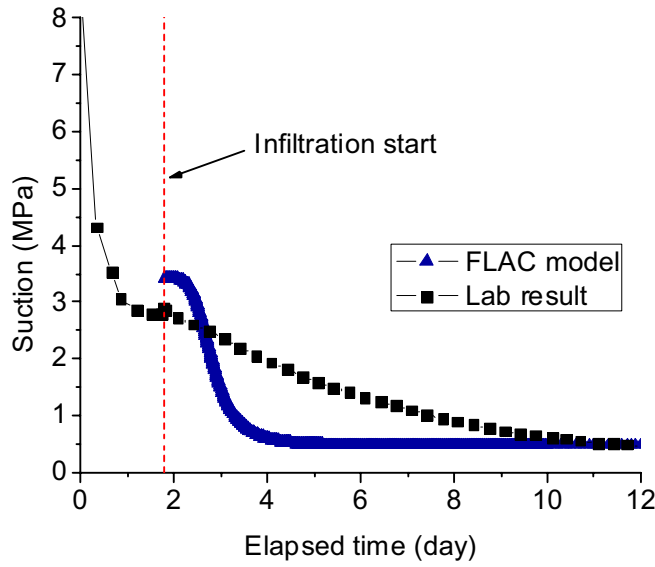
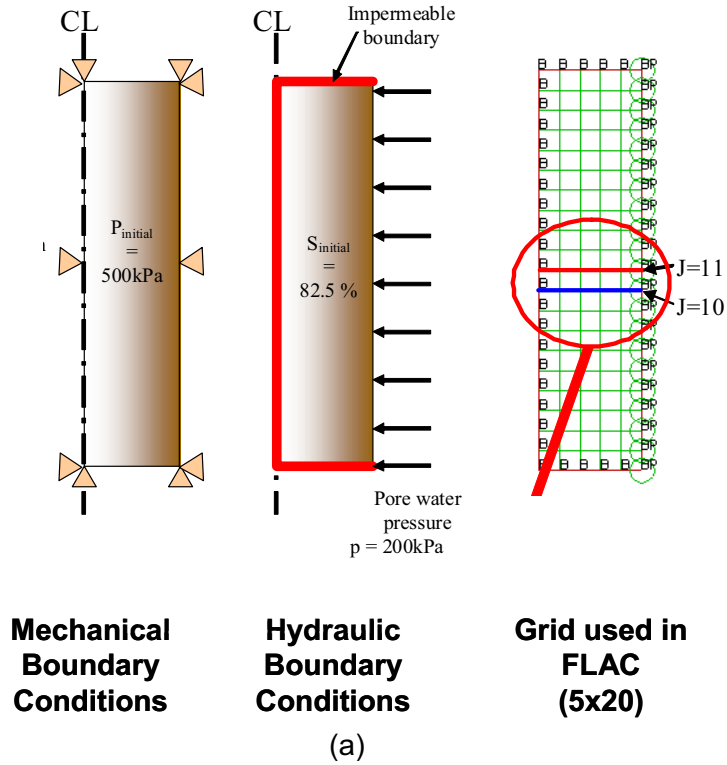
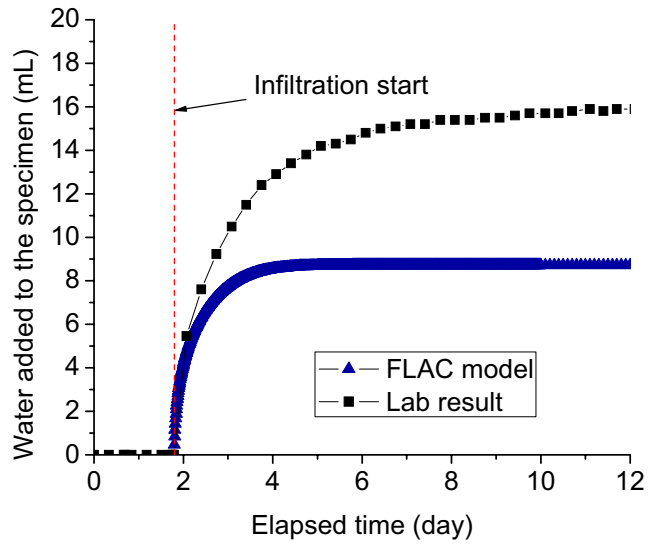
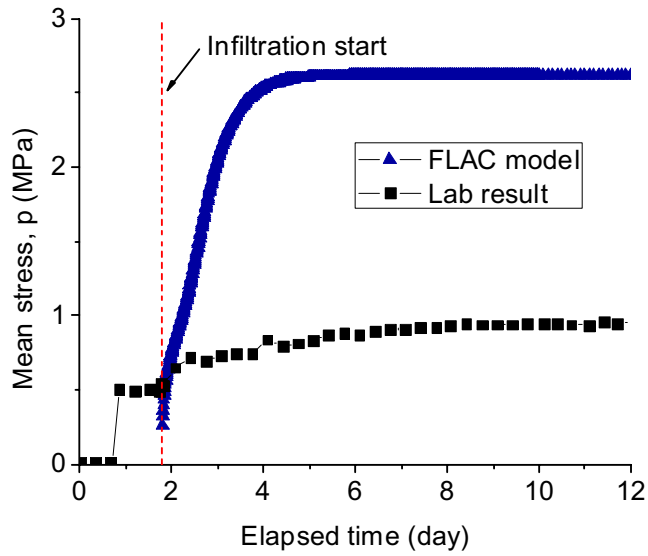


Figure 6.12 (a) Mechanical and hydraulic initial and boundary conditions; (b) Total suction; (c) Water added to the specimen; and (d) Total mean stress vs. time (after Priyanto et al. 2006)



(c)



(d)

Figure 6.12.(c) Water added to the specimen; (d) Total mean stress vs. time (after Priyanto et al. 2006) (continued)

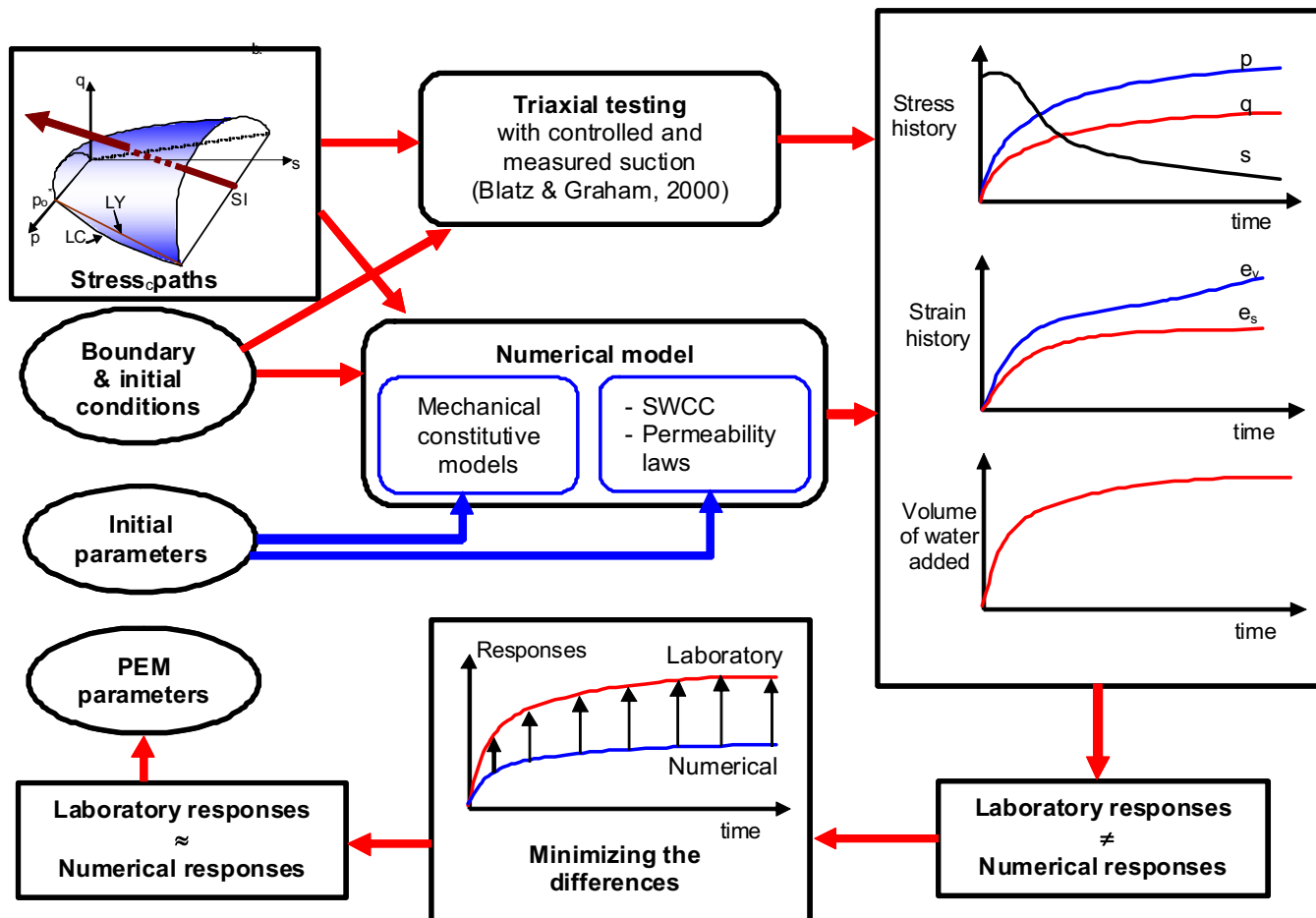


Figure 6.13 'Parameter generator concept' to determine mechanical and hydraulic constitutive models of unsaturated clay

PART 5:

APPLICATIONS OF CONSTITUTIVE MODELS

CHAPTER 7

MODELLING INFILTRATION TEST IN TRIAXIAL CELL

7.1 Introduction

Examination of the hydraulic-mechanical (H-M) behaviour of compacted unsaturated swelling clay under various boundary conditions was undertaken at the University of Manitoba using the triaxial apparatus with controlled suction and suction measurements (Siemens 2006). Siemens and Blatz (2006) have discussed the instrumentation and the results of these tests in detail.

Siemens (2006) presented a capillary tube model to simulate the process occurring in the system, but the application of this capillary tube model is still limited. The parameters used in this modelling cannot be applied directly in the numerical modelling using the finite element (FE) or finite difference (FD) analysis, because the basic formulations used in FE/FD methods is different from the capillary tube formulations. Application of the models in FE or FD analyses is required to simulate engineered systems that incorporate boundary value problems and various material interactions.

This chapter presents numerical modelling of small-scale infiltration tests (Siemens 2006) with specified boundary conditions using FLAC (Itasca 2001). The two-phase fluid flow option in FLAC is used to model the H-M processes occurring in the system.

The objective of this chapter is to examine the performance of the mechanical and hydraulic constitutive models to model the H-M behaviour during infiltration tests on unsaturated swelling clay. Two mechanical constitutive models the linear elastic model (LE) and the Blatz and Graham (2003) Model (BGM) are used to define the mechanical behaviour of unsaturated swelling clay. Two types of hydraulic constitutive models (i.e., van Genuchten (1980) (VG) and porosity-dependent permeability (kwn) models) are used in the analysis. Two types of boundary conditions used in the infiltration experiments (Siemens 2006) (e.g., constant volume (CV) and constant mean stress (CMS)) are simulated using several combinations of hydraulic and mechanical constitutive models.

7.2 General Overview of Laboratory Tests

7.2.1 Bentonite-Sand Buffer Material

The material used in this study is a 50:50 mixture (by dry mass) of sodium bentonite and silica sand. This material, called the bentonite-sand buffer (BSB) material, is one of the materials proposed in the Engineered Barrier System (EBS) in the deep geologic repository (DGR) concept examined by Atomic Energy of Canada Limited (AECL) (Russell and Simmons 2003, Maak and Simmons 2005). The bentonite component is highly plastic bentonite clay, while the silica sand is a well-graded material. All specimens are prepared to a target initial gravimetric water content (w) of 19.4% and dry

density (ρ_{dry}) of 1.67 Mg/m^3 to achieve a degree of water saturation (S_w) of 85% (Siemens 2006).

7.2.2 Triaxial Apparatus with Controlled Suction and Suction Measurement

Blatz and Graham (2000) introduced a triaxial cell with controlled suction and suction measurement designed to test soil specimens at high suction. Siemens (2006) developed a modification so that the application of various types of boundary conditions can be made using this triaxial apparatus. The evolution of suction, water added to the specimens, radial, axial, and volume strains are measured during the tests. The measurements of gravimetric water contents (w) and dry density (ρ_{dry}) within three radial distances are made immediately at the end-of the test (Siemens 2006).

Various types of boundary conditions are provided in the test including: constant volume test (CV); constant mean stress (CMS); constant mean stress-drained (CMS-d); vertical flow (VF) tests; and constant stiffness tests (CS25 and CS75) (Siemens 2006). Two of the boundary conditions (CV and CMS) are simulated using numerical models in this chapter. Details regarding specimen preparation and laboratory tests are available in the original publications (Siemens 2006).

7.2.3 Definition of the Stages and Conditions

Figure 7.2 illustrates the measurement of the volume of water added to the specimen in the infiltration test using triaxial cell with controlled suction and suction measurement by Siemens (2006). This infiltration test can be divided into two stages: equilibration and infiltration stages. These two stages are divided by three conditions: as-compacted; pre-infiltration; and the end-of-test (EOT) conditions. At the equilibration stage, the

confining pressure increase cause the changes in volume strain, but no water is added to the system. Water is then added to the system during infiltration stage, confining pressure or volume strain are controlled and measured. The total suction are measured in both stages using psychrometer.

The numerical modelling in this chapter only models the second stage (infiltration stage), when the water is added to the system. Thus, the pre-infiltration condition of the test is used as the initial conditions of the numerical models.

The as-compacted, pre-infiltration, and the EOT conditions of the CV and CMS with confining pressure of 500 kPa are summarized in Tables 7.1 and 7.2. Calculations of volume-mass relationships and volume compositions in Tables 7.1 and 7.2 use the following assumptions:

1. There is no water added to the specimen during the pre-infiltration stage, so that the gravimetric water content (w) is constant during as-compacted and pre-infiltration conditions.
2. The soil solid is incompressible, so that the volume of solid is constant.
3. Specific gravity (G_s) is constant and it is taken as 2.7

If the soil solids are incompressible, the water added to the system is equal to the water added to the pores, so that the possible maximum water added to the specimens

($V_{w \max}^{\text{add}}$) is:

$$V_{w \max}^{\text{add}} = V_{\text{void}}^{\text{EOT}} - V_w^{\text{pre-inf}} \quad [7.1]$$

where

$V_{\text{void}}^{\text{EOT}}$ is volume of void at the end of the test;

$V_{\text{w}}^{\text{pre-inf}}$ is volume of water at the pre-infiltration stage.

7.3 Hydro-Mechanical Analysis using FLAC

7.3.1 Boundary Conditions

The specimen has a cylindrical shape with 50 mm diameter and 100 mm height. Two types of boundary conditions used in the analyses include: constant volume test (CV) and constant mean stress (CMS) (Figure 7.1). Using the symmetry, the CV and CMS are modelled using 5x5 finite difference grids.

There is a difference between the mechanical boundary conditions of numerical models and laboratory tests, especially in the constant volume (CV) tests. The numerical model used rigid boundary conditions around the perimeter, as well as the top and bottom of the specimen, while the laboratory tests adjusts the magnitude of the isotropic cell pressure to produce zero volume strain during infiltration process (Siemens 2006).

7.3.2 Mechanical Constitutive Models

The mechanical constitutive model used in the analysis includes the LE model and the BGM. The parameters used in the analysis are summarized in Tables 7.3 and 7.4. The linear elastic model parameters in Table 7.3 follows the laboratory measurement by Graham et al. (1997). The BGM parameters (Table 7.4) are calibrated based on the data from Blatz (2000), Anderson (2003), and Siemens (2006). The stress states

variables used in the implementation of the BGM in FLAC incorporate the degree of water saturation (S_w) as a variable as discussed in Chapter 3. The different stress states variables used in the implementation of the BGM in FLAC reflect in the different values of the parameters presented in Table 7.3 from the parameters in Chapter 6.

7.3.3 Hydraulic Constitutive Models

The hydraulic constitutive model used in the analyses is the van Genuchten (1980) (VG) model. The parameters and equations of the VG model are presented in Table 7.5. Table 7.6 summarizes the equations the porosity dependent permeability (kwn) model. The parameters used for this model are summarized in Table 7.7. These parameters are obtained from the curve fitting of laboratory test results presented in Chapter 4.

7.3.4 Summary

Two types of mechanical constitutive models and two types of hydraulic constitutive models presented previously are combined to model the infiltration process with two boundary conditions. The combinations of boundary conditions, mechanical constitutive models, and hydraulic constitutive models are summarized in Table 7.8

7.4 Comparison of the Numerical Model Results with Laboratory Measurements

The comparison of the numerical model results includes the following:

- The relationship of the volume of water added to the specimen; volume, radial, and axial strains; suction; and mean stress as a function of time.
- The volume-mass relationships at various locations of the specimen at the end of the test, which include: gravimetric water content (w), water degree of saturation (S_w), dry density (ρ_{dry}), and bulk density (ρ).

The numerical modelling results of the constant volume (CV) test using three H-M constitutive models are illustrated in Figures 7.3 to 7.8 and those of constant mean stress (CMS) test are illustrated in Figures 7.9 to 7.14. The results of post measurements of volume-mass relationship are illustrated in Figures 7.15 to 7.18.

7.5 Discussion

7.5.1 Constant Volume (CV) test

The volume of water added to the specimen as a function of time of the three constitutive models (LE, BGM, and BGM-kwn models) underestimates the laboratory measurements (Figure 7.3). The linear elastic (LE) model result shows that the volume of water added is more than the BGM and BGM-kwn models (Figure 7.3). The difference in the numerical modelling and the laboratory measurements may be due to the limitation of the model that will be discussed later. The volume strain (Figure 7.4), radial strain (Figure 7.5), and axial strain (Figure 7.6) for constant volume (CV) test are applied as the boundary condition, so that they are the same as the measurements.

The suction average, suction at the center and perimeter are illustrated in Figures 7.7a-c. Note that the suction decreases with the increase of degree of saturation and the total suction at the perimeter (Figure 7.7b) is always smaller than that at the center (Figure 7.7c). Although the total suction in the LE model is the closest to the laboratory measurement (Figures 7.7a-7.7c), the mean stress of the LE model overestimates the laboratory measurements (Figures 7.8a-7.8c). The total mean stress for BGM and BGM-kwn models show a good agreement with the laboratory test results (Figure 7.8).

7.5.2 Constant Mean Stress (CMS) test.

The volume of water added to the specimen of the three constitutive models (LE, BGM, and BGM-kwn models) is smaller than the laboratory measurements (Figure 7.9). In the case of the CMS test, the LE model shows the volume of water added to the specimens is less than the other two (BGM and BGM-kwn) models (Figure 7.9). Results of the water added to the specimens of the BGM and BGM-kwn are relatively similar and they more closely match the laboratory results than the LE model (Figure 7.10).

The volume of water added to the specimens in the CMS test is significantly dependent on the volume strain of the specimens, since the volume of water added to the specimens is dependent on the total volume and the void ratio (e). The change of volume, axial, and radial strains of the BGM and BGM-kwn models are greater than that of the measurements (Figures 7.10-7.12). The volume strain for LE model shows good agreement with the laboratory measurements (Figures 7.10-7.12), but it underestimates the volume of water added to the specimen. A dilemma develops in the relationship of the volume strain and the water added to the specimens that may indicate a limitation of the numerical models that assumes a constant volume of solid.

The total suction of the three hydro-mechanical constitutive models (Figures 7.13a-7.13c) are only slightly different between the three models. The average mean stress (Figure 7.14a), and mean stress at the center (Figure 7.14b) are smaller than the applied mean stress (500 kPa) due to the time to transfer the stress from the perimeter to the center. Stress should be transferred instantly. It must be related to the evolution in suction at the centre, which will affect mean stress. At the perimeter (Figure 7.14c), the

mean stress is greater than the applied mean stress due to the effect of the impact in the application of boundary conditions (Figure 7.14).

The results of the BGM and BGM-kwn models show very slight differences in the CMS models (Figures 7.9-7.14). The porosity-dependent permeability (kwn) models are effective only in the fixed-boundary conditions, such as in the CV test.

7.5.3 Volume-Mass Relationship at the End of the Test

The volume-mass relationships at the end of the test for constant volume (CV) tests and constant mean stress (CMS) tests are illustrated in Figures 7.15-7.18. The results of the degree of saturation (S_w) and porosity (n) are used to calculate the rest of the volume-mass relationships. The porosity (n) is calculated from the volume strain of each element based on the assumption that the soil solid is incompressible. The rest of the volume-mass relationships are calculated using degree of saturation (S_w) and porosity (n) with the specific gravity (G_s) of 2.7 (Graham et al. 1997). The detailed calculation of the volume-mass relationship is discussed in Appendix 3.

The distribution of the degree of saturation (S_w) at the end of CMS test for the three constitutive models (Figure 7.15b) shows a good agreement with the laboratory measurements. The BGM and LE models overestimate the laboratory test measurement for the CV test. The BGM-kwn model is the closest to the laboratory measurements (Figure 7.15).

The use of the porosity dependent model to simulate the CV test creates 'pseudo impermeable layer' mechanism. The term 'pseudo' is used to describe this mechanism, because this layer may not be impermeable, but this layer has very low water

permeability (k_w) due to a decrease of porosity and an increase of dry density. This 'pseudo impermeable layer' is an analogy of the interface of the water and air phase.

The existence of the 'pseudo impermeable layer' is shown by the sudden change in the degree of water saturation S_w between distance of 15 and 20 mm due to the BGM-kwn model for CV tests in Figure 7.15. The existence of the 'pseudo impermeability layer' is also indicated from the dry density spatial distribution (Figure 7.16a), where the dry density at distance of 17.5 mm increases for BGM-kwn model. Note that an increase of dry density decreases the porosity and the permeability.

In general dry density of the numerical models is greater than the laboratory measurements for both constant volume (CV) and constant mean stress (CMS) tests (Figure 7.16). The higher dry density (ρ_{dry}) means lower porosity (n). Although the degree of saturation (S_w) at the end-of test measurement for CMS test shows reasonable agreement with the laboratory measurements (Figure 7.15b), the dry density (ρ_{dry}) is higher than the measurements; consequently the volume of water added to the specimens for the CMS test is lower than the measurement (Figure 7.9).

In the case of constant volume (CV) tests, the degree of saturation (S_w) at the end of the test (Figure 7.15a) is higher than the measurements and the dry density (ρ_{dry}) is much higher than the measurements. Consequently, the water added to the specimen is much lower than the measurements (Figure 7.3). As a result of the overestimation of dry density (Figures 7.16), the gravimetric water content (w) of the model is less than the measurements, while the bulk density is higher than the measurements (Figure 7.17 and 7.18). Although there are magnitude differences between the numerical model and the laboratory measurements (Figures 7.3 to 7.18), the models shows similar pattern with the laboratory measurements.

7.5.4 Model Limitations

The calculated maximum water added to the specimens (Table 7.1) is 16.18 mL assuming 100% degree of water saturation (S_w). The dry density at the pre-infiltration and end-of the test are constant in this calculation, assuming the soil solids are incompressible. The measurement shows a large change of the dry density at pre-infiltration (1.67 Mg/m^3) and post measurement ($1.52\text{-}1.57 \text{ Mg/m}^3$) (Figure 7.16). If the measured water added is equal to the water added to the specimens (no leakage occurs), then the assumption of incompressible volume of solids might not be adequate for the case of swelling clay. The insertion of this compressible volume of solids may be incorporated using the three-dimensional water retention surface (WRS) presented in Chapter 5 (Figure 5.1). Application of this WRS is the implication that the clay particles compressed with increasing suction.

The distribution of volume-mass relationship at the end of the test for LE and BGM models (Figures 7.15-7.18) shows a variation with distance. If the models (LE and BGM) were allowed to continue for longer time, the degree of saturation in the specimen will be uniform at 100% degree of water saturation, which is not the case in the laboratory measurements. Siemens (2006) observed that the variation of the gravimetric water content at the end of test, which disagrees with the model. Using the BGM-kwn model, the 'pseudo impermeable layer' is created and prevents this from occurring, but this 'pseudo impermeable layer' only exists in one layer of the elements. It is also shown that the porosity-dependent permeability model (kwn) only affects the modelling results in the constant volume (CV) test.

The application of the porosity-dependent permeability (kwn) model only incorporates some effects of the boundary conditions. The combination of this porosity-dependent

permeability model and the three-dimensional water retention surface (WRS) that incorporates the effect of the boundary condition presented in Chapter 5 can resolve this limitation. The effect of the boundary condition is addressed in the WRS (Figure 5.1) by the maximum saturation line defining the relationship of the maximum degree of water saturation (S_w) as a function of specific volume (v). The implementation of this WRS is beyond the scope of this research and is left as a suggestion for future research.

7.6 Concluding Remarks and Future Research

The application of three constitutive models (LE, BGM, and BGM-kwn) to model the infiltration process in swelling clay with two different boundary conditions presented in this chapter results in the following conclusions:

- The porosity-dependent permeability models create a 'pseudo impermeable layer' implies that a skin of low permeability material forms on the outside of the specimen. This 'pseudo impermeable layer' inhibits moisture movement and slows the rate of saturation at the center of the specimen.
- The porosity-dependent permeability (kwn) model only affects the results of the rigid boundary conditions in the constant volume (CV) test.
- Some of the aspects of behaviour in the swelling clay soil can be modelled using 2-phase flow hydraulic-mechanical analysis in FLAC. The limitation of the numerical modelling presented in this chapter maybe due to the assumption of the incompressible soil solids. This limitation maybe reduced by application of the water retention surface presented in Chapter 5, which is suggested for future research.

- In the CMS test, the model allowed the specimens to expand radially, hence there was no internal increase in density and corresponding reduction in the water permeability (k_w) (N. A. Chandler, personal communication, 29 June 2007).

Table 7.1 As-compacted, Pre-infiltration, and End-of-test Conditions of Constant Volume (CV) Test with 500 kPa Confining Pressure

	As-compacted	Pre-infiltration	End-of Test
Gravimetric water content, w (%)	18.75	18.75	23.95
Dry density, ρ_{dry} (Mg/m ³)	1.57	1.67	1.67
Void ratio, e	0.72	0.61	0.61
Porosity, n	0.42	0.38	0.38
Specific volume, v	1.72	1.61	1.61
Degree of saturation, S (%)	69.91*	82.68	105.58*
Volume of water added to the system (mL)	0.00	0.00	16.00
Volume strain (%)	0.00	6.49	6.47
Total volume, mL	196.35	183.61	183.65
Volume of void (mL)	82.47	69.73	69.76
Volume of solid (mL)	113.88	113.88	113.88
Volume of water (mL)	57.65	57.65	73.65
Volume of air (mL)	24.81	12.08	-3.89
Possible maximum water added (mL)			16.18
Duration from pre-infiltration to the end-of-test (day)			12.11

Note: *Calculated based on the assumption of soil solids are incompressible and $G_s = 2.7$

Table 7.2 As-compacted, Pre-infiltration, and End-of-test Conditions of Constant Mean Stress (CMS) Test with 500 kPa Confining Pressure

	As-compacted	Pre-infiltration	End-of Test
Gravimetric water content, w (%)	18.75	18.75	26.98
Dry density, ρ_{dry} (Mg/m ³)	1.57	1.66	1.58
Void ratio, e	0.72	0.63	0.71
Porosity, n	0.42	0.39	0.42
Specific volume, v	1.72	1.63	1.71
Degree of saturation, S_w (%)	69.91*	80.31	102.27*
Volume of water added to the system (mL)	0.00	0.00	25.31
Volume strain (%)	0.00	5.44	0.69
Total volume, mL	196.35	185.67	195.00
Volume of void (mL)	82.47	71.79	81.12
Volume of solid (mL)	113.88	113.88	113.88
Volume of water (mL)	57.65	57.65	82.96
Volume of air (mL)	24.81	14.13	-1.84
Possible maximum water added (mL)			23.47
Duration from pre-infiltration to the end-of-test (day)			14.87

Note: *Calculated based on the assumption of soil solids are incompressible and $G_s = 2.7$

Table 7.3. Linear Elastic (LE) Model Parameters

Linear elastic model	
Bulk modulus (K)	42 MPa*
Shear modulus (G)	34 MPa*

*after Graham et al. 1997.

Table 7.4. Blatz and Graham (2003) model (BGM) Parameters

BGM (Blatz and Graham 2003)	
Poisson ratio, ν	0.18
Maximum bulk modulus, $K_{\max}^{(a)}$	$2 \times 42 \text{ MPa}^{(b)}$
Maximum shear modulus, $G_{\max}^{(a)}$	$2 \times 36 \text{ MPa}^{(b)}$
Critical state slope, M^p	$0.5^{(d)}$
Critical state slope, M^s	$0.2^{(d)}$
Coefficient of compressibility, κ	$0.05^{(c)}$
Coefficient of compressibility, λ	$6.7 \times \kappa^{(c)}$
Coefficient of compressibility, κ_s	$0.05^{(c)}$
Coefficient of compressibility, λ_s	$4 \times \kappa_s^{(c)}$
Reference pressure, $p_1^{(a)}$	$100 \text{ Pa}^{(e)}$
Initial preconsolidation pressure at $s=0$, p_0^*	$0.5 \text{ MPa}^{(e)}$
Slope of the LY-line	$0.3^{(e)}$
Slope of T-line	$-0.04^{(d)}$
Suction yield line, s_0	$10 \text{ MPa}^{(f)}$

^(a) Additional parameters required in FLAC;

^(b) These parameters are generated as twice of linear elastic model parameters for BSB material after Graham et al. (1997).

^(c) Based on laboratory test results of Anderson (2003) and Siemens (2006).

^(d) Follow Blatz and Graham (2003).

^(e) Priyanto et al. (2006) using data from Blatz (2000).

^(f) Based on data from Anderson (2003) and Blatz (2000).

Table 7.5. Hydraulic constitutive model equations and parameters for van Genuchten models (1980) for Bentonite Sand Buffer (BSB) material.

Van Genuchten (1980)	
Water retention curve	
(1)	$P_c(S_w) = P_o (S_e^{-1/a} - 1)^{1-a}$
where:	
(2)	$S_e = \frac{S_w - S_{res}}{1 - S_{res}}$
<hr/>	
Water and air permeability function	
Water permeability	
(3)	$k_w = k_{w-sat} \cdot \kappa_{rw}$
where:	
(4)	$\kappa_{rw} = S_e^b [1 - (1 - S_e^{1/a})^2]$
Air permeability	
(5)	$k_a = \frac{\mu_w}{\mu_a} k_{w-sat} \cdot \kappa_{ra}$
(6)	$\kappa_{ra} = (1 - S_e)^c [1 - S_e^{1/a}]^2$
Parameters, a	0.12
Parameters, b	0.5
Parameters, c	0.5
Threshold pressure, P_o (MPa)	0.67
Residual water degree of saturation, S_{res}	0.1
Saturated water mobility coefficient, k_{w-sat} ($m^2/Pa\cdot sec$) (related to water permeability, $k_{w-sat} = 5 \times 10^{-13} m/s$ (Graham et al. 1997))	5×10^{-16}
Viscosity ratio, μ_w/μ_a	50

Table 7.6. Hydraulic constitutive model equations for porosity-dependent model (kwn) for Bentonite Sand Buffer (BSB) material.

Water retention curve	
$P_c(S_w) = P_o (S_{e1}^{-1/a} - 1)^{1-a}$	(1)
where:	
$S_{e1} = \frac{S_w - S_{res}}{1 - S_{res}}$	(2)
Permeability function	
Water permeability	
$k_w = k_w^{sat}(n) \cdot \kappa_{rw}$	(3)
where:	
$\kappa_{rw} = S_{e2}^b [1 - (1 - S_{e2}^{1/a})^a]^2$	(4)
$k_w^{sat}(n) = k_{w-max}^{sat} \cdot n_e^{nb} \left[1 - (1 - n_e^{1/na})^{na} \right]^2$	(5)
$n_e = \frac{n - n_{min}}{n_{max} - n_{min}}$	(6)
$S_{e2} = \frac{S_w - S_{res}}{S_{max} - S_{res}}$	(7)
$S_{max} = \frac{G_s}{v - 1} (A \cdot v - B)$	(8)
$v = 1 / (1 - n)$	(9)
Air permeability	
$k_a = \frac{\mu_w}{\mu_a} k_w^{sat}(n) \cdot \kappa_{ra}$	(10)
$\kappa_{ra} = (1 - S_{e2})^c [1 - S_{e2}^{1/a}]^2$	(11)

Table 7.7. Hydraulic constitutive model parameters for porosity-dependent model (kwn) for Bentonite Sand Buffer (BSB) material.

Parameters	Value
Parameters, a	0.12
Parameters, b	0.5
Parameters, c	0.5
Threshold pressure, P_o (MPa)	0.67
Residual water degree of saturation, S_{res}	0.1
Saturated water mobility coefficient, k_{w-sat} ($m^2/Pa\cdot sec$) (related to water permeability, $k_{w-sat} = 5 \times 10^{-13} m/s$ (Graham et al. 1997))	5×10^{-16}
Viscosity ratio, μ_w/μ_a	70
Minimum porosity, n_{min}	0.30
Maximum porosity, n_{max}	0.45
Parameter relating permeability and porosity, na	1
Parameter relating permeability and porosity, nb	2.5
Maximum saturated permeability, k_{w-max}^{sat} (m/s) (correlated with maximum porosity, n_{max})	1×10^{-12}
Maximum saturation parameter, A (after Siemens 2006)	38.49
Maximum saturation parameter, B (after Siemens 2006)	-3.7829
Specific gravity of the BSB, G_s	2.7

Table 7.8. Combinations of boundary condition, mechanical constitutive models, and hydraulic constitutive models used in the analyses

No	File name	Boundary conditions	Mechanical constitutive model	Hydraulic constitutive model
1.	CV-le	Constant volume	LE	VG
2.	CV-bgm	Constant volume	BGM	VG
3.	CV-bgm-kwn	Constant volume	BGM	kwn
4.	CMS-le	Constant mean stress	LE	VG
5.	CMS-bgm	Constant mean stress	BGM	VG
6.	CMS-bgm-kwn	Constant mean stress	BGM	kwn

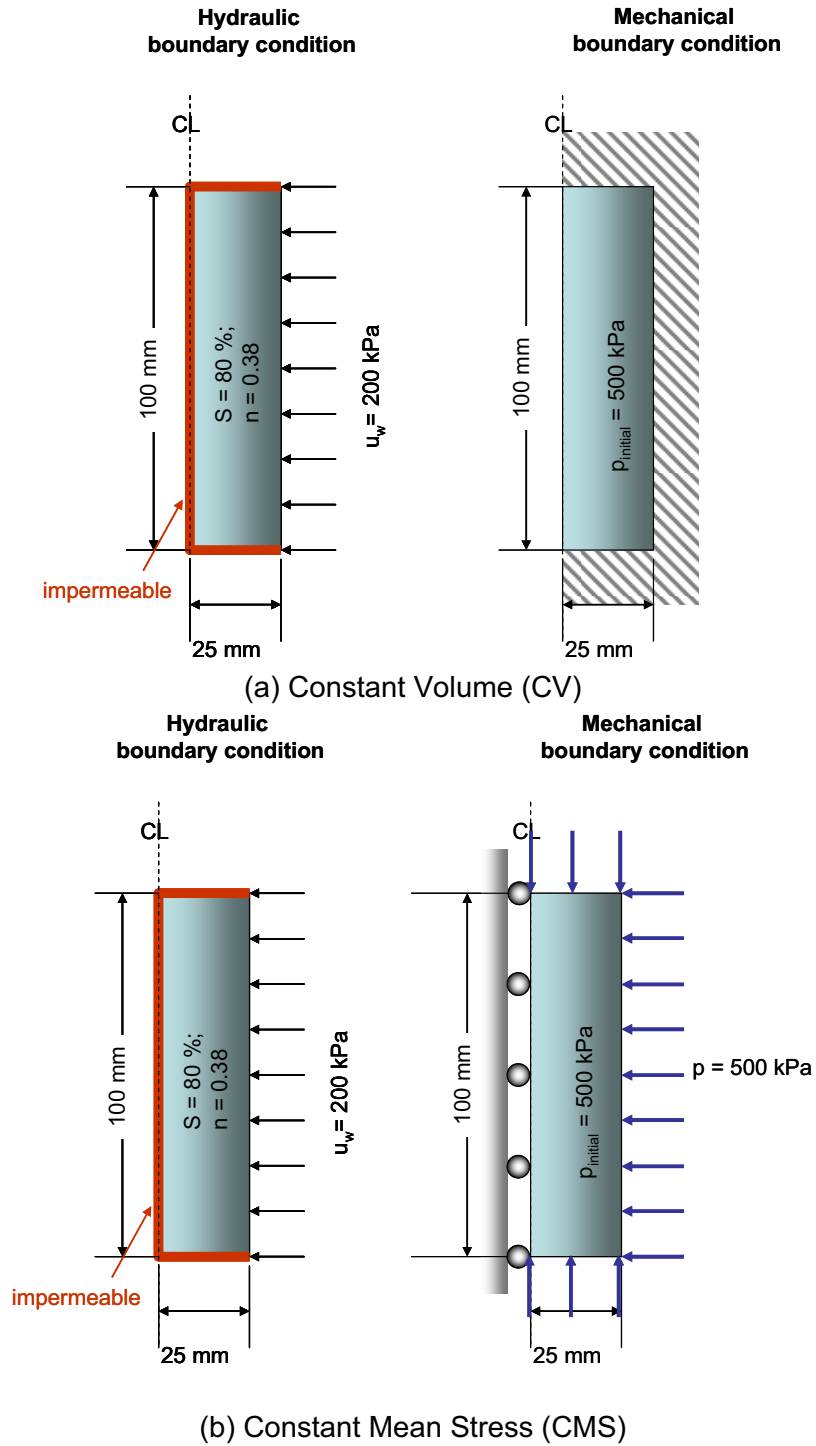


Figure 7.1 Hydraulic and mechanical boundary conditions used in numerical modelling of the constant volume (CV) and constant mean stress (CMS) tests

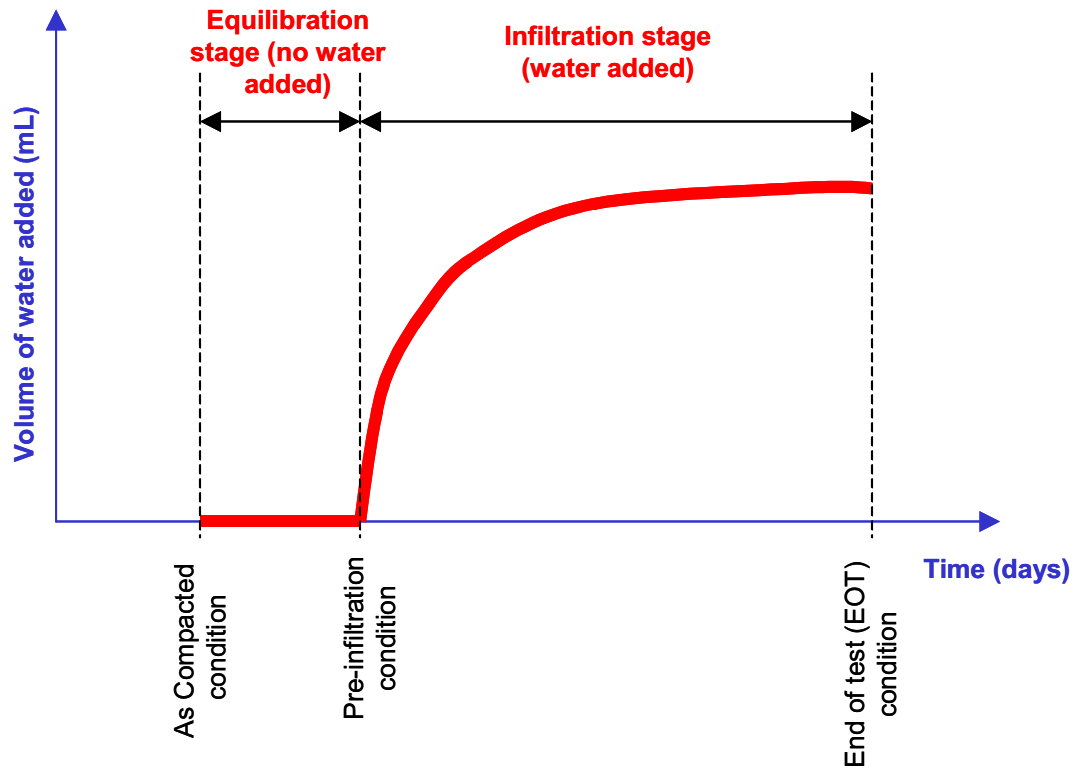


Figure 7.2 Stages and conditions in the infiltration test

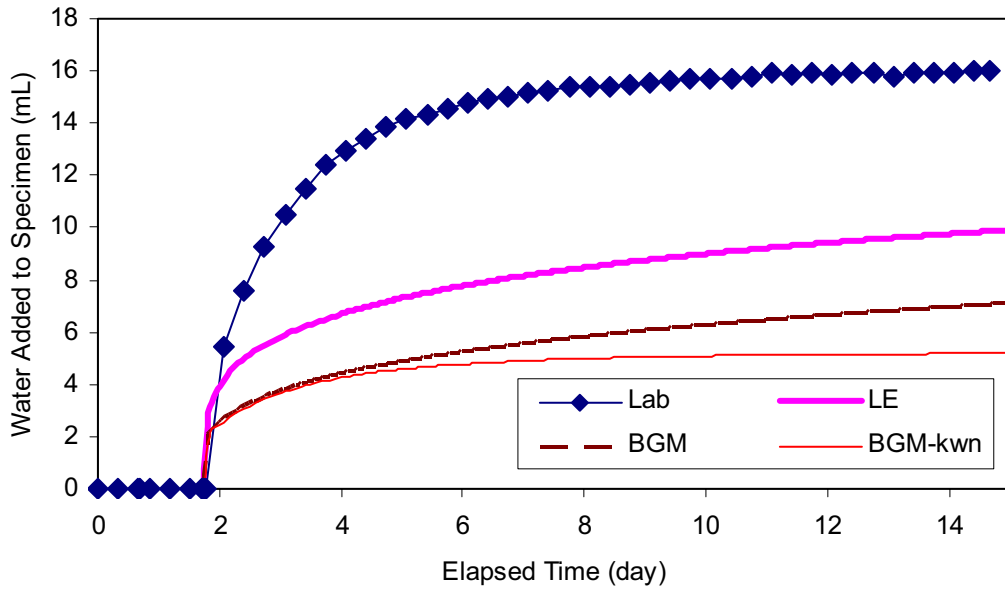


Figure 7.3 Volume of water added to the specimen versus time for constant volume (CV) test

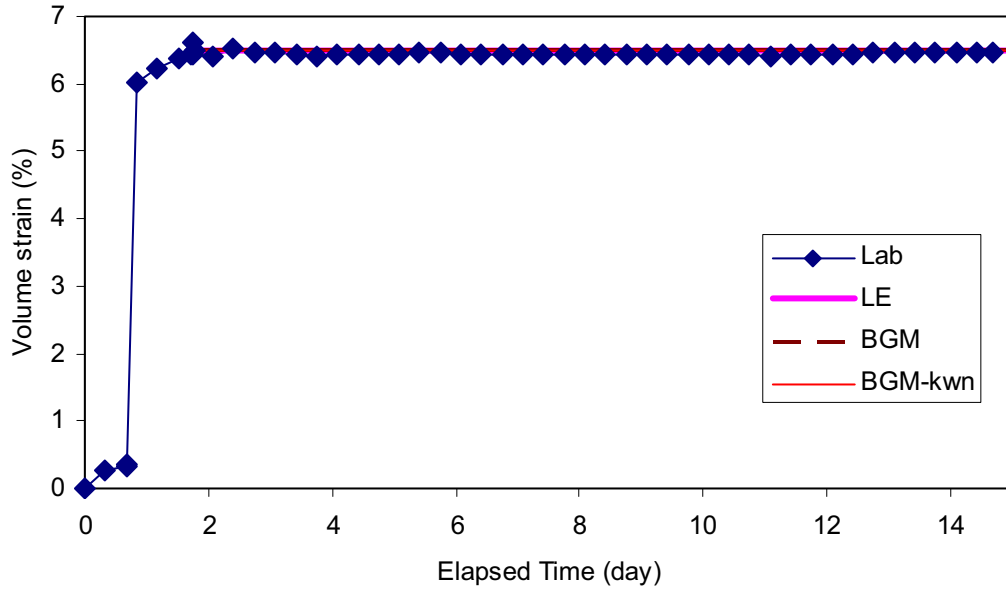


Figure 7.4 Volume strain versus time for constant volume (CV) test

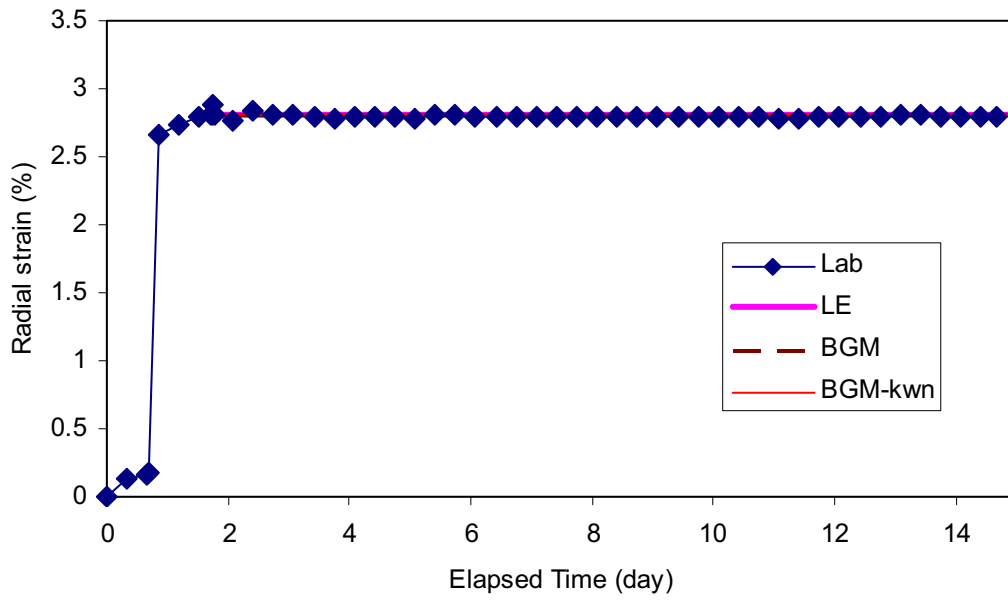


Figure 7.5 Radial strain versus time for constant volume (CV) test

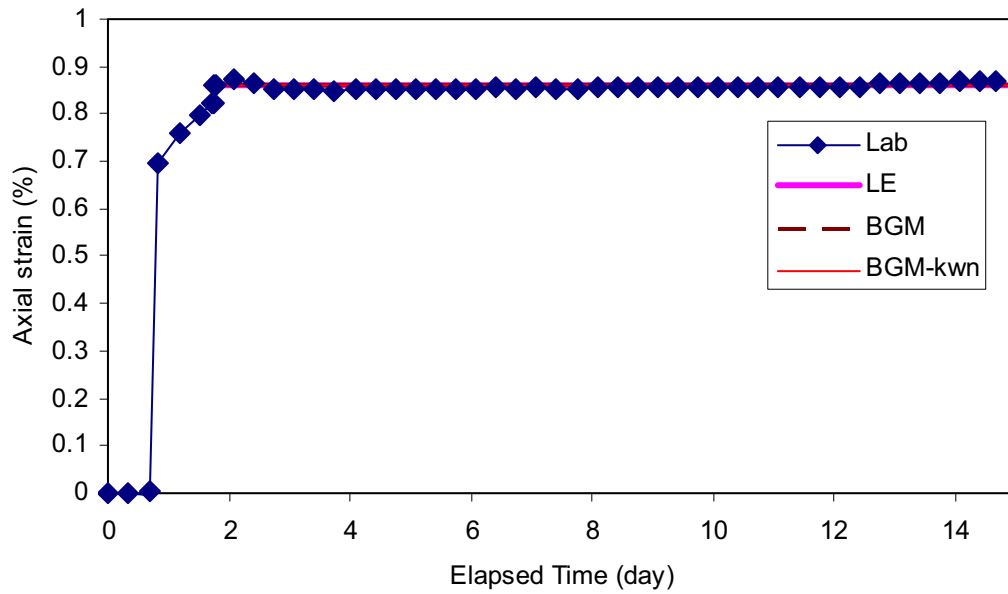
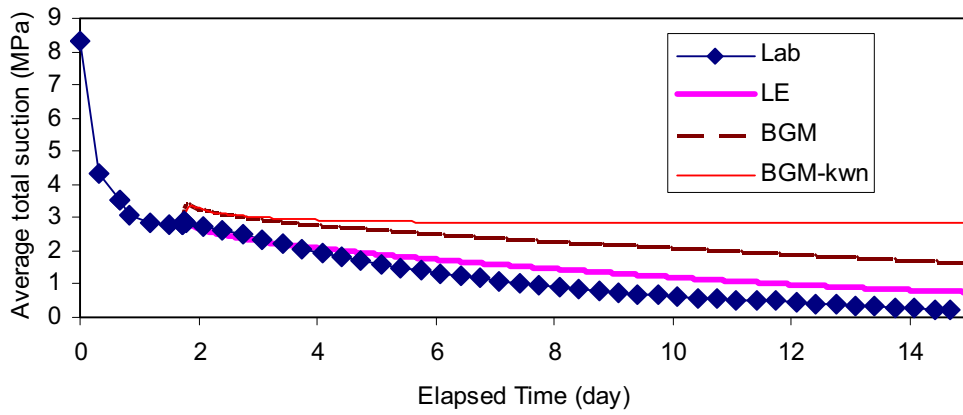
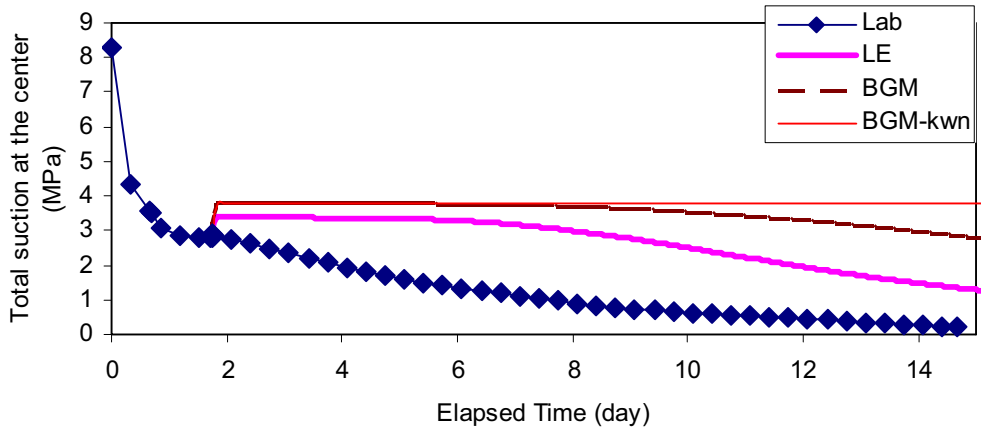


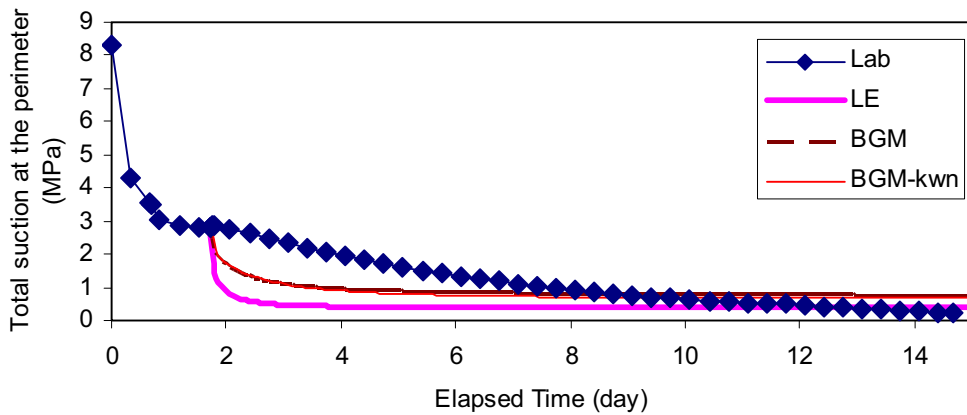
Figure 7.6 Axial strain versus time for constant volume (CV) test



(a)

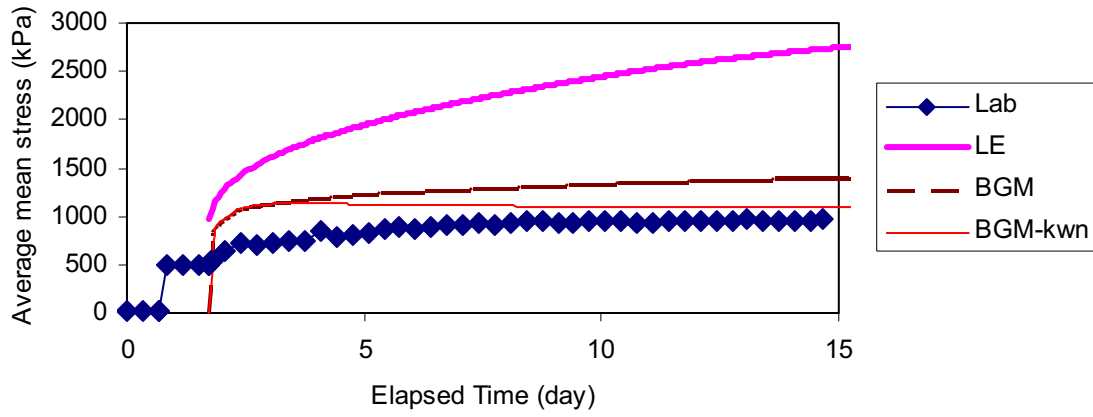


(b)

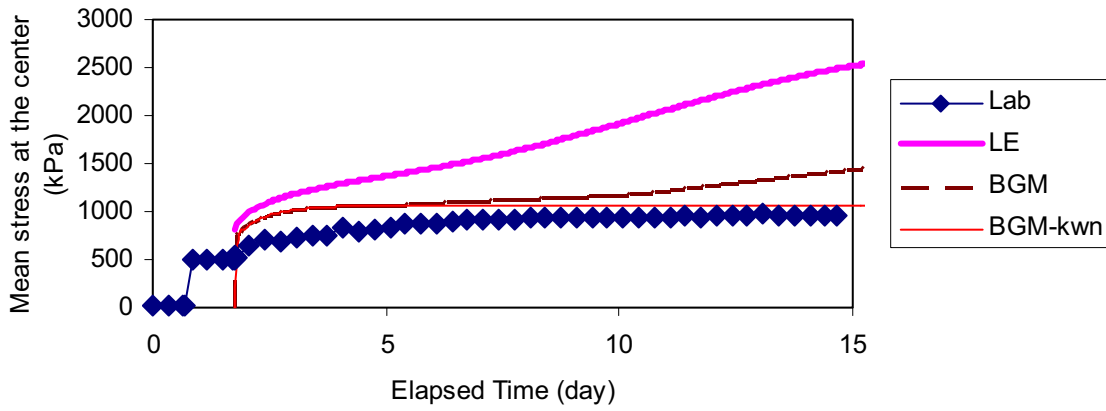


(c)

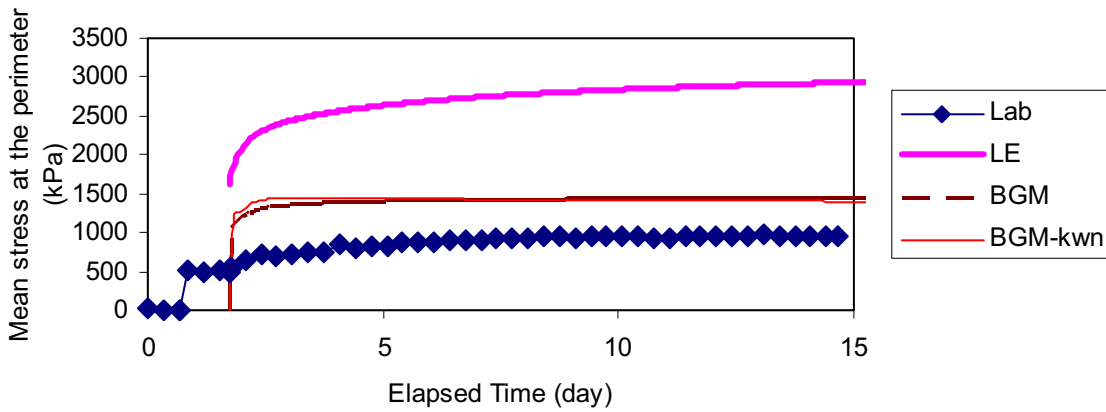
Figure 7.7 Total suction versus time for constant volume (CV) test (a) average; (b) at the center; (c) at perimeter



(a)



(b)



(c)

Figure 7.8 Total mean stress versus time for constant volume (CV) test (a) average; (b) at the center; (c) at perimeter

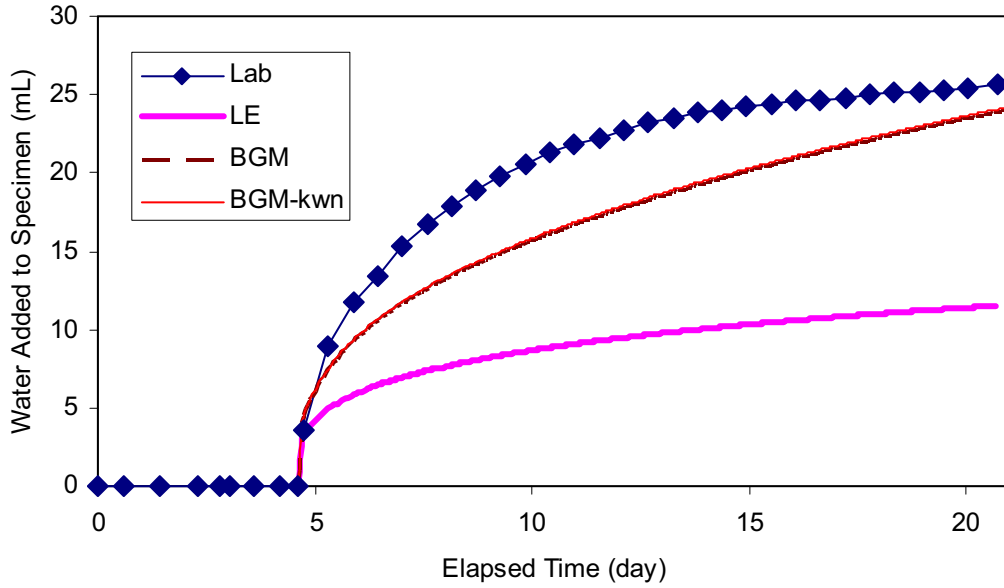


Figure 7.9 Volume of water added to the specimen versus time for constant mean stress (CMS) test

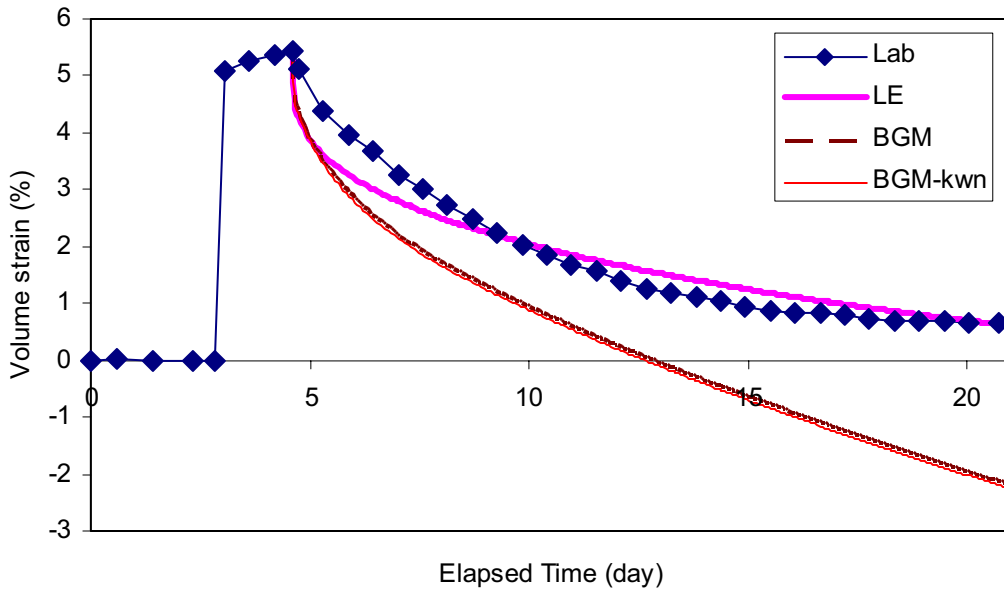


Figure 7.10 Volume strain versus time for constant mean stress (CMS) test

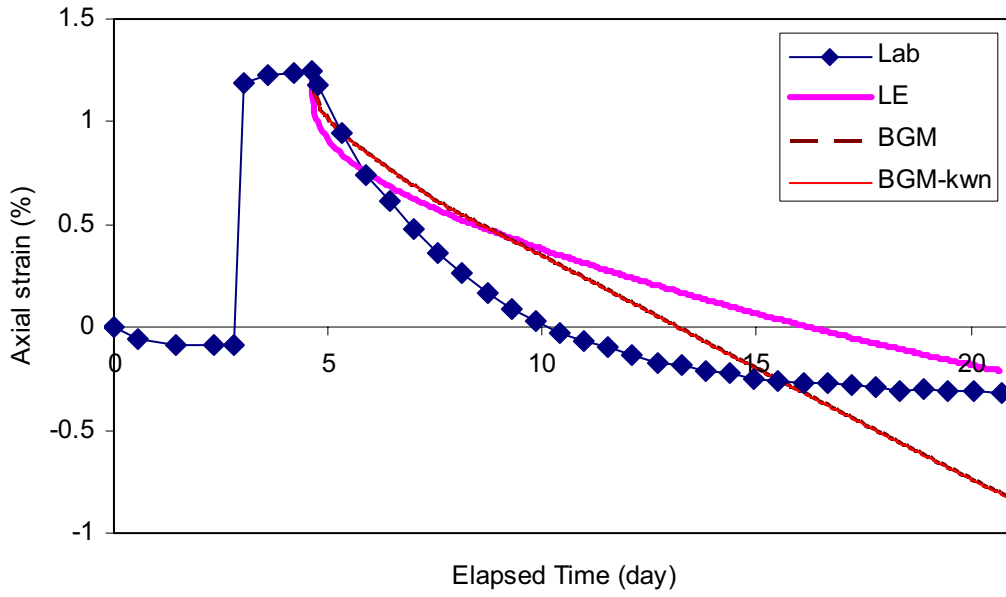


Figure 7.11 Radial strain versus time for constant mean stress (CMS) test

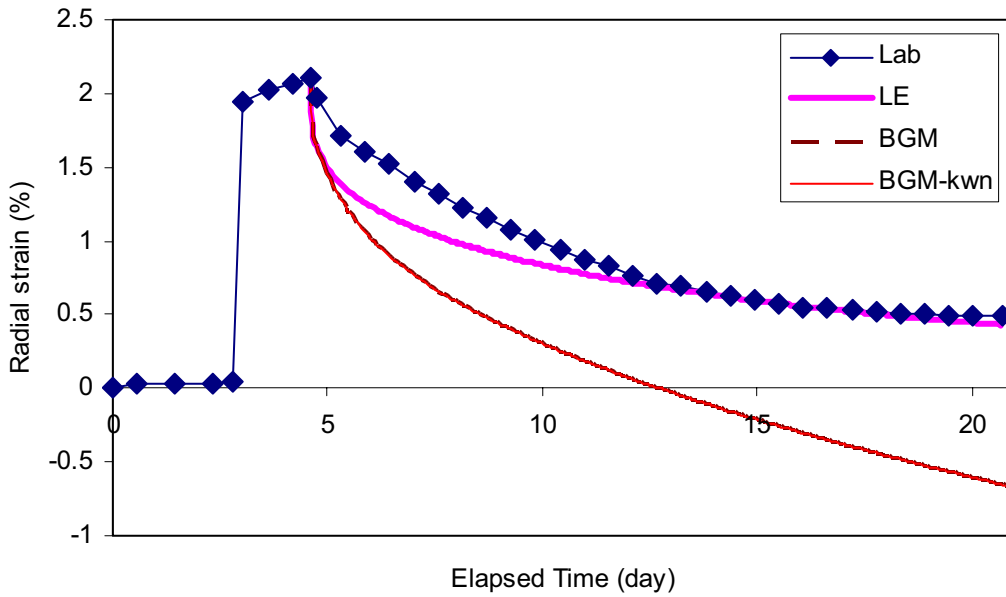
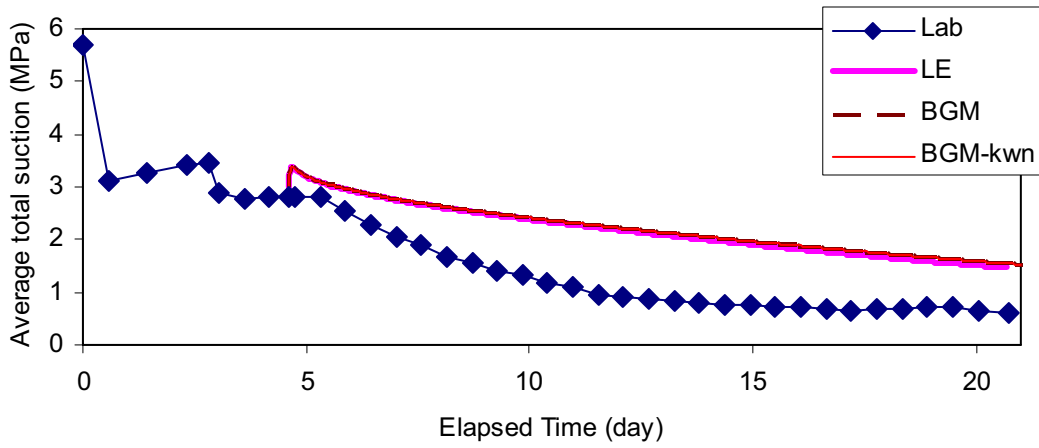
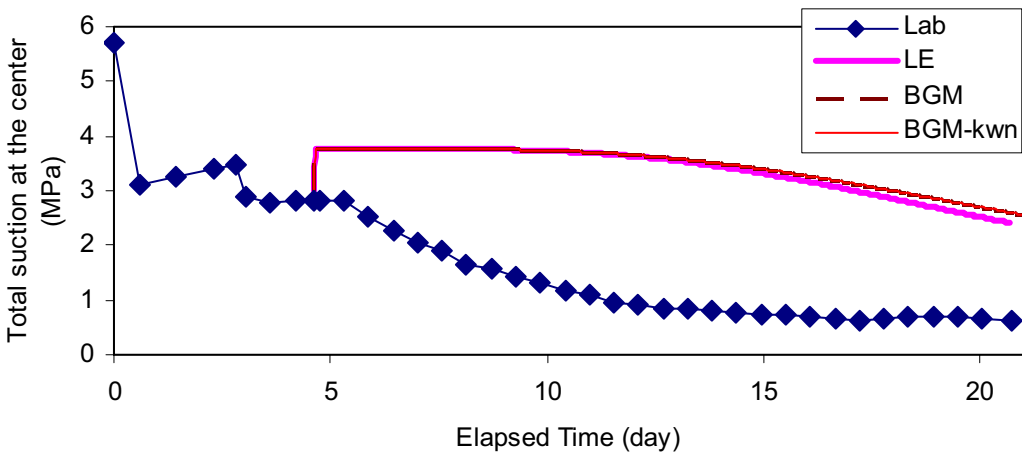


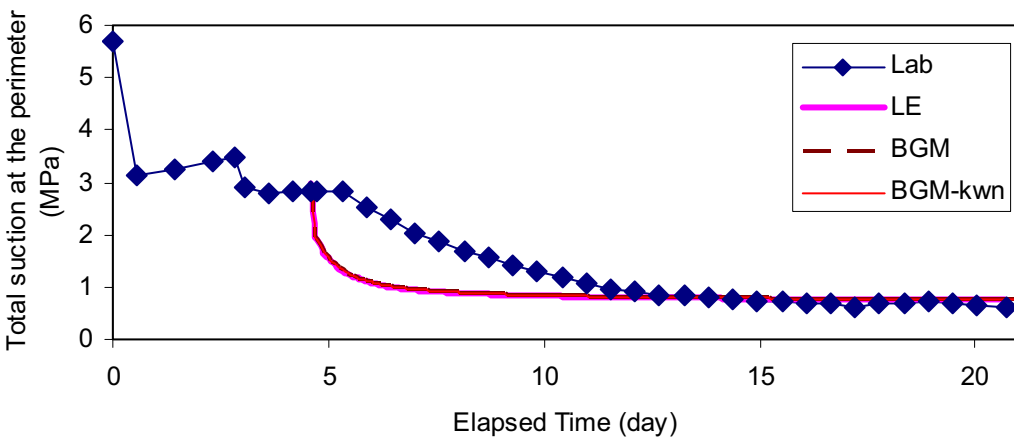
Figure 7.12 Axial strain versus time for constant mean stress (CMS) test



(a)

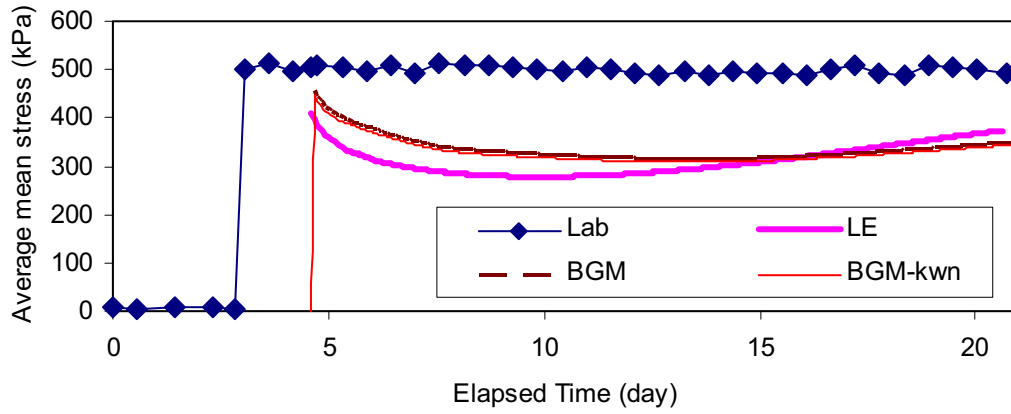


(b)

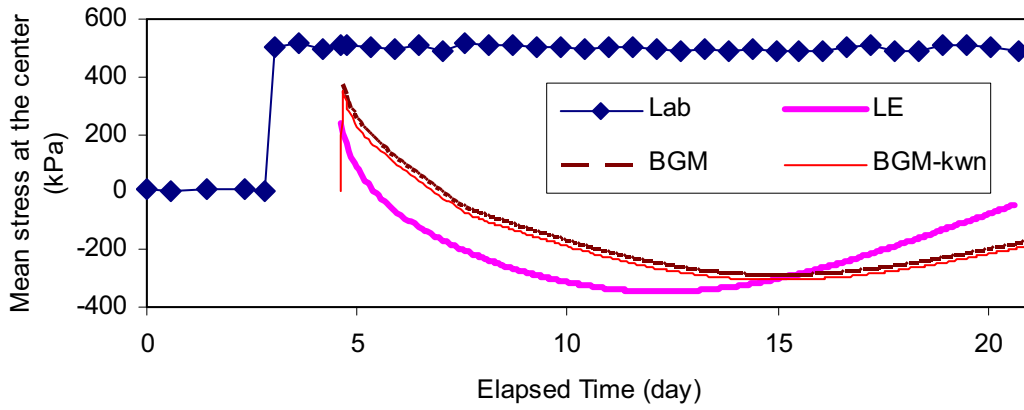


(c)

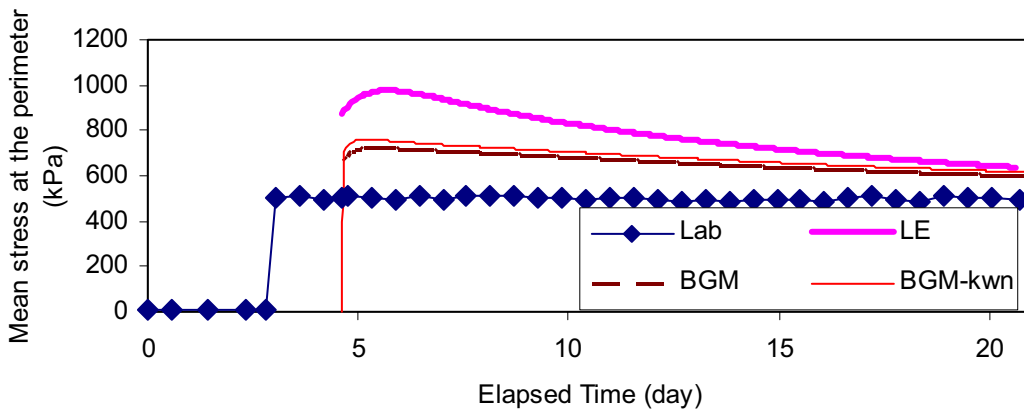
Figure 7.13 Total suction versus time for constant mean stress (CMS) test (a) average; (b) at the center; (c) at perimeter



(a)

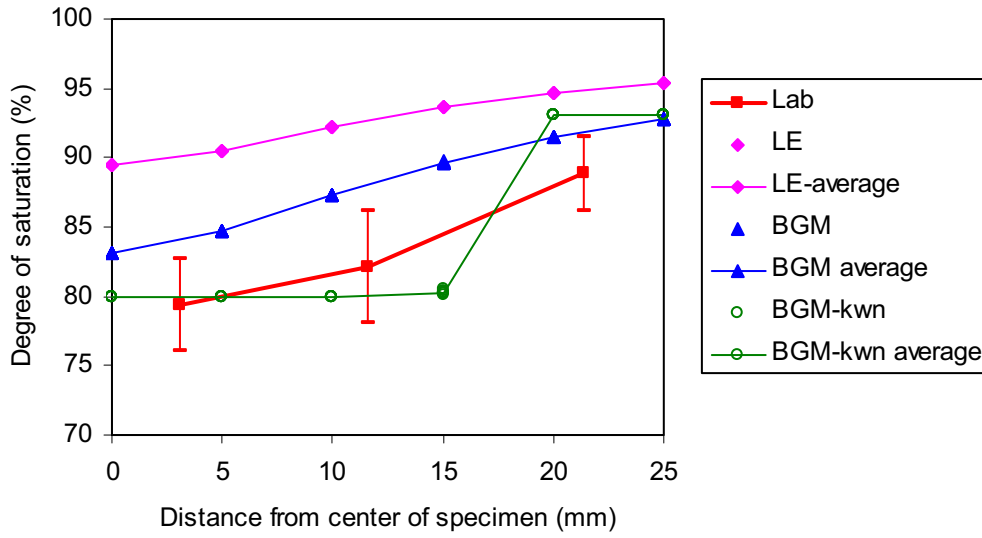


(b)

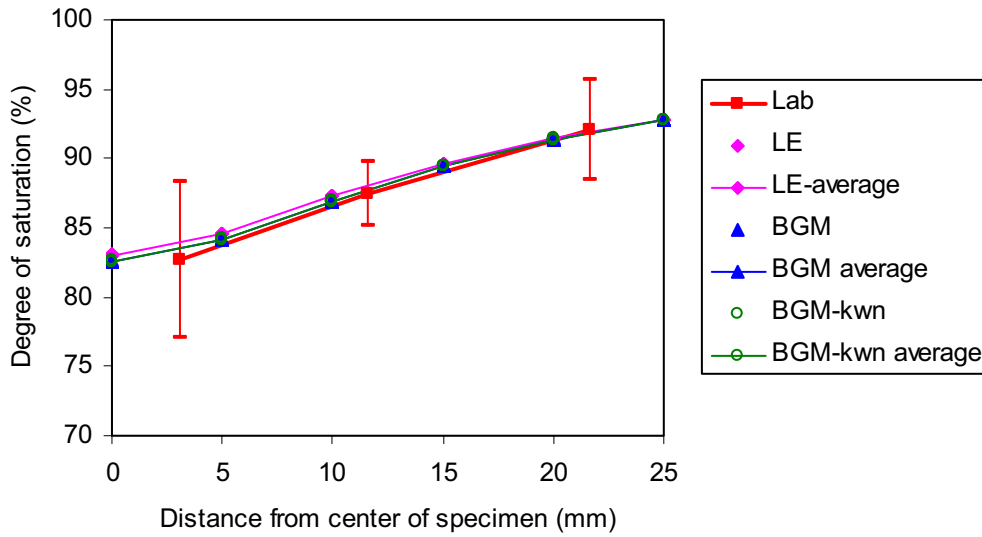


(c)

Figure 7.14 Total mean stress versus time for constant mean stress (CMS) test (a) average; (b) at the center; (c) at perimeter

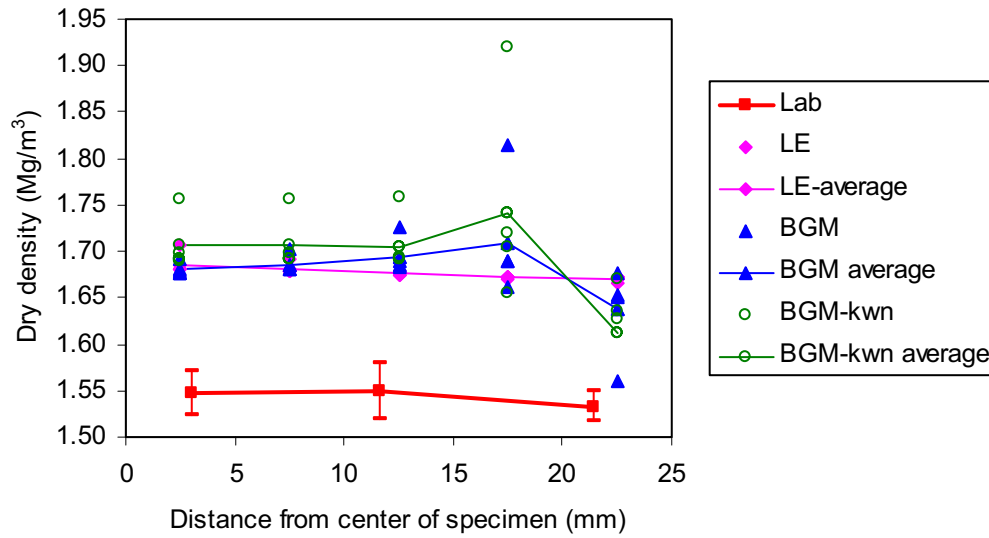


(a) CV

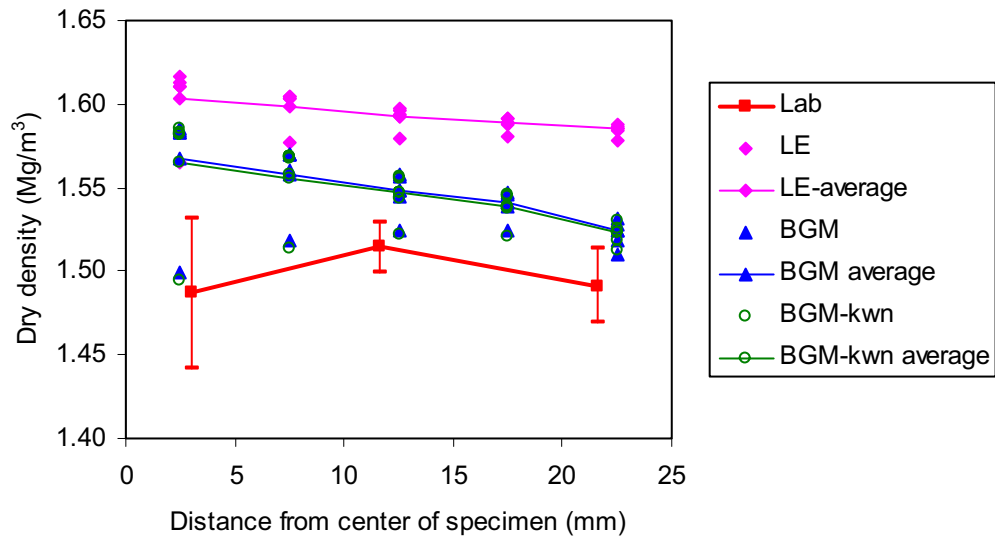


(b) CMS

Figure 7.15 Degree of saturation versus radial distance at the post-test for: (a) constant volume (CV) test; (b) constant mean stress (CMS) test

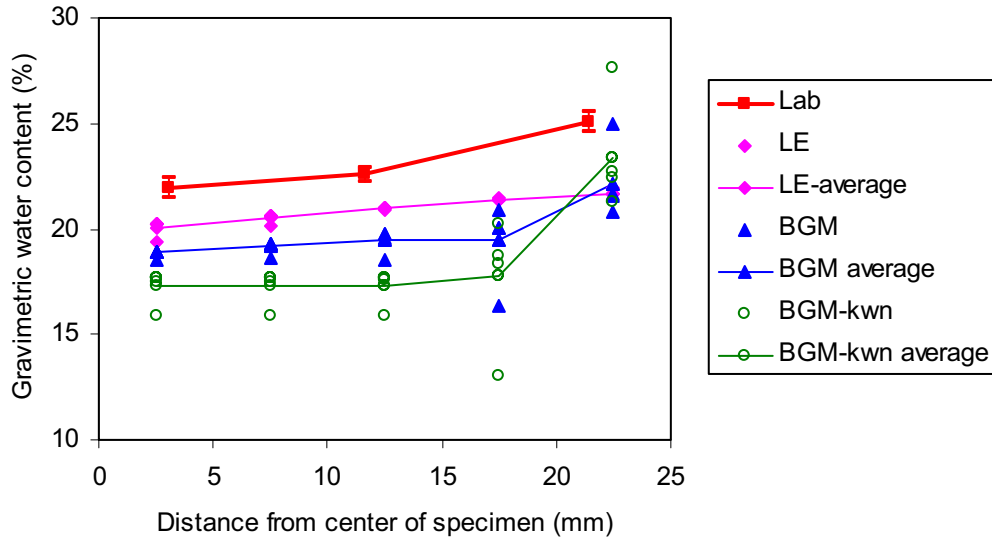


(a) CV

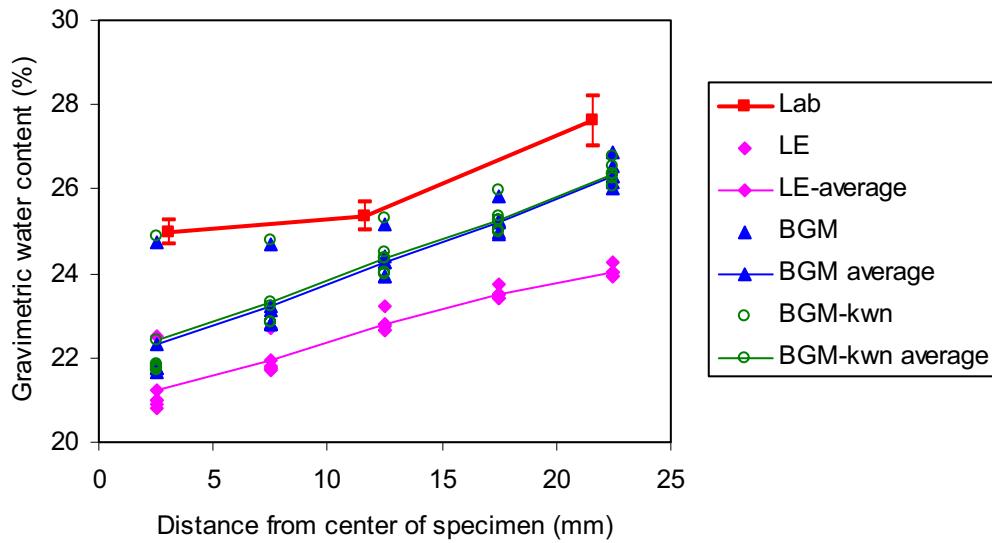


(b) CMS

Figure 7.16 Dry density versus radial distance at the post-test for: (a) constant volume (CV) test; (b) constant mean stress (CMS) test

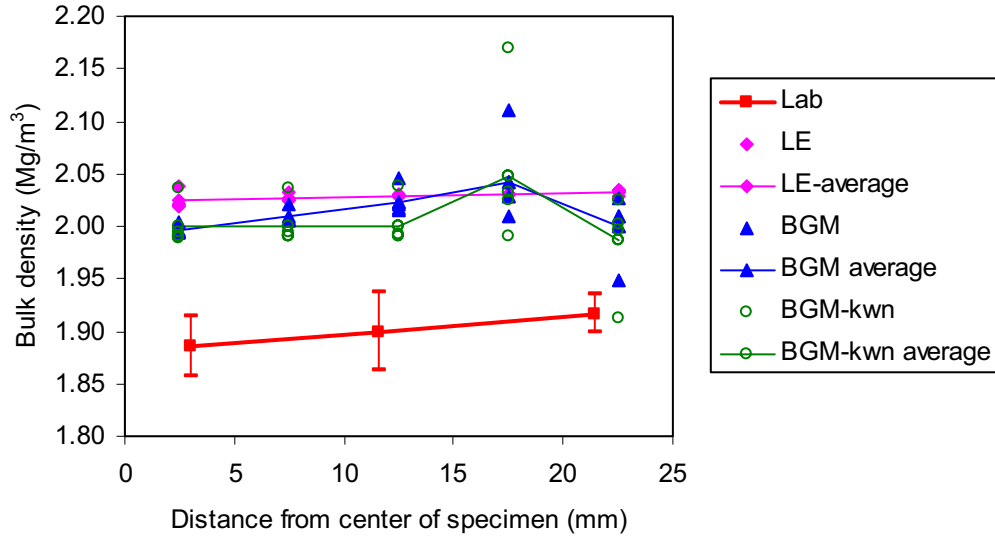


(a) CV

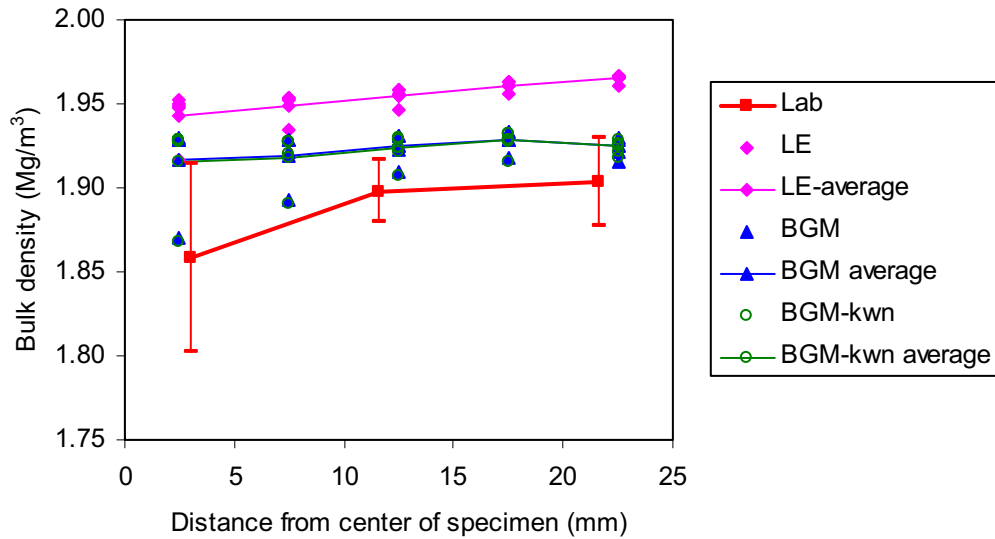


(b) CMS

Figure 7.17 Gravimetric water content versus radial distance at the post-test for: (a) constant volume (CV) test; (b) constant mean stress (CMS) test



(a) CV



(b) CMS

Figure 7.18 Bulk density versus radial distance at the post-test for: (a) constant volume (CV) test; (b) constant mean stress (CMS) test

CHAPTER 8

MODELLING FULL-SCALE ISOTHERMAL TEST (ITT)

8.1 Introduction

High plastic clays have very low hydraulic conductivity and self-sealing ability; due to this reason they are considered to be excellent candidates as a nuclear waste disposal barriers (Graham et al. 1997, Russell and Simmons 2003). The characterization of unsaturated high plastic clay behaviour can be made by means of laboratory testing, field testing and numerical modelling. Both of the methods are complementary to each other. Parameters and understanding of material behaviour from laboratory and field tests are then used to develop mathematical formulations and models to be used to predict the behaviour of engineered materials.

Several full-scale experiments were conducted at the Atomic Energy of Canada Limited (AECL)'s Underground Research Laboratory (URL) in Canada (Dixon et al. 2002). One of experiments was the large-scale isothermal test (ITT) (Dixon et al. 2002) that monitored infiltration processes into high plastic clay from the surrounding host rock. The pore pressures, stress, and strain in the system were monitored for approximately 6.5 years (Dixon et al. 2002). Seepage into the empty 1.25 m diameter rock borehole before

and after the test was also measured. The spatial volume-mass relationship in the bentonite-sand buffer (BSB) at the end of the test showed the variation of density and gravimetric water content in radial and vertical directions (Dixon et al. 2002).

Initial attempts to model the evolution of moisture content in the unsaturated BSB material resulted in an overestimate of the end of test degree of water saturation (Thomas et al. 2003). A subsequent attempt to simulate the hydraulic-mechanical behaviour of this process resulted in a permeability function, called the 'exponential relationship', to capture the behaviour of unsaturated high-plastic clay (Thomas et al. 2003). This 'exponential relationship' permeability function indicated a decrease of water permeability with an increase in degree of saturation for the degree of water saturation greater than 95% as shown in Figure 8.1. This 'exponential relationship' is contradictory to conventional permeability functions that show an increase of water permeability with an increase of degree of water saturation (Figure 8.1). This thesis has proposed a three-dimensional permeability surface, called porosity-dependent permeability (k_{wn}) model (Chapter 4) shown in Figure 8.2. The unconventional 'exponential relationship' permeability model is a trace in this surface when changes of porosity (n) are considered (Figure 8.2).

This chapter presents modelling of the hydro-mechanical process in the ITT test using the constitutive models developed in the previous chapters. The focus of the numerical modelling is toward the simulation of the H-M behaviour of the BSB material or buffer within the ITT test. A simple linear elastic model and an elasto-plastic model BGM (Blatz and Graham 2003) are used to define the mechanical behaviour of the buffer. A hydraulic constitutive model of van Genuchten (1980) (vG) and porosity dependent permeability (k_{wn}) model (Figure 8.2) are used to describe the hydraulic behaviour of

the buffer. Two types of boundary conditions are discussed: the buffer-only model (BO); and buffer-rock model (BR).

8.2 General Overview of Large Scale Isothermal Test (ITT)

The ITT was located in room 205 on the 240 Level of the URL as shown in Figure 8.3. The configuration of the ITT (Dixon et al. 2002) is illustrated in Figure 8.4. The ITT consists of the interaction of three types of materials: rock, buffer, and concrete. The focus of this thesis is toward the H-M behaviour of the buffer. The buffer is called the bentonite-sand buffer (BSB). The BSB material was a mixture of sodium bentonite and silica sand in equal parts by mass and compacted in situ to a dry density of 1.73 Mg/m^3 and gravimetric water content of 17.5%. The BSB material in this chapter will be addressed as buffer.

The buffer was installed within a 5-m-deep by 1.24-m diameter borehole in the unfractured, homogeneous, grey granite on the 240 level of the URL. The buffer material was compacted in situ into the bottom 2 m of the borehole. A 1.25m-thick concrete plug overlaid the compacted buffer to provide a vertical restraint against swelling (Figure 8.4).

Pore water pressures in the rock surrounding the borehole were monitored using different kinds of sensors including hydraulic and pneumatic piezometers and geological packer. A series of collection rings were installed to measure the inflow into the empty borehole, before and after the ITT experiment to provide a physical measurement of the water flux from the rock. The configuration of the seepage collection system of the ITT is illustrated in Figure 8.5. Four rings, SR1, SR2, SR3 and SR4, collected the inflow from different parts of the borehole. SR1 collected the water from the excavation damaged rock in the floor of the tunnel and from between the rock and the concrete floor. SR2

collected the water from the rock up to the base of the concrete plug. SR3 and SR4 collected the seepage that would be flowing into the buffer in the experiment. SR3 collected the water from the top of the BSB up to the mid-height of BSB, while SR4 was a borehole drilled into the rock at the base of the borehole (Chandler 2000, Dixon et al. 2001).

During the decommissioning stage, intensive sampling of the gravimetric water content and dry density determination of the buffer was conducted with up to 107 moisture content samples and 33 density samples being taken at eight elevations (Dixon and Chandler 2000). A number of psychrometers were installed inside the buffer to monitor the changes of the relative humidity (RH) values during the test. The RH measurements were related to the suction and gravimetric water contents within the buffer. The spatial measurements of the total stress in the buffer were also made during the tests (Dixon et al. 2002). The displacements at the top of the concrete were also measured during the test (Dixon et al. 2002).

The groundwater pressure contours in fracture zone 2 just below the 240 level of the URL before the start of the ITT is illustrated in Figure 8.6. The groundwater pressure around the ITT of approximately 1600 kPa (Figure 8.6) was used to define the boundary conditions for the modelling.

8.3 Material Properties

The material properties required as input into the numerical modelling using FLAC (Itasca 2001) include the properties of fluids (water and air), buffer, rock, and concrete.

8.3.1 Fluid Properties

The properties of fluids (e.g. water and air) are highly dependent on the temperature (Lide 2007). The temperature around the ITT was approximately ± 12.5 °C (Dixon et al. 2001). The viscosities of water (μ_w) and air (μ_a) at this temperature are 9.00×10^{-4} N·s/m² and 1.84×10^{-5} N·s/m², which produces a viscosity ratio (μ_w/μ_a) of 70 (Lide 2007). The density of water (ρ_w) is 1 Mg/m³. The water bulk modulus (K_w) and air bulk modulus (K_a) at STP conditions are 2.15×10^9 Pa and 1.42×10^5 Pa respectively (Munson et al. 1994).

8.3.2 Buffer Properties

8.3.2.1 Mechanical Parameters

Two types of mechanical constitutive models are used in the analysis: Linear Elastic (LE) model; and the BGM (Blatz and Graham 2003). The linear elastic model and elastoplastic model of Blatz and Graham (2003) are addressed as LE and BGM models respectively. The LE model has a bulk modulus (K) of 42 MPa and a shear modulus (G) of 36 MPa (Graham et al. 1997).

The parameters for the BGM are summarized in Table 7.4. These parameters were obtained from the calibration of the laboratory tests on the BSB material (Blatz 2000, Anderson 2003, and Siemens 2006). The coefficients of compressibility were derived from laboratory results on BSB material (Anderson 2003). The coefficient of compressibility (κ) of 0.05 (Table 7.4) generates an initial bulk modulus (K) of approximately 42 MPa. FLAC (Itasca 2000b) calculates the current bulk modulus (K_c) from specific volume (v), Bishop's effective stress (p'), and the coefficient of compressibility (κ):

$$K = \frac{v \cdot p'}{\kappa} \quad [8.1]$$

The relationship of this coefficient of compressibility (κ) and other coefficients of compressibility (κ_s , λ , λ_s) were derived from the curve fitting of the laboratory tests on the BSB material (Blatz 2000, Anderson 2003, and Siemens 2006).

The coefficients of compressibility presented in Table 7.4 is greater than in Tables 6.1 and 6.2, because the different stress state variables used in FLAC formulation and the original BGM model. Unlike the original BGM formulation that does not include the degree of water saturation (S_w), the modification of this constitutive model is required in FLAC formulation to include the degree of water saturation (S_w) to couple the mechanical (M) and hydraulic (H) behaviours. This modification has been discussed in Chapter 3. The Parameter Evaluation Method (PEM) in Chapter 6 and the parameter modification in chapter 3 were used to define yield surface of the model.

Considering the yield due to increase in suction has not been investigated even for a very high suction for the BSB material (Blatz 2000, Anderson 2003, and Siemens 2006), the yield line due to suction is defined as high as 10 MPa (Table 7.4), which is higher than the suction range of this modeling.

8.3.2.2 Hydraulic Parameters

The hydraulic constitutive models consist of a water retention curve (WRC) and a permeability model. The equations of the van Genuchten (1980) model and the kwn model are summarized in Tables 7.5-7.6. The parameters of the water retention curve (WRC) and the permeability functions of the van Genuchten (1980) model used in the

analyses are summarized in Tables 8.1. Table 8.2 summarizes the parameters of the kwn model. The parameters in Tables 8.1 and 8.2 were obtained from the curve fitting with the laboratory test results and consideration of the range of the degree of water saturation in the analyses. The range of degree of saturation used in the analysis and in the isothermal test varies from 75% to 100%. Figure 8.7 shows the plot of the WRC with the parameters from Tables 8.1 and 8.2 compared with laboratory test results (Siemens 2006, Anderson 2003, Blatz 2000, Tang 1999, Wiebe 1996, and Wan 1996) (Figure 8.7).

The water and air relative permeabilities (κ_w and κ_a) versus water degree of saturation (S_w) generated using parameters in Tables 8.1 and 8.2 are illustrated in Figure 8.8. The water permeability increases with an increase in degree of water saturation, but the relative air permeability decreases with an increase in water degree of saturation (Figure 8.8).

The dependence of the hydraulic conductivity on porosity is determined using Equation (5) in Table 7.6 and the parameters in Table 8.3. Figure 8.9 shows the plot of Equation 5 in Table 7.6 compared with the laboratory measurements from permeability tests (Dixon et al. 2002). The buffer material had an initial gravimetric water content of 18%, dry density of 1.73 Mg/m^3 , and specific gravity of 2.7 (Dixon et al. 2001, Chandler 2000), which resulted in the initial degree of water saturation (S_w) of 87%. The buffer had an initial suction of between 3.8 and 4.0 MPa.

8.3.2.3 Rock

The parameters of the rock are taken from previous numerical modelling by Thomas et al. (2003), which were also used by Guo and Dixon (2005). The mechanical behaviour of the rock is described using a linear elastic model with Young's modulus (E) and Poisson's

ratio (ν) of 60 GPa and 0.22 respectively that were measured experimentally by Annor and Jackson (1987). The threshold pressure of 0.25–5.5 MPa is determined from the intrinsic permeability based on the empirical relationship by Davies (1991). A threshold pressure of 0.7 MPa is used in the analysis (after Thomas et al. 2003). The van Genuchten (1980) model used to define the WRC of the rock with parameter (a) as 0.33 (Gens et al. 1998, Thomas et al. 2003). The saturated permeability of the rock is taken as 5.5×10^{-13} m/s (Graham et al. 1997). The hydraulic parameters of the rock are summarized in Table 8.4. The WRC for threshold pressures (P_o) of 0.25, 0.7, and 5.0 are illustrated in Figure 8.10. The rock is in a saturated condition and has a porosity (n) of 0.005 and a density of 2.65 Mg/m^3 (Chandler 2000).

8.3.2.4 Concrete

The concrete used in the isothermal test has a density of 2.397 Mg/m^3 and compressive strength of 105 MPa (Dixon et al. 2001). These density and compressive strength resulted in Young's modulus of concrete as 43.5 GPa (CPCA 1995). The Poisson's ratio of concrete was estimated as 0.11 to 0.27 (CPCI 1996), a Poisson's ratio (ν) of 0.2 can be used. Whitting (1988) measured the permeability of various concrete. Concrete permeability increases due to the increase of water to cement ratio w/cm (Whitting 1988, CAC 2006). Concrete with the w/cm of 0.26 and compressive strength of 105 MPa (Dixon et al. 2001) has an air permeability of 2.81×10^{-10} m/s and water permeability of 2×10^{-13} m/s (CAC 2006, Whitting 1998). Considering the concrete mechanical and hydraulic properties, as a fixed mechanical boundary condition and an impermeable boundary condition were applied in the numerical modelling of the ITT test.

8.4 Numerical Modelling

8.4.1 Fast Lagrangian Analysis of Continua (FLAC)

The numerical modelling of the ITT in this chapter is conducted using FLAC (Itasca 2001). The hydraulic-mechanical analysis with the two-phase flow option is used to consider the unsaturated state of the materials. User-defined functions are created in the FISH language (Itasca 2001) to implement the elasto-plastic model (BGM, Blatz and Graham 2003) and permeability surface model. The FISH embedded programming language in FLAC enables users to create user-defined function (Itasca 2001).

8.4.2 Boundary Conditions

The numerical analyses in this chapter use two types of boundary conditions: buffer-only (BO) analysis and buffer-rock (BR) analyses (Figure 8.11). The axisymmetric models are used for both models (BO and BR).

Figure 8.11a illustrates the hydraulic and mechanical of the BO analysis. The BO analysis only considered the buffer material. The fixed mechanical boundary condition was applied at the top, bottom, and perimeter of the buffer, where the buffer-rock and buffer-concrete interface were located in the ITT test. The impermeable hydraulic boundary condition was applied at the top of the buffer, where the buffer-concrete interface was located in the ITT test. A constant pore water pressure of 200 kPa was applied around the perimeter and at the bottom of the buffer as hydraulic boundary condition, where the buffer-rock interface was located in the ITT test. The BO analysis used linear the LE model to describe the mechanical behaviour of the buffer and the vG model to describe the hydraulic behaviour.

The buffer-rock (BR) analyses used two coupled constitutive models to describe the hydraulic-mechanical behaviour of the buffer. First, the BR-LE analysis used the LE model and the vG model. Second, the BR-BGMkwn used the BGM combined with the vG model to describe the water retention curve and the kwn to describe the permeability model. The rock in both cases is assumed to follow a linear elastic (LE) model and the vG model.

The axisymmetric domain of 20x30 m² is used for the buffer-rock (BR) analysis (Figure 8.11b). The far-field pore water pressure at the URL 240 level, where the isothermal test is located, is approximately 1600 kPa (Chandler 2000) (Figure 8.6). The pore water pressure with linear variation of 1450 kPa to 1750 kPa is applied at the perimeter to give an average pore water pressure of 1600 kPa (Thomas et al. 2003). The top and the bottom of the buffer have pore water pressures of 1450 kPa and 1750 kPa respectively. The hydraulic impermeable and fixed mechanical boundaries are applied at the buffer-concrete and concrete-rock interfaces. A zero pore water pressure boundary condition is applied at the location of the ITT for the whole test. The grid generated for modelling the buffer-rock (BR) analysis is shown in Figure 8.12.

8.5 Comparison of the Numerical Models and Field Measurements

The ITT experiment consists of three stages:

Stage 1: Seepage into an empty borehole;

Stage 2: Seepage from the rock into the BSB material; and

Stage 3: Decommissioning of the ITT experiment.

The input files of all the analyses (buffer-only (BO) and buffer-rock (BR) analyses) are presented in Appendix 5.

8.5.1 Stage 1: Seepage into an Empty Borehole.

Stage 1 establishes the initial conditions of the ITT experimental modelling. This stage only comprises rock material such that only the BR analysis is used to model this stage (Figure 8.11b). The pore water pressure boundary condition (Figure 8.11b) is applied around the perimeter of the 20mx30m axisymmetric finite difference grid (Figure 8.12). The radial distance versus pore pressure from the BR model at time equal to 1 month, 1 year, 2 years, and 3 years shows a good agreement with the field measurement (Figure 8.13). The pore water pressure for various depths (Figure 8.14) indicates that the pore pressure increases with depth for given radial distance. The pore water pressure contours in the full domain (20x30m) and around the borehole at a time of 3 years are illustrated in Figure 8.15a. The pore water pressure contours with water flow velocity vectors around the borehole is illustrated in Figure 8.15b. The end of stage 1 modelling is used as the initial rock pore water pressure at the start of stage 2 modelling for the BR analyses.

8.5.2 Stage 2: Seepage from the Rock to the Buffer Material

The comparison of measurements and the model includes the pore water pressure, the total stress, and water content of the buffer and rock. Both numerical model boundary conditions (BO and BR) (Figures 8.11a and 8.11b) are used to model this stage. The evolution of the pore water pressure located at the buffer-rock interface for all three models are presented in Figures 8.16 to 8.18. The computed response is compared with measurements of pore water pressure in the buffer near the interface (IBP01 and IBP02). The BO-LE analysis generally underestimated the pore pressures at early years

compared to the measurements and it reaches equilibrium at 2.5 years (Figure 8.16). The BR-LE analysis underestimates the measurements at all times and does not reach equilibrium (Figure 8.17). Pore pressures at the bottom (IBP2, Figure 8.18) from BR-BGMkwn model over estimates the measurements, while it underestimates the measurements around the top perimeter of the buffer-rock interface (IBP1, Figure 8.18). Unlike the BO analysis, both of the BR-LE and BR-BGMkwn do not reach an equilibrium state. Incorporating the rock material into the models (BR-LE and BR-BGMkwn) makes the desaturation process due to the movement of pore air pressure from the BSB to the rock possible to occur. The reduction of the degree of saturation for BR-LE and BR-BGMkwn models around the buffer-rock interface are illustrated in Figure 8.19. The decrease in the degree of water saturation in the rock reduces the water permeability of the rock. The rate of change of pore water pressure for the BR analyses was slower than for the BO analysis, and as a result that the BR analyses did not reach equilibrium. Considering that the piezometers (IBP1 and IBP2) only measured the positive pore water pressure and that IBP1 recorded nearly zero pressure throughout the test, the results of the BR-BGMkwn and BR-LE models at IBP1 may not be compared to the field measurements (Figures 8.17-8.18).

The comparisons of field measurements of total stress at the buffer-rock interface (IBG1, 2, 3) for BO-LE, BR-LE, and BR-BGMkwn analyses are illustrated in Figures 8.20-8.22 respectively. The BO-LE analysis overestimates the total pressure field measurement (Figure 8.20). The BR-LE analysis (Figure 8.21) is close to the field measurements, but the computed total stress continues to increase with time due to the characteristics of the linear-elastic (LE) model. The BR-BGMkwn uses the BGM model (Blatz and Graham 2003) (Figure 8.22). It produced total stresses that do not continue to increase with time such as shown in the field measurement (Figure 8.22). The field measurements shows

that the initial condition of the buffer-rock is not the same for IBG1, 2 and 3 (Figures 8.20, 8.21, and 8.22) at the beginning of the ITT experiment, while the models (BR-LE and BR-BGMkwn) uses uniformly distributed total stress at the buffer-rock interface at the start of the stage 2. Taking into account the nonuniformly distributed total stress at the initial condition of the ITT experiments may improve the comparison between the model and the computed responses. The difference between these models and the measurements may also be caused by the possible anisotropic permeability of the rock that is not taken into consideration. The degree of anisotropic permeability of the rock can be estimated using the time-dependent boundary condition analysis in Chapter 9. However, further investigation of the degree of anisotropic permeability is beyond the scope of this research and a suggestion for future research.

Figures 8.23-8.28 compare the measurements of the total pressure. The IBR1 and IBR2 were right at the concrete-rock interface, while the IBR3 was very close to the buffer-rock interface. The BO-LE analysis overestimates the total stress in the buffer at IBR1-3 (Figure 8.23) and IBK1-4 (Figure 8.26). Both of the BR-LE and BR-BGMkwn models are close to the field measurements at locations IBR1-3 (Figures 8.24 and 8.25) and IBK1-4 (Figures 8.27 and 8.28). Again, the linear-elastic model shows a continuous increase in total stress in the BR-LE model (Figures 8.24 and 8.27). The combination of the elastoplastic model (the BGM) and porosity dependent permeability (kwn) models prevents the continual increment of total stress in the BR-BGMkwn model (Figures 8.25 and 8.28). An improvement to the models' parameter calibration is still required for the BGM and kwn models as indicated by the total pressure comparison in Figures 8.25 and 8.28 and it is suggested for future research.

The evolution of gravimetric water content in the BSB material for the three models is illustrated in Figures 8.30-8.32. The location of the psychrometers measurements is illustrated in Figure 8.29. The BO-LE analysis reaches maximum gravimetric water content of 20.3% at 3 years (Figure 8.30). The gravimetric water content at the end of the test is uniformly distributed throughout the sample (Figure 8.30), which shows the limitations of this model. The computed gravimetric water contents from the BR-LE and BR-BGMkwn analyses do not reach 100% saturation (Figures 8.31 and 8.32). Both of the models (BR-LE and BR-BGMkwn) show a variation of the gravimetric water content with location, which is also the case with the field measurements (Figures 8.31 and 8.32).

Compared with the BR-LE model (Figure 8.31), the gravimetric water content produced by the BR-BGMkwn model (Figure 8.32) shows a greater gravimetric water content difference between the gravimetric water content at the outer layer (IBX 2, 3, 5, 8, 10, 13, 15, 18, 20, 23, 24) and inner layer (IBX 7,12, 4, 6, 9, 11, 14, 16, 19, 21, 17, 22) (Figure 8.29). Considering the buffer material as the finite difference grid, the increase in volume at the outer layer due to the increase of degree of saturation will squeeze the the next layer towards the inside of the buffer and decrease the volume or porosity. Consequently, the decrease in porosity will decrease the water permeability when using a porosity-dependent permeability (kwn) model. This mechanism creates 'pseudo impermeable layer' that moves from the outer layer to the inner layer and creates gravimetric water content difference in the BR-BGMkwn model (Figure 8.32). This mechanism in the kwn model incorporates the reduction of a flow not only at the buffer-rock interface, but also inside the buffer material. Figure 8.33 illustrates the calculated water content versus time at IBX18 (Figure 8.29 shows the location of the IBX18) from the three analyses (e.g. BO-LE, BR-LE, and BR-BGMkwn) compared with the

measurements. Both the BR-LE and the BR-BGMkwn analyses show good agreement with the field measurements at IBX18 location (Figure 8.33). Although the BO-LE models reach the same gravimetric water content at the end of the test, the maximum gravimetric water content is reached much faster than the measurements (Figure 8.33).

The evolution of the water uptake measurements from the psychrometer measurement at the top 1 m and bottom 1 m of the BSB material (Chandler 2000) is compared with the results of the models (BO-LE, BR-LE, and BR-BGMkwn) (Figures 8.34-8.36). The evolution of the water uptake from the BR-BGMkwn analysis (Figure 8.36) is closest to the psychrometer measurement compared to the evolution of the water uptake from BO-LE and BR-LE analyses (Figures 8.34 and 8.35). Assuming that the psychrometer measurement is accurate, the total water uptake measurement was calculated from the end-of-test psychrometer reading (without any correction) is 43.62 litres. Table 8.4 summarizes the percent difference of these values with the calculated total water from the three analyses.

Chandler (2000) reported that the total water uptake based on measured post-test gravimetric water contents and dry densities was 82 litres, which indicated that the water uptake calculated based on the psychrometer reading underestimated the actual gravimetric water content. The correction in the calculation of the total water uptake based on psychrometer data was introduced by linear extrapolation of 3-year rate of water uptake. This correction resulted in the total water uptake of 68 litres. Based on this extrapolation, Dixon et al. (2001) concluded that either:

- First, the diminished rate of water uptake indicated by the psychrometers during the last two years of the test was not an accurate reflection of the rate of water uptake and that rate of water uptake was relatively uniform throughout the tests;

- Second, the corrected psychrometer data underestimated the water uptake for the entire duration of the test.

Based on the first conclusion (Dixon et al. 2001), the peak of the water uptake measurements should not exist, which were observed from the evolution of the calculated water uptake from the three analyses (BO-LE, BR-LE, and BR-BGMkwn) (Figure 8.34 to 8.36). The total water uptake calculated directly from the psychrometer measurements presented in Table 8.4 underestimated the measured total water uptake based on the second conclusion (Dixon et al. 2001).

Although Table 8.4 shows that the BR-BGMkwn results in a water uptake closest to the field measurements with percent differences less than 10%, this comparison cannot be made (Table 8.4). However, considering of the 'trend' of water uptake evolution is more important than the 'magnitude' of the total water uptake at the end of test to evaluate the ability of the model to capture the behaviour of the system. Table 8.4 is presented that comparison of the 'magnitude' at the end of test alone is not sufficient to evaluate the performance of the constitutive models. Improvement of the parameters of the constitutive models and the boundary conditions used in the numerical modeling can reduce the difference in the magnitude of the modeling and the measurements. The interaction of people doing numerical modelling and laboratory or field testings is very important to capture the actual behaviour of the system.

8.5.3 End-of-Test Measurement

The profiles of gravimetric water content and dry density at the end of the test calculated from the three models are presented in Figures 8.37 and 8.38. The buffer material

having 2 m height is divided into 8 layers (A to H). Layer A to H is used as the x-axis in Figures 8.37 and 8.38; layer A is the top of the BSB specimen, while H is the base of the borehole. The right end of each layer is the outer perimeter of the specimen, while the other end is the central axis (Figures 8.37 and 8.38).

The field measurement shows that the gravimetric water content increases with depth. It ascends from the central axis to the outer perimeter (Figure 8.37). The BO model results in a uniformly distributed gravimetric water content after only 3 years of elapsed time (Figure 8.37), which is inadequate to represent the field measurements. The BR-LE and BR-BGMkwn models show the same trend as the field measurements (Figure 8.37). The difference between the outer layer and the central axis increases with an application of the BGM and kwn models, which agree with the field measurements (Figure 8.37). The water content contours within the buffer material at the end of the test for the BR-LE and BR-BGMkwn models, as well as the field measurements (Dixon et al. 2002) are illustrated in Figure 8.40.

The BO-LE analysis shows the dry density is uniform throughout the sample at the end of the test (Figure 8.38). The BR-LE and BR-BGMkwn model shows the variation of dry density with the radial distance and depth, which agrees with the trends in the field measurements (Figure 8.38). The range of the variation of the dry density with the depth and radial distance also increases with the application of BGM and kwn models (Figure 8.38).

The dry density versus water content from all FLAC analysis compared with the field measurements indicate that the additional features introduced in the constitutive models increase the variability of this result (Figure 8.39). Note that the BO-LE analysis results

in the uniform gravimetric water content versus dry density throughout the sample at the end of the test, so that it only gives one point in Figure 8.39. Although the magnitude of the dry density of the BR-LE and BR-BGMkwn models at the end of the test has generally less range than the field measurements (Figure 8.39), the contours of dry density in the BSB sample of the BR-LE and BR-BGMkwn gives the same pattern as the field measurements (Figure 8.41).

Figure 8.42 shows the degree of water saturation versus radial distance of two FLAC models (i.e. BR-LE and BR-BGMkwn) at initial and final conditions. This indicates desaturation occurring along the radial direction at the buffer-rock interface. This desaturation has also been observed in Figure 8.19. This desaturation process also takes place at the bottom of the borehole for the BR-LE and BR-BGMkwn models as shown by Figure 8.19.

Figure 8.43 shows the degree of water saturation versus depth for radial distances (i.e. 0, 0.2 m, 0.4 m, and 0.62 m (buffer-rock interface)) from the BR-LE and the BR-BGMkwn analyses. The degree of water saturation versus depth for the BR-LE analysis is generally greater than that of the BR-BGMkwn analysis (Figure 8.43). Considering that a decrease in the degree of water saturation reduces the permeability. The desaturation around the bottom of the borehole for the BR-LE analysis (Figure 8.43a) is greater than that of the BR-BGMkwn analysis (Figure 8.43b). The desaturation zone in the rock for both models is approximately 0.5 m (Figure 8.43). The difference between degree of saturation at the outer layer and the inner layer at the BR-BGMkwn models indicates the 'pseudo impermeable layer' mechanism produced by permeability-dependent (kwn) constitutive models (Figure 8.43). Unlike the BR-LE model, the decrease of permeability

in the BR-BGMkwn model is not only due to the desaturation at the buffer-rock interface, but also due to the decrease of porosity inside the buffer (Figure 8.43).

Figure 8.44 shows the pore water pressure versus depth for radial distances (i.e. 0, 0.2 m, 0.4 m, and 0.62 m (buffer-rock interface)) from the BR-LE and BR-BGMkwn analyses.

The desaturation mechanism in the rock is possible to occur with the increase of the pore air pressure, although the positive pore water pressure in the rock was observed in the BR-LE and BR-BGMkwn analyses (Figure 8.44). Considering the analyses were conducted using 2-phase flow formulation, unlike 1-phase flow formulation the pore air pressure (u_a) is not constant. Although the pore water pressure (u_w) slightly increases above zero at the buffer-rock interface (Figures 44a and b), the increase of the pore air pressure (u_a) induced by the air movement from the buffer to the rock is greater than the pore water pressure (u_w) increase at the buffer-rock interface. This will result in an increase of suction ($u_a - u_w$) and a decrease in the degree of saturation.

The following scenario can explain this de-saturation mechanism. Initially there is air within the buffer as it is in unsaturated condition when it is emplaced in the borehole. The flow of water from the surrounding rock into the buffer causes the flow of air from the buffer to the rock. The flow of water results in the increase of pore water pressure, while the flow of air results in the increase of pore air pressure. An increase in pore air pressure is greater than an increase in pore water pressure at the rock close to the buffer and result in a decrease of degree of water saturation at this location.

8.6 Concluding Remarks

Modelling the full-scale isothermal test (ITT) has been undertaken using a 2-phase flow hydraulic-mechanical analysis in FLAC2D (Itasca 2001) with 3 combinations of boundary conditions, mechanical and hydraulic constitutive models:

- 1) buffer only analysis using constant pore pressure boundary conditions, linear elastic and van Genuchten (1980) models (BO)
- 2) buffer-rock interaction analysis using far-field boundary condition, linear elastic and van Genuchten (1980) models (BR-LE)
- 3) buffer-rock interaction analysis using far-field boundary condition, Blatz and Graham (2003) and van Genuchten (1980) models (BR-BGMkwn).

The following conclusions can be made based on the analysis:

- Analyses that include the rock (e.g. BR-LE and BR-BGMkwn) provide a better simulation of the ITT (Dixon et al. 2002) than buffer only analysis (BO). This indicates that the rock properties and boundary conditions have a significant role in the ITT test.
- The desaturation mechanism at the buffer-rock interface is investigated around the borehole in the buffer-rock (BR-LE and BR-BGMkwn) analysis. This mechanism could not be investigated in the buffer-only analysis. This mechanism prevents the buffer from reaching 100% water degree of saturation (S_w) and creates a gravimetric water content gradient at the end on the test, which is also the case with the field measurements.
- Application of the elasto-plastic (BGM) and porosity-dependent permeability (kwn) models in the buffer-rock (BR) analysis creates a 'pseudo impermeable layer' mechanism, which has been investigated in Chapter 7. This results in the

- higher gravimetric water content variation in the outer and inner layer in the buffer (Figures 8.30 and 8.31).
- The plots of computed gravimetric water content (Figure 8.33) and dry density (Figure 8.44) can illustrate the various mechanisms reproduced by the models. The BO analysis does not have any mechanism to inhibit 100% saturation. The BR-LE analysis has a 'desaturation' mechanism in the rock close to the buffer, while the BR-BGMkwn has both 'desaturation' in the rock and 'pseudo impermeable layer' mechanisms within the buffer to inhibit 100% saturation.
 - The end-of-test measurements of the small-scale infiltration test (Siemens 2006) show the variations of the degree of saturation with radial distance. Thus, there should be mechanism within the buffer that inhibits complete saturation. In the case of large-scale isothermal test, there could be 2 mechanisms that slow the rate of buffer saturation: one within the buffer and the other is in the rock near the interface. The BR-BGMkwn analysis produces two mechanisms: 'desaturation' in the rock near the interface and 'pseudo impermeable skin' within the buffer.
 - Since both 'desaturation' and 'pseudo impermeable skin' mechanisms can inhibit complete saturation. In general, two-phase flow formulation in FLAC2D can simulate the hydro-mechanical behaviour of the buffer in the ITT tests, if the rock is being considered in the modelling.

8.7 Future Research

Figure 8.45 shows comparison between FLAC models (BR-LE and BR-BGMkwn) and field measurements of the pore water pressure versus radial distance from borehole center at initial and final conditions. The overall pore water pressure at the final is greater than at the initial condition (Figure 8.45). In the buffer (radial distance < 0.62 m),

the BR-LE model gives greater pore water pressure than BR-BGMkwn model. In the rock both models produce greater response than the measurements (Figure 8.42).

Modelling the large-scale ITT experiments requires adequate constitutive models and properties of the buffer and the rock. The improvement in the modelling of the buffer-rock interface zone is significant. Guo and Dixon (2005) introduced an application of the excavation damage zone (EDZ) at the interface of the BSB and rock that has higher water permeability. This study focuses on the behaviour of the BSB material, so that the application of the EDZ is beyond the scope of this study and it is left as a suggestion for future research.

The rock properties can also be estimated by back-analysis using time-dependent pore water pressure boundary condition. This idea is presented as suggestion for future research in the last chapter. A preliminary study of time-dependent pore water pressure boundary conditions is presented in Chapter 9.

Table 8.1. Hydraulic constitutive model equations and parameters for van Genuchten (1980) model for Bentonite Sand Buffer (BSB) material.

Parameters	Value
Parameters, a	0.2
Parameters, b	0.5
Parameters, c	0.5
Threshold pressure, P_o (MPa)	3.5
Residual water degree of saturation, S_{res}	0.1
Saturated water mobility coefficient, k_{w-sat} ($m^2/Pa-sec$) (related to water permeability, $k_{w-sat} = 5 \times 10^{-13}$ m/s (Graham et al. 1997))	5×10^{-16}
Viscosity ratio, μ_w/μ_a	70

Table 8.2. Hydraulic constitutive model parameters for porosity-dependent model (kw-n) for Bentonite Sand Buffer (BSB) material.

Parameters	Value
Parameters, a	0.2
Parameters, b	0.5
Parameters, c	0.5
Threshold pressure, P_o (MPa)	3.5
Residual water degree of saturation, S_{res}	0.1
Saturated water mobility coefficient, k_{w-sat} ($m^2/Pa-sec$) (related to water permeability, $k_{w-sat} = 5 \times 10^{-13}$ m/s (Graham et al. 1997))	5×10^{-16}
Viscosity ratio, μ_w/μ_a	70
Minimum porosity, n_{min}	0.30
Maximum porosity, n_{max}	0.45
Parameter relating permeability and porosity, na	1
Parameter relating permeability and porosity, nb	2.5
Maximum saturated permeability, k_{w-max}^{sat} (m/s) (correlated with maximum porosity, n_{max})	1×10^{-12}
Maximum saturation parameter, A (after Siemens 2006)	38.49
Maximum saturation parameter, B (after Siemens 2006)	-3.7829
Specific gravity of the BSB, G_s	2.7

^(a) Additional parameters required in FLAC;

^(b) These parameters are generated as twice of linear elastic model parameters for BSB material after Graham et al. 1997.

Table 8.3. Hydraulic constitutive model equations and parameters for van Genuchten models for the rock (1980)

Van Genuchten (1980)	
Parameters, a	0.33
Parameters, b	0.5
Parameters, c	0.5
Threshold pressure, P_o	0.7 MPa
Residual water degree of saturation, S_{res}	0
Saturated water permeability, k_{sat}	5.5×10^{-13}
Viscosity ratio, μ_w/μ_a	70

Table 8.4. Water uptake calculations of the numerical models

Models	Total water uptake (litres)	Percent difference with the end of test psychrometer measurements (%)
BO-LE	108.91	+ 149.68 %
BR-LE	58.14	+33.29 %
BR-BGMkwn	47.76	+9.49 %

End of test psychrometer measurement without correction
= 43.62 litres (from Figures 8.38-8.40)

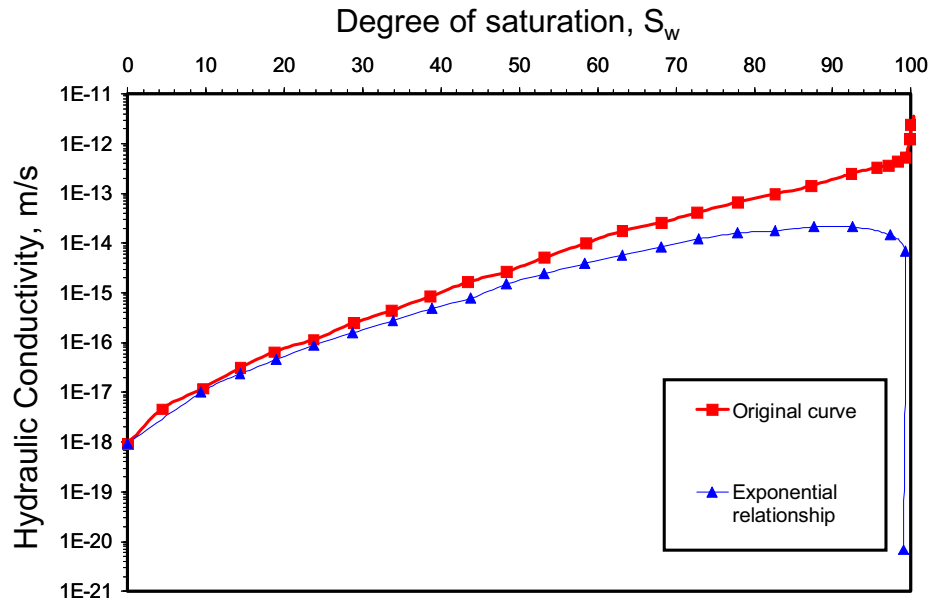


Figure 8.1 Two types of permeability function to model large scale Isothermal Test (after Thomas et al. 2003)

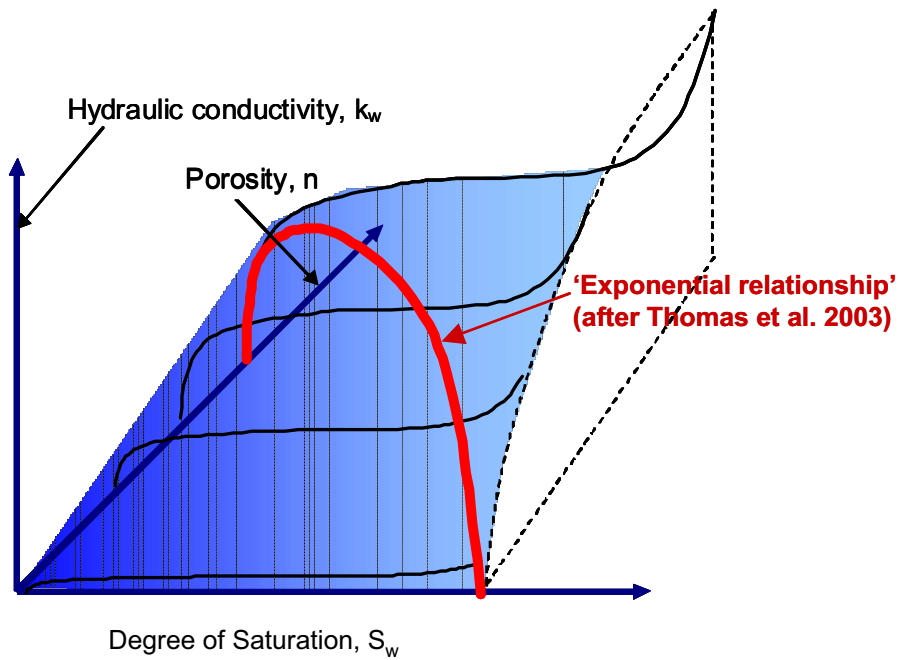


Figure 8.2 Permeability surface in S_w - n - k_w space

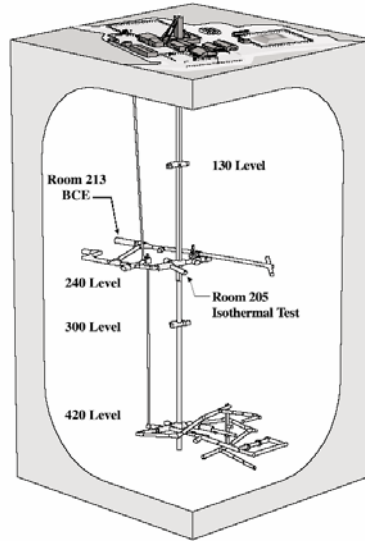


Figure 8.3 General layout of the AECL's Underground Research Laboratory (URL) at Lac du Bonnet, Manitoba, Canada (Dixon et al. 2002)

Used with permission by Dixon, July 23, 2007.

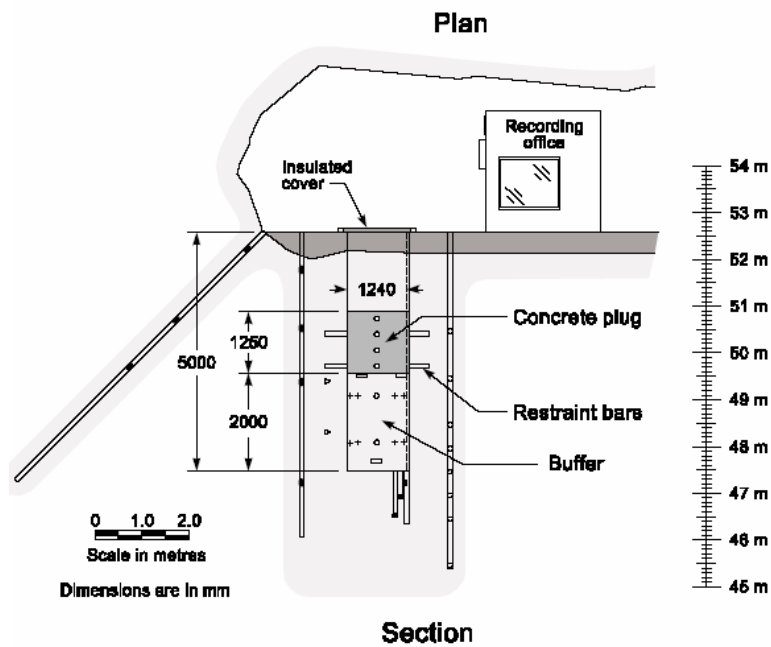


Figure 8.4 Configuration of the isothermal test (Dixon et al. 2002)

Used with permission by Dixon, July 23, 2007.

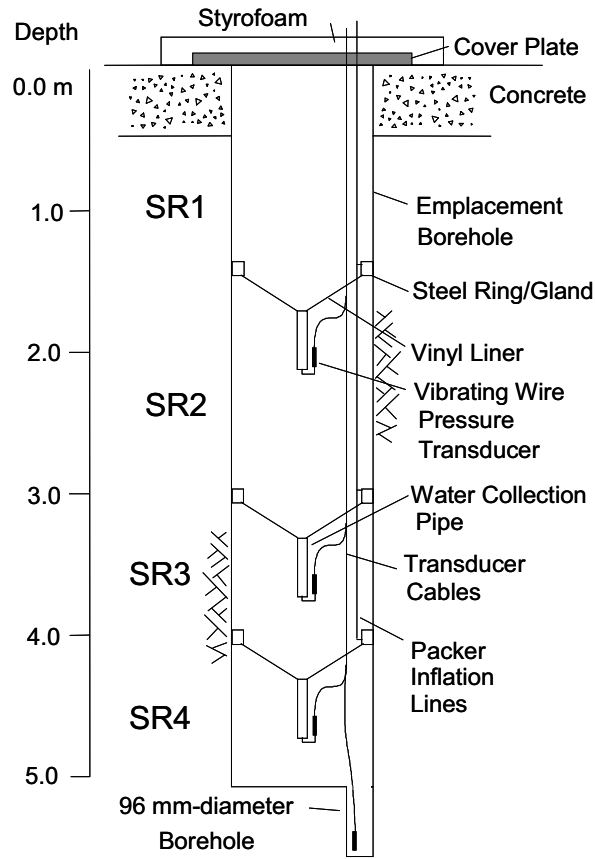


Figure 8.5 Configuration of the Isothermal Test Seepage Collection System (Dixon et al. 2001)

Used with permission by King, July 23, 2007.

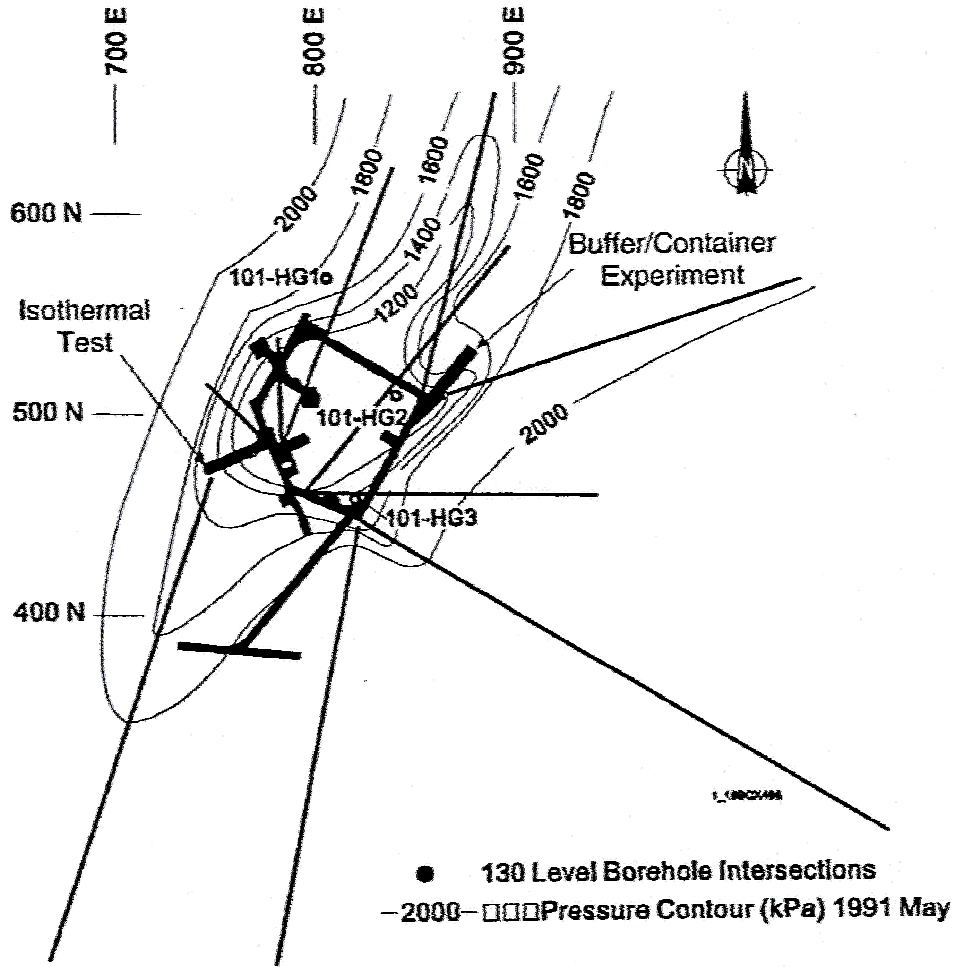


Figure 8.6 Groundwater pressures (kPa) at the 240 level of the URL (Dixon et al. 2001)

Used with permission by King, July 23, 2007.

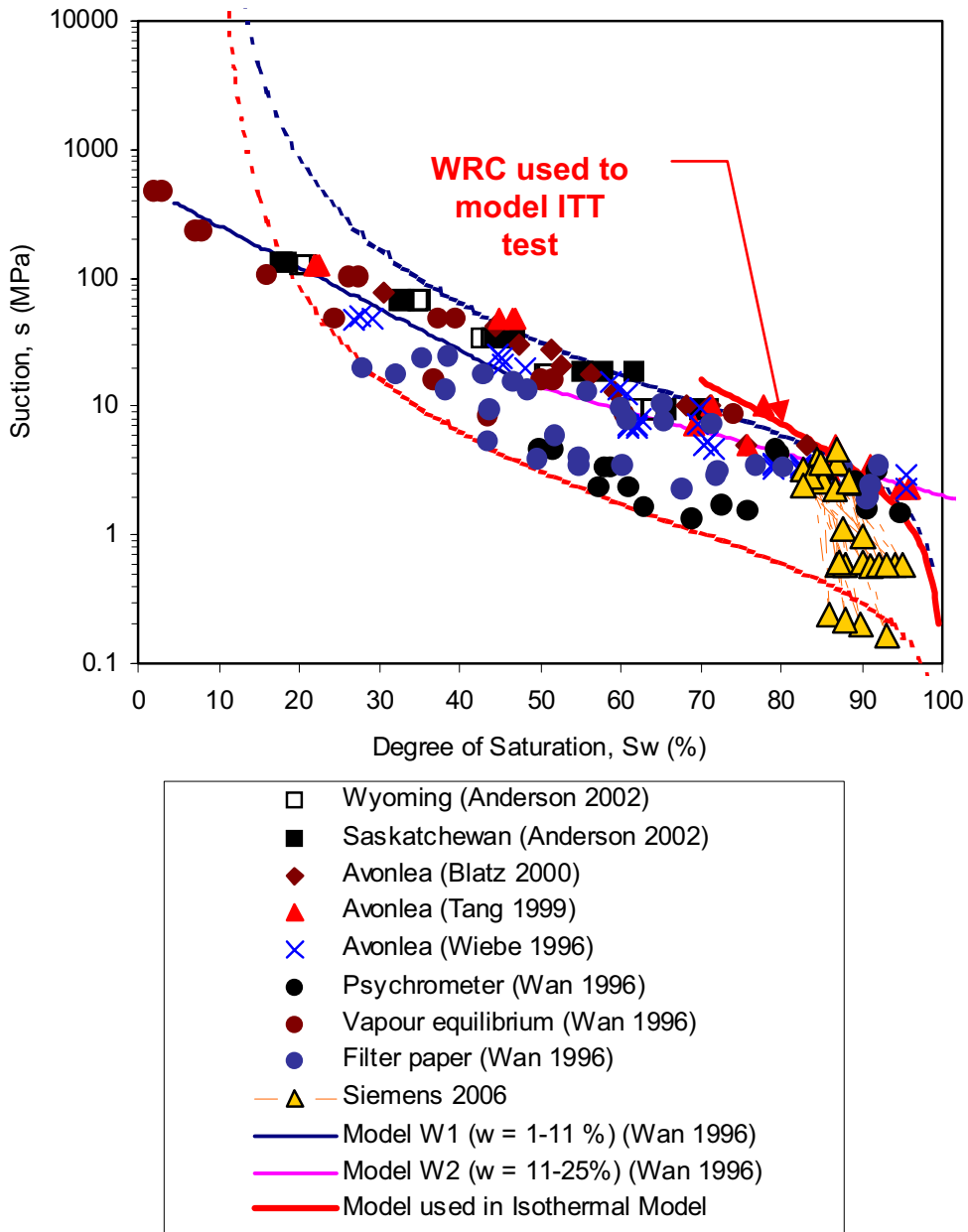


Figure 8.7 Water retention curve used to in the model compared with the laboratory measurements of the BSB material

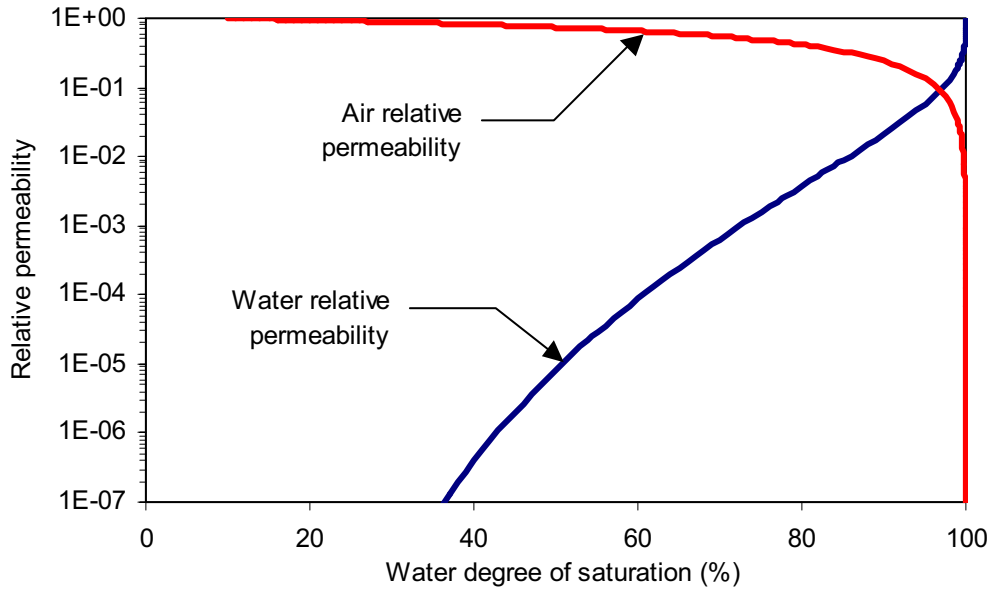


Figure 8.8 Water and air relative permeability as a function of degree of water saturation

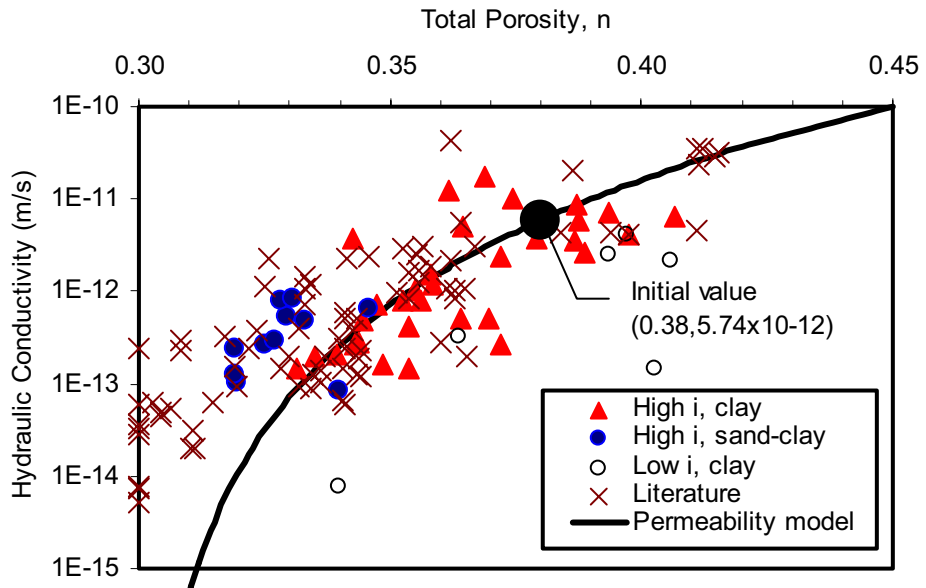


Figure 8.9 Hydraulic conductivity as a function of the effective flow porosity (data points after Dixon et al. 1999)

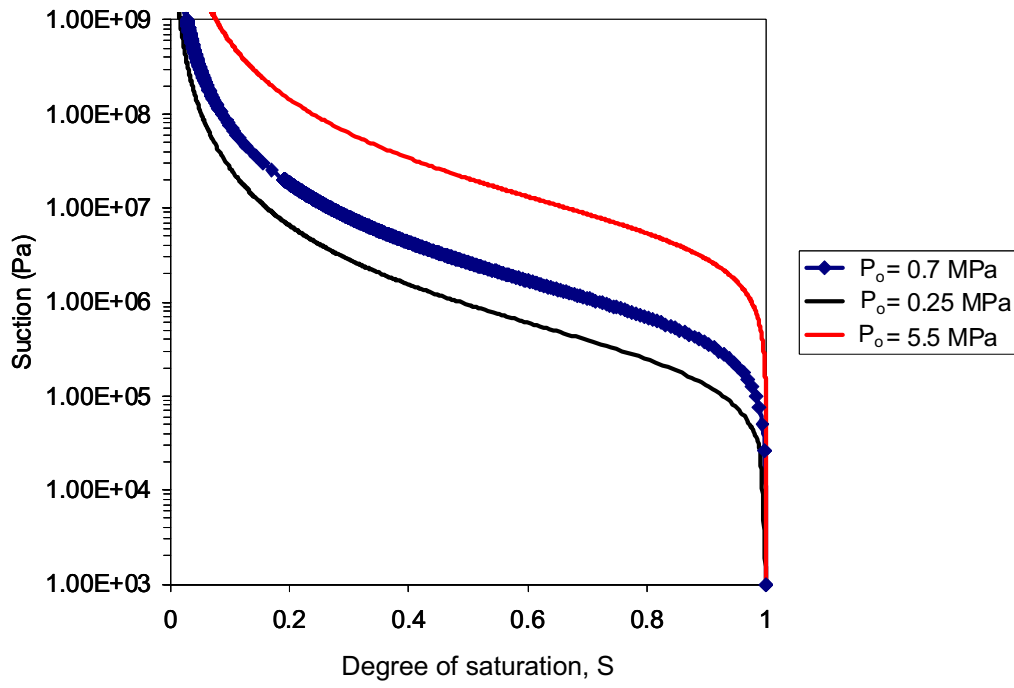
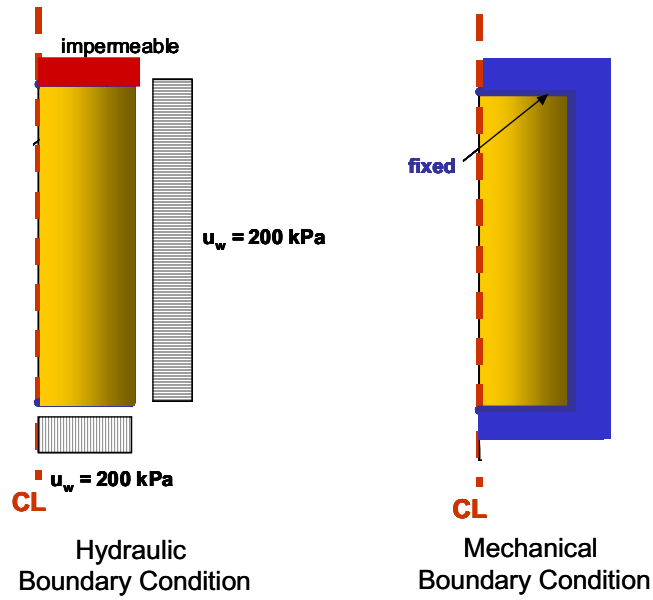


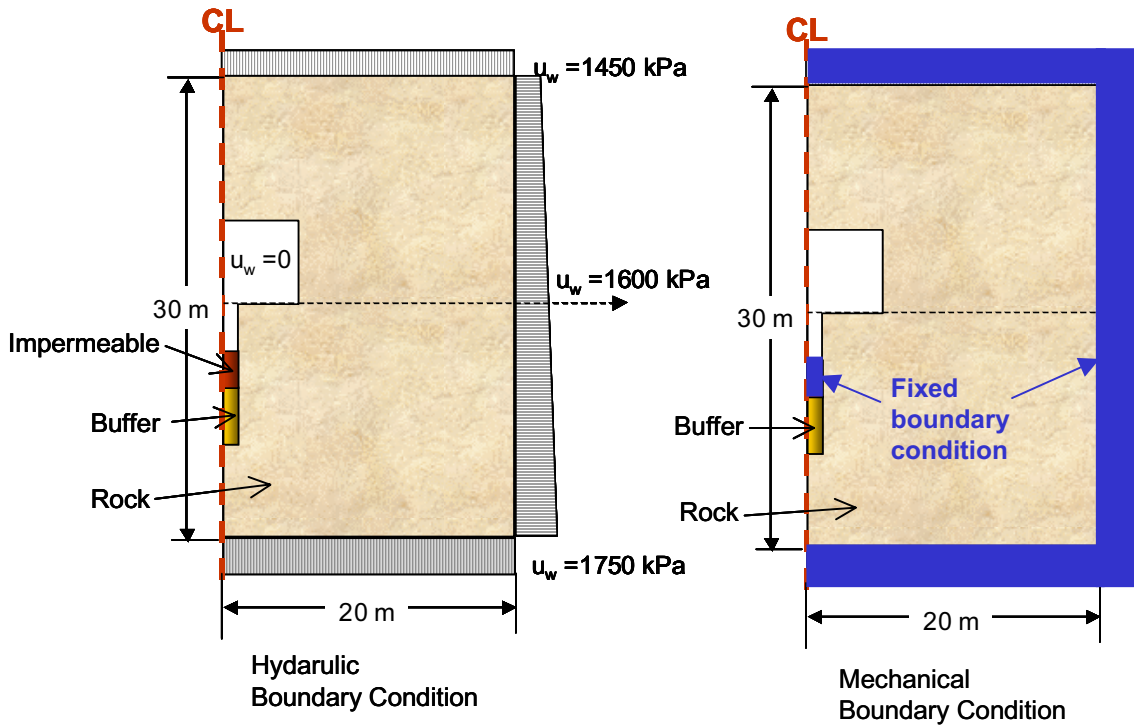
Figure 8.10 Water retention curve for the rock

Buffer Only Analysis (BO)



(a)

Buffer-Rock Interaction (BR)



(b)

Figure 8.11 Two types of boundary conditions used in the numerical models

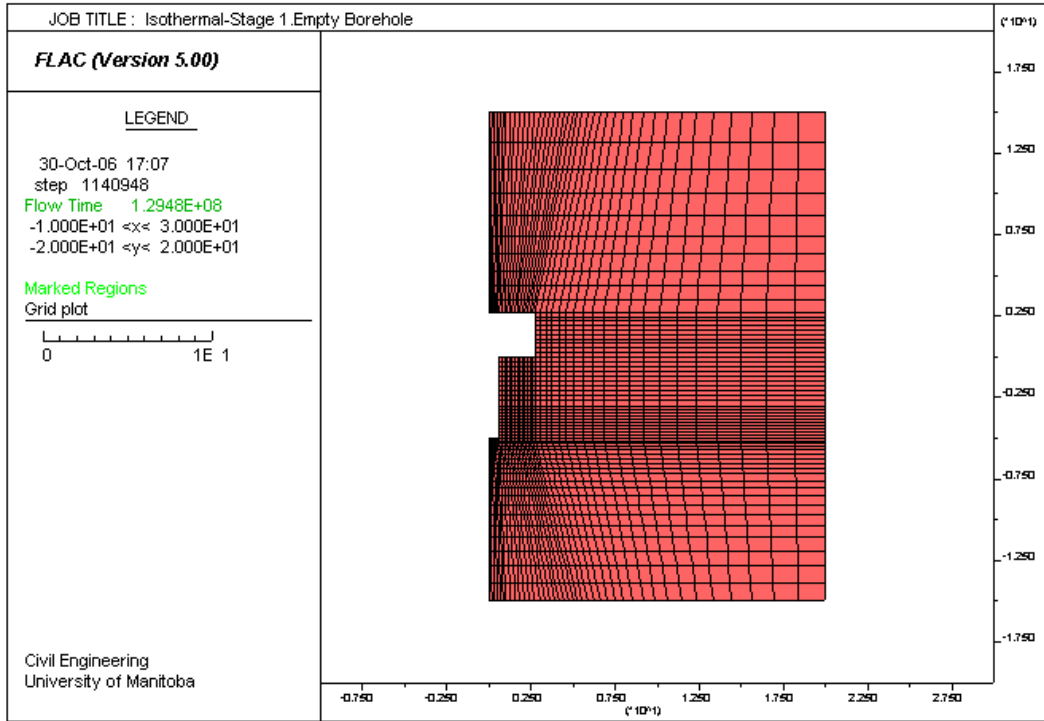


Figure 8.12 Finite difference grids used to model stage 1 of the isothermal test (ITT)

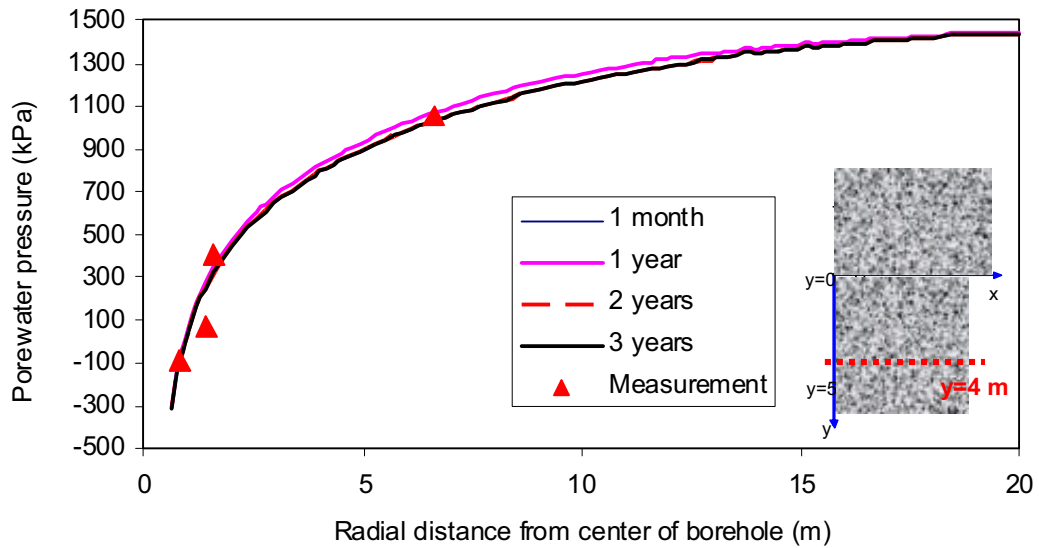
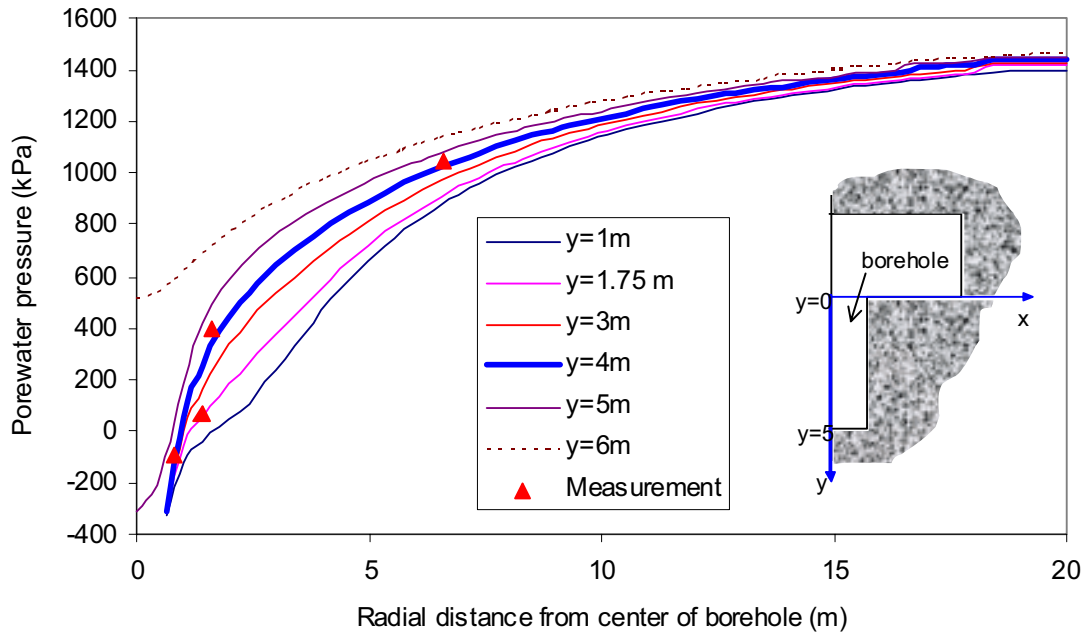
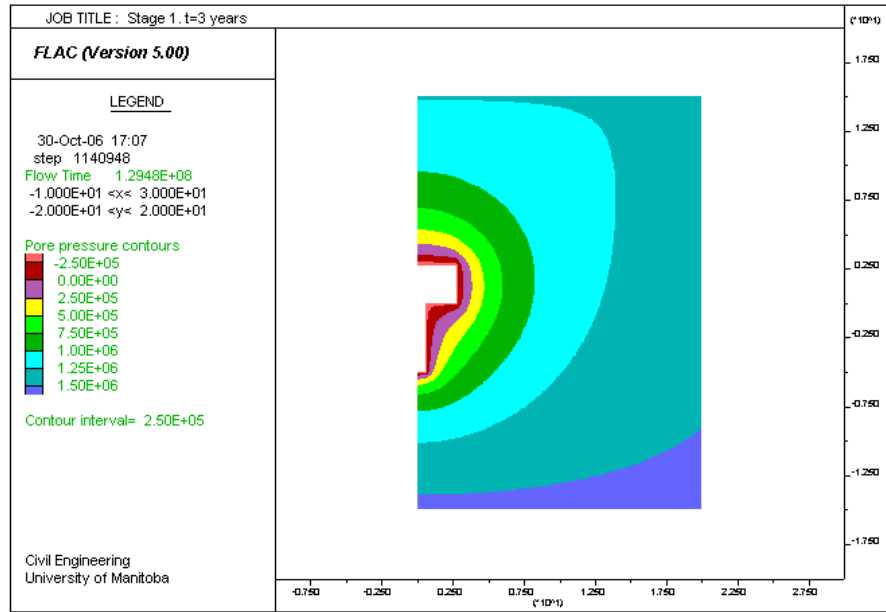


Figure 8.13 Pore pressure versus radial distance from center of borehole in the empty borehole at $t = 1$ month, 1 year, 2 years, and 3 years at $y = 4$ m (middle of the buffer)

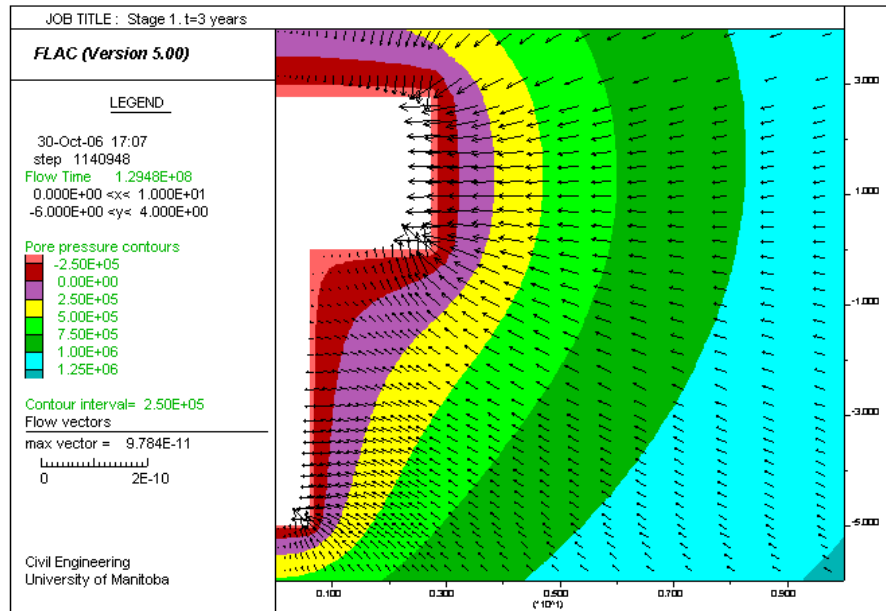


Error!

Figure 8.14 Pore pressure versus radial distance from center of borehole in the empty borehole at various depths at the initial conditions of isothermal test (t = 3 years)



(a) 20m x 30m domain



(b) around the borehole
 (with water flow velocity vectors)

Figure 8.15 Pore pressure contours at the start of isothermal test

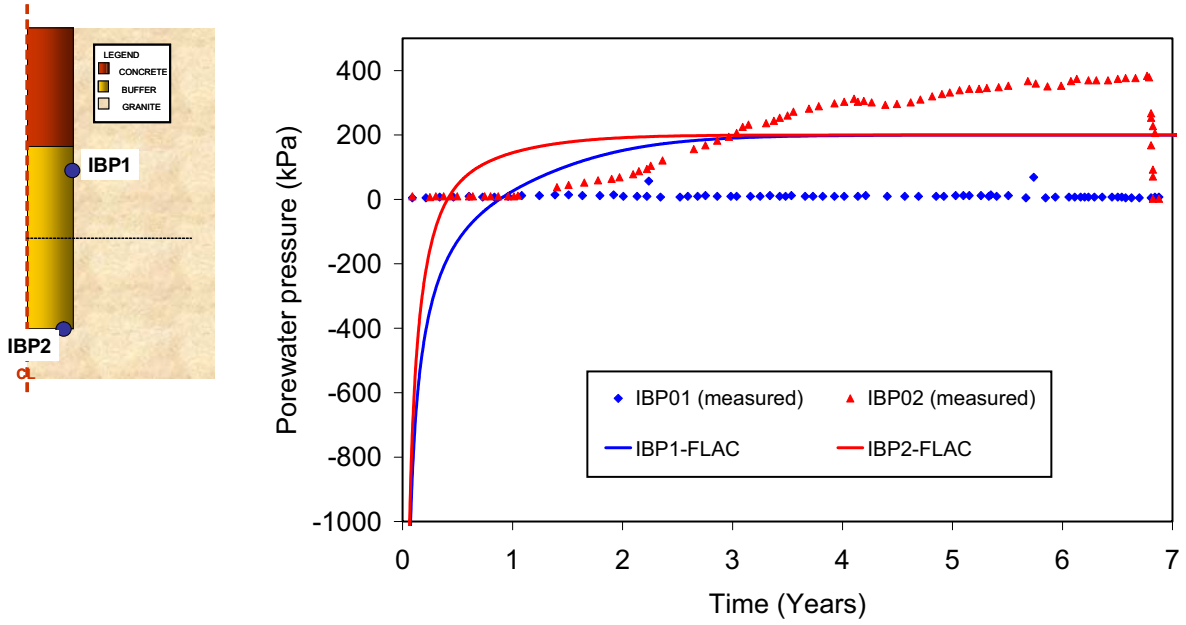


Figure 8.16 Pore water pressure measurements compared with buffer-only analysis using linear elastic model (BO-LE) at locations IBP01 and IBP02

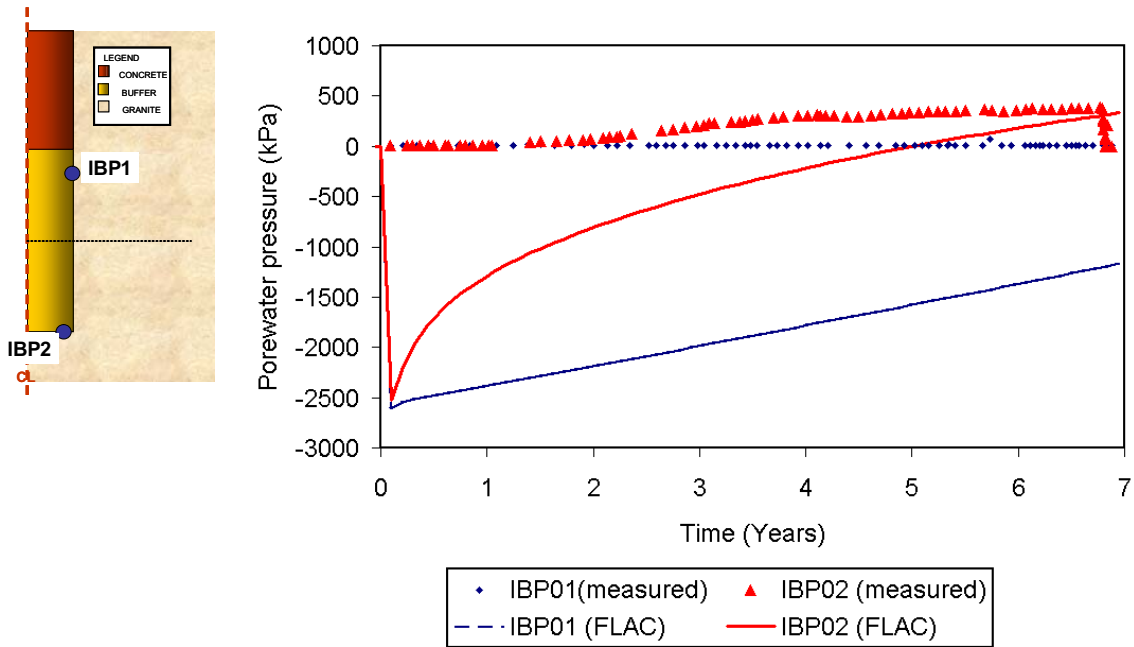


Figure 8.17 Pore water pressure measurements compared with buffer-rock analysis using linear elastic model (BR-LE) at locations IBP01 and IBP02

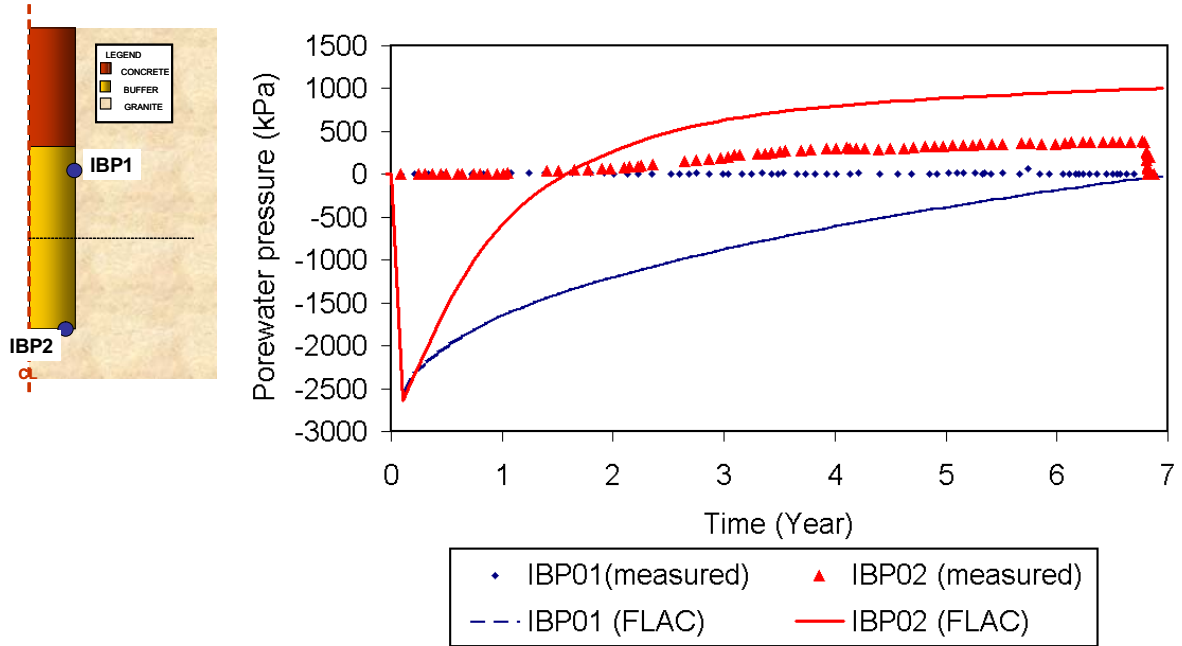


Figure 8.18 Pore water pressure measurements compared with buffer-rock analysis using BGM and porosity-dependent models (BR-BGMkwn) at locations IBP01 and IBP02

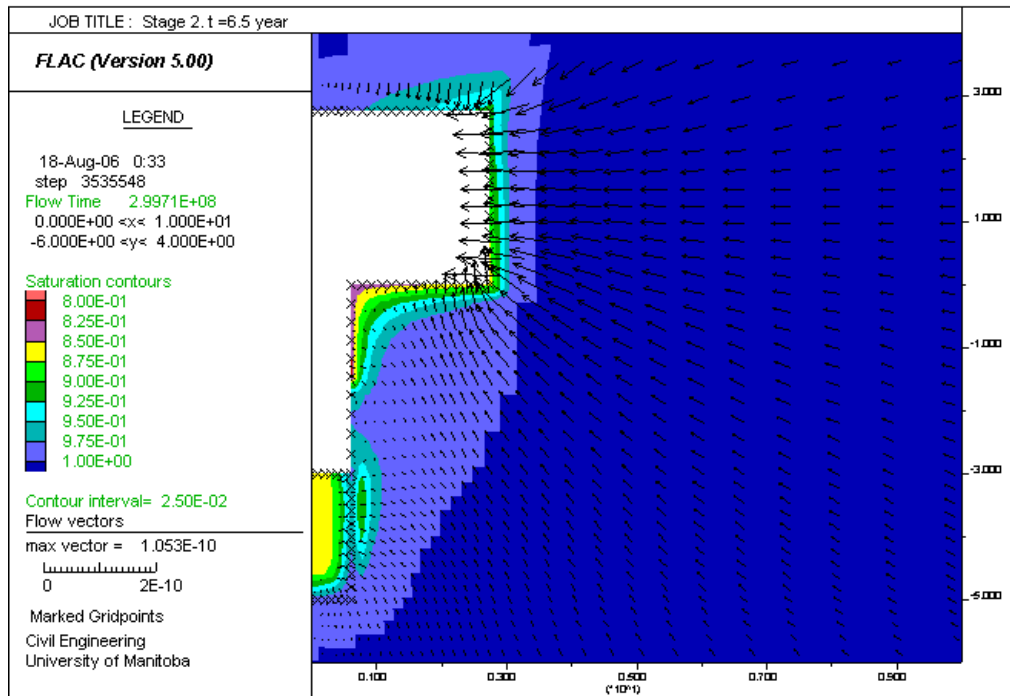


Figure 8.19 De-saturation mechanism in the buffer-rock interface (BR-BGMkwn analysis)

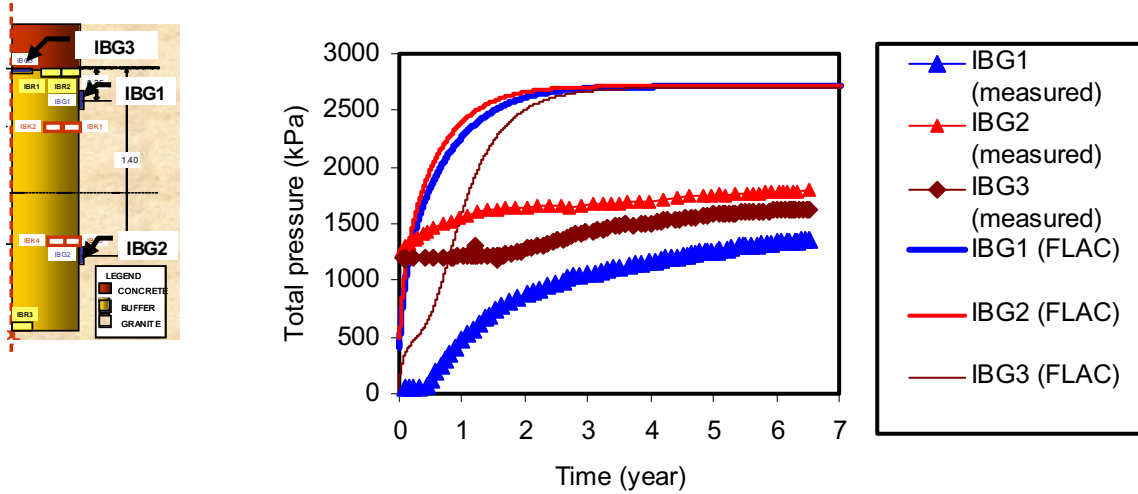


Figure 8.20 Total pressure measurements compared with buffer-only analysis using linear elastic model (BO-LE) at locations IBG1, IBG2, and IBG3

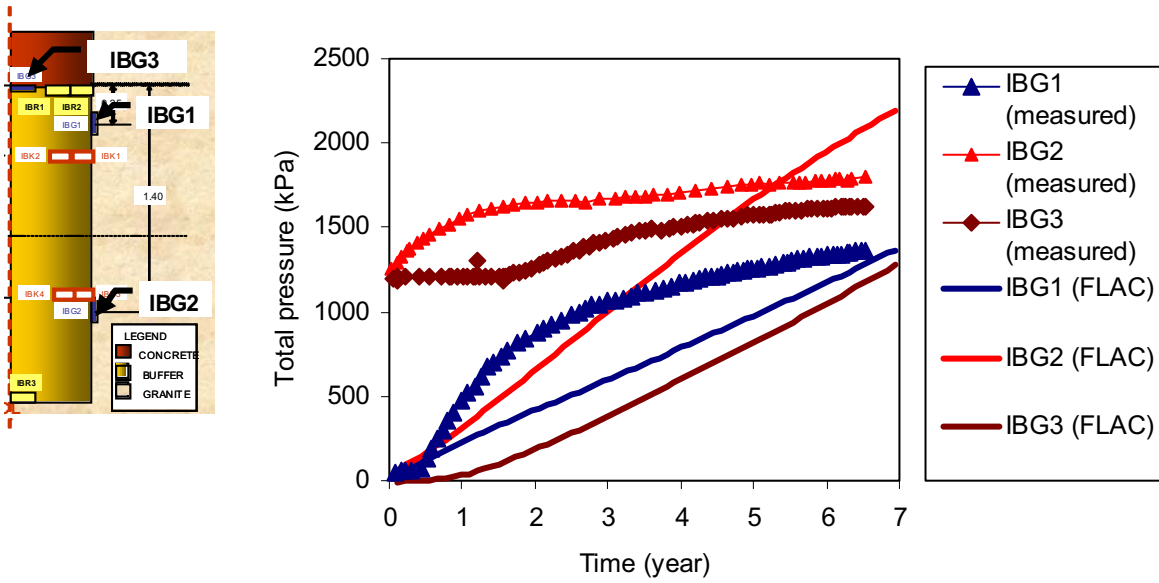


Figure 8.21 Total pressure measurements compared with buffer-rock analysis using linear elastic model (BR-LE) at locations IBG1, IBG2, and IBG3

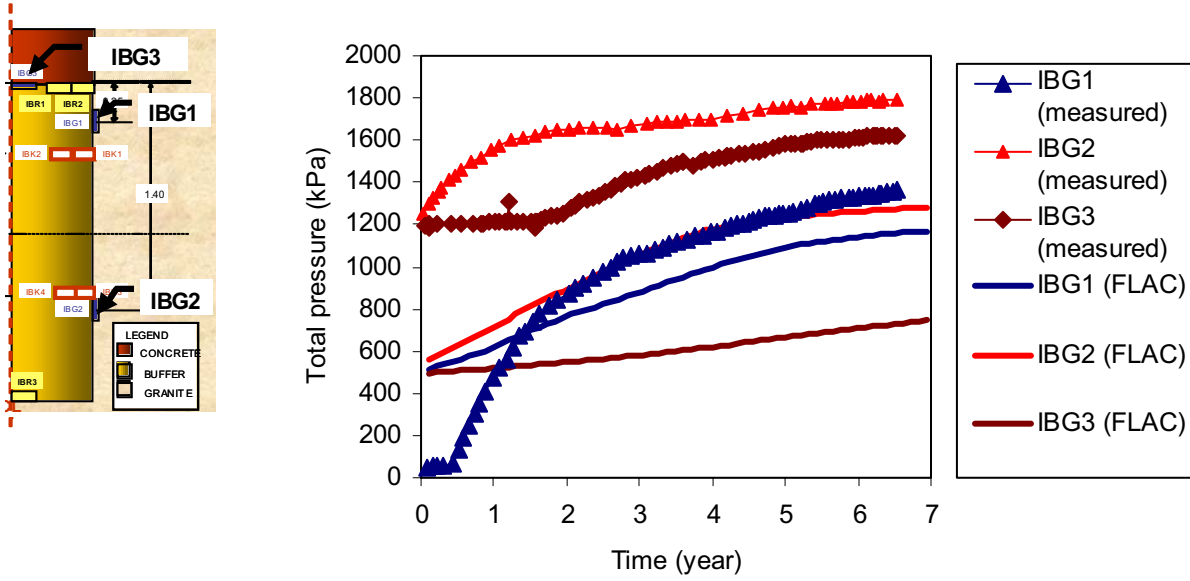


Figure 8.22 Total pressure measurements compared with buffer-rock analysis using BGM and kwn model (BR-BGMkwn) at locations IBG1, IBG2, and IBG3

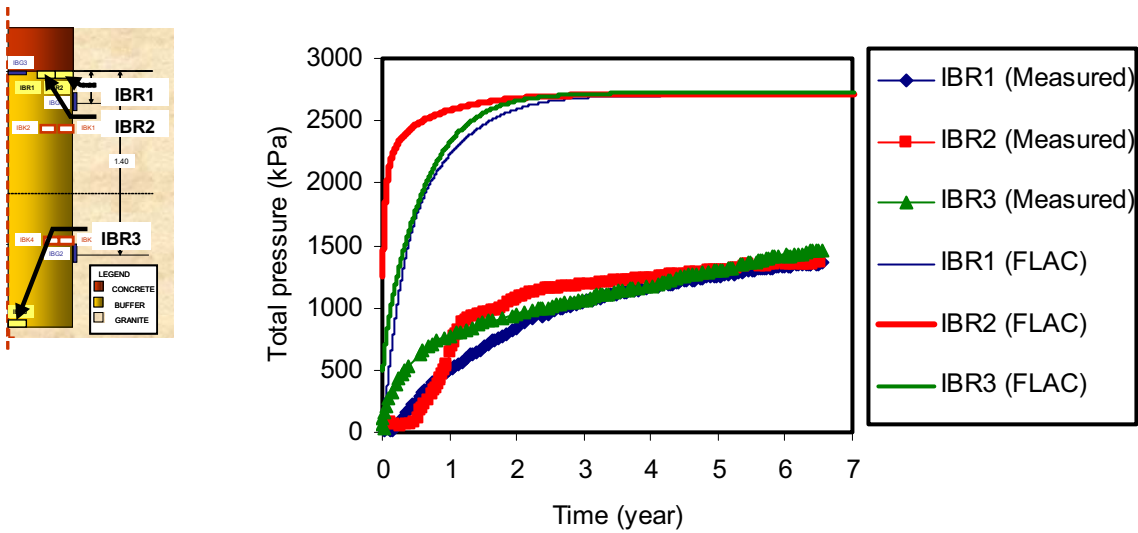


Figure 8.23 Total pressure measurements compared with buffer-only analysis using linear elastic model (BO-LE) at locations IBR1, IBR2, and IBR3

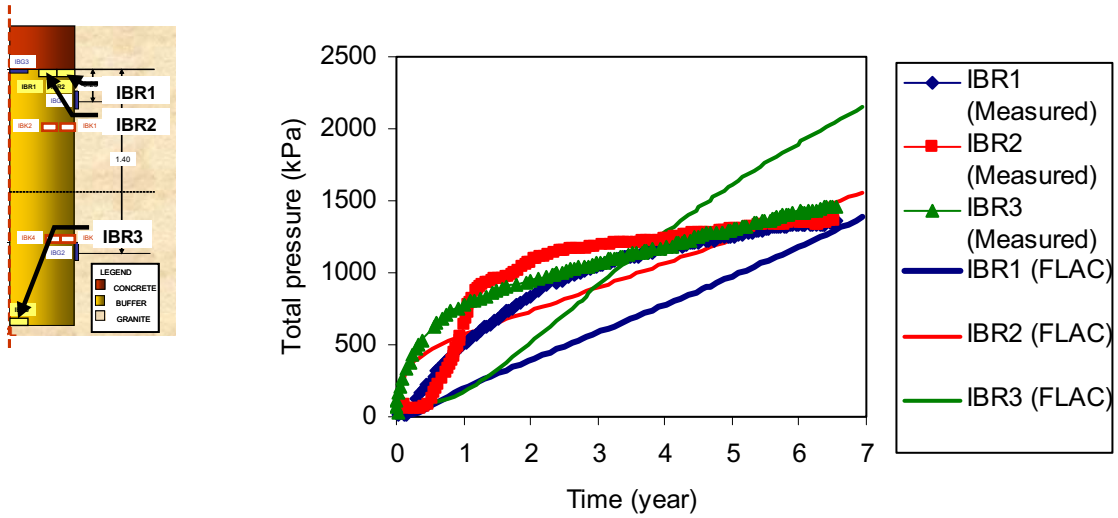


Figure 8.24 Total pressure measurements compared with buffer-rock analysis using linear elastic model (BR-LE) at locations IBR1, IBR2, and IBR3

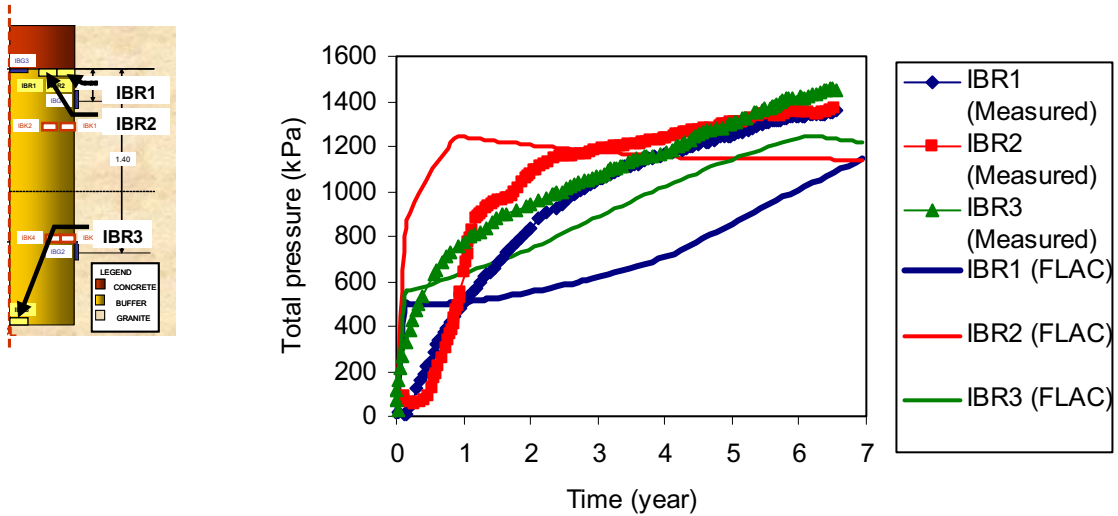


Figure 8.25 Total pressure measurements compared with buffer-rock analysis using BGM and kwn model (BR-BGM kwn) at locations IBR1, IBR2, and IBR3

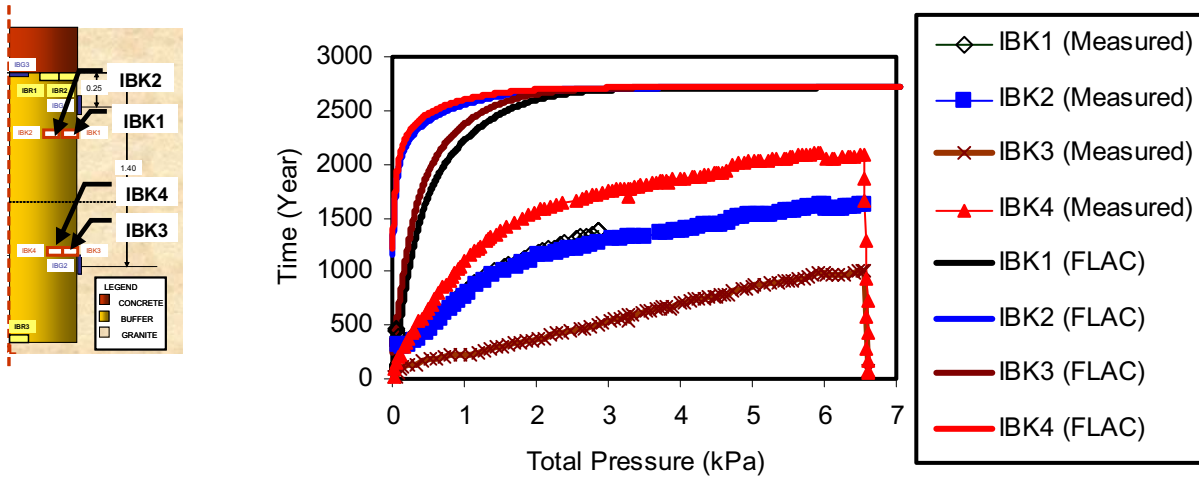


Figure 8.26 Total pressure measurements compared with buffer-only analysis using linear elastic model (BO-LE) at locations IBK1, IBK2, IBK3 and IBK4

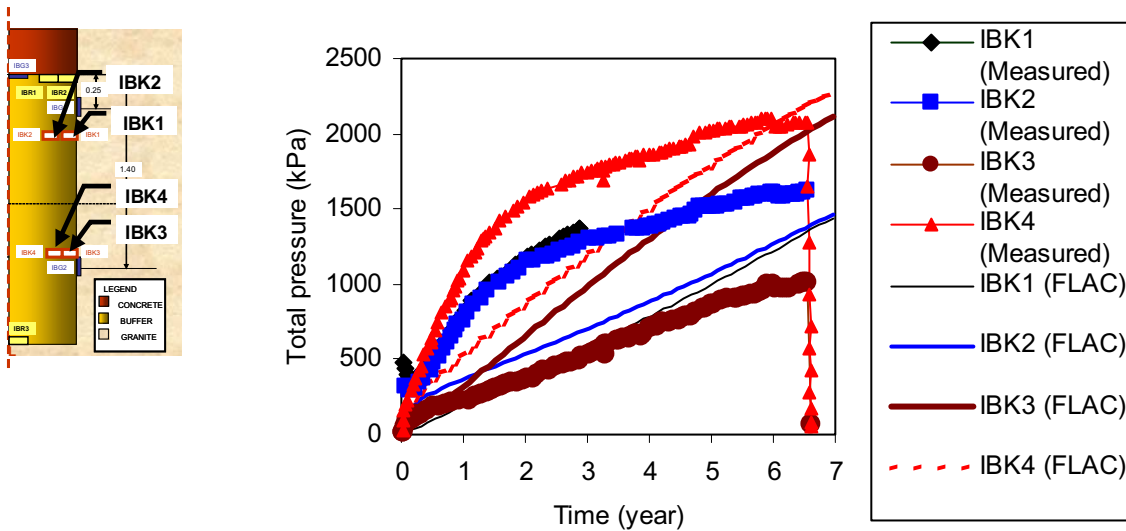


Figure 8.27 Total pressure measurements compared with buffer-rock analysis using linear elastic model (BR-LE) at locations IBK1, IBK2, IBK3 and IBK4

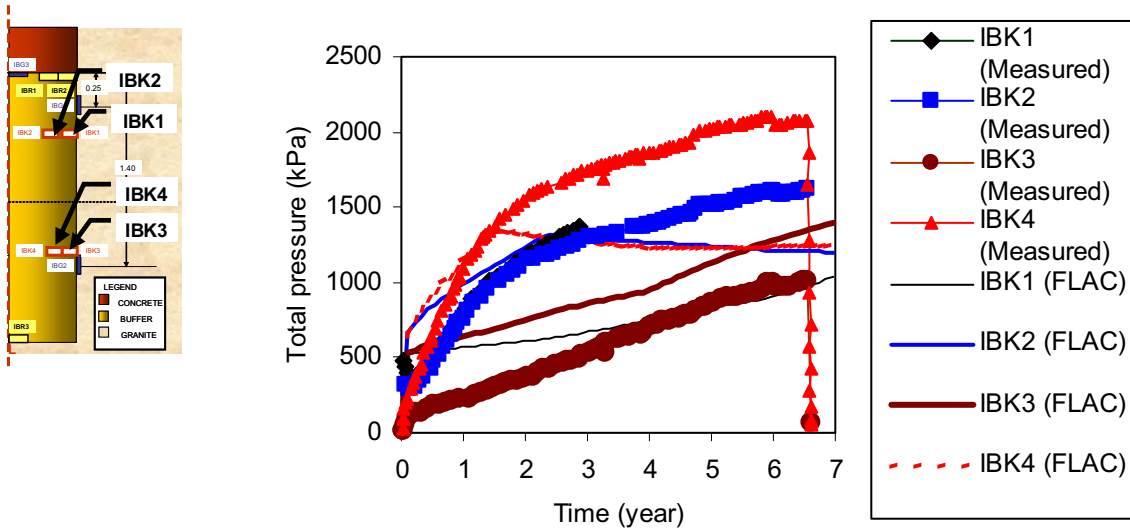


Figure 8.28 Total pressure measurements compared with buffer-rock analysis using BGM and kwn model (BR-BGM kwn) at locations IBK1, IBK2, IBK3 and IBK4

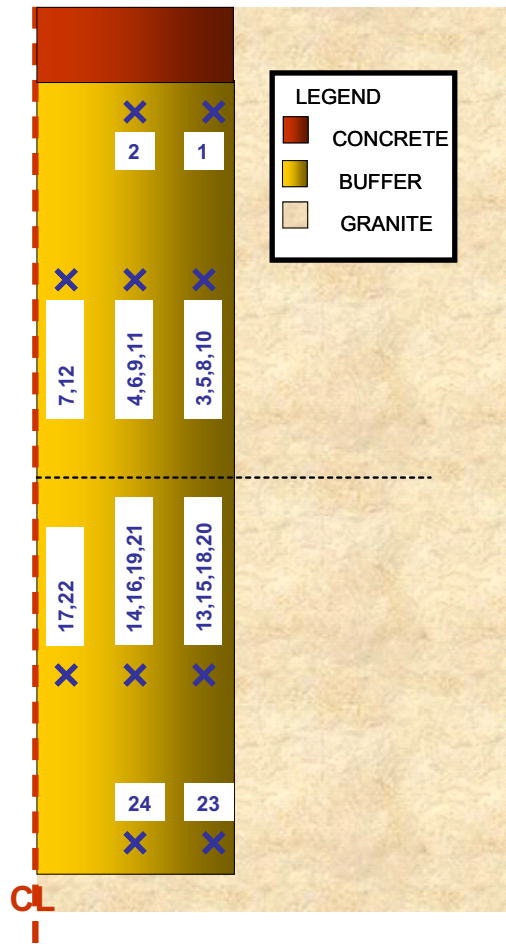


Figure 8.29 Psychrometer locations at the large-scale isothermal test (IBX1-24) (after Dixon et al. 2001)

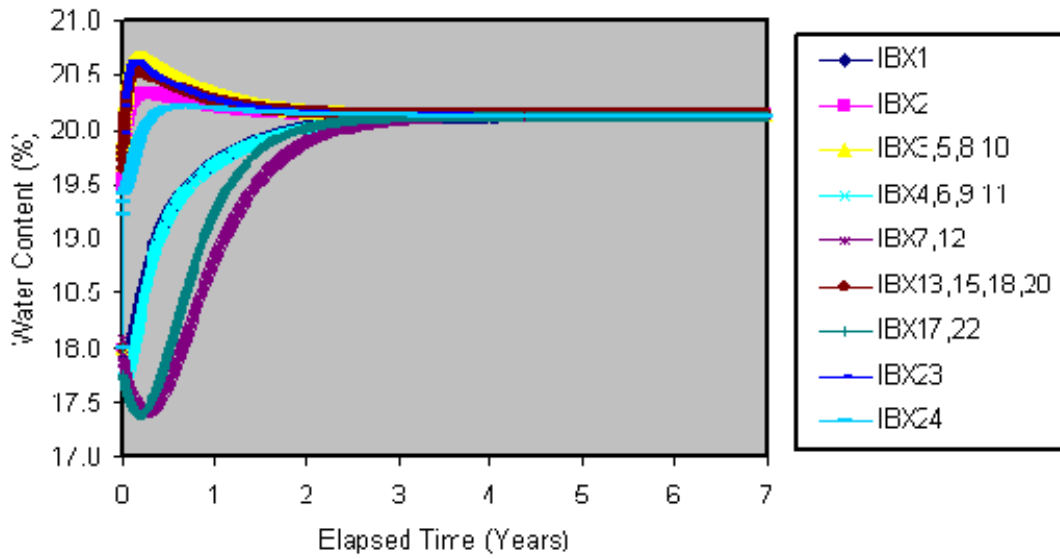


Figure 8.30 Evolution of water content of buffer-only analysis using linear elastic model (BO-LE) at psychrometer locations

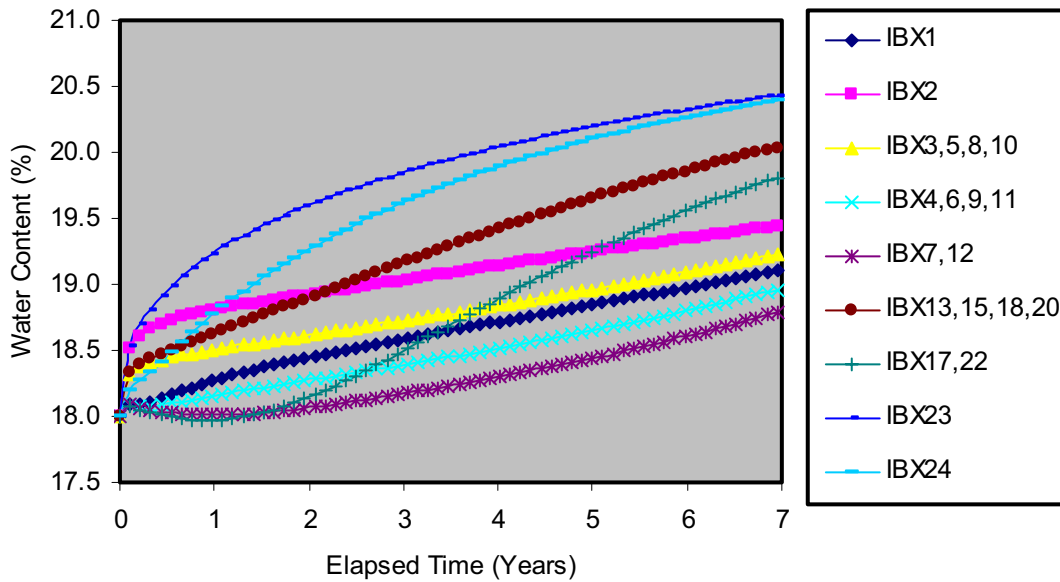


Figure 8.31 Evolution of water content of buffer-rock analysis using linear elastic model (BR-LE) at psychrometer locations

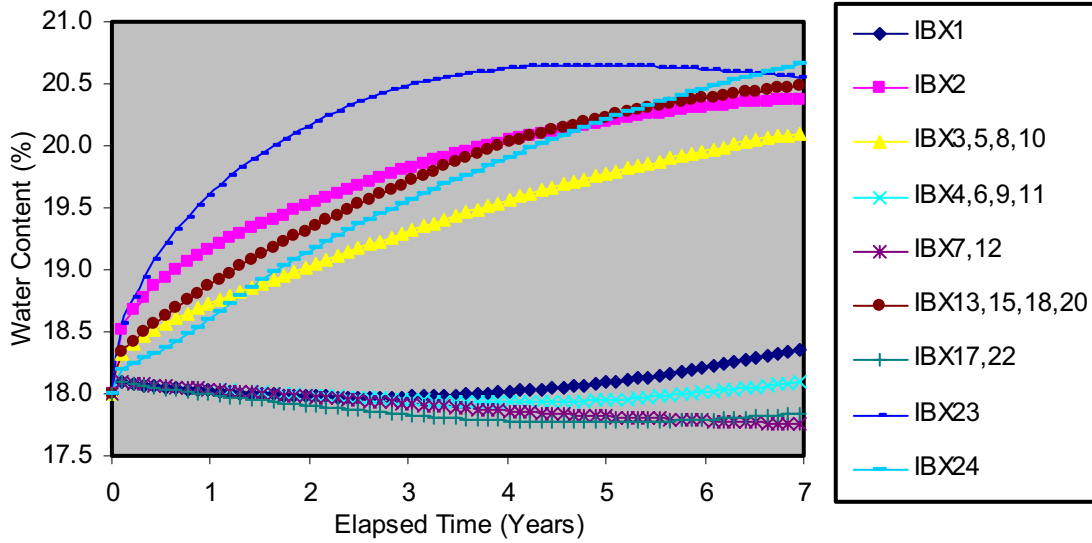


Figure 8.32 Evolution of water content of buffer-rock analysis using BGM and kwn model (BR-BGM kwn) at psychrometer locations

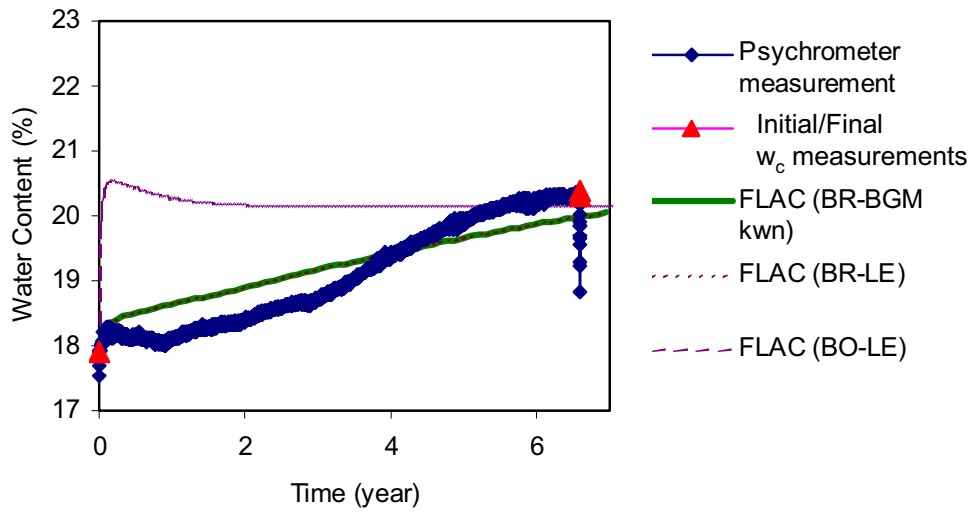


Figure 8.33 Evolution of gravimetric water content measurements compared with the three FLAC model results at location IBX18

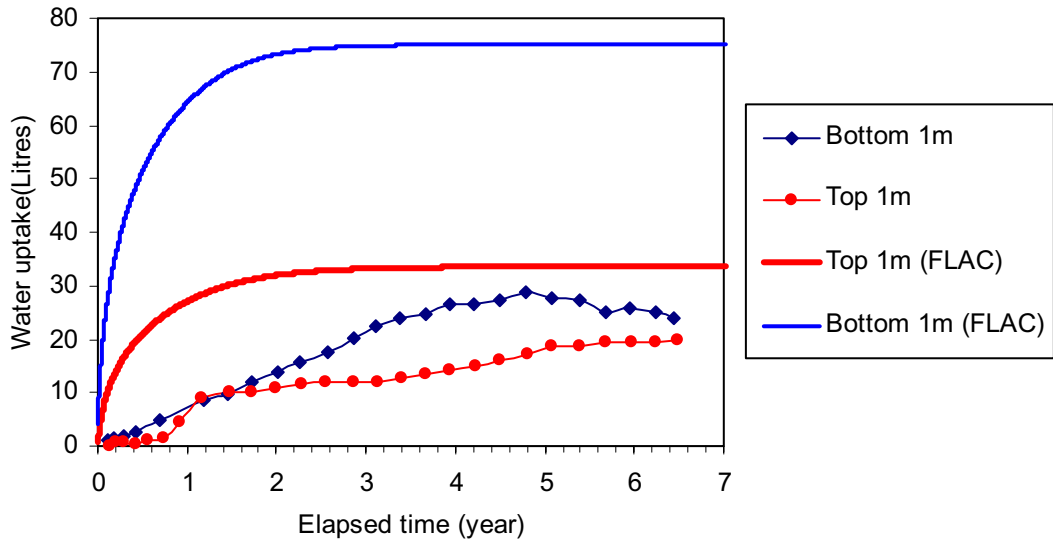


Figure 8.34 Water uptake measurements compared with buffer-rock analysis using linear elastic model (BR-LE) (Total water uptake = 108.91 litres)

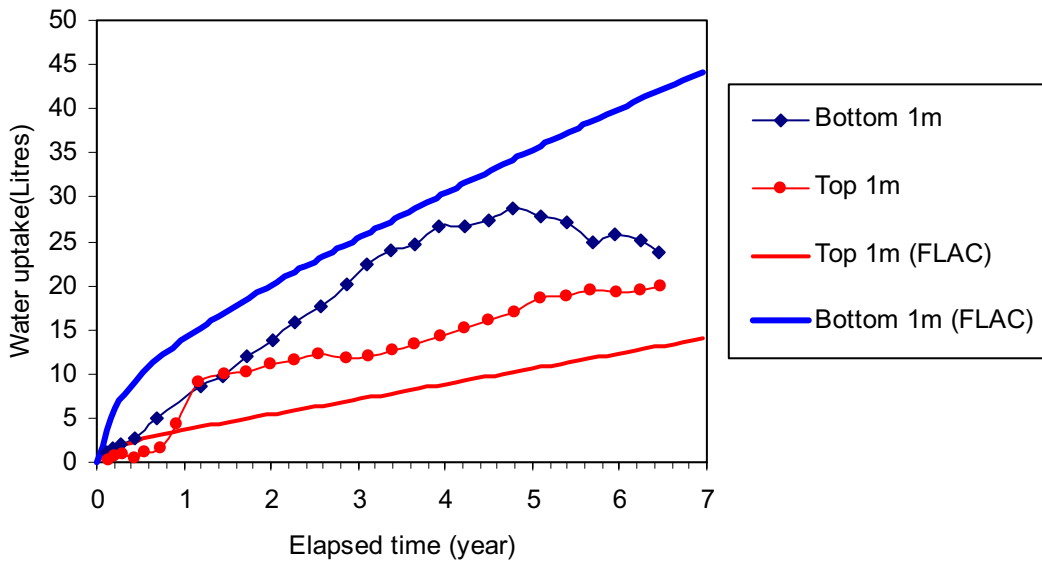


Figure 8.35 Water uptake measurements compared with buffer-rock analysis using linear elastic model (BR-LE) (Total water uptake = 58.14 litres)

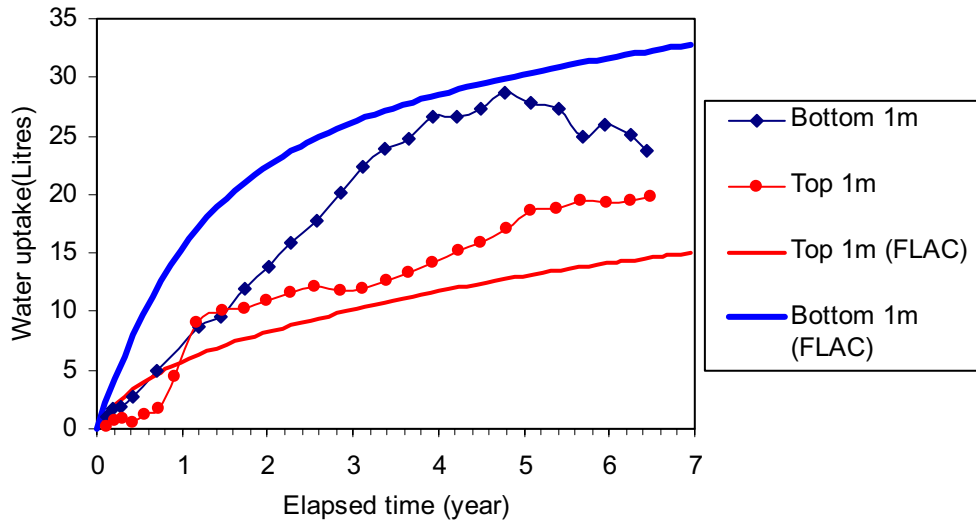


Figure 8.36 Water uptake measurements compared with buffer-rock analysis using BGM and kwn model (BR-BGM kwn) (Total water uptake = 47.76 litres)

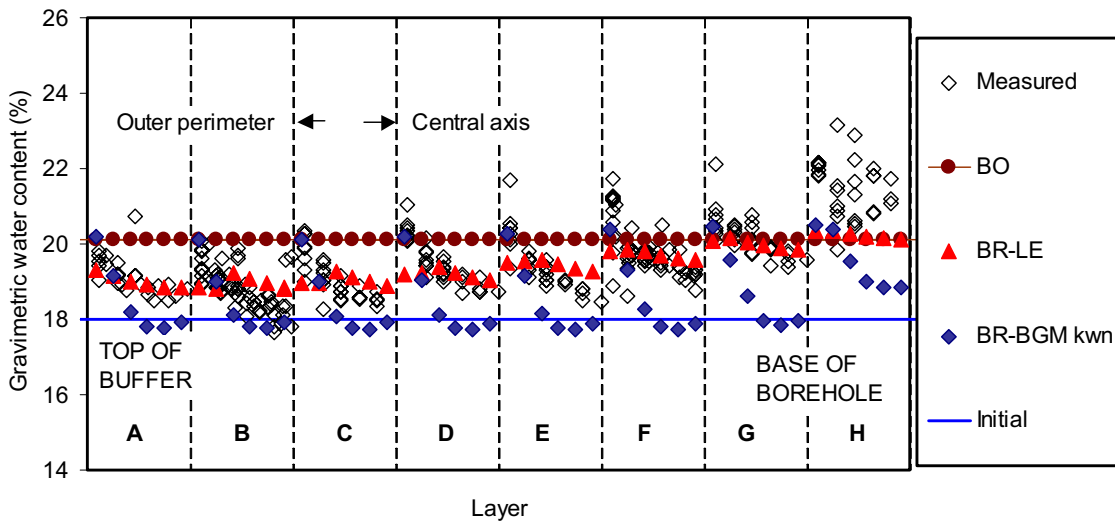


Figure 8.37 End of test gravimetric water content measurements compared with the three FLAC models

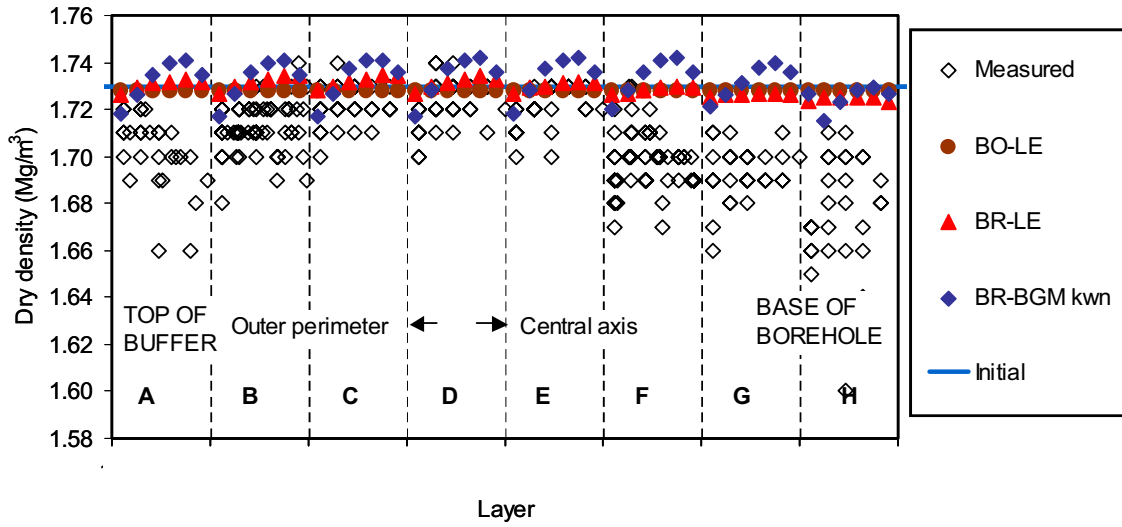
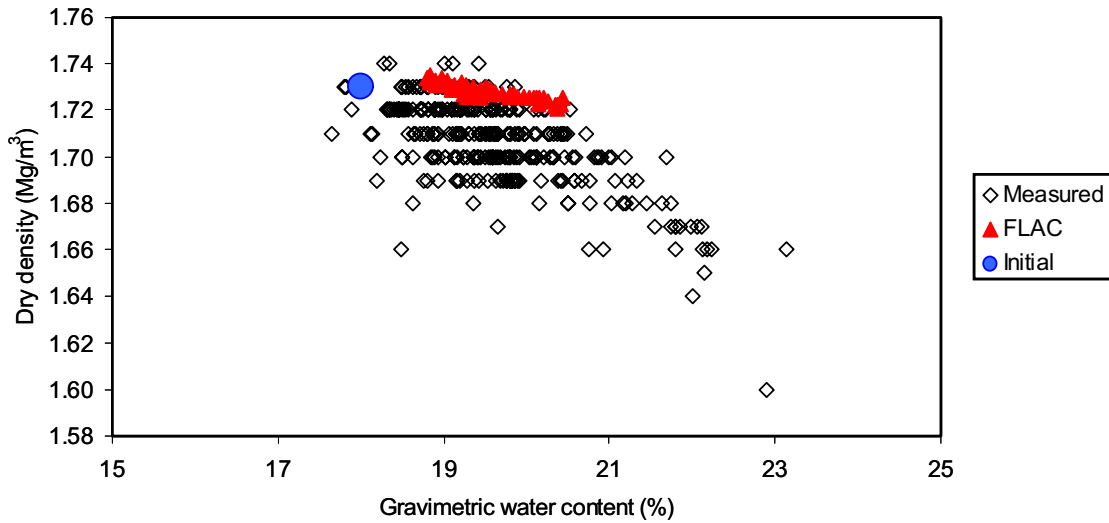
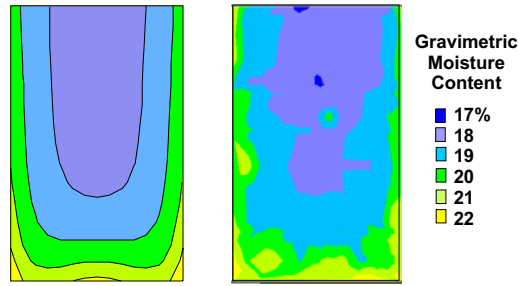


Figure 8.38 End of test dry density measurements compared with the three FLAC models

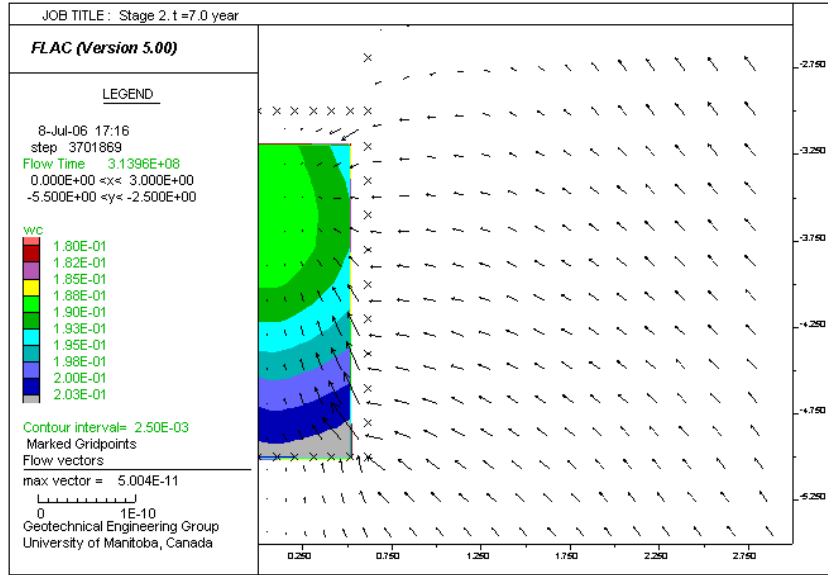


Notes: *) all the three FLAC analyses (BO-LE, BR-LE, and BR-BGMkwn)

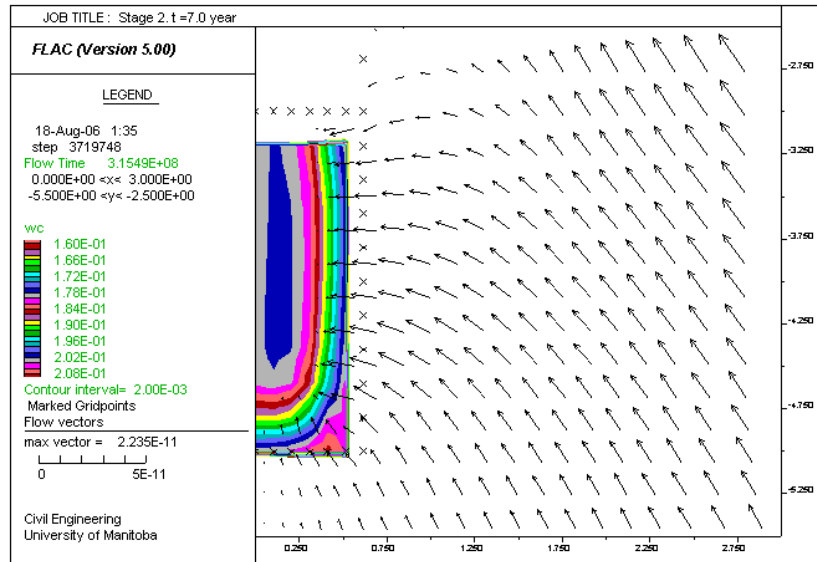
Figure 8.39 Gravimetric water content versus dry density at the end of test measurements compared with the three FLAC models



(a) Measurements (Dixon et al. 2001) Used with permission by King, July 23 , 2007.

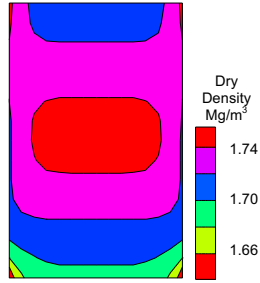


(b) FLAC (BR-LE)

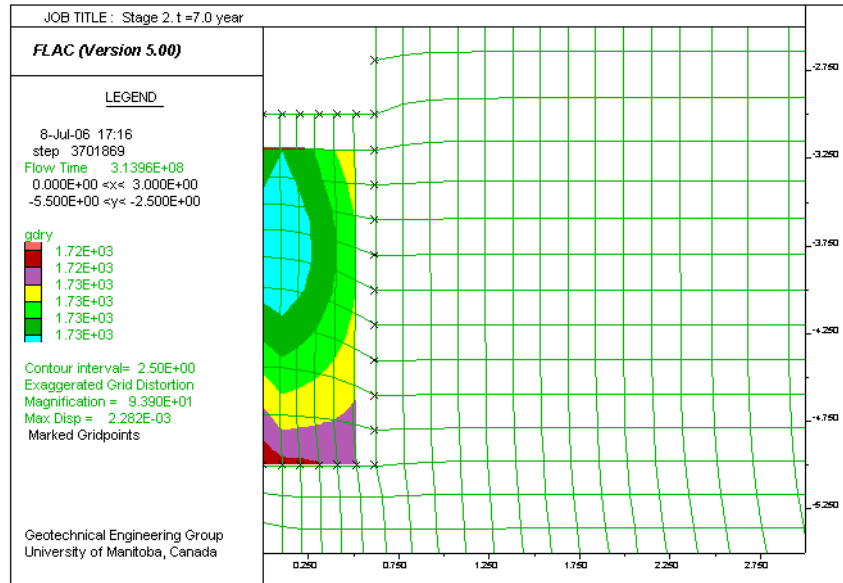


(c) FLAC (BR-BGM kwn)

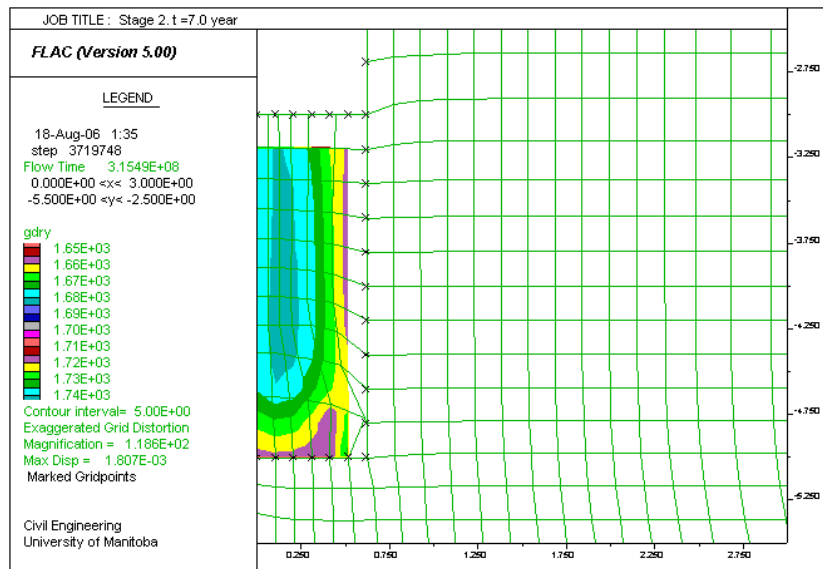
Figure 8.40 Gravimetric water content contours at the end of test from: (a) field measurements; (b) BR-LE analysis; and (c) BR-BGM kwn analysis



(a) Measurements (Dixon et al. 2001) Used with permission by King, July 23, 2007.



(b) FLAC (BR-LE)



(c) FLAC (BR-BGM kwn)

Figure 8.41 Dry density contours at the end of test from: (a) field measurements; (b) BR-LE analysis; and (c) BR-BGM kwn analysis

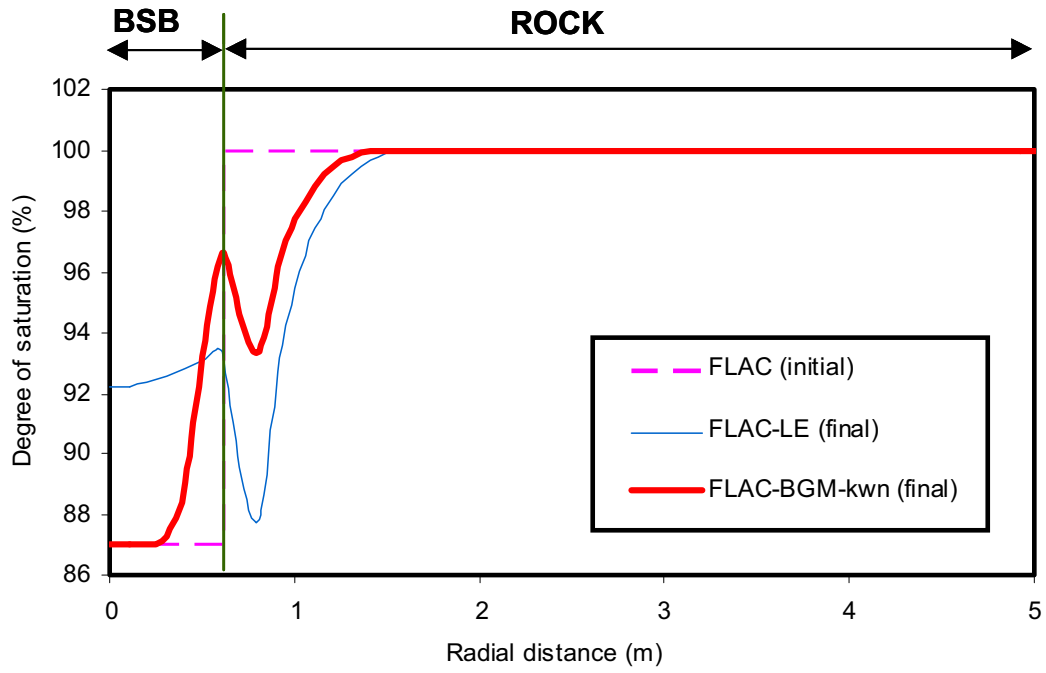
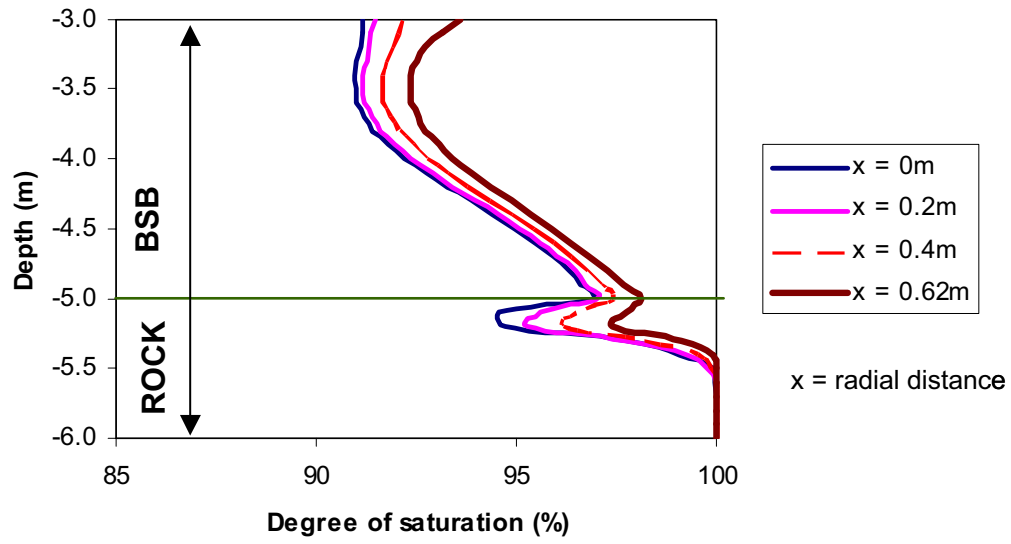
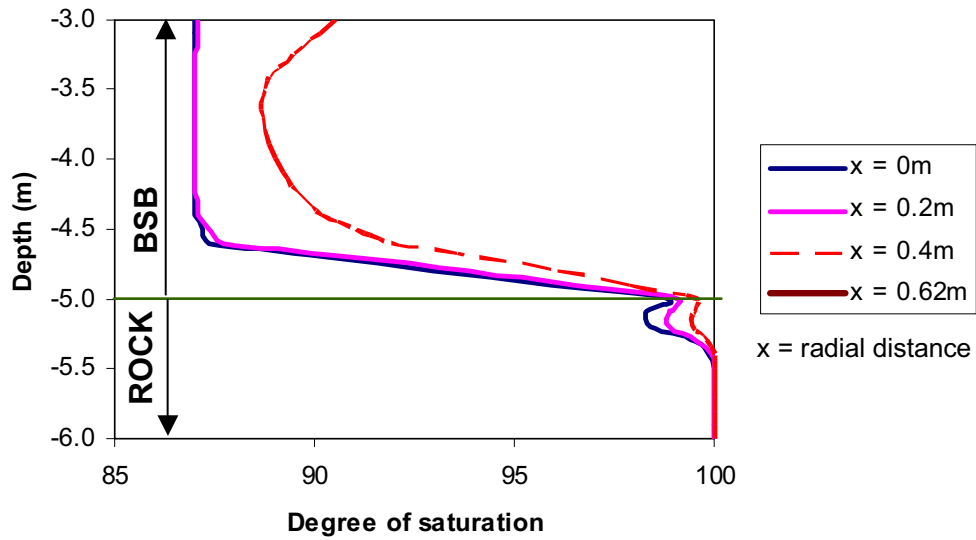


Figure 8.42 Degree of saturation versus radial distance of two FLAC models at initial and final conditions

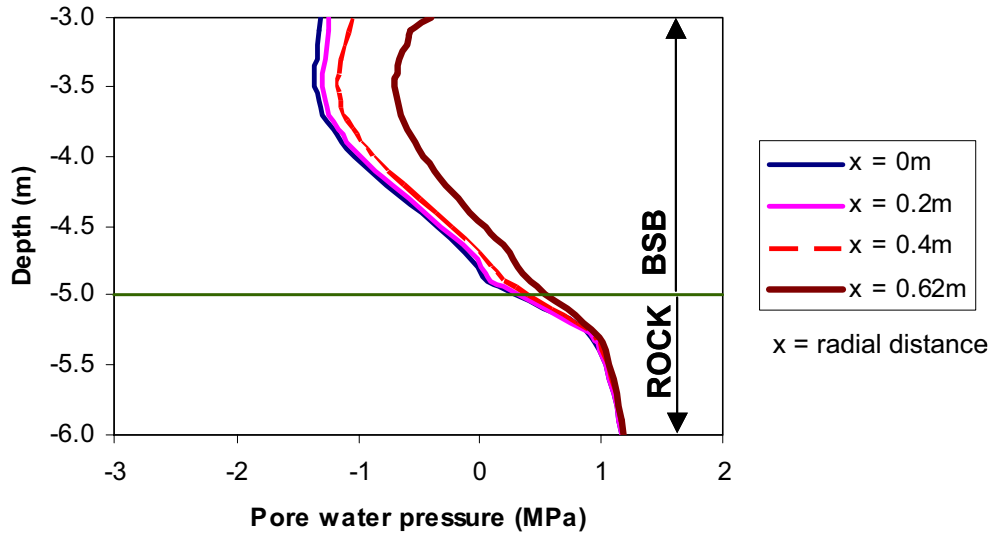


(a) LE

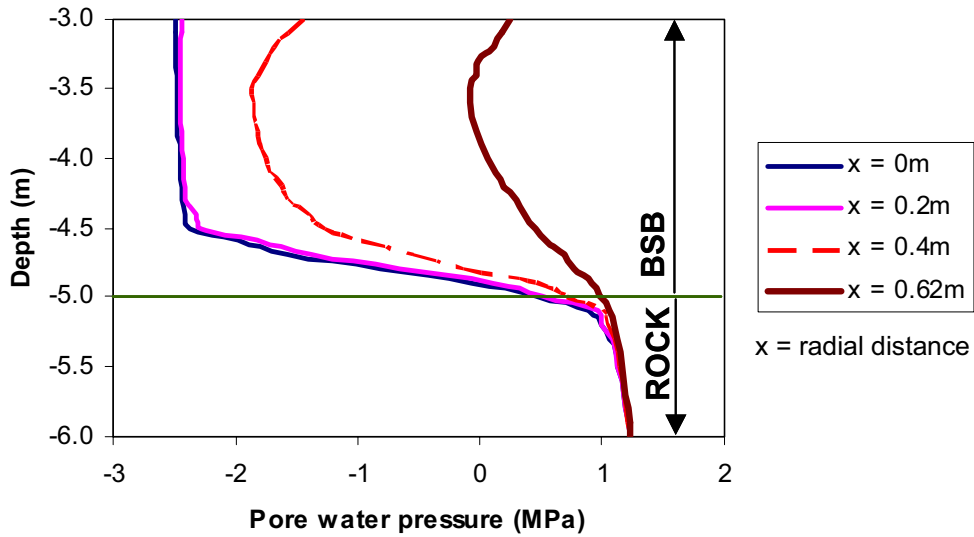


(b) BGM-kwn

Figure 8.43 Degree of water saturation versus depth for various radial distance of two different FLAC models



(a) LE



(b) BGM-kwn

Figure 8.44 Pore water pressure versus depth for various radial distance of two different FLAC models

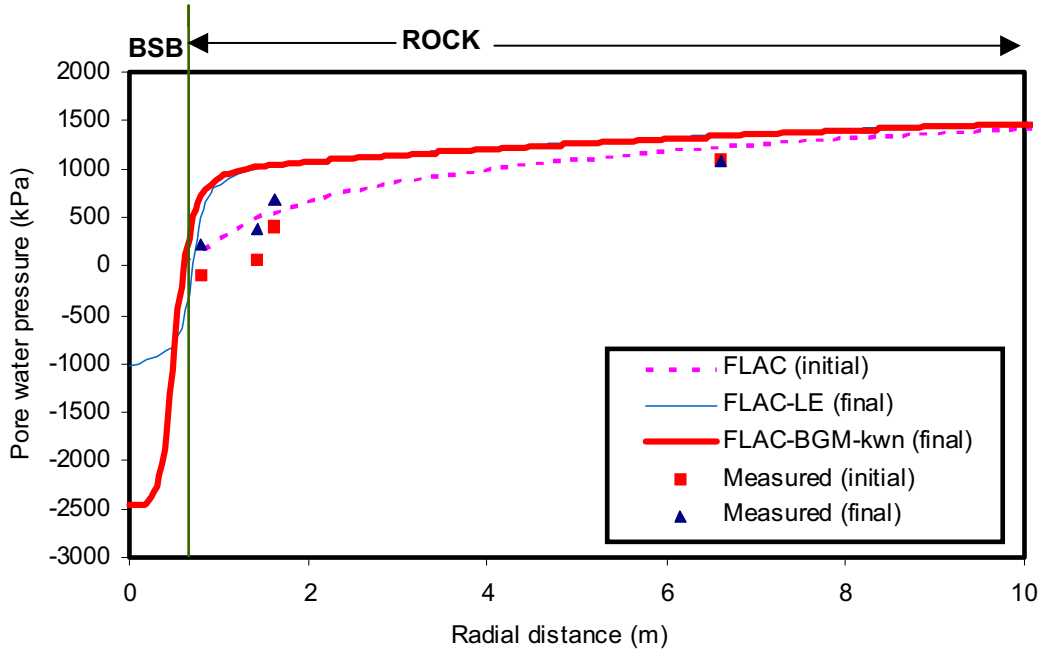


Figure 8.45 Comparison between FLAC models and field measurements of the pore water pressure versus radial distance from borehole center at initial and final conditions

CHAPTER 9

TIME-DEPENDENT BOUNDARY CONDITIONS TO SIMULATE LARGE-SCALE ISOTHERMAL TEST (ITT)

9.1 Background

The modelling of the large-scale isothermal test presented in Chapter 8 indicates that the properties of both the BSB and the rock significantly affect the results of the simulations. Properties of the rock used in the numerical modelling in Chapter 8 are based on the literature study (e.g. Thomas et al. 2003), while the properties of the buffer are calibrated based on the intensive laboratory measurements. Consequently, the properties of the rock have a higher uncertainty compared to the properties of the buffer. The percentage of the area of the rock domain that are characterized by field measurements is much less than that of the buffer.

The boundary condition applied in the far field may also increase the uncertainty of the modelling. Guo and Dixon (2005) used lower farfield pore water pressure compared to those used by Thomas et al. (2003) to obtain agreement between the far field measurements and the modelling. Guo and Dixon (2005) also introduced the excavation damage zone (EDZ) in the rock close to borehole that has higher permeability. Guo and

Dixon (2005) assumed that 30 cm deep of the borehole wall was the excavation damage zone (EDZ) in the analysis.

The problem of how to reduce the effect of the uncertainty of the rock properties and the boundary conditions led to the idea of a 'time-dependent' boundary condition (discussion with Chandler 2006). This chapter investigates modelling the large-scale isothermal test (ITT) with a time-dependent boundary condition (BCt). Using time-dependent boundary conditions (BCt) reduces the domain area to reduce the time for analysis. The portion of rock involved in the system is also reduced, so that the effect of the uncertainty of the rock properties in the analysis is also reduced. Using the time-dependent boundary condition (BCt), the actual variation field pore water pressure measurement versus time in the rock can be used as the boundary condition, instead of considering the farfield measurement that was only measured at one particular time.

9.2 Time-Dependent Boundary Conditions

During the ITT test (Dixon et al. 2002), the pore water pressures in the rock were measured using borehole packers at the locations IRW1-7 (Figure 9.1). Figure 9.2 illustrates the modelling domain and boundary conditions as a function of time. The axisymmetric model grid with radius of 1.62 m and depth of 7 m are used as the domain of the model (Figure 9.2). The porewater pressure measurements at location IRW4-7 are used as the boundary condition at the perimeter (Figure 9.2). These measurements are simplified to reduce fluctuation during the test and to ignore the effect of depressurization and deaeration of the packer (Figure 9.2). The pore water pressure at the bottom is taken from extrapolation of IRW6 and IRW7 measurements, which is also a function of time (Figure 9.2).

9.3 Constitutive Models

The ITT test (Dixon et al. 2002) consists of three material components: buffer, rock, and concrete. Only the buffer and rock are included in this model (Figure 9.2). The buffer-concrete and rock-concrete interface is considered as a rigid and impermeable boundary. The rock properties and buffer properties have the same parameters as presented in Chapter 8. The linear elastic (LE) model and Blatz and Graham (2003) model (BGM) are used to defined the mechanical behaviour of the buffer, while the hydraulic behaviour is defined using the van Genuchten (1980) model and porosity dependent permeability models. The parameters of these models are summarized in Chapter 8. Three combinations of hydro-mechanical constitutive models are used in this Chapter and summarized in Table 9.1.

9.4 Comparison of the Model and Field Measurements

9.4.1 Seepage into an Empty Borehole

The comparison of the water seepage with the time-dependent boundary condition model (BCt) and the buffer-rock model (BR) are illustrated in Figure 9.3. The vertical flow at the bottom of the borehole for the BCt model is greater than the radial flow at borehole perimeter (Figure 9.3a), while the BR model has the opposite phenomenon (Figure 9.3b).

9.4.2 Pore water Pressure at the Buffer-Rock Interface

Figures 9.5-9.7 illustrates the pore water pressures at the rock-buffer interfaces versus time at the infiltration stage for three models (BCt-LE, BCt-BGM, and BCt-BGM-kwn). The location of IBP1 and IBP2 are illustrated in Figure 9.4. The pore-water pressure evolution of all models (BCt-LE, BCt-BGM, and BCt-BGM-kwn) indicates that numerical

modelling results of the pore water pressure at the bottom (IBP2) of the borehole overestimate field measurements, while at the perimeter (IBP1) underestimate the measurements (Figure 9.5-9.7). Both seepage into the empty borehole (Figure 9.3) and the pore pressure history (Figure 9.5) may indicate that there is anisotropy in the permeability of the rock, where the vertical permeability of the rock is greater than the radial direction than that of vertical direction ($k_w \text{ vertical} > k_w \text{ radial}$). The characterization of the anisotropic permeability may be done using back analysis presented in the next section as a suggestion for future research.

The pore water pressure at the base of ITT from BCt-LE and BCt-BGM (Figures 9.5 and 9.6) increases rapidly at the beginning and overestimate the field measurements. The rate of increase is reduced when using the porosity dependent permeability models (BCt-BGMkwn) (Figure 9.6).

9.4.3 Gravimetric Water Content (w) and Dry Density (ρ_{dry}) in the Buffer

The gravimetric water content (w) at the end of the test for the three models in Table 9.1 (BCt-LE, BCt-BGM, and BCt-BGM-kwn), buffer only (BO) model and and buffer-rock with linear elastic model (BR-LE) compared with the field measurements at the spatial locations are illustrated in Figure 9.8. Note that layer A is located the top of the buffer and layer H is the base of the borehole. In each layer, the right side is the outer perimeter, while the left side is the central axis. The application of time-dependent boundary conditions (BCt-LE, BCt-BGM-kwn, BCt-BGM) increase the variability of the water content in the vertical direction, so that the results have better agreement with the field measurements (Figure 9.8). The results of the BCt-BGM-kwn indicate the most variation in vertical and radial distance compare to the other analyses (BCt-BGM and

BCt-LE), because of the porosity dependent permeability (kwn)'s pseudo permeable layer mechanism (Figure 9.8).

The gravimetric water content (w) evolution of the BCt-BGM-kwn models at location IBX9 (Figure 9.9) and IBX11 (Figure 9.10) show a good agreement with the field measurements. The location of the psychrometer IBX1-24 is illustrated in Figure 8.28. The evolution of the gravimetric water content at locations IBX1-24 for the BCt-BGM-kwn model is illustrated in Figure 9.11. The variation of the gravimetric water content at different location is observed due to the application of both the BGM and kwn model.

The contours of the dry density at the end of the test due to the BCt models are illustrated in Figure 9.12. Comparison of dry density contours due to the BCt-LE models with the BCt-BGM and BCt-BGM-kwn models indicate clearly the limitation of the linear elastic model and the role of the elasto-plastic (BGM) and porosity dependent permeability models (kwn). The strain hardening or strain softening mechanism, yielding mechanism, and change of permeability due to the change of volume cannot be replicated using the linear-elastic model. The countours of dry density at the end of the test (Figure 9.12) due to BGM and BGM-kwn models replicate field measurements. The magnitude of the dry density of the models overestimates the field measurements (Figure 9.13). This result can be improved by the increasing the specific gravity (G_s) or through back analysis of the system.

9.5 Concluding Remarks

The following conclusions can be drawn from the analysis:

- The time-dependent boundary condition (BCt) models can reduce the uncertainty caused by the far field boundary conditions in the rock and hydraulic properties of the rock.
- The result of BCt analysis suggests that there is a possible anisotropic permeability of the rock within the domain. Further investigation is required to examine the possible anisotropy.
- Comparison of end of test gravimetric water content due to the BCt-LE, BCt-BGM, and BCt-BGM-kwn analysis (Figure 9.8) with the laboratory measurements show that the analysis using the BGM (Blatz and Graham 2003) with a porosity dependent permeability (kwn) model in BCt-BGM kwn best describes the hydro-mechanical behaviour of the buffer.
- The elasto-plastic model (BGM) simulates some mechanisms (e.g. strain hardening or strain softening and yielding), which are not included in the linear elastic (LE) models. The porosity dependent permeability model (kwn) creates a 'pseudo impermeable layer' mechanism that cannot be produced by the conventional unsaturated clay permeability model where k is only dependent on the degree of saturation (S_w).
- Comparison of the end of test gravimetric water content of BCt-BGMkwn analysis (Figure 9.8) and BR-BGM-kwn analysis (Figure 8.33) indicates that the application of time-dependent boundary conditions can improve the prediction of changes of the volume-mass relationship within the buffer.

9.6 Suggestion for Future Research

The time-dependent permeability model indicates that there is a limitation of the rock properties used in the analysis. The anisotropic permeability of the rock may exist within

the domain. The properties of the rock may be defined using back analysis as illustrated in Figure 9.14. The ITT test is modelled using the domain in Figure 9.14. The pore water measurements IRW 1-3 are used as the boundary conditions. The comparison of the pore water pressure at locations IRW4-7 of the analysis and the measurement are made. The parameters of the rock used in the analysis are changed until the difference between the measurements and the models are minimal.

Dr. N. Chandler (personal communication, 29 June 2007) suggested that the lack of correlation in the IBP2 measurement (Figures 9.5 to 9.7) is due to the location of the IBP2 measurements and the magnitude of the lower pressure boundary condition. The IBP2 is actually located inside the buffer and not on the interface. Other pressure measurements (e.g. IRP3) can be used as the lower boundary conditions. This is suggested as a future research to confirm the existence the anisotropic permeability of the rock.

Table 9.1 Constitutive models used in the time-dependent boundary condition (BCt) models

No.	Name	Mechanical constitutive models	Hydraulic constitutive model
1.	BCt-LE	linear elastic	Van Genuchten (1980)
2.	BCt-BGM	Blatz and Graham (2003) model (BGM)	Van Genuchten (1980)
3.	BCt-BGM-kwn	Blatz and Graham (2003) model (BGM)	Porosity dependent permeability model (kwn)

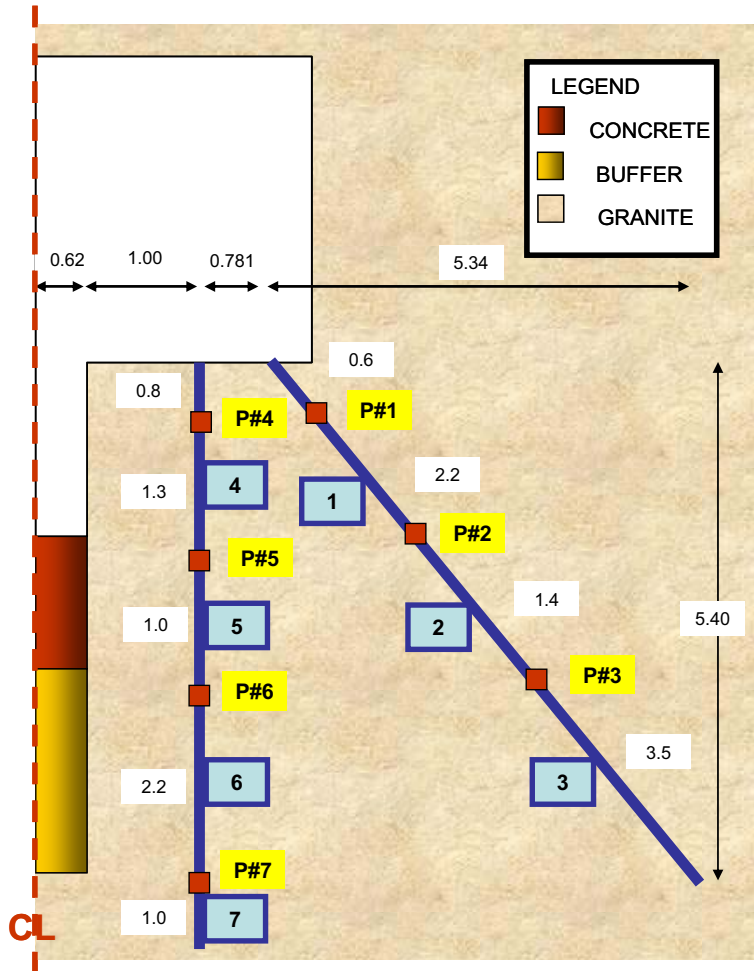


Figure 9.1 Location of pore water pressure measurements at rock

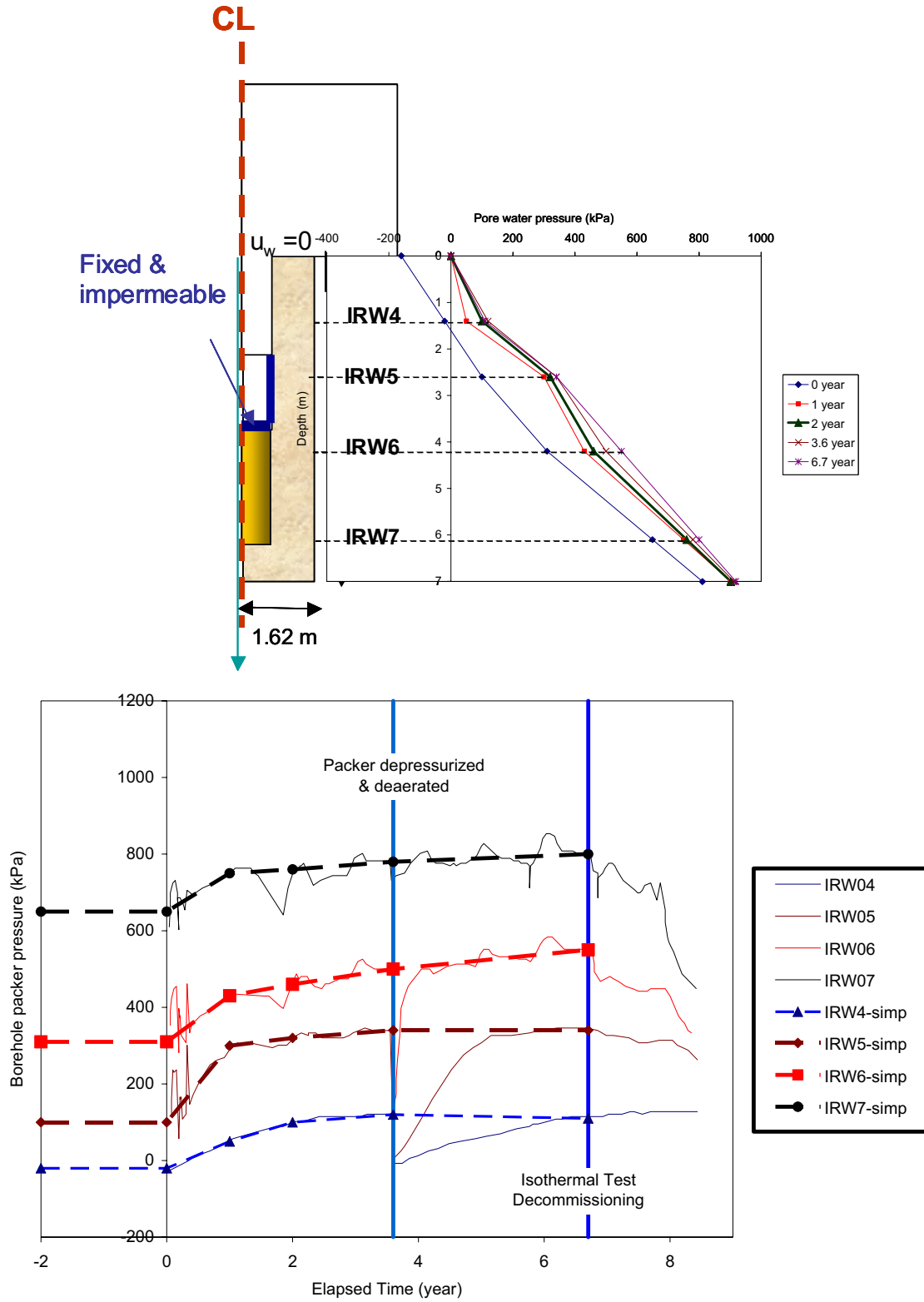
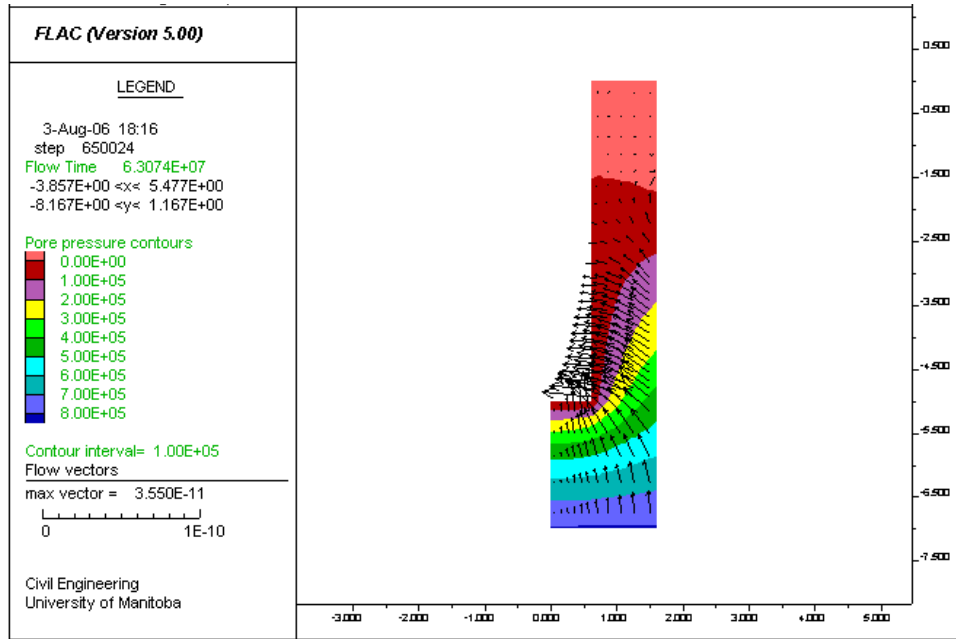
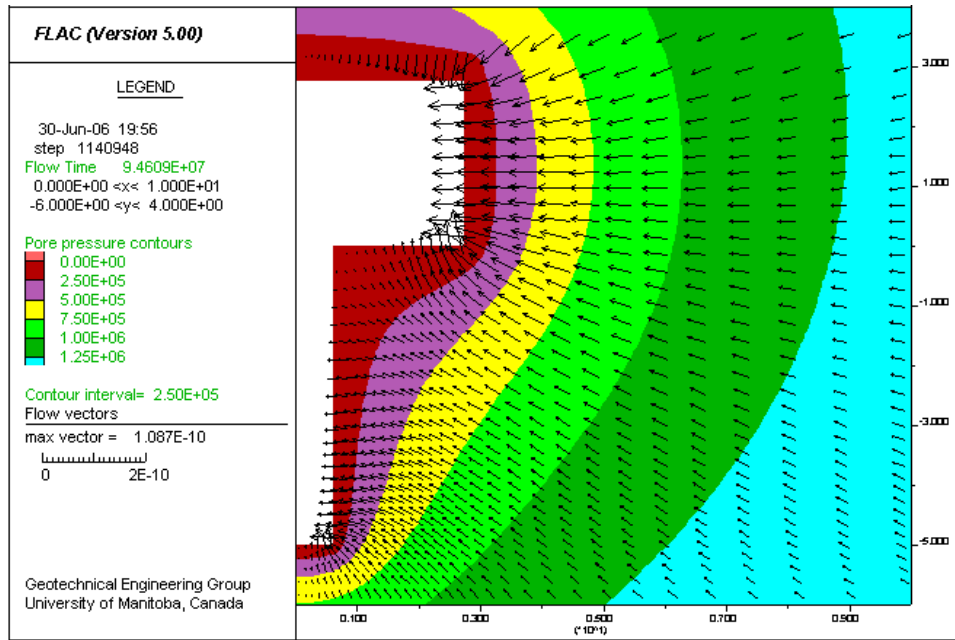


Figure 9.2 Boundary conditions as a function of time



(a) BCt model



(b) BR model

Figure 9.3 Seepage into an empty borehole: (a) time dependent boundary condition (BCt) model; (b) buffer-rock (BR) model

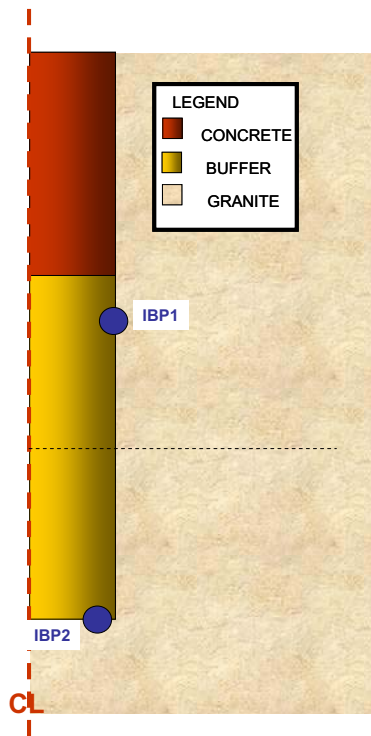


Figure 9.4 Locations of IBP1 and IBP2

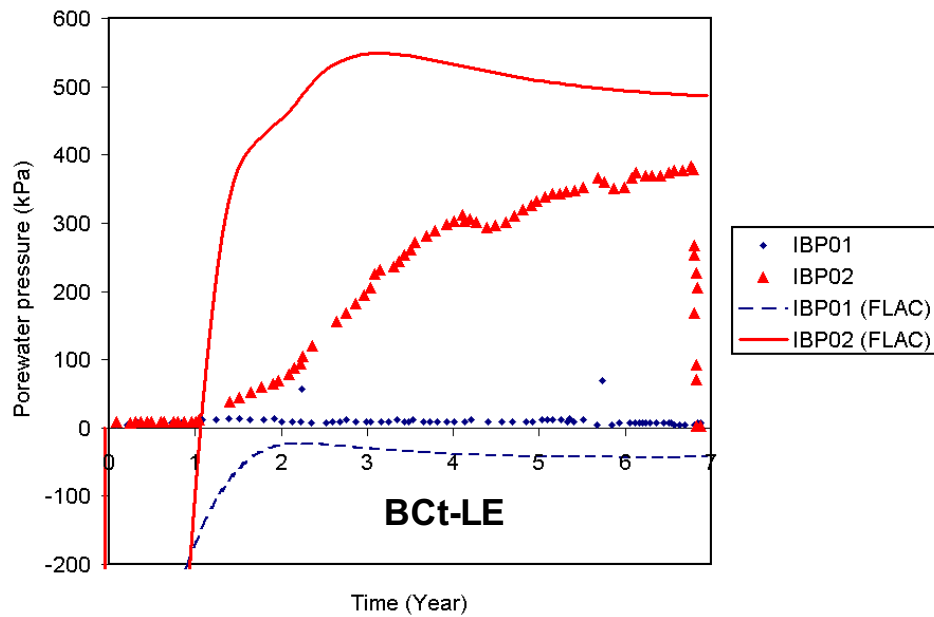


Figure 9.5 Pore water pressure measurements at locations IBP1 and 2 for Bct-LE model

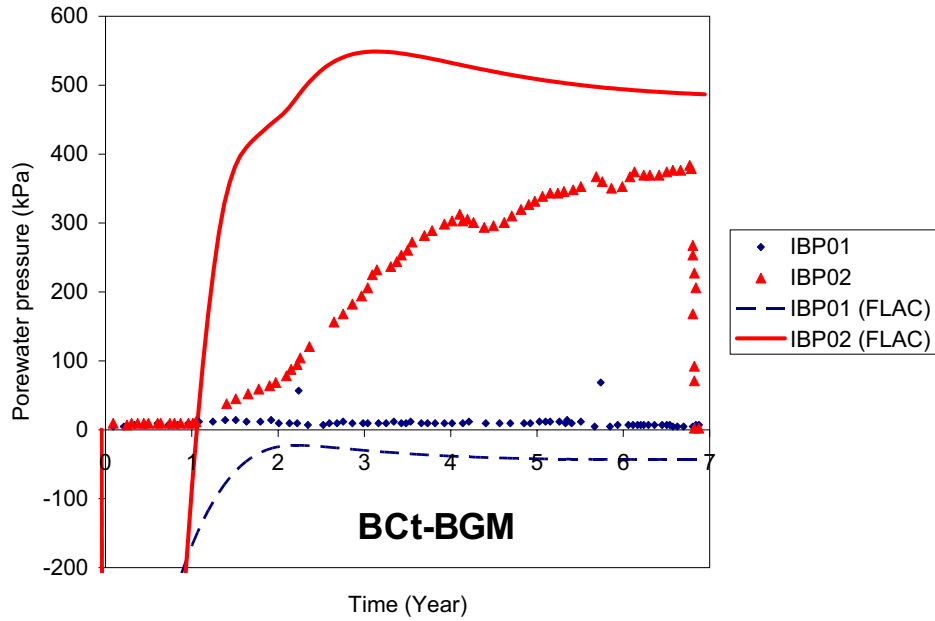


Figure 9.6 Pore water pressure measurements at locations IBP1 and 2 for BCt-BGM model

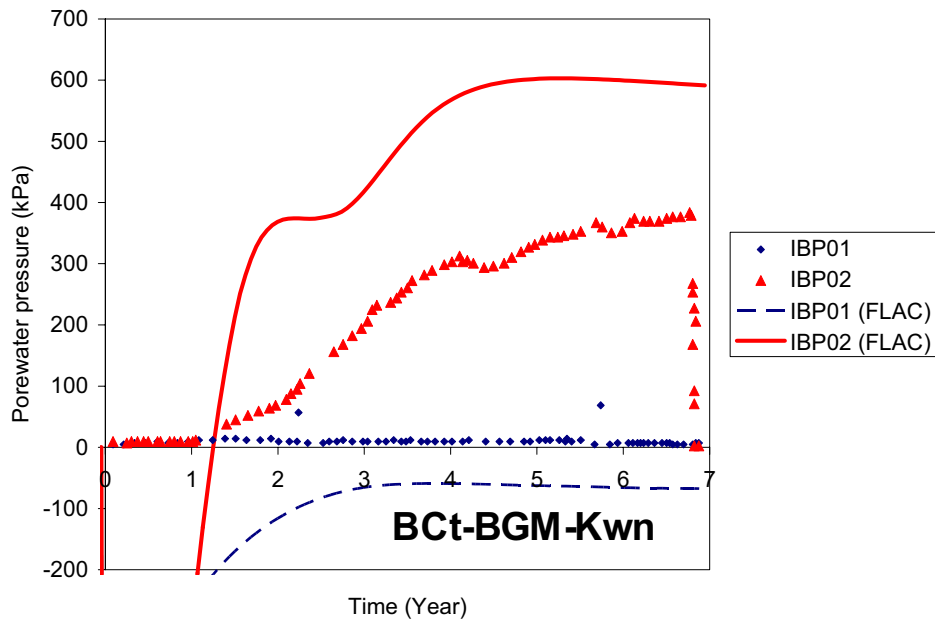


Figure 9.7 Pore water pressure measurements at locations IBP1 and 2 for BCt-BGM-kwn model

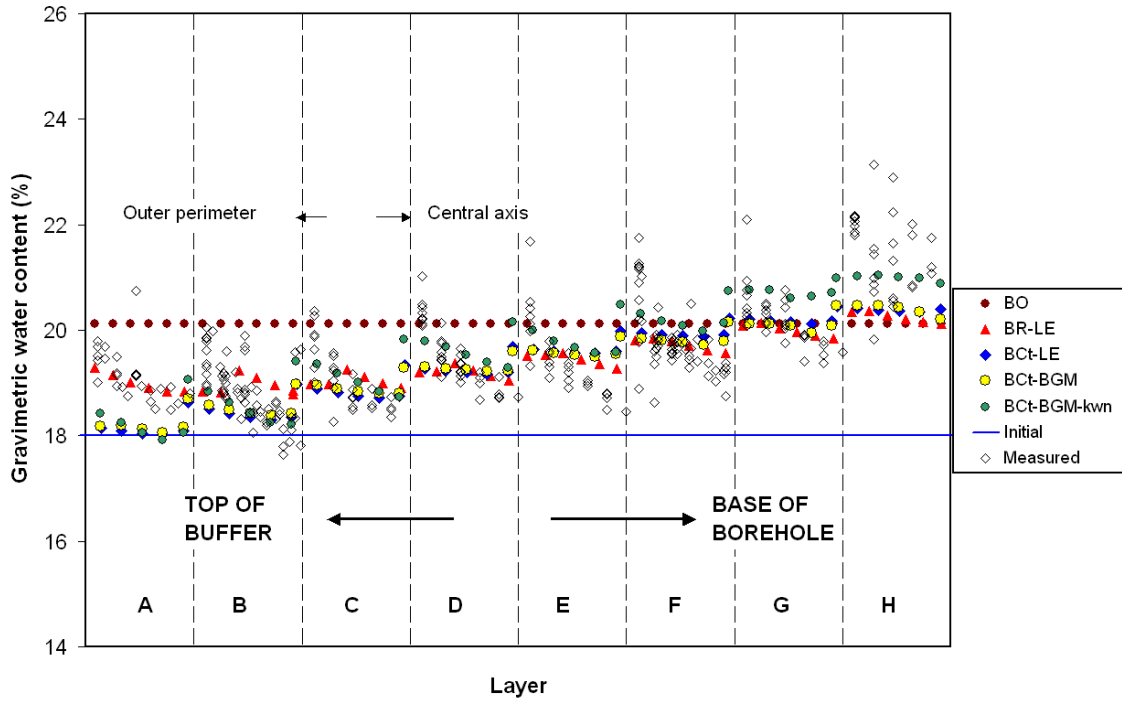


Figure 9.8 End of test gravimetric water content (w) measurements compared with the all FLAC models

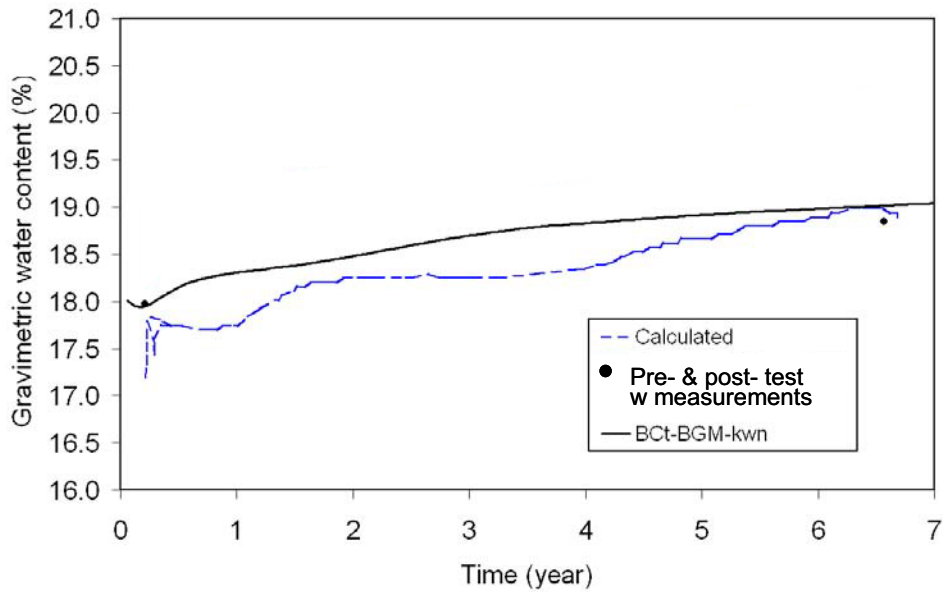


Figure 9.9 Gravimetric water content (w) evolution of BCT-BGM-kwn model at location IBX9 compared with the field measurements (calculated gravimetric water content after Dixon et al. 2000) (see Figure 8.28 for location)

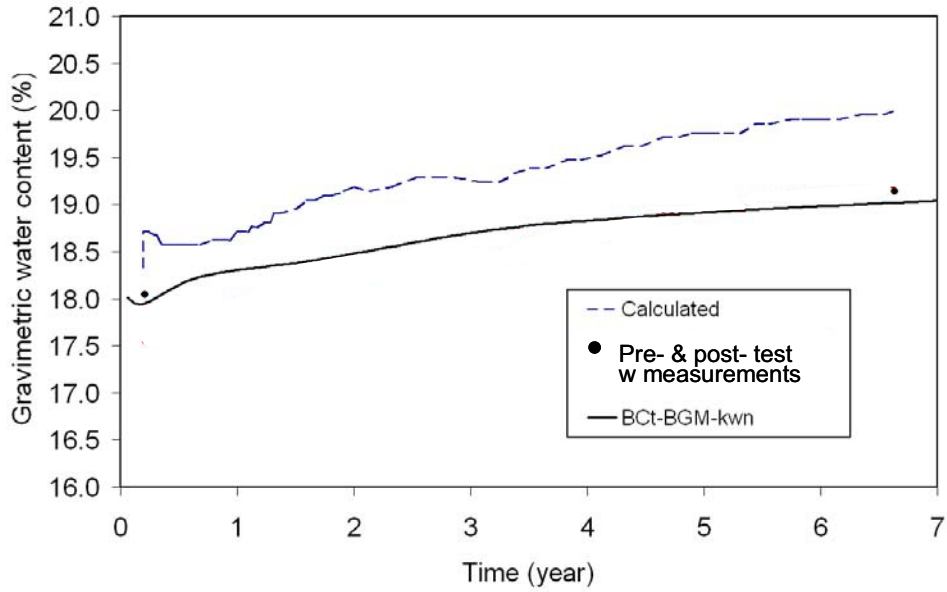


Figure 9.10 Gravimetric water content (w) evolution of BCt-BGM-kwn model at location IBX11 compared with the field measurements (calculated gravimetric water content after Dixon et al. 2000) (see Figure 8.28 for location)

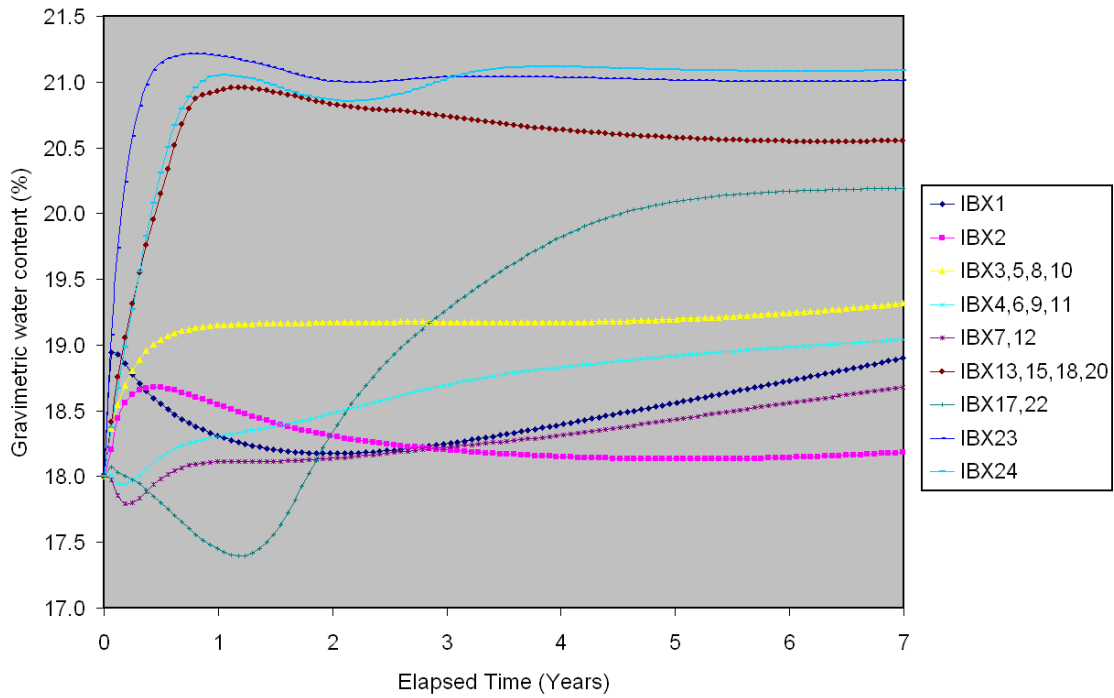
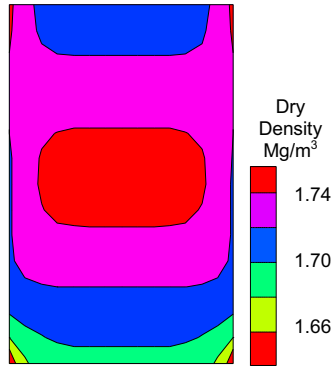
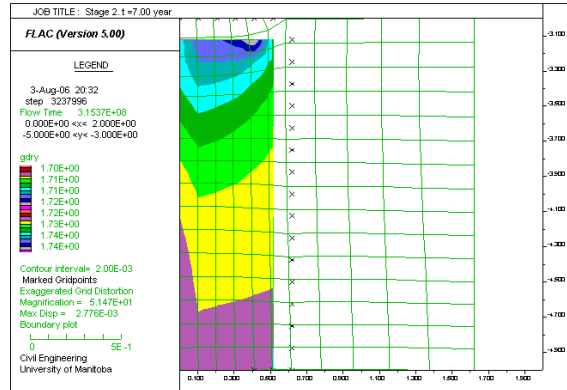


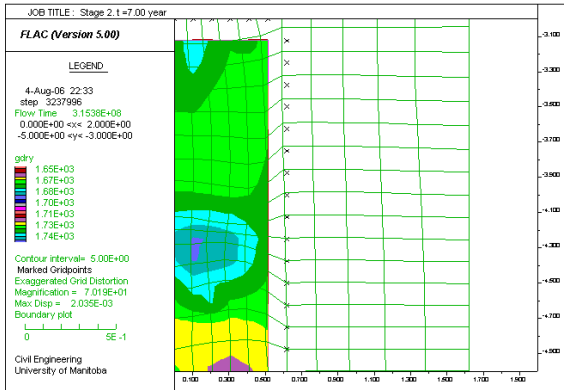
Figure 9.11 Gravimetric water content (w) evolution of BCt-BGM-kwn model at location IBX1-24 (see Figure 8.28 for locations)



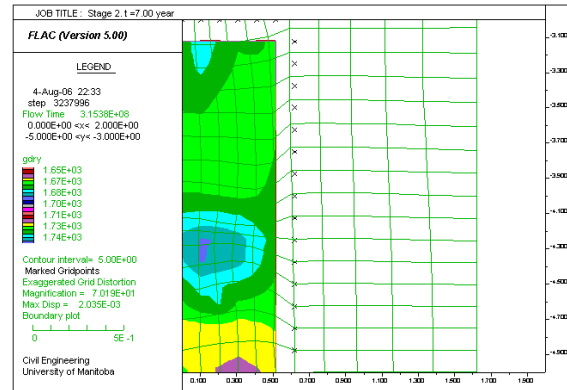
(a) Measurements



(b) BCT-LE



(c) BCT-BGM



(c) BCT-BGM Kwn

Figure 9.12 Dry density at the end of the test

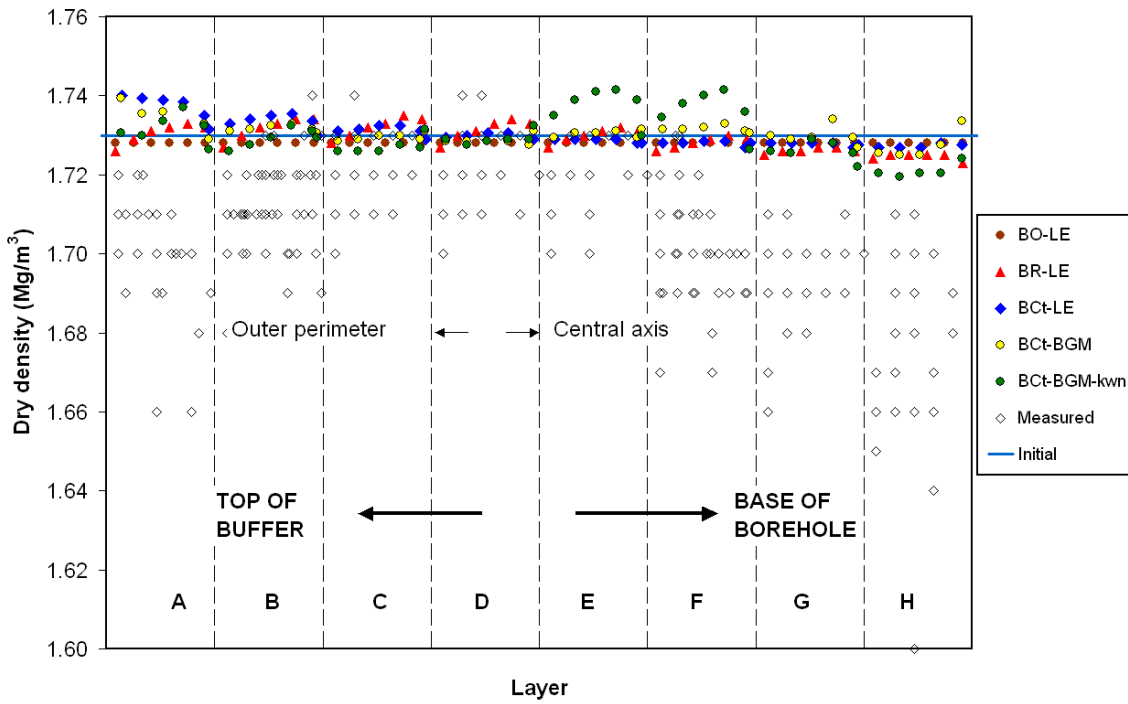


Figure 9.13 End of test gravimetric water content (w) measurements compared with the all FLAC models

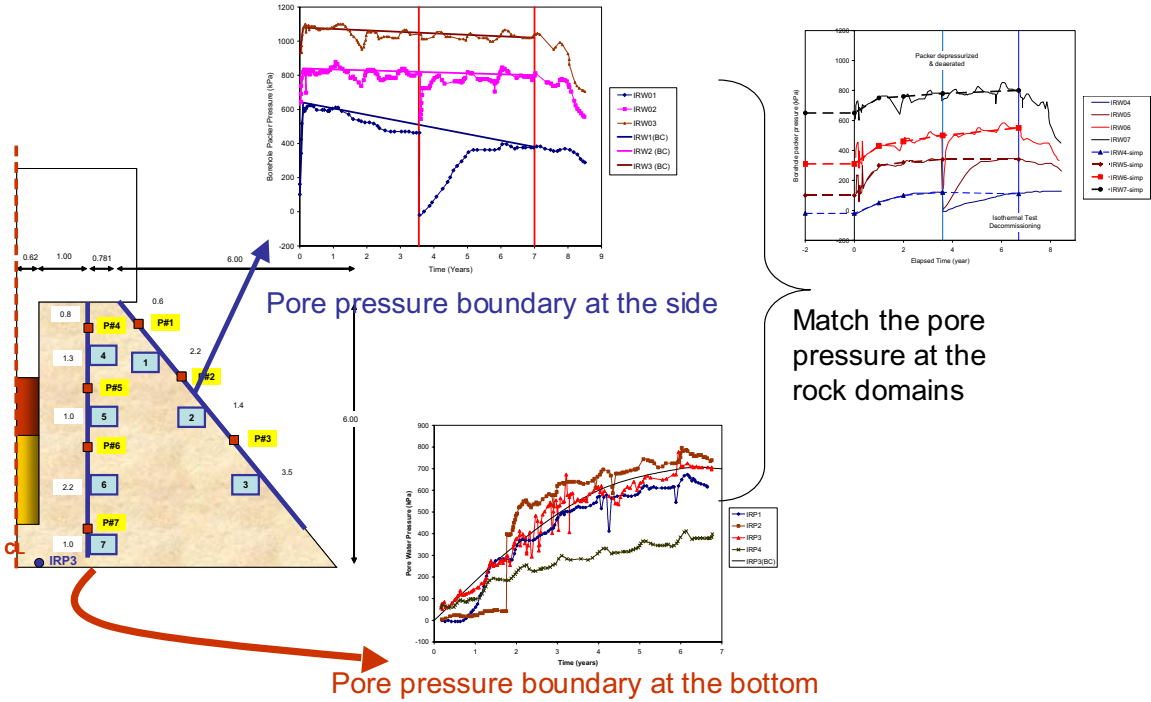


Figure 9.14 Back-analysis to define properties of the rock

PART 6:
SUMMARY, CONCLUSIONS, CONTRIBUTIONS, AND
SUGGESTIONS FOR FUTURE RESEARCH

CHAPTER 10

SUMMARY, CONCLUSIONS, CONTRIBUTIONS AND SUGGESTIONS FOR FUTURE RESEARCH

10.1 Summary and Conclusions

This research was aimed at developing constitutive models to simulate the hydraulic-mechanical behaviour of unsaturated swelling clays. This work includes: calibration of parameters and development of new constitutive models, implementation, and applications of hydro-mechanical constitutive models. This chapter provides a summary of the results of this research and the conclusions from the previous chapters.

Chapter 3- Mechanical Constitutive Models

The implementation of two elasto-plastic constitutive models (e.g. the BBM (Alonso et al. 1990) and the BGM (Blatz and Graham 2003) has been made using finite difference software (FLAC, Itasca 2001). The verification of the implementation for mechanical only analysis and hydro-mechanical analyses has also been presented. Appendix 1 presents the verification of the mechanical only analysis for the BBM model and Appendix 2 discuss the verification of the hydraulic-mechanical analysis using the BBM and BGM. Note that effective stress is used in the two-phase hydro-mechanical analysis (Itasca

2001) and the modifications of the mechanical constitutive models are required due to the different stress-state variables used in the models.

Chapters 4&5–Permeability Model and Water Retention Surface

A new porosity-dependent permeability (k_{wn}) model and water retention surface (WRS) for unsaturated swelling clay that are a function of degree of saturation (S_w) and specific volume (v) or porosity (n) have been presented. The mathematical equations of this surface have been presented and are ready to be implemented in the numerical analysis (e.g. finite difference (FD), finite element (FE), or finite volume (FV)) to solve boundary value problems. The parameters used in these models for BSB materials have been calibrated using laboratory measurements. The implementation of the porosity-dependent permeability (k_{wn}) model in 2-phase flow analysis using FLAC (Itasca 2001) has been completed.

The mathematical and numerical formulations to implement the water retention surface (WRS) in 2-D finite difference hydro-mechanical analysis have been presented in Chapter 5. The formulation in Chapter 5 is ready to be used to implement the WRS in 2D finite difference analysis.

Chapter 6-Parameter Evaluation Method (PEM).

This research proposes a method termed the ‘Parameter Evaluation Method’ (PEM) that has the ability to determine the parameters of constitutive models and to evaluate the performance of constitutive models. This algorithm has an ability to calibrate the constitutive model parameters simultaneously that can reduce the difficulty of calibration of constitutive models with many parameters, so that the number of parameters should

not be a measure used to define the complexity of constitutive models. The principal that 'when constitutive models are adequate to simulate the general behaviour of a material, their parameters should not change due to various input' is used to generate the criteria to evaluate the constitutive models.

In the case of mechanical constitutive models, criteria used to evaluate their performance are:

- 1) The simulated response and laboratory response for each of the stress path and response must be relatively similar in the magnitude and direction.
- 2) The variation of the parameters generated from different stress paths is relatively small.
- 3) The locations of the yield surface should not alter with various stress paths.

This PEM algorithm is used to simulate the mechanical behaviour of unsaturated swelling clay using two elasto-plastic mechanical constitutive models (e.g. BBM (Alonso et al. 1990) and BGM (Blatz and Graham 2003)). The results indicate some limitations of both constitutive models. Modifications were subsequently made to of the BGM model (Blatz and Graham 2003) have been made based on this evaluation.

The infiltration process in unsaturated swelling clay includes both fluid and mechanical behaviour. Considering a mechanical constitutive model independently is not adequate to simulate this behaviour. The recommendation is made to incorporate the hydraulic-mechanical process in the simulations program in the to implementation of the PEM algorithm.

Chapters 7– Modelling small scale infiltration tests

Modelling the small-scale infiltration test of unsaturated swelling clay with two types of boundary conditions (constant volume (CV) and constant mean stress (CMS)) has been presented in this study using three combinations of hydraulic and mechanical constitutive models:

- 1) LE (Linear Elastic – van Genuchten (1980) models)
- 2) BGM (Blatz and Graham 2003) – van Genuchten (1980) models)
- 3) BGM-kwn (Blatz and Graham 2003 – van Genuchten (1980) models)

The results of the analyses indicate that:

- 1) The porosity-dependent permeability model creates a 'pseudo permeability layer' greatly slowing the rate of saturation the inner layer from reaching 100% saturation.
- 2) The porosity-dependent permeability (kwn) model are only effective for the rigid boundary conditions such as that in constant volume (CV) test.

Chapters 8– Modelling Large-Scale Isothermal Test (ITT)

Modelling the full-scale isothermal test (ITT) has been made using 2-phase flow fluid-mechanical analysis in FLAC2D (Itasca 2001) with 3 combinations of boundary conditions, mechanical and hydraulic constitutive models, such as:

- 1) buffer only analysis using constant pore pressure boundary conditions, linear elastic and van Genuchten (1980) models (BO)
- 2) buffer-rock interaction analysis using far-field rock pore pressure boundary condition, linear elastic and van Genuchten (1980) models (BR-LE)
- 3) buffer-rock interaction analysis using far-field rock pore pressure boundary condition, Blatz and Graham (2003) and van Genuchten (1980) models (BR-BGMkwn).

The following conclusions can be made based on the analysis:

- 1) The rock properties and boundary conditions have a significant role in the ITT test.
- 2) The BO analysis does not have any mechanism to inhibit full saturation. The BR-LE analysis has 'desaturation' mechanism in the rock near the buffer-rock interface, while the BR-BGMkwn has both 'desaturation' and 'pseudo impermeable skin' mechanisms to inhibit full saturation.
- 3) In general, the two-phase flow formulation in FLAC2D can simulate the hydro-mechanical behaviour of the buffer in the ITT tests, if the rock is being considered in the modelling.

Chapter 9 – Time dependent boundary conditions

The buffer-rock analyses using the pore water pressure measurement in the rock as time-dependent boundary conditions (BCt) have been presented. Three combinations of hydraulic and mechanical constitutive models are used in the analyses:

- 1) BCt-LE (Linear Elastic – van Genuchten (1980) models)
- 2) BCt-BGM (Blatz and Graham 2003) – van Genuchten (1980) models)
- 3) BCt-BGM-kwn (Blatz and Graham 2003 , van Genuchten (1980), and porosity dependent permeability (kwn) model)

The following conclusions can be made from the results the analyses:

- 1) The time-dependent boundary condition (BCt) models can reduce the uncertainty of the far field boundary conditions in the rock and properties of the rock.
- 2) The result of BCt analysis indicates that there may be a possible anisotropic permeability of the rock within the domain.
- 3) Comparison of end of test gravimetric water content due to the BCt-LE, BCt-BGM, and BCt-BGM-kwn analysis (Figure 9.8) with the laboratory measurements show that the applications of the BGM (Blatz and Graham 2003) model and

porosity dependent permeability (kwn) model in BCt-BGM kwn analysis to describe the hydro-mechanical behaviour of the buffer can improve the performance of the numerical models.

- 4) Comparison of the end of test gravimetric water content of BCt-BGMkwn analysis (Figure 9.8) and BR-BGM-kwn analysis (Figure 8.33) indicates that the applications of the time-dependent boundary conditions can improve the prediction of the volume-mass relationship within the buffer.

The interaction of the numerical modeller that expert in the numerical models and other experts in the laboratory as well as the field tests is key element to build a better numerical model.

10.2 Objectives versus Findings

The overall objective of this research is to develop and apply constitutive models that can improve the performance of numerical modelling of hydraulic (H) and mechanical (M) behaviour of unsaturated swelling clay over existing constitutive models. Two questions presented in Chapter 1 will be answered based on the finding in this thesis.

Question 1:

'Is the application of a coupled critical state based mechanical constitutive model and hydraulic permeability model that include the effect of boundary conditions within the constitutive models can improve the performance of the numerical modelling of the infiltration process in unsaturated swelling clay over existing numerical models?'

The modelling small scale and large-scale isothermal tests (ITT) in Chapters 7-9 shows that the applications of the elasto-plastic mechanical constitutive models and porosity-dependent permeability model can improve the performance of the numerical model to

describe the behaviour of the systems by adding mechanisms that can be simulated using the constitutive models.

The elasto-plastic model (BGM) simulates some mechanisms (e.g. strain hardening or strain softening and yielding), which are not considered by linear elastic (LE) models. The porosity-dependent permeability model (kwn) creates 'pseudo impermeable skin' mechanism that cannot be produced by conventional permeability model that is only dependent on the degree of saturation (S_w).

The 'pseudo impermeable skin' mechanics occurs within the buffer. An application of the porosity-dependent permeability (kwn) model is one of the methods to incorporate the effect of boundary conditions into a hydraulic constitutive model. Another method, such as an application of the water retention surface in Chapters 4 and 5 can be used to implement the effect of the boundary conditions within the the hydro-mechanical constitutive models.

Comparison of the end-of-test gravimetric water content of BCt-BGMkwn analysis (Figure 9.8) and BR-BGM-kwn analysis (Figure 8.33) in Chapter 9 shows that the application of the time-dependent boundary condition can improve the model ability to simulate the hydro-mechanical behaviour of unsaturated swelling clay.

In conclusion, it has been proven from the study that an adequate mechanical and hydraulic constitutive model and boundary conditions are required to simulate the hydro-mechanical behaviour of unsaturated swelling clay.

Question 2:

'Can the estimation of parameter selection for rigorous constitutive models be automated using numerical search algorithm to identify parameters within user specified physical limits?'

The Parameter Evaluation Method (PEM) algorithm has an ability to estimate parameters of the mechanical constitutive models simultaneously. It also has the capability to evaluate the performance of the constitutive models. The implementations of the PEM algorithm in Chapter 6 have created a simulation program to reduce the difficulty of the determinations of constitutive model parameters (e.g. BBM (Alonso et al. 1990) and BGM (Blatz and Graham 2003)).

One of the PEM criteria 'examination of the variability of constitutive model parameters' can be used in determination of general hydraulic and mechanical constitutive models. This criterion has a potential to be applied automatically in the computer software following the back-fitting process. Creating this 'computer software' can isolate the difficult part of calibrations of complex constitutive model parameters, so that it can reduce the difficult of constitutive model application. The development of this 'computer software' is suggested as future research.

10.3 Contributions

This thesis has advanced the science of numerical simulation of unsaturated swelling clay on several fronts by providing several unique contributions as follows:

- This thesis has incorporated an existing mechanical constitutive model formulation (the BBM (Alonso et al. 1990)) on a new platform FLAC (Fast Lagrangian Analysis of Continua) (Itasca 2001) (in Chapter 3).
- The first ever numerical implementation in FLAC (Chapter 3) and application of the Blat-Graham Model (BGM) (Blatz and Graham 2003) for hydro-mechanical analysis of unsaturated swelling clay (Chapters 7 and 8).
- This thesis has provided the first ever comparison of two mechanical constitutive models (i.e., the BBM and the BGM) (Chapters 6, 7, and 8).
- This thesis has also provided a new method for multiple parameter determination for use in constitutive modelling, called the Parameter Evaluation Method (PEM). This method has introduced novel numerical approaches in application of rigorous constitutive models (Chapter 6).
- This thesis has proposed, implemented, and applied a new porosity dependent permeability (k_{wn}) hydraulic constitutive model that has not been previously proposed by any other researcher in the field (Chapter 4). This new model has also been applied for hydro-mechanical analysis of unsaturated swelling clay (Chapters 7 and 8)
- This thesis has proposed a new three-dimensional water retention surface (WRS) for unsaturated swelling clay that incorporate the effect of the boundary conditions complete with its mathematical equations (Chapter 4). The numerical formulations to apply the new three-dimensional water retention surface (WRS) in finite difference method has also been completed (Chapter 5). This new model and its numerical formulation have not been previously proposed by any other researcher in the field.
- This thesis has performed the first ever time-dependent pore water pressure boundary condition model (Chapter 9).

- This thesis has performed a three-fold assessment of this work that includes calibration to laboratory tests, simulation of laboratory tests with controlled stress paths and boundary conditions, and simulation of a large scale field test conducted by other researchers using a similar swelling clay.

10.4 Suggestions for Future Research

Several suggestions for future research based on the finding in the previous chapters are summarized as follows.

- 1) The limitation of volume-mass relationship for swelling clay is indicated from the transformation from gravimetric water content (w) (Figure 4.8a) into degree of saturation (S_w) space (Figure 4.8b). This limitation may be reduced by consideration of the soil solids as two independent structures: micro-pores and macro-pores. The ECDD and EMDD concepts may be used to build this volume-mass relationship for swelling soil that can improve the calibration of the constitutive models
- 2) Further calibrations of the parameters of porosity-dependent permeability (k_{wn}) models and water retention surface (WRS) for unsaturated swelling clay in Chapters 4 and 5 are still required.
- 3) The porosity dependent permeability (k_{wn}) models and water retention surface (WRS) formulation in Chapter 4 are developed based on the results of the laboratory testing of the BSB materials. The examination of the k_{wn} and WRS surface using other laboratory test results from different soils (e.g. Vanapalli et al. 1999) can extend the application of these constitutive models (S.K. Vanapalli, personal communication, June 29, 2007).

- 4) The numerical formulation to implement the water retention surface (WRS) in 2D finite difference fluid-mechanical analysis has been generated in Chapter 5. The implementation of these formulations into computer program is still required to investigate the performance of the WRS.
- 5) The simulation program used to implement the PEM algorithm only considers mechanical constitutive model independently. The infiltration process in unsaturated swelling clay includes both fluid and mechanical behaviours. Considering mechanical constitutive models independently is not adequate to simulate this behaviour. The recommendation is made to incorporate hydro-mechanical constitutive models in the simulations program to implement the PEM algorithm. The numerical formulations in Chapter 5 can be used to create a simulation program to implement the PEM algorithm.
- 6) The last PEM criterion of “the variation of the parameters generated from different stress paths” has a potential to be applied automatically in the computer software following the back-fitting process. Creating this computer software can isolate the difficult part of calibrations of complex constitutive model parameters, so that it can reduce the difficulty in constitutive model application.
- 7) Test stress paths can be optimized to produce parameters that are well constrained as part of a formalized calibration process (N. Chandler, personal communication, June 29, 2007).
- 8) Some of the aspects in the swelling clay behaviour can be modelled using 2-phase flow hydro-mechanical analysis in FLAC. The limitation of the numerical modelling presented in Chapter 7 is due to the assumptions of the incompressible soil solids. This limitation may be reduced with an application of water retention surface presented in Chapter 6, which is suggested as future research.

- 9) Models with time-dependent pressure boundary condition indicate that there is a limitation of the rock properties used in the analysis. The anisotropic permeability of the rock may exist within the domain. Using back analysis and time dependent models the properties of the rock including the anisotropic permeability and the excavation damage zone (EDZ) can be estimated.
- 10) Applications of the hydro-mechanical constitutive models to simulate other geotechnical engineering structures, such as shallow foundation, pavement, and dams.
- 11) Two-phase flow formulation in FLAC has used in the analysis in this thesis. The investigation of the modelling of the same problem using one-phase flow formulation may be made to investigate the importance of 2-phase flow formulation. The analysis using 1-phase flow formulation may reduce the difficulty in the modelling air transport when using 2-phase flow formulation (N. Chandler, personal communication, 29 June 2007).

REFERENCES

- AECL. (1994). Environmental impact statement on the concept for disposal of Canada's nuclear fuel waste. *Atomic Energy of Canada Limited Report, AECL-10711, COG-93-1*.
- Agus, S. S., Leong, E-C., & Rahardjo, H. (2005). Estimating permeability functions of Singapore residual soils. *Engineering Geology, 78*, 119-133.
- Al-Mukhtar, M., Robinet, J. C., Liu, C. W., & Plas, F. (1993). Hydromechanical behaviour of partially saturated low porosity clays. *Proceedings of the International Conference on Engineered Fills, Newcastle-Upon-Tyne, U.K.*, 87–98.
- Alonso, E. E., Gens, A., & Hight, D. W. (1987). Special problem soils - General report. *Proc. 9th European Conf. Soil Mech. Fdn Engng, Dublin, 3*, 1087-1146.
- Alonso, E. E., Gens, A., & Josa, A. (1990). A constitutive model for partially saturated soils. *Géotechnique, 40*(3), 405-430.
- Alonso, E. E., Lloret, A., Gens, A., & Yang, D. Q. (1995). Experimental behaviour of highly expansive double-structure clay. *Proc. 1st Int. Conf. on Unsaturated Soil, Balkema, Paris, 1*, 11–16.
- Alonso, E. E., Vaunat, J., & Gens, A. (1999). Modelling the mechanical behaviour of expansive clays. *Engineering Geology, 54*, 173-183.
- Anandarajah, A. (1994). Discrete-Element Method for Simulating Behaviour of Cohesive Soil. *Journal of Geotechnical Engineering, ASCE, 120*(9), 1593-1613.
- Anderson, D., Blatz, J., Graham, J., & Chandler, N. (2002, October 20-23). Yielding behaviour of unsaturated and compacted bentonite. *Proceedings of the 55th Canadian Geotechnical and 3rd Joint IAHCNC and CGS Groundwater Specialty Conferences, Niagara Falls, Ontario, 2*, 1255-1260.
- Anderson, D. E. S. (2003). Evaluation and comparison of mechanical and hydraulic behaviour of two engineered clay sealing material. *M.Sc Thesis, Dept. Civil Engineering, University of Manitoba, Winnipeg, Manitoba*.
- Annor, A., & Jackson, R. (1987). Mechanical, thermomechanical and joint properties of rock samples from the Lac du Bonnet batholith, Manitoba. In T. J. Katsube, & J. P. Hume (Eds.), *Geotechnical studies at Whiteshell Research Area (RA-3), Divisional Report MRL 87-52 (Int)*, 52-94. CANMET Mining Research Laboratories, Ottawa.

- Averjanov, S. F. (1950). About permeability of subsurface soils in case of complete saturation. *English Collection*, 7, 19-21.
- Barbour, S. L., & Krahn, J. (2004, December). Numerical modelling – prediction or process? *GEOSPEC, Geotechnical News*, 44-52.
- Baumgartner, P., & Snider, G. R. (2002). Seal Evaluation and Assessment Study (SEAS); Light Backfill placement trials. *Atomic Energy of Canada Limited Technical Record, TR-793*.
- Biot, M. (1941). General theory of three-dimensional consolidation. *Journal of Applied Physics*, 12, 155–164.
- Biot, M. (1955). Theory of elasticity and consolidation for a porous anisotropic solid. *Journal of Applied Physics*, 26, 182–185.
- Bishop, A.W. (1959). The principle of effective stress. *Teknisk Ukeblad*, 106(39), 859–863.
- Blatz, J. A. (2000). Elastic-plastic modelling of unsaturated high-plastic clay using results from a new triaxial test with controlled suction. *Ph.D Thesis, Dept. Civil Engineering, University of Manitoba, Winnipeg, Manitoba*.
- Blatz, J. A., & Graham, J. (2000). A system for controlled suction in triaxial tests. *Géotechnique*, 50(4), 465-478.
- Blatz, J. A., & Graham, J. (2003). Elastic plastic modelling of unsaturated high-plastic clay using results from a new triaxial test with controlled suction. *Géotechnique*, 53(1), 113-122.
- Blatz, J. A., Anderson, D., & Siemens, G. A. (2005). Evaluation of elastic-plastic model parameters for two unsaturated compacted bentonite mixtures. Manuscript submitted to *Canadian Geotechnical Journal*.
- Bolzon, G., Schrefler, B. A., & Zienkiewicz, O. C. (1996). Elastoplastic soil constitutive laws generalized to partially saturated states. *Géotechnique*, 46, 279-289.
- Brooks, R. H., & Corey, A. T. (1964). Hydraulic properties of porous media. *Hydrology paper number 3, Colorado State University, Fort Collins*.
- Campbell, J. D. (1973). Pore pressures and volume changes in unsaturated soils. *Ph.D Thesis, University of Illinois at Urbana-Champaign, Urbana-Champaign, Illinois*.
- Canadian Standard Association. (1984). *Design of concrete structure for Buildings, CAN3-A23.3 M84*. Toronto.
- Cement Association of Canada (CAC). (2006). Testing Hardened Concrete Permeability. Retrieved June 21, 2006, from <http://www.cement.ca/cement.nsf/>

- Chandler, N. A. (2000). Water inflow calculations for the isothermal buffer-rock-concrete plug interaction test. *Ontario Power Generation Report No: 06819-REP-01200-10046-R0*.
- Chapman, D. L. (1913). A contribution to the theory of electrocapillarity. *Philosophical Magazine*, 25, 475–481.
- CPCA. (1995). *Concrete design handbook*. Ottawa, Ontario: Canadian Portland Cement Association.
- CPCI. (1996). *Design Manual* (3rd ed.). Canadian Prestressed Concrete Institute.
- Cross, H. (1949). Analysis of Continuous Frames by Distributing Fixed-End Moments. In L. B. Grinter (Ed.), *Numerical Methods of Analysis in Engineering*. Successive Corrections. New York.
- Dangla, P. (1999). *Approches Energetique et Numerique des Milieux Poreux Non Satures*. Memoire d'habilitation a diriger des rechrces. Ecole Nationale des Ponts et Chaussees. Ecole Normale Superiure de Cachan. Universite de Marne-la-Valee.
- Davidson, J. M., Stone, L. R., Nielson, D. R., & Larue, M. E. (1969). Field measurement and use of soil-water properties. *Water Resources Research*, 5, 1312-1321.
- Davies, P.B. (1991). Evaluation of the role of threshold pressure in controlling flow of waste-generated gas into bedded salt at the Waste Isolation Pilot Plant. *Technical Report SAND-90-3246*. Albuquerque: Sandia National Laboratories.
- Davis, R.O., & Selvadurai, A. P. S. (1995). *Elasticity and Geomechanics*. Cambridge: Cambridge University Press.
- Davis, R. O., & Selvadurai, A. P. S. (2002). *Plasticity and Geomechanics*. Cambridge: Cambridge University Press.
- Delage, P., & Graham, J. (1996). Understanding the behaviour of unsaturated soils requires reliable conceptual models. State-of-Art Report, Session 1, Soil Properties. In *Proceedings of the 1st International Conference on Unsaturated Soils, Paris, France, September 1995* (E.E. Alonso & P. Delage, Eds.) A.A. Balkema, Rotterdam, The Netherlands, 3, pp. 1223-1256.
- Dixon, D. A. (1999). Towards an understanding of water structure and water movement through dense clays. *Ph.D Thesis, Department of Civil and Geological Engineering, University of Manitoba, Winnipeg, Manitoba*.
- Dixon, D. A., & Chandler, N. A. (2000). Physical properties of the materials recovered from the isothermal buffer-rock-concrete plug interaction test conducted at the URL. Used Fuel Disposal Program Supporting Technical Report 06819-REP-01300-10003-R00. Ontario Power Generation.
- Dixon, D. A., & Miller, S. H. (1995). Comparison of the mineralogical composition, physical, swelling and hydraulic properties of untreated sodium bentonites from

- Canada, the United States and Japan. *Atomic Energy of Canada Limited Report, AECL-11303*.
- Dixon, D. A., Graham, J., & Gray, M. N. (1999). Hydraulic conductivity of clays in confined tests under low hydraulic gradients. *Can. Geotech. J.*, 36, 815-825.
- Dixon, D. A., Chandler, N. A., Stroes-Gascoyne, S., & Kozak, E. (2001). *The Isothermal Buffer-Rock-Concrete Plug Interaction test: Final Report. Report No: 06819-REP-01200-10056-R00*. Ontario Power Generation, Nuclear Waste Management Division. Toronto, Canada.
- Dixon, D., Chandler, N., Graham, J., & Gray, M. N. (2002). Two large-scale sealing tests conducted at Atomic Energy of Canada's underground research laboratory: the buffer-container experiment and the isothermal test. *Canadian Geotechnical Journal*, 39, 503-518.
- Dueck, A. (2004). Hydro-mechanical properties of a water unsaturated sodium bentonite, Laboratory study and theoretical interpretation. *Doctoral Thesis, Department of Building and Environmental Technology, Lund University, Division of Soil Mechanics and Foundation Engineering, Lund*.
- Farrel, D., & Larson, W. (1972). Modelling the pore structure of porous media. *Water Resources Research*, 8, 699-705.
- Fleureau, J. M., Kheirbek-Saoud, S., & Taibi, S. (1995, September 6-8). Experimental aspects and modelling of the behaviour of soils with a negative pressure. *Proceedings of the 1995 1st International Conference on Unsaturated Soils. Part 1 (of 2)*. Paris, France.
- Fredlund, D. G., & Morgenstern, N. R. (1977). Stress-state variables for unsaturated soils. *J. Geotech. Eng. Division, Am. Soc. Civil Engineers*, 103, 447-466.
- Fredlund, D. G., & Rahardjo, H. (1993). *Soil mechanics for unsaturated soils*. New York: John Wiley & Sons.
- Fredlund, D. G., & Xing, A. (1994). Equations for the Soil-Water Characteristic Curve. *Canadian Geotechnical Journal*, 31(3), 521-532.
- Gallipoli, D., Gens, A., Sharma, R. S., & Vaunat, J. (2003). An elasto-plastic model for unsaturated soil incorporating the effect of suction and degree of saturation on mechanical behavior. *Géotechnique*, 53(1), 123-135.
- Gardner, W. R. (1958). Some steady state solutions of the unsaturated moisture flow equation with application to evaporation from a water table. *Soil Science*, 85(4), 220-232.
- Gens, A., Garcia-Molina, A. J., Olivella, S., Alonso, E. E., & Huertas, F. (1998). Analysis of full scale in situ test simulating repository conditions. *Int. J. Numer. Anal. Methods Geomech.*, 22, 515-548.

- Gens, A., & Alonso, E. E. (1992). A framework for the behaviour of unsaturated expansive clays. *Can. Geotech. J.*, 29, 1013-1032.
- Gouy, G. (1910). Electric charge on the surface of an electrolyte. *Journal of Physics*, 4(9), 457.
- Graham, J., Chandler, N. A., Dixon, D. A., Roach, P. J., To, T., & Wan, A. W. L. (1997). The Buffer/Container Experiment: Results, synthesis, issue. *Report AECL-11746, COG-97-46-1*. Atomic Energy Canada Limited, Ontario.
- Gray, M. N., Cheung, S. C. H., & Dixon, D. A. (1984). The influence of sand content on swelling pressures and structure developed by statically compacted Na-Bentonite. *Atomic Energy of Canada Limited Report, AECL 7825*.
- Guo, R., & Dixon, D. A. (2005). Coupled Hydromechanical Modelling of AECL's Isothermal Test and Comparison with Measured Data. *Ontario Power Generation Report No: 06819-REP-01200-10153-R00*.
- Haines, W. B. (1930). Studies in the physical properties of soil. V. The hysteresis effect in capillary properties and the modes of moisture distribution associated therewith. *Journal of Agricultural Science*, 20, 97-116.
- Holtz, W.G., & Kovacs, W. G. (1981). *An Introduction to Geotechnical Engineering*. Englewood Cliffs, NJ: Prentice-Hall.
- Israelachvili, J. (1992). *Intermolecular & Surface Forces* (2nd ed.). San Diego: Academic.
- Itasca Consulting Group, Inc. (2000a). *FLAC Fast Lagrangian Analysis of Continua, FISH in FLAC*. Minneapolis, Minnesota: Itasca Consulting Group, Inc.
- Itasca Consulting Group, Inc. (2000b). *FLAC Fast Lagrangian Analysis of Continua, Theory and Background*. Minneapolis, Minnesota: Itasca Consulting Group, Inc.
- Itasca Consulting Group, Inc. (2001). *FLAC Fast Lagrangian Analysis of Continua, Fluid-Mechanical Interaction*. Minneapolis, Minnesota: Itasca Consulting Group, Inc.
- Iwata, S., Tabuchi, T., & Wakertin, B. P. (1995). *Soil-Water Interactions: Mechanisms and Applications* (2nd ed.). New York: Marcel Dekker.
- Jennings, J. E., & Burland, J. B. (1962). Limitations of the use of effective stresses in partly saturated soils. *Géotechnique*, 12(2), 125-144.
- Jones, D. E., & Holtz, W. G. (1973). Expansive soils – the hidden disaster. *Civil Eng., ASCE*, 43(8), 49-51.
- Karube, D., Kato, S., Hamada, K., & Honda, M. (1995). The relationship between the mechanical behaviour and the state of pore water in unsaturated soil (in Japanese). Accepted for publication in *JSCE Journal of Geotechnical Engineering*.

- Kato, S., Karube, D., Honda, M., & Fujiwara, T. (1995). Influence of pore water arrangement on the compression behaviour of unsaturated soil (in Japanese). Accepted for publication in *JSCE Journal of Geotechnical Engineering*.
- Khalili, N., & Khabbaz, M. H. (1998). A unique relationship for χ for the determination of the shear strength of unsaturated soils. *Géotechnique*, 48(2), 1-7.
- Khalili, N., Khabbaz, M. H., Valliappan, S. (2000). An effective stress based numerical model for flow and deformation in unsaturated soils. *Comput. Mech.*, 26, 174-184.
- Koerner, R. M. (1998). *Designing with Geosynthetics*. NJ: Prentice Hall.
- Lade, P. V. (2005, January 23-27). Overview of constitutive models for soils. Keynote lecture at the G-I Geo-Frontiers 2005 Conference in Hilton Austin Convention Center, Austin, Texas.
- Leong, E. C., & Rahardjo, H. (1997a). Reviews of soil-water characteristic curve equations. *Journal of Geotechnical and Geoenvironmental Engineering*, 123, 1106-1117.
- Leong, E. C., & Rahardjo, H. (1997b). Permeability functions for unsaturated soils. *Journal of Geotechnical and Geoenvironmental Engineering*, 123, 1118-1126.
- Lide, D. R. (2007). CRC Handbook of Chemistry and Physics, Internet version 2007 (87th ed.), from <http://www.hbcnetbase.com>
- Lu, N., & Likos, W. J. (2004). *Unsaturated Soil Mechanics*. New Jersey: John Wiley & Sons Inc.
- Maak, P., & Simmons, G. R. (2005, May 8-11). Deep geologic repository concepts for isolation of used fuel in Canada. In *Proc. of Waste Management, Decommissioning, and Environmental Restoration for Canada's Nuclear Activities - Current Practices and Future Needs*. Ottawa, Canada.
- Malvern, L. A. (1969). *Introduction to the Mechanics of a Continuous Medium*. Englewood Cliffs, NJ: Prentice-Hall.
- Marti, J., & Cundall, P. A. (1982). Mixed Discretisation Procedure for Accurate Solution of Plasticity Problems. *Int. J. Num. Methods and Anal. Methods in Geomechanics*, 6, 129-177.
- Martin, R. T. (1962). Adsorbed water on clay: a review. 9th Nat. Conf. On Clays and Clay Minerals, pp. 28-70. Oxford: Pergamon.
- McKee, C. R., & Bumb, A. C. (1984, March). The importance of unsaturated flow parameters in designing a monitoring system for hazardous wastes and environmental emergencies. *Proceedings, Hazardous Materials Control Research Institute National Conference, Houston, TX*, pp. 50-58.

- McKee, C. R., & Bumb, A. C. (1987, December). Flow-testing coalbed methane production wells in the presence of water and gas. *In SPE Formation Evaluation*, pp. 599-608.
- Mualem, Y. (1978). Hydraulic conductivity of unsaturated porous media: Generalized macroscopic approach. *Water Resources Research*, 14(2), 325-334.
- Mualem, Y. (1984). A modified dependent domain theory of hysteresis. *Soil Science*, 137, 283-291.
- Mualem, Y. (1986). Hydraulic conductivity of unsaturated soils: prediction and formulas. In A. Klute (Ed.), *Methods of soil analysis. Part I Physical and mineralogical methods (2nd ed.)*. Agronomy (pp. 799-823). Madison, Wisconsin: American Society of Agronomy, Inc. & Soil Society of America, Inc.
- Munson, B. R., Young, D. F., & Okiishi, T. H. (2005). *Fundamentals of fluid mechanics* (5th ed.). New York: Wiley and Sons.
- Nimmo, J. R. (1992). Semiempirical model of soil water hysteresis. *Soil Science Society of America Journal*, 56, 172-173.
- Oberg, A.-L., & Sallfors, G. (1995). Rational approach to the determination of the shear strength parameters of unsaturated soils. *Proc 1st Int. Conf. Unsaturated Soils*, 1, 151.
- Olivella, S., Gens, A., Carrera, J., & Alonso, E. E. (1996). Numerical formulation for a simulator (CODE_BRIGHT) for the coupled analysis of saline media. *Engineering Computations*, 13(7), 87-112.
- Peaceman, D. W. (1977). *Fundamentals of Numerical Reservoir Simulation*. *Developments in Petroleum Science*, 6. Elsevier.
- Potts, D. M. (2003). Numerical analysis: a virtual dream or practical reality? *Géotechnique*, 53(6), 535-573.
- Priyanto, D. G., Blatz, J. A., Siemens, G. A., & Graham, J. (2004, October 24-27). The parameter evaluation method (PEM) of elastic-plastic model properties for unsaturated high-plastic clay. *The 57th Annual Canadian Geotechnical Conference, Quebec City*.
- Priyanto, D. G., Blatz, J.A., & Siemens, G. A. (2005, September 18-21). Comparison of two constitutive models to simulate the behaviour of unsaturated swelling clay. *The 58th Annual Canadian Geotechnical Conference, Saskatoon, Saskatchewan*.
- Priyanto, D. G., Siemens, G. A., Blatz, J. A. (2006, April 2-6). Evaluation of two constitutive models to simulate behavior during constant volume infiltration on a swelling clay soil. *The Fourth International Conference on Unsaturated Soils. Unsaturated Soils 2006. Carefree, AZ*.

- Priyanto, D.G. (2007). Computer code for H-M analysis in FLAC using two elasto-plastic mechanical constitutive models and porosity dependent permeability model. A report submitted to: Dr. James Blatz, Department of Civil Engineering, University of Manitoba, Canada (*unpublished material*).
- Pusch, R., Karnland, O., & Hökmark, H. (1990). GMM- A general microstructural model for qualitative and quantitative studies on smectite clays. *SKB Technical Report 90-43*. 94 pp.
- Richards, L. A. (1931). Capillary conduction of liquids through porous media. *Physics*, 1, 318-333.
- Roscoe, K. H., Schofield, A. N., & Wroth, C. P. (1958). On the yielding of soils. *Géotechnique*, 8, 22-53.
- Roscoe, K. H., & Burland, J. B. (1968). On the generalized stress-strain behaviour of 'wet' clay. In J. Heyman & F. Leckie (Eds.), *Engineering Plasticity* (pp. 535-609). Cambridge: Cambridge University Press.
- Russell, S. B., & Simmons, G. R. (2003). Engineered barrier system for a deep geologic repository. *International High-Level Radioactive Water Management Conference, Las Vegas, NV*.
- Schofield, A. N., & Wroth, C. P. (1968). *Critical state soil mechanics*. London: McGraw Hill.
- Siemens, G. A. (2006). Influence of boundary conditions on the hydraulic-mechanical behaviour of an unsaturated swelling soil. *Ph.D Thesis, Dept. Civil Engineering, University of Manitoba, Winnipeg, Manitoba*.
- Siemens, G. A., & Blatz, J. A. (2006). A triaxial apparatus for applying liquid infiltration under controlled boundary conditions with internal suction measurement. *ASCE Journal of Geotechnical and Geoenvironmental Engineering*, In Review.
- Simms, P. H., & Yanful, E. K. (2005). A pore-network model for hydromechanical coupling in unsaturated compacted clayey soils. *Can. Geotech. J.*, 42, 499–514.
- Spasito, G., & Prost, R. (1982). Structure of water adsorbed on smectites. *Chem. Rev.*, 82, 554-573.
- Tamagnini, R. (2005). An extended cam-clay model for unsaturated soils with hydraulic hysteresis. *Géotechnique*, 54(3), 223-228.
- Tang, G. X. (1999). Suction characteristics and elastic-plastic modelling of unsaturated sand-bentonite mixture. *Ph.D Thesis, Dept. Civil Engineering, University of Manitoba, Winnipeg, Manitoba*.
- Tang, G. X., & Graham, J. (2002). A possible elastic-plastic framework for unsaturated soils with high-plasticity. *Can. Geotech. J.*, 39, 894-907.

- Tang, G. X., Graham, J., Blatz, J., Gray, M., & Rajapakse, R. K. N. D. (2002). Suctions, stresses and strengths in unsaturated sand-bentonite. *Engineering Geology*, 64, 147-156.
- Terzaghi, K. (1936). The shear resistance of saturated soils. In *Proc. 1st Int. Conf. Soil Mech. Found. Eng.*, 1, pp. 54-56. Cambridge, MA.
- Thomas, H. R., Cleall, P. J., Chandler, N., Dixon, D., & Mitchell, H. P. (2003). Water infiltration into a large-scale in-situ experiment in an underground research laboratory. *Géotechnique*, 53(2), 207-224.
- Toll, D. G. (1990). A framework for unsaturated soils behaviour. *Géotechnique*, 40(1), 31-44.
- Toll, D. G., & Ong, B. H. (2003). Critical-state parameters for an unsaturated residual sandy clay. *Géotechnique*, 53(1), 93-103.
- Vanapalli, S. K., Fredlund, D. G., & Pufahl, D. E. (1999). The influence of soil structure and stress history on the soil-water characteristics of a compacted till. *Géotechnique*, 49(2), 143-159.
- van Genuchten, M. Th. (1980). A Closed Form Equation for Predicting the Hydraulic Conductivity of Unsaturated Soils. *Soil Sc. Soc. Am. J.*, 44, 892-898.
- Vicol, T. (1990). Comportement hydraulique et mécanique d'un sol fin non saturé. Application à la modélisation. *PhD Thesis, Ecole Nationale des Ponts et Chaussées, Paris.*
- Villar, M. V. (2002). Thermo-hydro-mechanical characterization of a bentonite from Cabo de Gata. A study applied to the use of bentonite sealing material in high level radioactive waste repositories. *Ph.D. Dissertation and ENRESA Technical Publication 01/2002, Madrid.*
- Wan, A. W. L. (1996). The use of thermocouple psychrometers to measure in-situ suctions and water contents in compacted clays. *Dept. Civil and Geological Engineering, University of Manitoba, Winnipeg, Manitoba.*
- Wheeler, S. J., & Karube, D. (1996). Constitutive modelling. *Proc. 1st Int. Conf. on Unsaturated Soils*. E.E. Alonso and P. Delage (Eds.), Balkema, Paris: Presses des Ponts et Chaussées, 3, 1323-1356.
- Wheeler, S. J., & Sivakumar, V. (1995). An elasto-plastic critical state framework for unsaturated soil. *Géotechnique*, 45(1), 35-53.
- Wiebe, B. J. (1996). The effect of confining pressure, temperature, and suction on the strength and stiffness of unsaturated buffer. *M.Sc. Thesis, Department of Civil and Geological Engineering, University of Manitoba, Winnipeg, Manitoba.*
- Wiebe, B., Graham, J., Tang, G. X., & Dixon, D. (1998). Influence of pressure, saturation, and temperature on the behaviour of unsaturated sand-bentonite. *Canadian Geotechnical Journal*, 35(2), 194-205.

- Williams, P. J. (1982). *The surface for the earth, an introduction to geotechnical science*. New York: Longman Inc.
- Williams, J., Prebble, R. E., Williams, W. T., & Hignett, C. T. (1983). The influence of texture, structure and clay mineralogy on the soil moisture characteristic. *Australian Journal of Soil Research*, 21, 15-32.
- Wind, G. P. (1955). Field experiment concerning capillary rise of moisture in heavy clay soil. *Netherland Journal of Agricultural Science*, 3, 60-69.
- Whitting, D. (1988). Permeability of selected concretes. ACI special publication. *Permeability of concrete SP-108*, 195-222.
- Yin, J. -H. (1990). Constitutive modelling of time-dependent stress–strain behaviour of soils. *Ph.D. Thesis, University of Manitoba, Winnipeg, Manitoba*.
- Yin, J. -H., & Graham, J. (1999). Elastic viscoplastic modelling of time-dependent stress–strain behavior of soils. *Canadian Geotechnical Journal*, 36, 736-745.
- Yong, R. N., & Warkentin, B. P. (1975). *Soil properties and behaviour, developments in geotechnical engineering*. New York, NY: Elsevier.

APPENDICES

Appendix 1. Verification of the BBM Implementation in FLAC for Constant Suction

A1. Summary

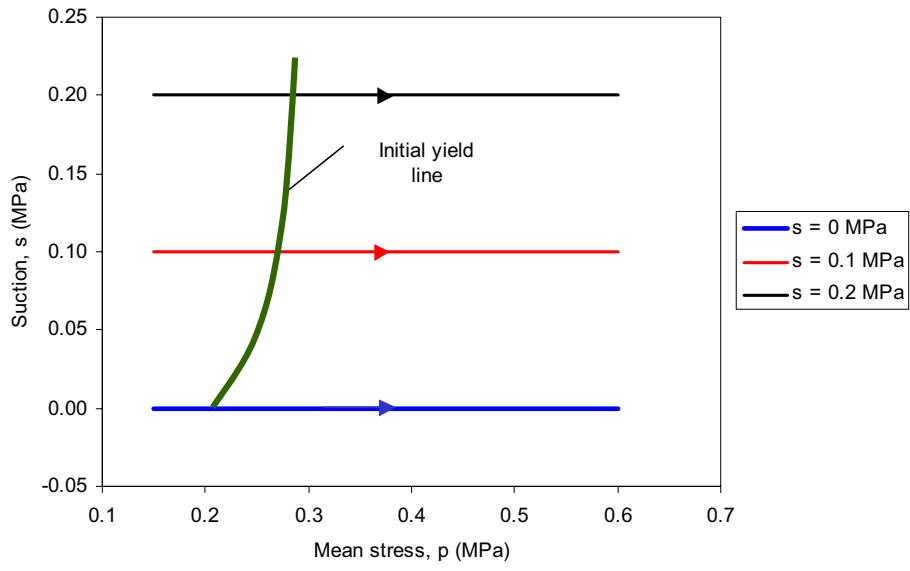
The objective of this section is to verify the implementation algorithm of the BBM (Alonso et al. 1990) in FLAC (Itasca 2000). The BBM is used to simulate an isotropic test with a constant suction using FLAC with a single axisymmetric finite difference grid. Stress path of this simulation is illustrated in Figure A1.1a. The BBM parameters are summarized are similar to those of Alonso et al. (1990):

$$\begin{aligned} \lambda(0) = 0.2 & \quad ; \kappa = 0.02 & \quad ; r = 0.75 & \quad ; \beta = 12.5 \text{ MPa}^{-1} ; p^c = 0.10 \text{ MPa} \\ \lambda_s = 0.08 & \quad ; \kappa_s = 0.008 & \quad ; G = 10 \text{ MPa} ; M = 1 & \quad ; k_s = 0.6 \end{aligned}$$

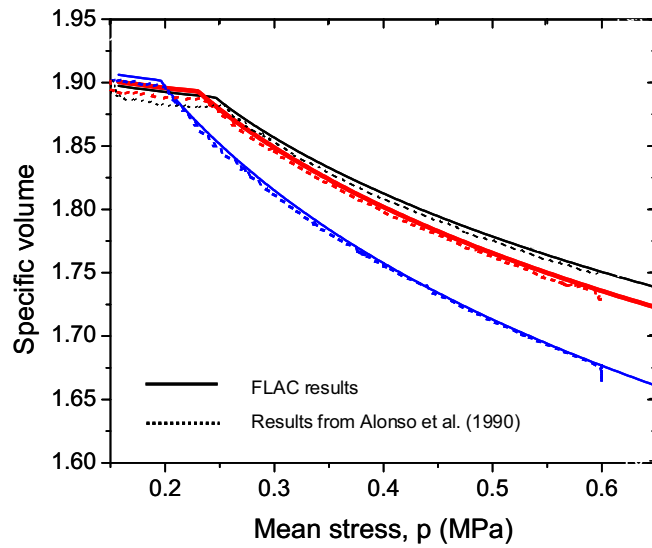
The initial volume for $s = 0.2 \text{ MPa}$ is 1.9, while the initial specific volumes v_0 for suction s of 0.0 and 0.1 are 1.909 and 1.903, which are calculated from:

$$dv = -\kappa_s \frac{ds}{(s + p_{at})} \quad (\text{A.1})$$

The boundary conditions and initial conditions are illustrated in Figure A1.2. The initial isotropic pressure ($\sigma_{xx}, \sigma_{yy}, \sigma_{zz} = -0.15 \text{ MPa}$) is applied at the boundary giving initial mean stress of 0.15 MPa (Figure A1.2). The velocities in axial and radial direction of $0.5 \times 10^{-5} \text{ m/s}$ are applied at the perimeter and the top of specimen to simulate the isotropic loading increase (Figure A1.2). This analysis is mechanical only analysis. The input data **Alonso01.dat** and constitutive model file **bbmtp.fis** are provided in Priyanto (2007). The results of this analysis are compared to the simulation results from the original publication by Alonso et al. (1990) in Figure A1.1b. The similarity of the FLAC response to the simulation from original publication (Alonso et al. 1990) in Figure A1.1b indicates that the algorithm used to implement the BBM constitutive models is sufficient.



(a)



(b)

Figure A1.1. The FLAC simulation results using the BBM compared with the results from Alonso et al. (1990) in: (a) p - s space; and (b) p - v space

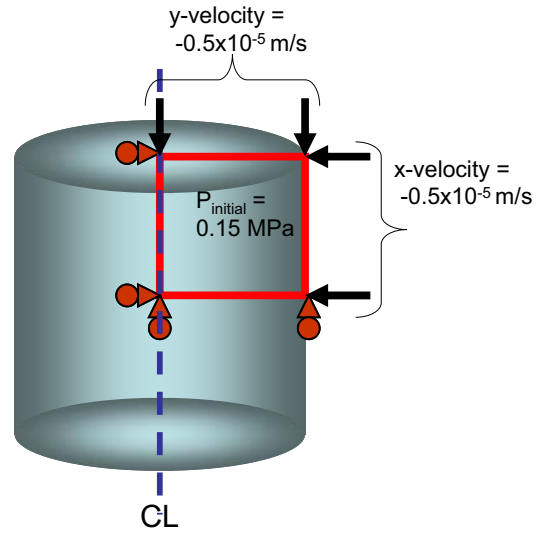


Figure A1.2. Boundary condition for isotropic loading test

Appendix 2. Verification of the Implementation of the BBM and the BGM in FLAC for H-M Analysis (Suction Changes)

A2.1 Summary

This objective of this section is to verify that the implementation algorithm used to implement the Basic Barcelona Model (BBM) (Alonso et al. 1990) and the BGM (Blatz and Graham 2003) for H-M Analysis. The BBM and the BGM are used to simulate two types of infiltration tests, constant volume and constant confining pressure tests. Single axisymmetric grid is used with two-phase flow option in FLAC is utilized to perform hydraulic-mechanical (H-M) analysis. The boundary and initial conditions of the tests are illustrated in Figures A2.1a-d. The BBM and the BGM constitutive models in FISH language (Itasca 2000) and the input data are provided in Priyanto (2007). The results are presented in Figures A2.2-A2.5.

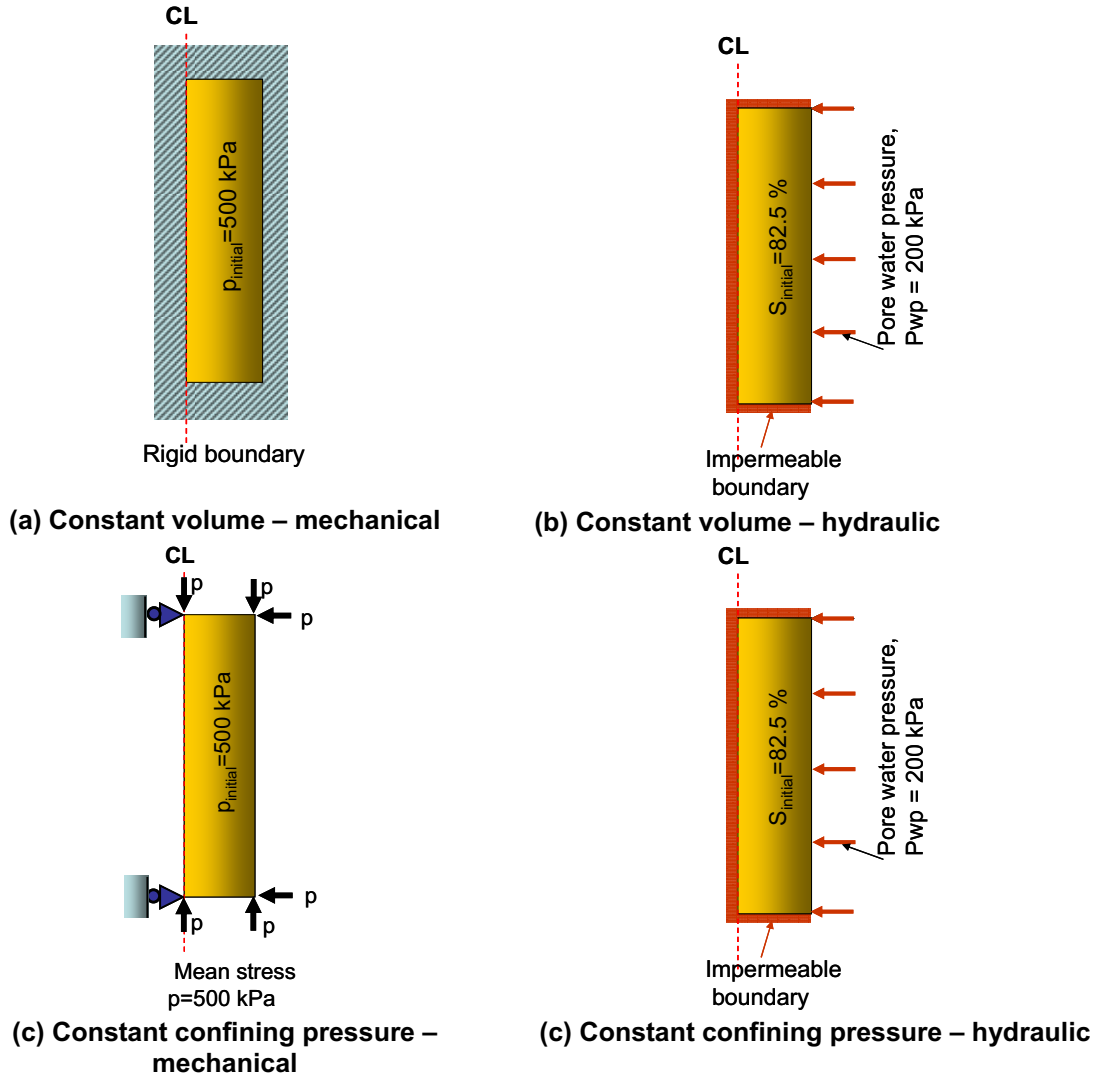
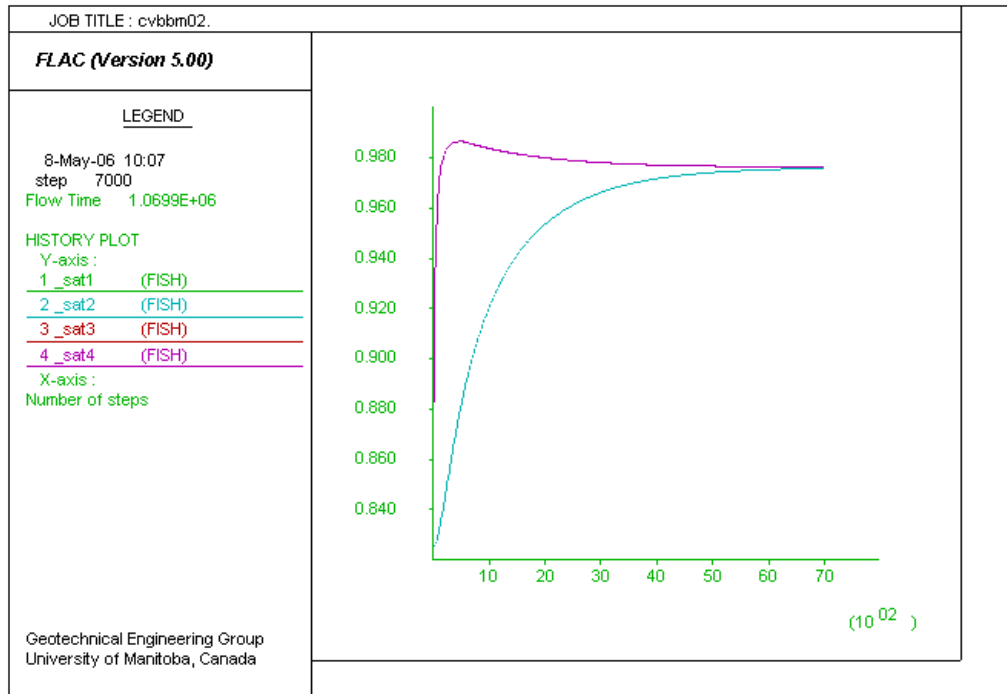
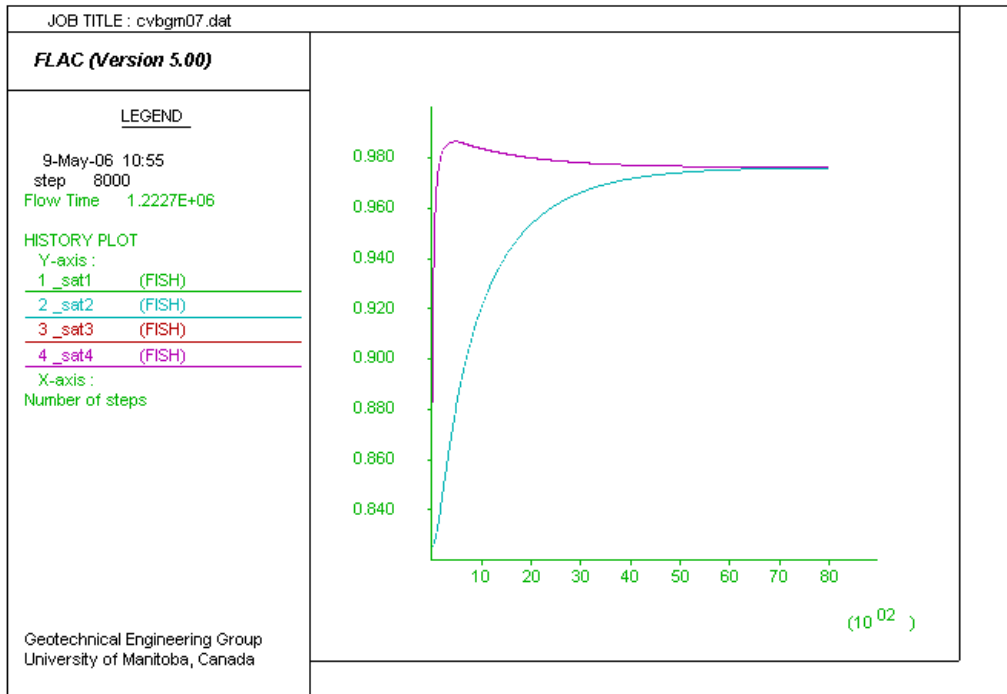


Figure A2.1 Boundary and initial conditions

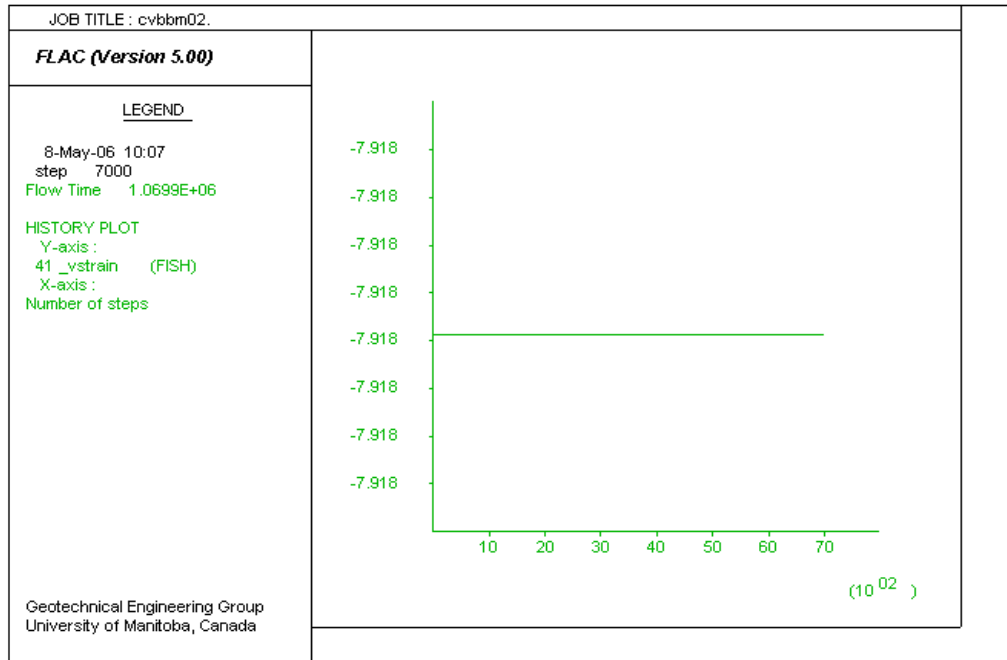


(a) BBM Model

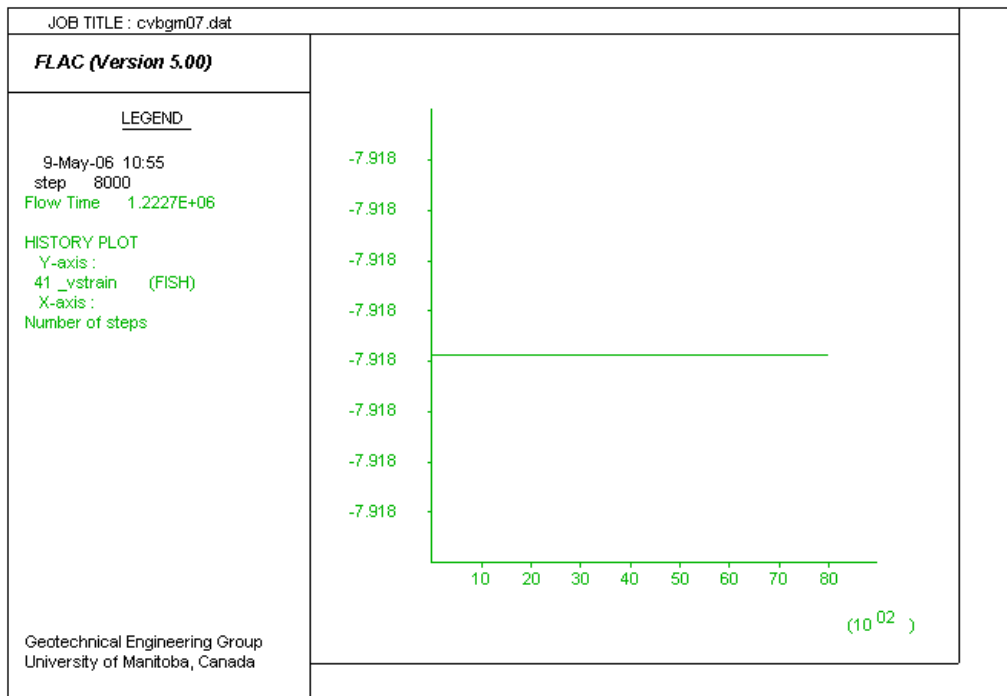


(b) BGM Model

Figure A2.2 Degree of saturation of the constant volume test using the: (a) BBM; (b) BGM

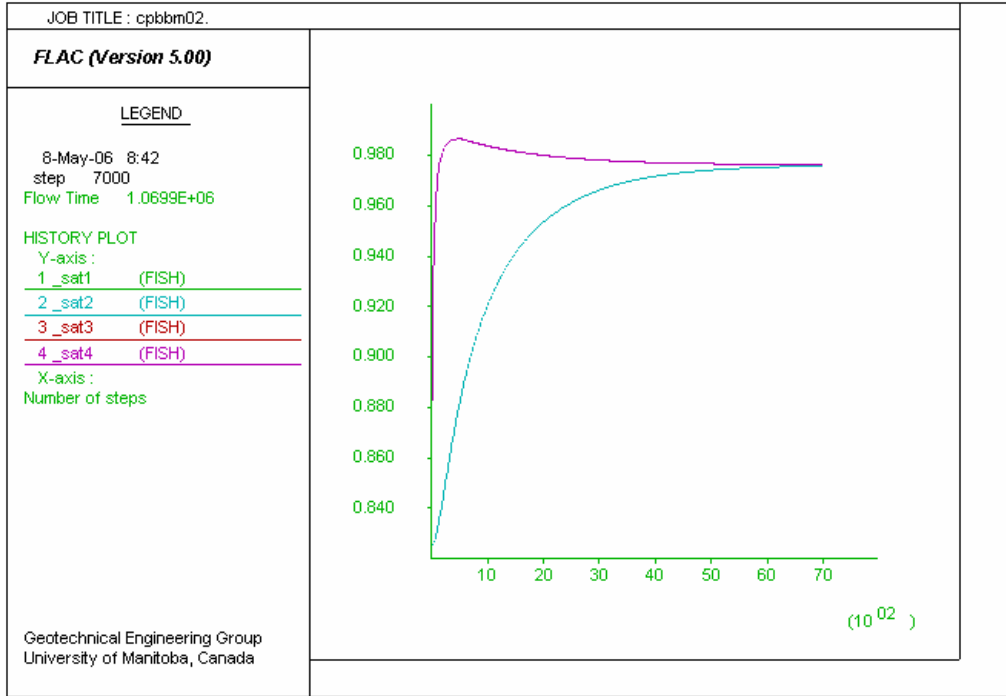


(a) BBM Model

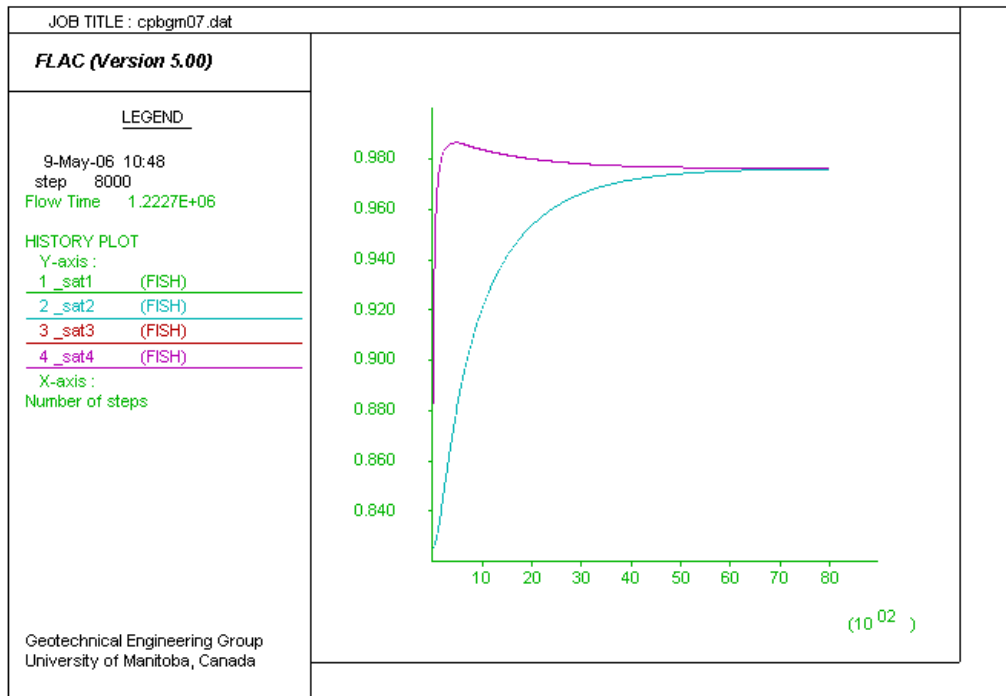


(b) BGM Model

Figure A2.3 Volume of the constant volume test using the: (a) BBM model; (b) BGM model

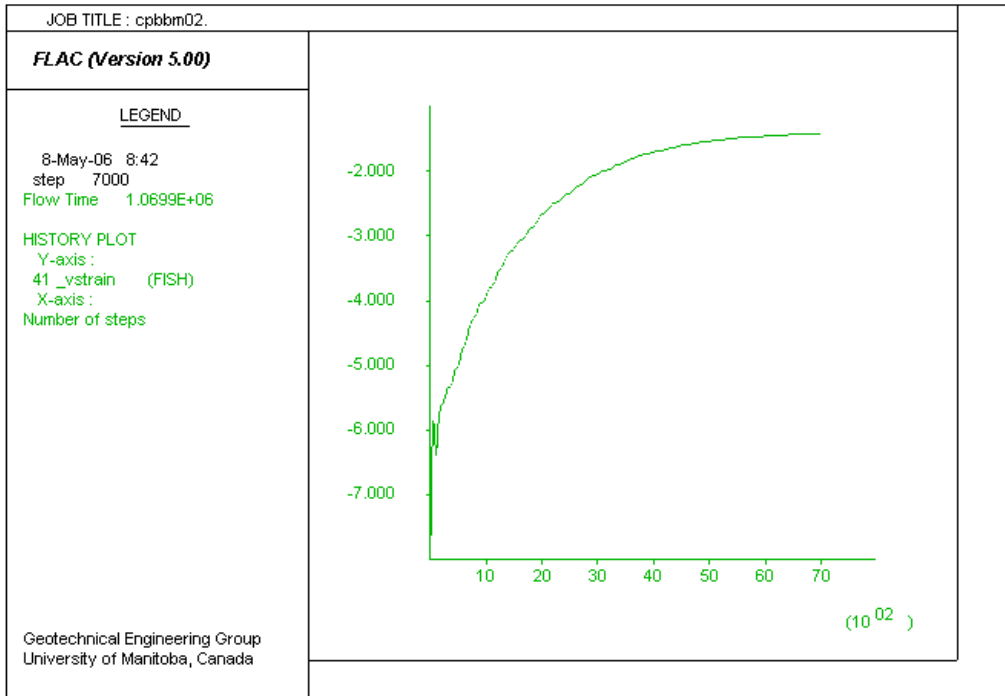


(a) BBM Model

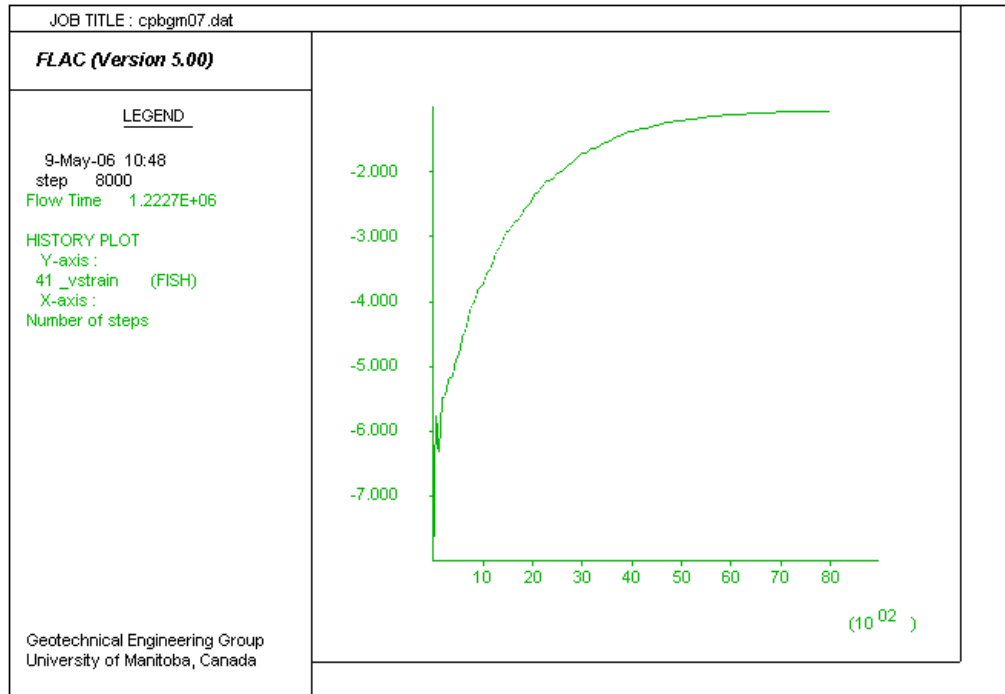


(b) BGM Model

Figure A2.4 Degree of saturation of the constant confining pressure test using the: (a) BBM; (b) BGM



(a) BBM Model



(b) BGM Model

Figure A2.5 Volume of the constant confining pressure test using the: (a) BBM; (b) BGM

Appendix 3.**Algorithm to Calculate Volume-Mass Relationships in FLAC****A3.1 Calculation of Volume Strain (N. K. Chandler, personal communication, 2006)**

Figure A3.1 illustrated the calculation of the rectangular area from the coordinates points. Assuming the node at (x_i, y_i) moves by dx_i and dy_i in the x and y directions respectively we can calculate the new area by substituting $x_i + dx_i$ for x_i . The change in area dA is simply $A(x_i+dx_i, y_i+dy_i) - A(x_i, y_i)$ (or $A' - A$). After expanding and collecting terms, the solution for the change in area is:

$$dA = (aa + bb + cc)/2$$

where:

$$aa = a_1 + a_2 + a_3 + a_4$$

$$bb = b_1 + b_2 + b_3 + b_4$$

$$cc = c_1 + c_2 + c_3 + c_4$$

and

$$a_1 = (x_1 + x_2) * (dy_1 - dy_2)$$

$$a_2 = (x_2 + x_3) * (dy_2 - dy_3)$$

$$a_3 = (x_3 + x_4) * (dy_3 - dy_4)$$

$$a_4 = (x_4 + x_1) * (dy_4 - dy_1)$$

$$b_1 = (dx_1 + dx_2) * (y_1 - y_2)$$

$$b_2 = (dx_2 + dx_3) * (y_2 - y_3)$$

$$b_3 = (dx_3 + dx_4) * (y_3 - y_4)$$

$$b_4 = (dx_4 + dx_1) * (y_4 - y_1)$$

$$c_1 = (dx_1 + dx_2) * (dy_1 - dy_2)$$

$$c_2 = (dx_2 + dx_3) * (dy_2 - dy_3)$$

$$c_3 = (dx_3 + dx_4) * (dy_3 - dy_4)$$

$$c_4 = (dx_4 + dx_1) * (dy_4 - dy_1)$$

for volume for the case of axi-symmetry add $\frac{\Delta r}{r}$ (which is very nearly the average of

$\frac{\Delta x}{x}$ for all four nodes of the element)

A3.2 Volume-Mass Relationship

The specific volume (v) of the element can be calculated from the volume strain e_v as: $v = v_{\text{initial}} \times (1 + e_v)$. where the v_{initial} is the initial specific volume. The other volume-mass relationship can be calculated using FLAC from this specific volume v and degree of saturation, S_w by assuming constant value of specific gravity G_s . In this study the specific gravity for BSB material is 2.7 (Graham et al. 1997). The other volume-mass relationships are calculated as follows:

Void ratio (e)

$$e = v - 1$$

Porosity (n)

$$n = \frac{e}{1 + e}$$

Gravimetric water content (w)

$$w_c = \frac{S_r \cdot e}{G_s}$$

Dry density (γ_{dry})

$$\gamma_{\text{dry}} = \frac{G_s \cdot \gamma_w}{1 + e}$$

Bulk density (γ_{bulk})

$$\gamma = \frac{(G_s + S_r \cdot e) \cdot \gamma_w}{1 + e}$$

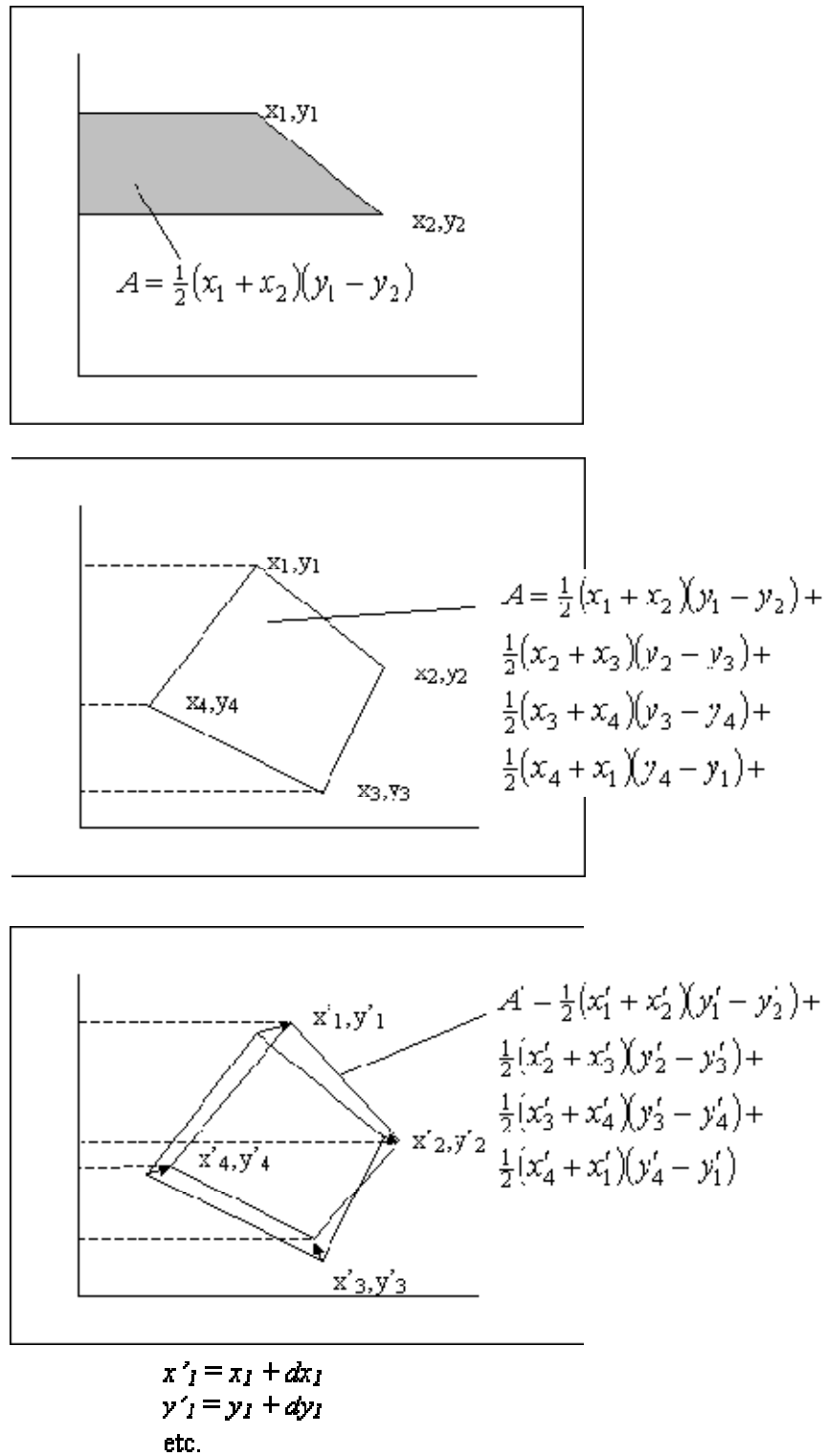


Figure A3.1 Calculation of the rectangular area from the coordinates points

Appendix 4. Input Data Files for Modelling Small-Scale Infiltration Test

A4.1. Linear Elastic Model

The input file for linear elastic model consists of:

- DAT files :
 - o cvle.dat for constant volume (CV) test.
 - o cmsle.dat for constant mean stress (CMS) test.
- FISH file:
 - o vol.fis to calculate volume-mass relationship and output.

A4.2. Blatz and Graham (2003) Model (BGM)

The input file for linear elastic model consists of:

- DAT files :
 - o cvbgm.dat for constant volume (CV) test.
 - o cmsbgm.dat for constant mean stress (CMS) test.
- FISH files :
 - o vol.fis to calculate volume-mass relationship and output.
 - o bgm2b.fis user-defined constitutive model

A4.3. Blatz and Graham (2003) Model with Porosity Dependent Permeability Model (BGM-kwn)

The input file for linear elastic model consists of:

- DAT files :
 - o cvbgmkwn.dat for constant volume (CV) test.
 - o cmsbgmkwn.dat for constant mean stress (CMS) test.
- FISH files :
 - o vol.fis to calculate volume-mass relationship and output.
 - o bgm2b.fis user-defined constitutive model

All the files are provided in Priyanto (2005)

Appendix 5. Input Data Files for Modelling Large Scale Isothermal Test

A5.1 Buffer Only Model (BO)

Input files for buffer-only model consists of the following files:

- isob01.dat
- iso01.fis

A5.2 Buffer-Rock Linear Elastic Model (BR-LE)

Input files for buffer-rock model with linear elastic constitutive model consists of the following files:

- isobr01.dat
- iso01.fis : FISH file to generate volume-mass relationship.

A5.2 Buffer-Rock using BGM (Blatz and Graham 2003) and Porosity-dependent Permeability Model (BR-BGM-kwn)

Input files for buffer-rock model with Blatz and Graham model (BGM) and porosity-dependent permeability model consists of the following files:

- isobr02.dat
- bct.fis : FISH file to generate volume-mass relationship.
- bgm2b00.fis : user-defined constitutive model

All the files are provided in Priyanto (2005).